

Syracuse University

SURFACE at Syracuse University

Dissertations - ALL

SURFACE at Syracuse University

8-23-2024

Studies Towards Improved Gravitational Wave Detector Thermodynamics

Daniel Vander-Hyde
Syracuse University

Follow this and additional works at: <https://surface.syr.edu/etd>



Part of the [Optics Commons](#)

Recommended Citation

Vander-Hyde, Daniel, "Studies Towards Improved Gravitational Wave Detector Thermodynamics" (2024).
Dissertations - ALL. 1987.
<https://surface.syr.edu/etd/1987>

This Dissertation is brought to you for free and open access by the SURFACE at Syracuse University at SURFACE at Syracuse University. It has been accepted for inclusion in Dissertations - ALL by an authorized administrator of SURFACE at Syracuse University. For more information, please contact surface@syr.edu.

Abstract

Since the first gravitational wave detection, the Laser Interferometric Gravitational Wave Observatories (LIGO) combined with an expanding and co-observing global gravitational wave network (i.e. Virgo, KAGRA) has worked to increase a novel and growing astronomical data catalog of gravitational wave detections. With each additional observing run, rates of detection continue to increase with iterative upgrades to detector technology. Discussed within this thesis are considerations pertinent to the improvement of Dual Recycled Fabry-Perot Michelson interferometer (DRFPMI) thermodynamics proposed during LIGO's third observing run (O3) for present and future detectors. The first chapter reviews fundamental material relevant to gravitational waves and how DRFPMI are used to detect them. The second discusses commissioning work on LIGO's thermal compensation system during O3 for detector operation at high power. The third introduces thermal noise and birefringent noise for a proposed highly reflective crystalline ($\text{GaAs}/\text{Al}_{0.92}\text{Ga}_{0.08}\text{As}$) coating candidate propped up for its ultra-low thermal noise properties. The fourth proposes a measurement strategy to acquire a calibrated electro-optic noise estimate. The fifth is a published paper providing a calibrated electro-optic response. The final chapter provides conclusive retrospection of the work covered in the prior chapters.

Studies Towards Improved Gravitational Wave Detector Thermodynamics

by

Daniel Vander-Hyde

B.S. California State University - Fullerton, 2015

M.S. Syracuse University, 2017

Dissertation

Submitted in partial fulfillment of the requirements

For the degree of

Doctor of Philosophy in Physics

SYRACUSE UNIVERSITY

August 2024

Copyright © Daniel Vander-Hyde 2024

All Rights Reserved

Acknowledgements

There are a number of people I'd like to thank who contributed significantly to my efforts contained in this dissertation:

First, I'd like to thank my advisor Stefan. The brilliant perspectives you provided never ceased to amaze me. Not only that, but the time while doing this dissertation work has been the most challenging of my life and you took time to let me learn in the lab at my own pace and surrounded me with wonderful collaborators.

To Fabian Magaña-Sandoval and Gabriela Serna. You were with me through the highest of highs and lowest of lows. The countless hours of engaging conversation in and out of the lab constantly live in my mind and the lessons taken from them are an invaluable part of who I am. I'm forever grateful to you both.

To Duncan Brown, for helping us grad students get that big picture perspective.

To Peter Saulson, for showing me that behind every idea there is a scientist who most likely spent a lot of time to formulate and organize it, and for the fantastic stories about quick and dirty solutions that are sometimes enough to do really interesting science.

To Erik Muniz, Ari Pedersen, Derek Davis, Varun Srivastava, Steven Reyes, Nick Didio, Soumi De, Daniel Finstad, and Elenna Capote for all the shared ideas, laughs, and tears that molded us through this common grad school experience.

To Lorena Magaña-Zertuche and Mike Senatore, for all the times we struggled and got through first year problem sets and practice exams together, all while still having fun.

To Thomas Vo, for keeping me in the loop during all the talks and meetings about the

Hanford detector and for reminding me the value in saying more with less.

To Satoshi Tanioka. Research during the pandemic was starting to feel tricky but the clear and fresh perspectives you brought to the lab kept me focused on the important things.

To the LIGO Hanford / Caltech crew. To Daniel Sigg, Shiela Dwyer, Jenne Driggers, Jeff Kissel, Peter King, Aidan Brooks, and Terra Hardwick for taking the time to teach me priceless skills and letting me heat the core optics all hours of the day. To Dan Brown, Georgia Mansell, and Craig Callihane for letting me stick by you all hours of the night poking at the detector while playing some of my favorite tunes. To Mike Laundry, Sheila, and Jenne, for reminding me of my humanness when working on ambitious scientific projects.

To Phil Arnold, Charlie Brown, and Dave Pratt. You treated me like family in the machine shop and humored all of my ideas. Thanks for your infinite patience and letting me get my hands greasy.

To Josh Smith and Mike Loverude, for showing me early on the joys of collaborative science.

To Jenny Ross, for helping provide practical solutions to organizing all the work I have done for the audience I want to reach.

To my family. My mom Michele, my sister Erin, my brother Mikey, my dad Charles, and my nana Alice. Without the love and hard work from you, I don't think I would have had the opportunity to satisfy the curiosity that this field has so far fulfilled. Thanks for believing in me.

To the Duffys. Your love, guidance, and understanding during these last few years have helped me immensely in completing this chapter of my life.

To Jimmy and Porkchop the dog. You're my world. Thanks for always grounding me.

Dedication

In memory of Michael (“Mikey”) Vander-Hyde (1990-2017)

Beloved brother, son, and friend.



Contents

1	Introduction	1
1.1	Gravitational waves	1
1.2	Detector configurations	3
1.2.1	Interferometry with a Michelson configuration	3
1.2.2	Fabry-Pérot Michelson (FPMI)	8
1.2.3	Dual-Recycled Fabry-Pérot Michelson (DRFPMI)	17
1.3	aLIGO	21
1.3.1	Thermodynamic considerations	21
2	Comissioning Adaptive Optics for O3a	25
2.1	Motivation	25
2.1.1	Thermal Compensation System	26
2.1.2	Thermo-optic transients	27
2.2	Dynamic Thermal Compensation	29
2.2.1	Reducing Parametric Instabilities	33
2.2.2	Limitations	34
2.3	A priori TCS pre-load methodology for O3a	35
2.4	A posteriori thermal compensation for O3a	37
2.4.1	Point absorption in O3a	37
2.5	Results	39

2.5.1	Custom CO2 mask	40
2.5.2	Beam position offset	40
2.5.3	Test Mass replacement	40
3	Introduction to thermal noise, birefringence, and electro-optical noise of highly reflective crystalline coatings	42
3.1	Motivation	42
3.1.1	Coating Thermal Noise	43
3.1.2	Coating Electro-optic Noise	47
3.2	Birefringence in zincblende materials	47
3.2.1	The Indicatrix	47
3.2.2	GaAs and Al _{0.92} Ga _{0.08} As crystal classification	49
3.2.3	Linear electro-optic effect (Pockel's effect)	50
3.2.4	New principal (electro-optic) dielectric axis for zincblende structures .	51
3.2.5	The photoelastic effect	52
3.2.6	The generalized indicatrix	52
3.3	Electro-optic noise of a GaAs / Al _{0.92} Ga _{0.08} As stack	53
3.3.1	Static Birefringence / Miller indices from a HR GaAs / Al _{0.92} Ga _{0.08} As coating	53
3.3.2	Electro-optic coupling to the reflected phase of a HR mirror coating .	55
3.3.3	Initial projected DARM coupling	58
4	Measurement of electro-optic noise in a GaAs/Al_{0.92}Ga_{0.08}As mirror coating	59
4.1	Electro-optic measurement apparatus	59
4.1.1	Servo Parameters	60
4.2	FSS transfer function (LTSPICE)	62
4.2.1	Longitudinal Pockels Cell mirror mount assembly	65
4.2.2	Assembly Mount Tests/Development	69

5	Study on electro-optic noise in crystalline coatings toward future gravitational wave detectors	79
5.1	Foreword	79
5.2	Introduction	79
5.3	Theory of electro-optic effect	80
5.4	Experiment	83
5.4.1	Setup	83
5.4.2	Axis identification	87
5.4.3	Measurement scheme	88
5.4.4	Calibration	89
5.5	Results	94
5.6	Discussions	96
5.6.1	Comparison to theoretical estimation	96
5.6.2	Implications for gravitational wave detectors	99
5.7	Conclusion	103
5.8	Acknowledgments	104
6	Conclusion	105
6.1	Adaptive optics comissioning	105
6.2	GaAs/Al _{0.92} Ga _{0.08} As Electro-optic noise	106
	Appendices	108
A	Paraxial equation	109
B	Cavity stability criteria ($G(g_1, g_2)$)	110
C	The Equipartition theorem and the Fluctuation dissipation theorem	111
D	Misc. thermo-optic filters	112
D.1	COMSOL self heating filter	112
D.2	CO2 filter	112

E	Thermo-optic Path Distortion	113
E.1	Thermorefractive aberration	113
E.2	Thermoelastic aberration	113
F	CO2 mask	114
G	Anisotropic media	115
G.1	Monochromatic plane wave propogation	115
G.2	The Dielectric tensor	116
H	EO Modulation (Application)	118
I	Miller indices for highly reflective GaAs/Al _{0.92} Ga _{0.08} As coatings	120
J	Laplacian in Cylindrical coordinates (Numerical Recipe)	121
K	Mode matching data for Electro-optic sample cavity	126
K.1	Pre MMT beam scan	126
K.2	Post MMT beam scan	127
L	Interferometer Configurations (code)	128
L.1	ifo_configs.py	128
L.2	MICH	130
L.3	FPMI	134
L.4	DRFPMI	140
M	RH control pre-filter	150
M.1	recipe	150
M.2	code	151
N	LaplacE code	165
N.1	laplace.py	165
N.2	set_params.py	175
N.3	run.py	182
O	Calibration code	189

References

Relevant Publications

- T. Hardwick, V. J. Hamedan, C. Blair, A. Green, and D. Vander-Hyde, “Demonstration of dynamic thermal compensation for parametric instability suppression in advanced ligo,” *Classical and Quantum Gravity*, vol. 37, p. 205021, Sep 2020
- A. Buikema, C. Cahillane, G. L. Mansell, C. Blair, R. Abbott, . D. Vander-Hyde ..., and J. Zweizig, “Sensitivity and performance of the advanced ligo detectors in the third observing run,” *Phys. Rev. D*, vol. 102, p. 062003, Sep 2020
- S. Tanioka, D. Vander-Hyde, G. D. Cole, S. D. Penn, and S. W. Ballmer, “Study on electro-optic noise in crystalline coatings toward future gravitational wave detectors,” *Phys. Rev. D*, vol. 107, p. 022003, Jan 2023

Chapter 1

Introduction

1.1 Gravitational waves

“Space-time tells mass how to move; mass tells space-time how to curve” can provide a concise and sufficient summarization of Einstein’s theory of general relativity (GR). While providing the most complete theory of gravity to date, GR provides tools that allow considerations of high energy astrophysical phenomena (highly massive binary coalescences, spherically asymmetric compact objects, etc.) whose fractional mass/energy output generate distortions in space-time known as gravitational waves (GW). This is represented as a perturbation ($|h_{\mu\nu}| \ll 1$) in the Minkowski metric tensor defining a local linearized space-time [4]:

$$g_{\mu\nu} = \eta_{\mu\nu} + h_{\mu\nu}$$

The wave-like behavior for $h_{\mu\nu}$ is realized after imposing the Lorentz gauge; producing 10 harmonic wave amplitudes from the Einstein field equations. Imposing a wave vector (k_j) onto one of three linearly independent spatial coordinates ($h^{ij}k_j$), the non-trivial amplitudes from the equations imply a transverse and traceless (h_i^i) gauge [5]:

$$\nabla^2 h_+ - \frac{1}{c^2} \frac{\partial}{\partial t} h_+ = 0$$

$$\nabla^2 h_\times - \frac{1}{c^2} \frac{\partial}{\partial t} h_\times = 0$$

In other words, there exists a wave solution with two separate transverse polarizations h_+ and h_\times with a 45° separation between them.

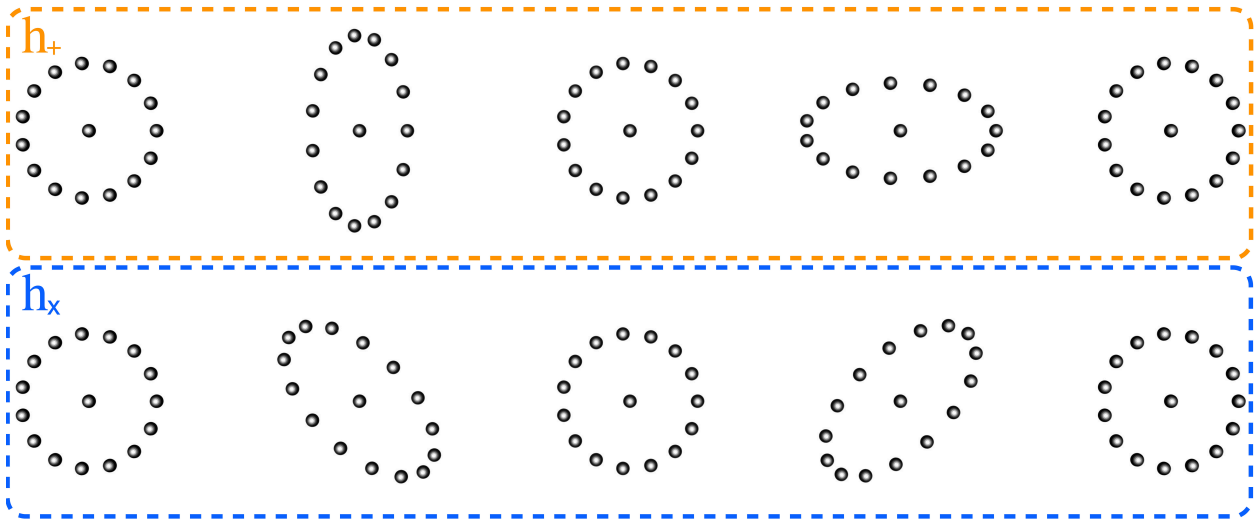


Figure 1.1: A stop motion pictograph displaying the influence of a single gravitational wave period from the two polarizations on a ring of particles. The top row shows the influence of the ‘+’ polarization while the bottom row demonstrates that of the ‘ \times ’ polarization

When measured and analyzed, these waves allow astronomers to extract novel information from their progenitors through the testing of various hypotheses pertinent to the violent dynamics of these systems. On September 14th, 2015 the Laser Interferometric Gravitational Wave Observatories made the first direct gravitational wave detection from a pair of coalescing black holes 1.3 billion light years away, and since then other gravitational wave detectors (i.e. Virgo, KAGRA) have joined the search; continuing the search for novel events. The current GW detector network has developed a track record with an ever increasing list and rate of detections including the first multimessenger event and a surprising population of compact binary coalescences [6, 7, 8].

A more experienced reader may be familiar with the following primer to gravitational wave instrumentation, but it is all done with the hope of providing context of novel contributions within the body of this work while also demonstrating reverence to those whose work prior made this dissertation possible.

1.2 Detector configurations

The current gravitational wave detector network primarily uses terrestrial bound Dual-Recycled Fabry-Pérot Michelson interferometers; though to configure them into a state of observing, fundamental modes of operation are necessary to acquire first. A quick review of these modes provides some of the basic “whats” and “hows” of detector operation with the intention of developing a holistic view of the LIGO detection schema especially as it pertains to the studies to be discussed. Most introductory detector configuration discussions start with the Michelson interferometer and end at the dual-recycled Fabry-Pérot Michelson interferometer; this section follows in kind. Alongside the discussion are citations providing exceptional alternative and more detailed explanations of topics discussed.

1.2.1 Interferometry with a Michelson configuration

The Michelson interferometric detection schema (aka “The Michelson”), used by Michelson and Morley to test the existence of luminiferous aether, demonstrates inherent potential for measuring gravitational wave amplitudes generated by time varying quadrupole moments with high energy astrophysical progenitors; making it a prime candidate as a gravitational wave detector / observatory. The interferometry begins with a beam of coherent laser light split at a 50/50 beamsplitter (BS) along two perpendicular beam paths with respective lengths L_x and L_y , set by highly reflective end mirrors (ETMX, ETMY). Upon arrival at the length terminating mirrors, the respective beams are back-reflected towards the beam splitter where they are made to interfere. The fringe power from this interference is measured

at the anti-symmetric port photodiode, assuming we're operating on a half-fringe:

$$P_{\text{out}} = \frac{P_{\text{in}}}{2} \left[1 + \cos\left(\frac{4\pi}{\lambda}(L_x - L_y)\right) \right] \quad (1.1)$$

The Michelson detects microscopic differential length changes on the order of a fractional wavelength of the light used and are more aptly discussed as differential phase ($\Delta\phi(t)$) between the returning perpendicular phasefronts ($\phi_x(t)$, $\phi_y(t)$). Understanding this inherent method of detection, a time-varying metric perturbation ($h(t)$), like that generated from a gravitational wave, is tested on a Michelson interferometer with a nominal arm length of L and a laser with optical angular frequency of Ω :

$$\Delta\phi(t) = \phi_x(t) - \phi_y(t) = \int_{t-2L/c}^t \Omega \left[1 + \frac{1}{2}h(t) \right] dt - \int_{t-2L/c}^t \Omega \left[1 - \frac{1}{2}h(t) \right] dt \quad (1.2)$$

Evaluating the above as a function of frequency yields:

$$\Delta\phi(\omega) = h_0 \frac{2L\Omega}{c} e^{-iL\omega/c} \frac{\sin(L\omega/c)}{L\omega/c} = h_0 \cdot H(\omega, \phi_0) \quad (1.3)$$

With the wave amplitude h_0 , angular frequency ω , nominal interferometer arm length L , and speed of light c . The differential phase Equation 1.3 combined with the power at the anti-symmetric port Equation 1.1 provides a function of optical gain, dependent on frequency and a differential offset phase (ϕ_0):

$$\Delta P(\omega, \phi_0) = h_0 \frac{P_{\text{in}}}{2} \Delta\phi(\omega) \cdot \sin(\phi_0) \quad (1.4)$$

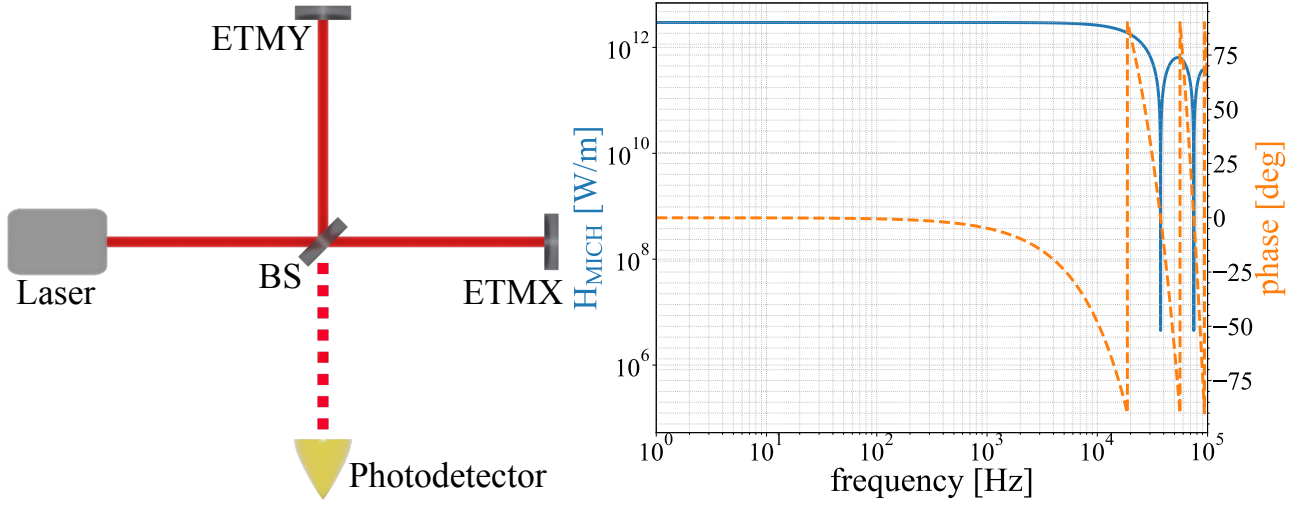


Figure 1.2: [Left] A simplified schematic of a Michelson interferometer. [Right] The associated optical transfer function with $H(\omega, \pi/2)$ defining the optical gain of a Michelson interferometer with 4 km long arms and an input power of 25 [W]

Assuming a 4km arm configuration with 25 Watts input power as indicated in figure Equation 1.3 the differential arm response provides a reasonable optical gain with the notches correlating to an integer number of gravitational wave half periods ($n\lambda_{gw}/2$) to the interferometer arm length in such a way that the response is null for corresponding frequencies. Though with sights set on optimizing detection bandwidth for neutron star (NS) binaries @ 100 Hz, the basic Michelson optical gain remains insufficient, with enhancements required. This is better visualized by computing the shot noise limited Michelson sensitivity which does not reach the requirement to confirm a NS-NS coalescence ($\approx 10^{-21} [\frac{1}{\sqrt{\text{Hz}}}]$) but demonstrates the high sensitivity of a Michelson interferometer to differential motion, and the promise of laser interferometers to detect GWs [9].

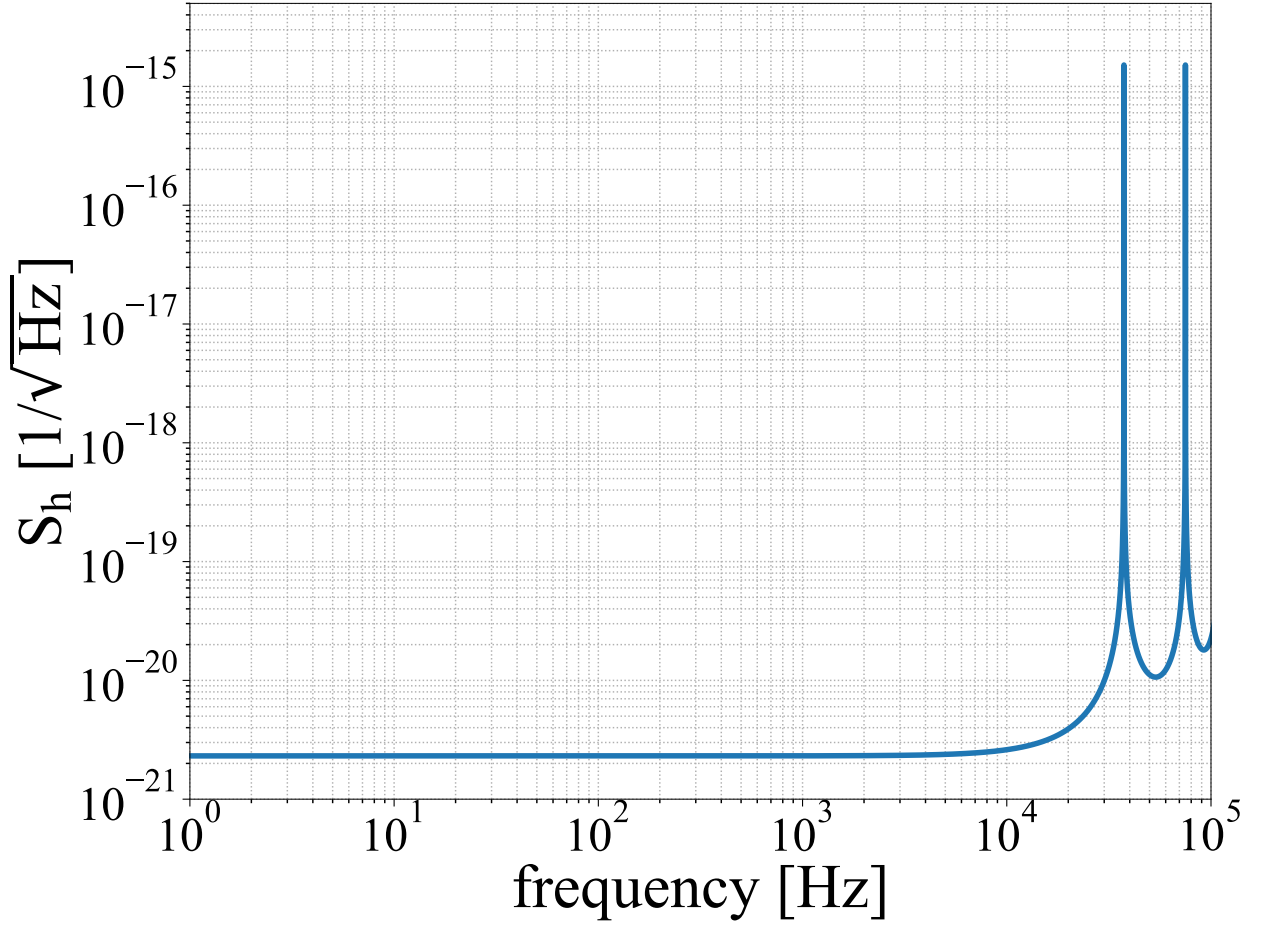


Figure 1.3: Shot noise limited sensitivity ($\sqrt{\hbar\Omega P_{\text{in}}}$) of a Michelson with 4 km long arms and an input power of 25 [W]. Compared to the a priori estimate of 10^{-21} [$\frac{1}{\sqrt{\text{Hz}}}$] the signal to noise (SNR) comes to be unity. The desired confidence is set at a much higher standard (a priori) with more unquestionable measurements set at $\text{SNR} = 5$.

1.2.1.1 Contrast (Mode Matching Pt. 1)

As presented, the functional behavior of the simple Michelson is to perform optical autocorrelation; though overly simplified depictions of interferometry suggest operation by periodic planar phasefronts and omit the full reality of Gaussian beam propagation. A standard laser carrier beam mode is represented by the Gaussian beam (TEM00 mode) with wavelength λ , and propagation axis (z):

$$E(r) = E_o \frac{\sqrt{[\lambda z_o]/\pi}}{W(z)} e^{-r^2/W^2(z)} e^{-ikz - ik[r^2/(2R(z))] + i\zeta(z)} \quad (1.5)$$

Where E_o is a complex field amplitude, $r^2/(2(R(z)))$ defines transverse coordinates $r = \sqrt{x^2 + y^2}$ on a hemisphere of uniform phase with a radius of curvature $R(z)$, k is the wave number, $W(z)$ is the radius from the beam axis that contains $(1 - 1/e^2) \times 100\%$ of the integrated beam power, and ζ is the Gouy phase [10].

An important consideration to make for any sufficiently long arm length (like that used for LIGO), is avoiding significant power loss due to beam divergence for the designed Michelson arm length, sans sufficiently large core optics. LIGO and most other terrestrial GW detectors manage with curved end mirrors that match and focus the impinging hemispherical wavefronts; symmetrically back-propagate them in each arm to maintain optimal interference at the beamsplitter. Mode overlap η provides a useful metric of this optimization:

$$\eta = \left| \int E_x E_y dA \right|^2 / (P_x P_y) \quad (1.6)$$

Significant length offsets between the arms reduce the integrated phasefront overlap and contribute to sub-optimal interference of the beam mode wavefronts at the beamsplitter. And even without 2D beam profiles at the output, measuring the dark and bright fringe power on single element photodiodes and computing contrast a.k.a interferometer visibility (ν) may do just as well without more involved beam mode analysis:

$$\nu = \frac{P_{\max} - P_{\min}}{P_{\max} + P_{\min}} \quad (1.7)$$

Operating on a scale from 0 to 1, $\nu \leq 1$ can be an indication of : mode mismatch at the beam splitter and/or asymmetrical optical loss. From a mode matching perspective $\nu = 1$ represents a mode overlap of $\eta = 100\%$ (assuming no optical loss and balanced reflectivities between the two mirrors $\nu_x = \nu_y$). Though optical losses and aberrations are often asymmetrically introduced between the orthogonal beam paths that often limit optimal interference and are indiscriminately accounted for in contrast measurements.

1.2.2 Fabry-Pérot Michelson (FPMI)

At the time of the LIGO proposal, constraints (physical and financial) for terrestrial gravitational wave detectors required a compact solution for increasing length (L) of the Michelson arms so to increase the beam phasefront lifetime within the Michelson arms. Two proposed arm folding techniques were considered: the Herriot Delay Line and the Fabry-Pérot cavity, though the Fabry-Pérot cavity is currently the predominant choice.

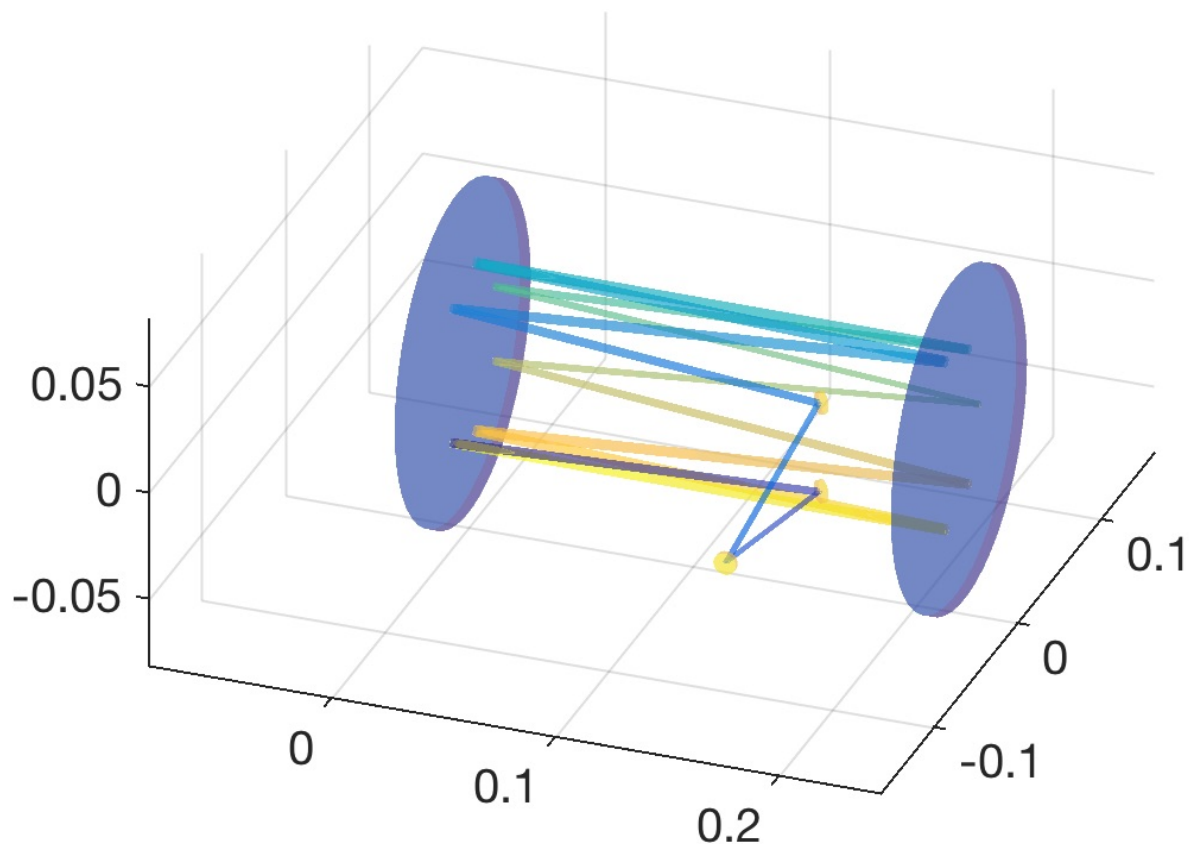


Figure 1.4: A 12 bounce Herriot Delay Line with a small mirror input / output couplers inserted into the beam path.

1.2.2.1 The Fabry-Pérot cavity

To inform of a folding mechanism, consider coherent light encountering an optical cavity with input and output mirror transmission and reflection coefficients of t_1 , r_1 and t_2 , r_2 respectively (assuming lossless mirrors $L_1 + L_2 = 0$).

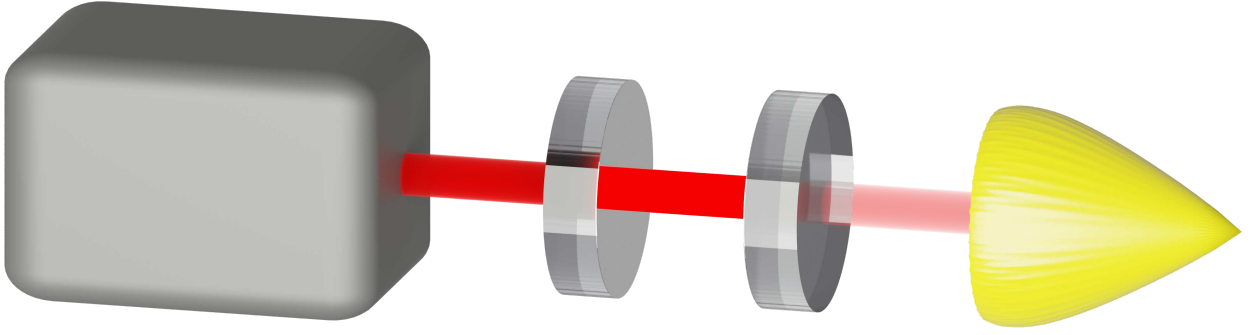


Figure 1.5: Figure of a Fabry Perot Cavity

Light enters the cavity only after passing the input mirror with the trivial solution indicating a field amplitude reduction proportional to the mirror reflection coefficient. Though by tuning the length between the input and end mirrors to an integer multiple of the beam wavelength, circulating light coherently adds with the input, achieving resonance. A cavity of length L , when configured, yields the following cavity reflection and transmission coefficients:

$$r_c = -r_1 + \frac{t_1^2 r_2 e^{-i2kL}}{1 - r_1 r_2 e^{-i2kL}} \quad (1.8)$$

$$t_c = \frac{t_1 t_2 e^{-ikL}}{1 - r_1 r_2 e^{-i2kL}} \quad (1.9)$$

Maintaining resonance for highly reflective mirrors and short wavelength light (i.e. λ 1064nm) requires strict length tuning ($\leq 1e-7$ [m]).

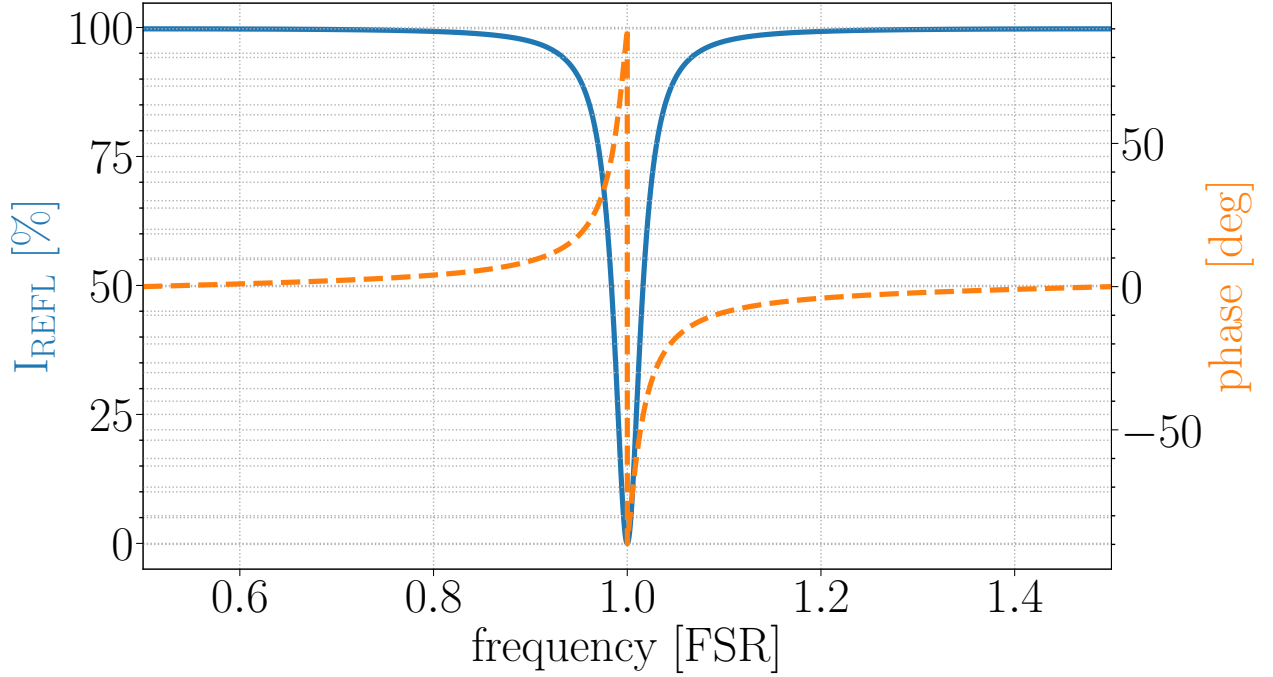


Figure 1.6: Reflected cavity intensity (I_{REFL}) around resonance. The resonance peak full width half maximum is set by mirror reflectivities and is succinctly quantified by the cavity **finesse** ($\mathcal{F} = \frac{\text{FWHM}_{\text{res}}}{f_{\text{FSR}}} = \frac{\pi\sqrt{r_1 r_2}}{1-r_1 r_2}$).

The ratio between circulating and cavity input power is set by the reflectivity parameters of the cavity mirrors, demonstrating the correlation to how long a given phasefront can remain stored between said mirrors at resonance. This “cavity storage time” ($\tau_s \propto Lr_1 r_2$) translates as a length elongation with the phasefront travel history encoded in the arrival time of its photons back at the beam splitter.

1.2.2.1.1 “Arm elongation”

An intuitive analogue of the Fabry-Pérot’s arm elongation capabilities is better illustrated when comparing against a computed Delay Line storage time (with \mathcal{N} number of bounces and length L) [9]:

$$\tau_s^{\text{DL}} = \frac{2\mathcal{N}L}{c} \quad (1.10)$$

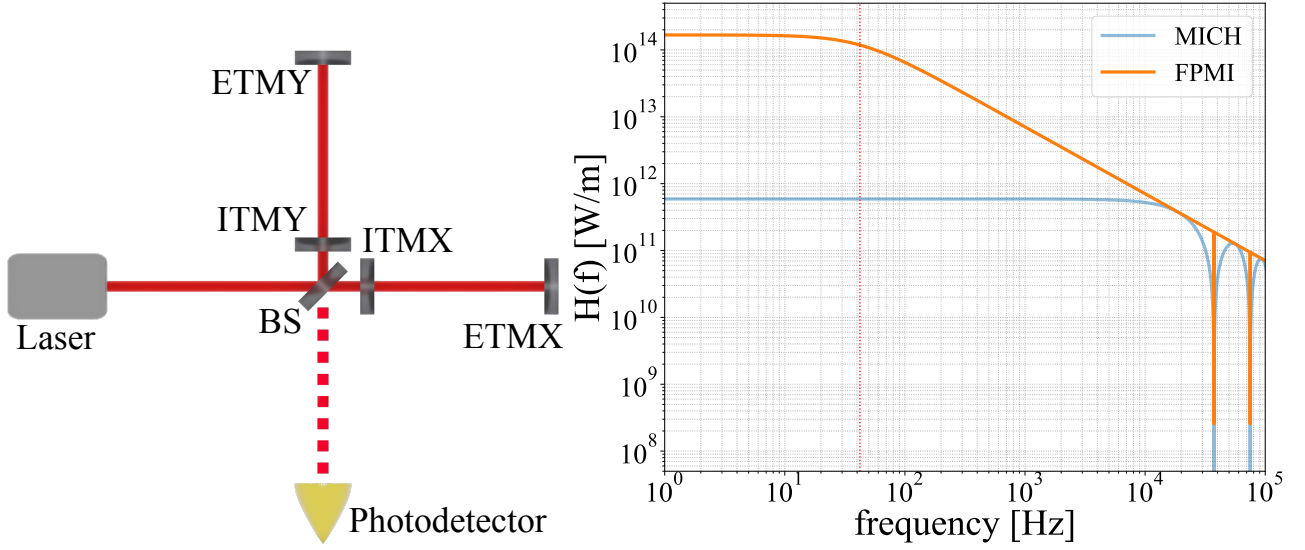


Figure 1.7: [Left] The Fabry-Pérot Michelson optical schema and [Right] an associated optical gain.

$$\tau_s^{\text{FP}} = \frac{L}{c} \frac{r_1 r_2}{1 - r_1 r_2} = \frac{1}{4\pi\mathcal{F}} \quad (1.11)$$

Advanced LIGO, with its 4km length and approximate finesse of 208 correlates to a storage time of $382\mu\text{s}$, whereas the simple Michelson has an arm storage time of $26\mu\text{s}$. The cooresponding optical gain increase is noted in Figure 1.7.

$$H_{\text{FPMI}} = \frac{t_1^2 r_2}{(t_1^2 + r_1^2)r_2 - r_1} \frac{H_{\text{MICH}}}{1 - r_1 r_2 e^{-2i\omega L/c}} \quad (1.12)$$

The noted gain improvements made by adding two mirrors to the optical schema are substantial, though in practice the benefits are contingent upon: 1) maintaining fixed mirror positions within a fraction of the wavelength of the light used and 2) reducing detector bandwidth. But with tools like the Pound-Drever-Hall (PDH) technique and signal recycling to mitigate these respective burdens, achieving sensitivities like those in Figure 1.7 becomes possible.

1.2.2.1.2 The Pound-Drever-Hall servo

The Pound-Drever-Hall technique, originally and commonly used for laser frequency stabilization to an ultra-stable length reference, allows the tracking of the linear phase response of an input carrier field through cavity resonance. The servo fully realizes the ability of an optical cavity to act as a length / frequency discriminator [11]:

$$\frac{\Delta f}{f} = -\frac{\Delta L}{L} \quad (1.13)$$

The alternative side-of-fringe lock provides a linear response in intensity, which is adequate for some applications but with reduced sensitivity due to the required power reduction by operating off resonance. Measurements of phase are extracted through an optical heterodyne; the co-propagation of a separate (but phase-locked) optical field with a known frequency separation to the carrier reflected from the cavity input [12]. The PDH servo bypasses the need for a complicated phase-locked two laser configuration by imposing a phase modulation of frequency Ω onto the carrier field with frequency ω via an electro-optic modulator (aka Pockels cell) § H:

$$E_{\text{mod}} = E_0 e^{i\omega t + \beta \sin(\Omega t)} \approx E_0 [J_0(\beta) e^{i\omega t} + J_1(\beta) e^{i(\omega + \Omega)t} - J_1(\beta) e^{i(\omega - \Omega)t}] \quad (1.14)$$

Where the Jacobi-Anger approximation has been used to characterize the modulated field into three different field components using the zeroeth order (J_0) and first order (J_1) Bessel functions of the first kind.

Setting a photodiode in reflection of the cavity with length (L) and a reflectivity coefficient of $r_{\text{cav}}(\omega, L)$, we measure the reflected power of the modulated input field E_0 given by Equation 1.14 :

$$\begin{aligned}
P_{\text{refl}} &\approx |E_{\text{refl}}|^2 \\
&\approx E_0^2 \left\{ J_0^2 |r_{\text{cav}}(\omega, L)|^2 + J_1^2(\beta) |r_{\text{cav}}(\omega + \Omega, L)|^2 - J_1^2(\beta) |r_{\text{cav}}(\omega - \Omega, L)|^2 + \right. \\
&\quad \left. J_0 J_1(\beta) [r_{\text{cav}}(\omega, L) r_{\text{cav}}^*(\omega + \Omega, L)] - J_0 J_1(\beta) [r_{\text{cav}}(\omega, L) r_{\text{cav}}^*(\omega - \Omega, L)] \right\} \quad (1.15)
\end{aligned}$$

The two trailing terms in the above equation for P_{refl} generate a beat frequency term between the carrier and lower / upper sidebands. The magnitude and sign of these beat terms directly relate to the phase of the reflected carrier field and can be measured and transformed to the error signal seen in Figure 1.8 using resonant electronics (tuned to a chosen sideband frequency) for amplification and a mixer for demodulation.

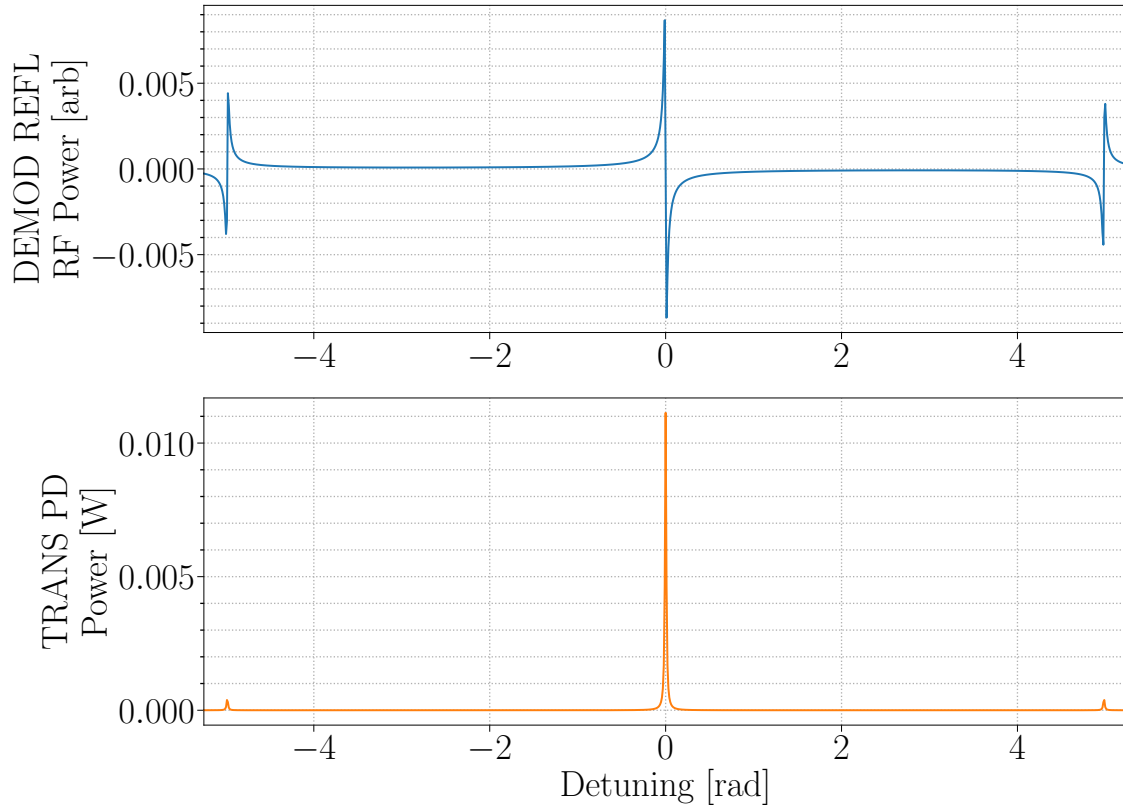


Figure 1.8: By imposing 25 MHz RF sidebands, a pair of reflected reference fields near carrier resonance are off cavity resonance while beating with the carrier and provide a linear response after demodulating the sideband power. With the introduction of high and low frequency sideband fields, their presence is also detected through the DCPDs and PDH error signal. Their separations from carrier resonance are equal in phase (length, and frequency) [13].

With this linearity and sensitivity at cavity resonance, implementation into PID feedback is the next task as any small detuning of the cavity can be registered as a drift from the loop's zero point and fed back to an actuator with an estimated calibration gain factor. When implemented into a low-noise design, this servo can also be used for precision length control, or a high sensitivity lock-in measurement; and with well characterized instrumentation, calibration of the induced differential phase of the light within the stable reference cavity into differential length (or frequency) [12].

1.2.2.1.3 Gaussian and Higher Order Modes (Mode Matching pt.2)

There are some additional caveats before exploiting any potential enhancement from the Fabry-Pérot when imposing a Gaussian beam. First is that of beam divergence, which can quickly limit the stored power between two flat finite sized mirrors (see § B). Though, as addressed for the simple Michelson, curving end mirrors focuses the Gaussian beam power and can also increase resonance robustness curving one or both cavity mirrors.

Additionally mentioned is the importance of the overlap between mirror radii of curvature to the beam phasefront. For resonators this becomes increasingly critical as the placement of mirrors with established curvatures (defining the cavity mode) need to be placed such that they preserve the TEM00 beam mode. Beam optics inform solutions for optimal mirror placement for a given incident beam and vice versa. The exercise sets the importance of matching the **Gaussian beam mode** to the spherical mirror **FP resonator mode**, but less obvious are the implications if there is a perturbation from the set solution. Alongside the TEM00 fundamental mode, the paraxial equation § A also produces families of solutions that exist for the two mirror cavity configuration, characterized by the Hermite-Gauss and Laguerre-Gauss bases:

Hermite-Gauss modes

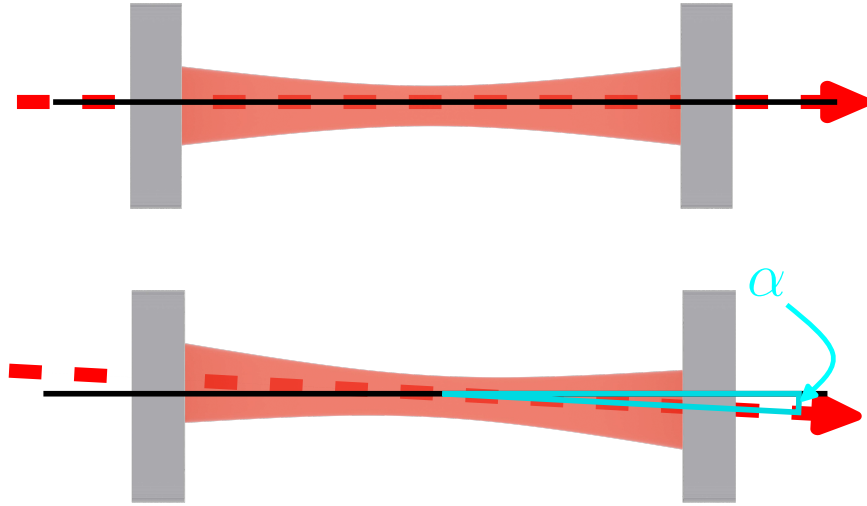


Figure 1.9: Figure depicting cavity-beam alignment (above) vs cavity-beam misalignment (below) with a angle α between the beam and cavity axes.

$$\begin{aligned}
 TEM_{n,m}(x, y, z) = & E_o \frac{\sqrt{[\lambda z_o]/\pi}}{W(z)} \mathbb{H}_n\left(\frac{\sqrt{2}x}{W(z)}\right) \mathbb{H}_m\left(\frac{\sqrt{2}y}{W(z)}\right) \\
 & \times \exp\left(\frac{-(x^2 + y^2)}{W^2(z)}\right) \exp\left(-ikz - ik\frac{x^2 + y^2}{2R(z)} + i(1 + n + m)\zeta(z)\right)
 \end{aligned}
 \tag{1.16}$$

As intensity, power and mode overlap are common computations, the Gaussian integrals might be more quickly expressed and computed with the more convenient bra-ket notation:

$$TEM_{n,m}(x, y, z) \rightarrow |U_{n,m}(x, y, z)\rangle$$

Laguerre-Gauss modes

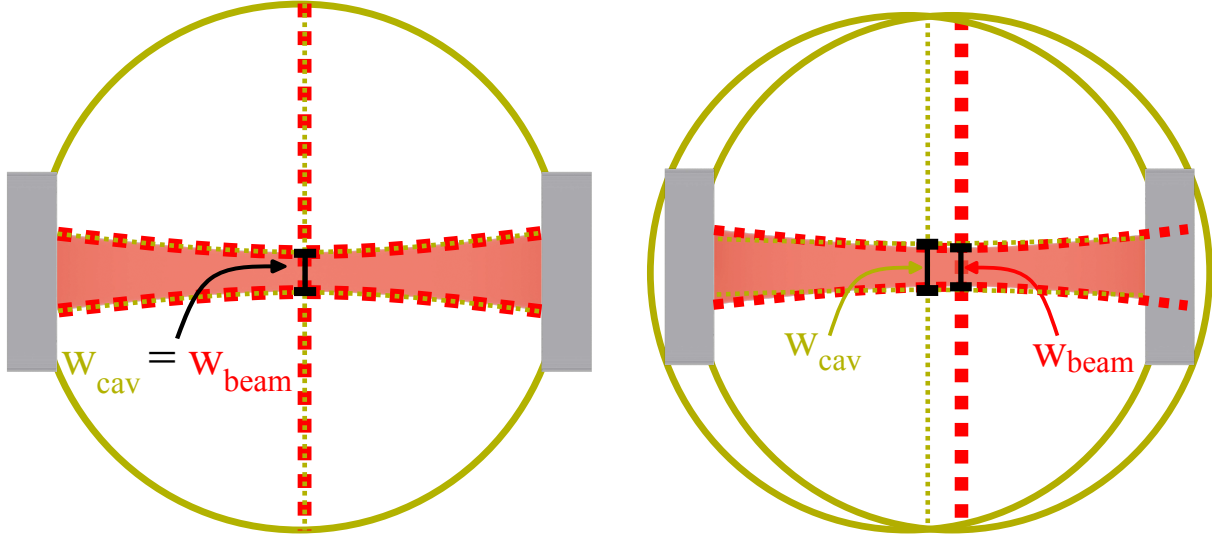


Figure 1.10: Figure depicting cavity-beam mode matching (left) vs. cavity-beam mode mismatch (right). In this particular case, the mode mismatch is a result of changing the macroscopic DC cavity length via a shift of the ETM position towards the ITM (assuming constant mirror ROC and input beam mode). Given that the mirror ROC alongside the beam wavelength remains the same, it is helpful to notice that for the new cavity configuration, arriving at the same mirror ROC within the shorter length requires a larger characteristic beam waist (shortening the Rayleigh length)

$$\begin{aligned}
 TEM_{p,l}(r, \phi, z) = & E_o \frac{\sqrt{[\lambda z_o]/\pi}}{W(z)} \left(\frac{\rho}{W(z)} \right)^p \mathbb{L}_l^p \left(\frac{\sqrt{2}x}{W(z)} \right) \\
 & \times \exp \left(-\frac{\rho^2}{W^2(z)} \right) \exp \left(-ikz - ik \frac{\rho^2}{2R(z)} - ip\phi + i(1+p+2l)\zeta(z) \right)
 \end{aligned} \tag{1.17}$$

$$TEM_{p,l}(r, \phi, z) \rightarrow |U_{p,l}(r, \phi, z)\rangle$$

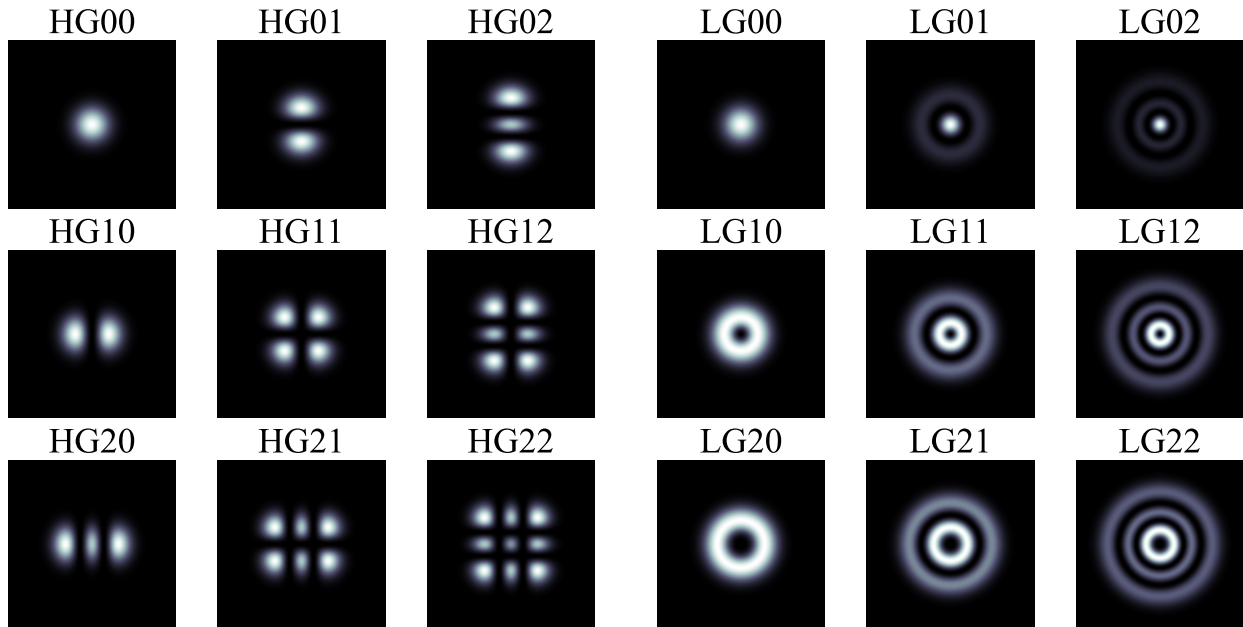


Figure 1.11: Various transverse mode intensity profiles, with Hermite-Gauss modes ($HG_{n,m}$, $[n,m \leq 2]$) to the left and Laguerre-Gauss modes ($LG_{l,m}$, $[l,m \leq 2]$) to the right.

Measurements of these HG and LG fields indicate the presence of imperfections in the beam-cavity alignment and mode matching respectively. The presence of power in these modes when sweeping a mirror along the beam axis (ΔFSR) indicate optical loss, while simultaneously providing useful feedback in reducing it through the construction and maintenance of a TEM00 beam-resonator coupling [14].

1.2.3 Dual-Recycled Fabry-Pérot Michelson (DRFPMI)

Recycling mirrors are an extension of the FPMI that exploits otherwise wasted optical power by providing a means of enhancing the optical gain and bandwidth of the instrument. Strategic tuning of mirror coating parameters and positions at symmetric and anti-symmetric ports can incorporate power recycling and signal recycling respectively [15].

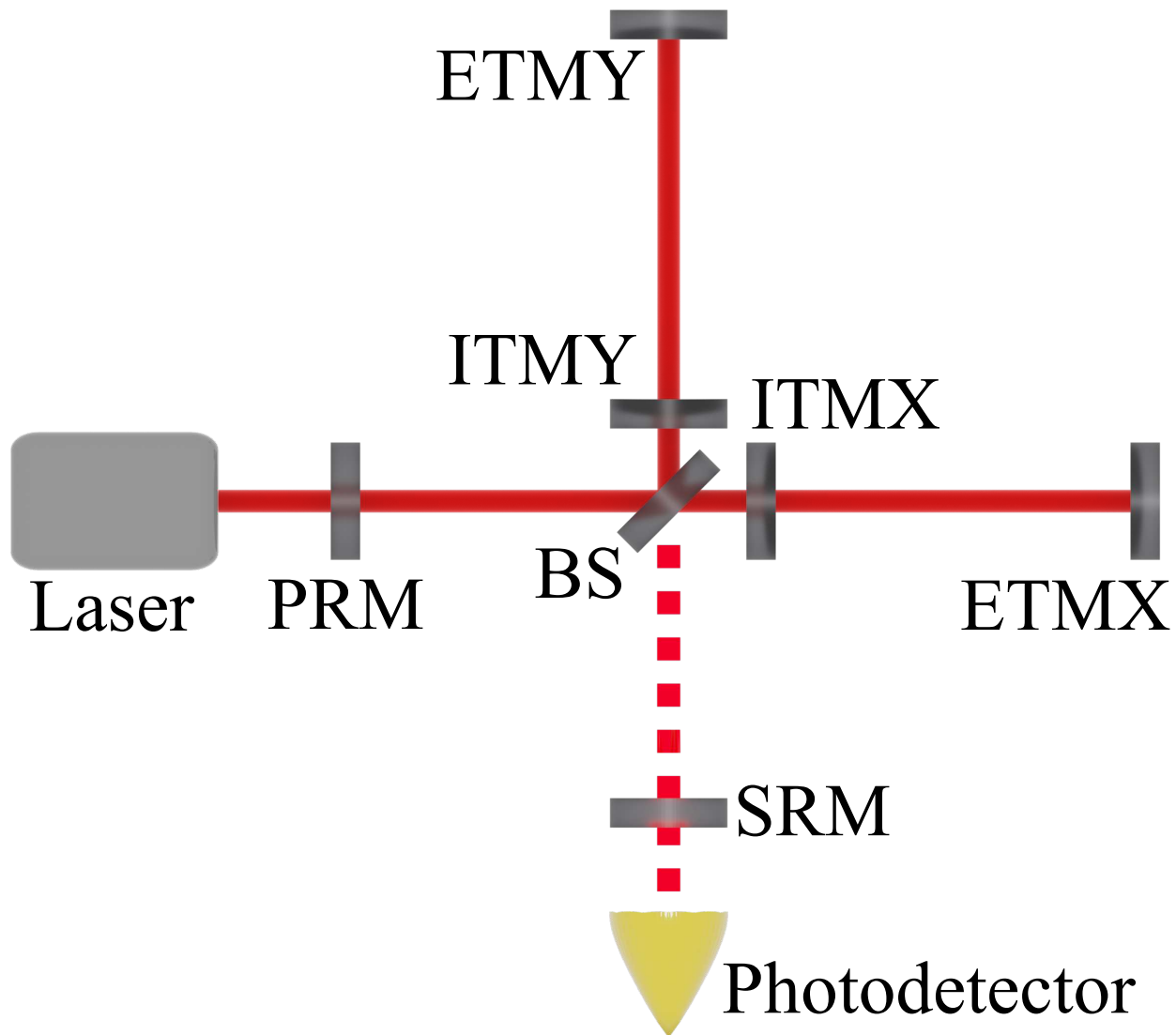


Figure 1.12: A simplified Dual-Recycled Fabry-Pérot Michelson optical schema

1.2.3.1 Power Recycling

When operating a FPMI at a dark fringe, a significant amount of power is reflected back to the symmetric port as mentioned in § 1.2.2.1 leading to wasted optical power if simply dumped. Placing an additional highly reflective mirror at the symmetric port while maintaining resonance of the carrier to the arms, you can reintroduce (or “recycle”) power back to the arm cavities [16]. A PDH loop is utilized for carrier resonance, while macroscopic mirror positioning of the PRM is informed by the choice of optical sideband frequency required

when applying PDH. This recycling gain is also sensitive to cavity arm Finesse \mathcal{F} and round trip loss \mathcal{L}_{RT} [17]:

$$G_{\text{PR}} = \frac{(1 - r_{\text{PRM}}^2)}{1 - r_{\text{PRM}}[1 - (\mathcal{F}\mathcal{L}_{\text{RT}})/\pi]} \quad (1.18)$$

With maximum recycling gain:

$$G_{\text{PR}}^* = \frac{\pi}{2\mathcal{F}\mathcal{L}_{\text{RT}}} \left[\frac{1}{1 - \frac{\mathcal{F}\mathcal{L}_{\text{RT}}}{2\pi}} \right] \quad (1.19)$$

1.2.3.2 Signal Recycling

As may be inferred, this technique requires a mirror installation at the anti-symmetric port, though with a more nuanced approach than that of power recycling. Placing a partially reflective mirror at the output port, it is understood that light leakage coming from the PRFPMI at the anti-symmetric port (caused by differential arm motion) is re-introduced to the arms, but the reflectivity of the new mirror cannot be set too high to prevent attenuating the PRFPMI output. And even then detector enhancement only comes after exacting a cost dependent on signal recycling cavity tuning. This cost resides between a trade off of detector bandwidth for increased detector gain or vice versa, with the operating point between the maxima of these two detector characteristics set as a function of the microscopic signal recycling cavity length (phase) tuning [17]:

$$H_{\text{DRFPMI}} = G_{\text{PR}} P_{\text{in}} L \Omega \left[\frac{t_{\text{ITM}}^2 r_{\text{ETM}}}{(t_{\text{ITM}}^2 + r_{\text{ITM}}^2) r_{\text{ETM}} - r_{\text{ITM}}} t_{\text{SRC}} \frac{e^{-i2\pi Lf/c} \sin(2\pi f/c)}{2\pi Lf} \frac{\sin(\phi_0)}{1 - r_{\text{SRC}} r_{\text{ETM}} e^{-i4\pi Lf/c}} \right] \quad (1.20)$$

$$t_{\text{SRC}} = \frac{t_{\text{SRM}}t_{\text{ITM}}e^{i\phi_{\text{SRC}}}}{1 - r_{\text{ITM}}r_{\text{SRM}}e^{i2\phi_{\text{SRC}}}}, \quad (1.21)$$

$$r_{\text{SRC}} = \frac{r_{\text{ITM}} - r_{\text{SRM}}e^{i2\phi_{\text{SRC}}}}{1 - r_{\text{ITM}}r_{\text{SRM}}e^{i2\phi_{\text{SRC}}}} \quad (1.22)$$

With Ω as the optical angular frequency, and ϕ_0 being the differential arm phase offset.

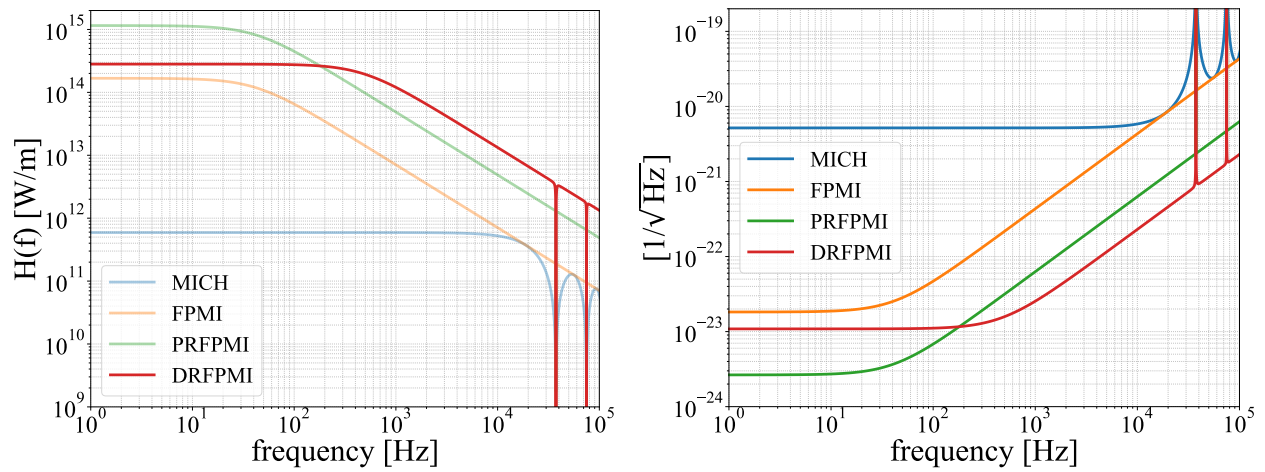


Figure 1.13: [Left] Comparison of all optical gain functions [Right] Coorelated shot noise strain sensitivity. Code and more detailed derivations used to generate optical gain and sensitivity curves can be found in § L

tive optics for high power operation, and 2) the thermodynamics of highly reflective mirror coatings that impose a fundamental limit to gravitational wave interferometer sensitivity.

1.3.1.1 Adaptive Optics

As mentioned in §1.2.2.1.3 , the microscopic longitudinal control of the mirror positions is only half the story for Gaussian beams and further consideration of macroscopic mirror position and radii of curvature are needed to maximize resonant power in the fundamental (TEM00) mode. Failure to plan and maintain this “mode matching” condition results in beam mode to cavity mode mismatch, scattering power into higher order Laguerre-Gauss modes. Additionally, even with ultra-low absorption HR mirror coatings and fused silica substrates, aLIGO circulating power is estimated to reach ≥ 750 kW, introducing a differential defocus to the arm cavities by $[m^{-1}]$; which can introduce significant optical loss due to mode mismatch (esp. for a coupled cavity configuration) [19]. As DRFPs like aLIGO approach designed sensitivity, instances of mode mismatch are a two-fold threat with optical loss to higher order modes that impact the ability to produce squeezed light states [20]. The further motivation and the implemented solution for aLIGO during O3a is discussed in Chapter 2.

1.3.1.2 Coating Thermal Noise

Generally speaking, sensed differential arm motion is more often than not produced by sources that are not gravitational waves. The sum and categorization of motion from non gravitational wave sources (both known and unknown) at a given point in time form what is known as a DARM noise budget. This tool aids commissioners in understanding the current limits of GWDs and additionally facilitates focused hypotheses for detector improvements / upgrades. One rapidly approaching limit is the coating thermal noise from the HR $SiO_2TiO_2 : Ta_2O_5$ Fabry-Pérot cavity mirror coatings which arises from the mirror surface position observable influenced by energy dissipated by the coating by way of its acoustic de-

degrees of freedom and causing uncorrelated phase fluctuations between the two arm cavities. Part of the upgrade discussions for current and future GWDs are HR coating materials with different material composition solely for the purpose of lowering this coating thermal noise. A promising candidate with 5 times lower thermal noise properties is the HR crystalline GaAs/Al_{0.92}Ga_{0.08}As stack. This alone motivates an inquiry into more of its properties, one of which is thoroughly discussed in Chapter 3.

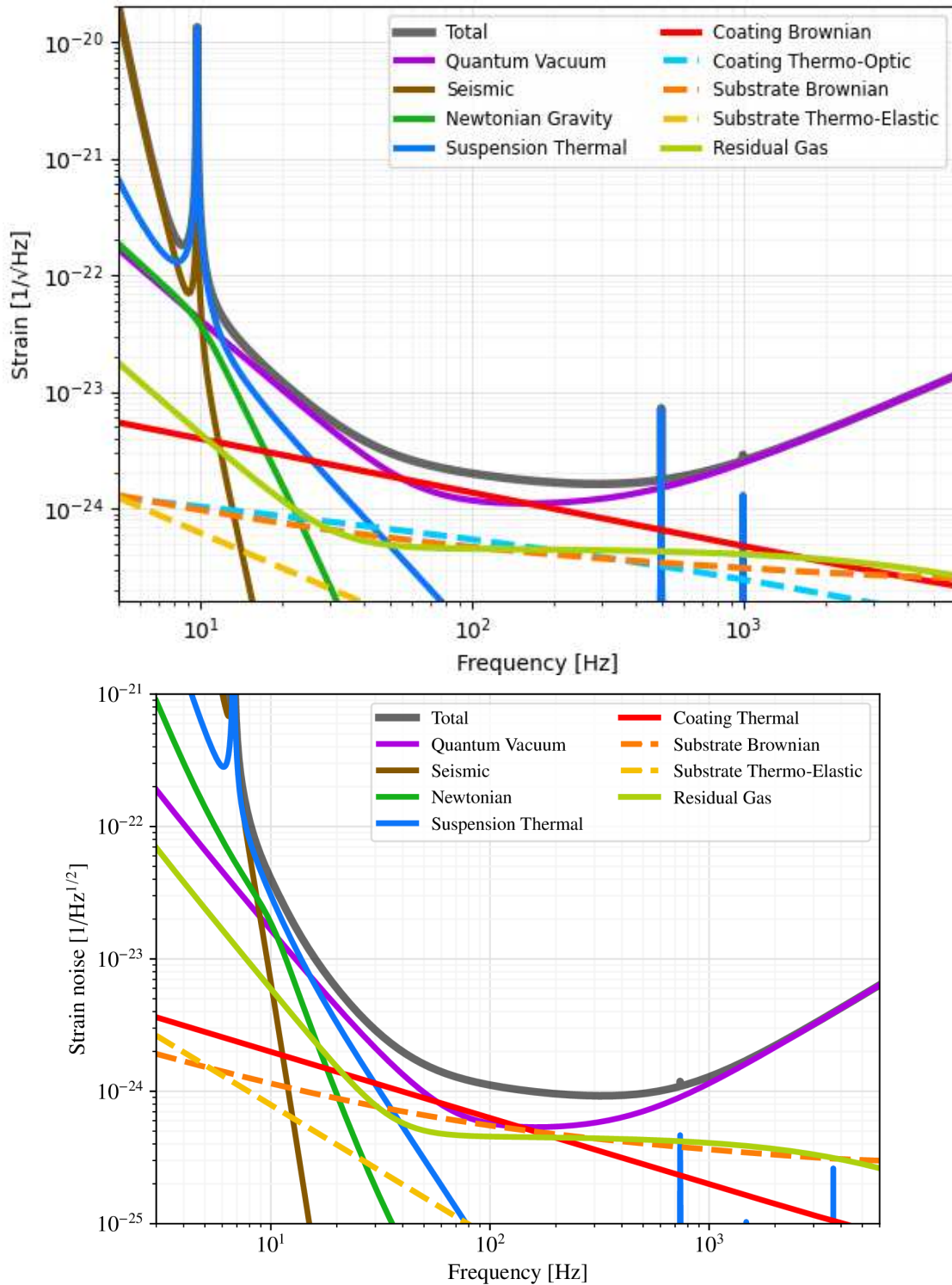


Figure 1.15: [Top] Noise budget for the next generation A+ interferometer using $\text{SiO}_2\text{TiO}_2 : \text{Ta}_2\text{O}_5$ coatings [Bottom] Noise budget for a parallel next generation A[‡] interferometer using $\text{GaAs}/\text{Al}_{0.92}\text{Ga}_{0.08}\text{As}$ coatings [21]. The adjustments to the Substrate Brownian and Substrate Thermo-Elastic noise for A[‡] are from modified beam sizes on the test masses for smaller coatings (5.5 cm ETM spot size and 4.5 ITM spot sizes) [22]

Chapter 2

Commissioning Adaptive Optics for O3a

2.1 Motivation

As seen in § 1.2, increasing detector input power leads to a direct sensitivity increase to gravitational waves. And even using optics with ultra-low absorption ($\approx 328 \text{ ppb} \pm 84 \text{ ppb}$), significant thermo-optic effects persist, especially with a designed circulating arm power of 750 kW in the Fabry-Pérot cavity arms [19, 23]. Thermal aberrations produced from the high circulating carrier power include substrate lensing and relatively smaller lensing from the differential HR surface curvature. The time varying optical path length change integrated over the carrier phasefront produces mode mismatch and contributes to the accumulated optical loss throughout the GWD, reducing sensitivity two-fold: 1) by loss of usable readout power, and 2) reduced efficacy producing squeezed light states in lowering the detector quantum noise limit.

During O3a the LIGO Hanford observatory increased circulating arm power beyond 180 kW; emphasizing importance on properly tuned thermal compensation in O3 to avert arm-cavity/carrier-beam mode mismatch. Detailed in this chapter is a summary of related commissioning efforts at LHO to prepare and preserve interferometer mode matching including but not exclusive to: a primer on the aLIGO adaptive optics schema (TCS), citations on the ini-

tial computed O3a TCS pre-load, the development and implementation of real-time digital filtering for an improved ring heater actuation response by a factor of ≈ 6 , and the impacts of high absorption points aka point absorbers discovered on arm cavity test masses along with efforts to mitigate them.

2.1.1 Thermal Compensation System

High power beams, even propagated by ultra low absorption mirror substrates and coatings, can impart a surface pressure that imposes non-negligible thermo-optic distortions via thermo-refractive and thermo-elastic effects [24]. The aLIGO adaptive optic system is intended to address the problem of dynamic mode mismatch in high power interferometry; as high power operation is a requirement in reaching designed sensitivity. The system is comprised of a feedback control system that uses four Hartmann wavefront sensors (HWS) combined with thermal actuators of two varieties: annular ring heaters and CO2 lasers heating [? 25].

2.1.1.1 Actuation

Both ITMs and ETMs (Fabry-Pérot arm cavity mirrors) are strategically monitored for differential lensing, but both are not prescribed equal actuation treatment. All arm cavity mirrors do possess negative lens ring heater actuation in the form of a wound nichrome wire annulus that outlines the outer barrel of the mirror substrate; while CO2 lasers, though not imaged onto the ITMs directly, are instead imaged onto a fused silica compensation plate (CP) ¹ placed promptly before the FP arm input coupling mirror [26].

2.1.1.2 Sensing Optical Path Distortion

Quantifying thermal distortion from both carrier as well as thermal actuators is performed with a set of four Hartmann wavefront sensors; each one measuring differential optical path

¹Decouples CO2 laser noise from the highly sensitive FP input test mass position

distortion at each FP cavity test mass. The sensor probe beams ² make a double pass through the test mass mirror substrate for all arm cavity mirrors and map the HR mirror surface; while the two input test mass sensors at the interferometer vertex make an additional double pass through the compensation plate (CP). Wavefront distortion maps are then used to compute relevant Zernike polynomial coefficients (i.e. $Z_{n=2}^{l=0}$) in real time to inform of differential defocus in diopters [18].

2.1.2 Thermo-optic transients

Thermo-optic transfer functions from high power carrier beams and implemented thermo-optic actuators suggest that these thermal transients are worthy of consideration to avoid long periods of mode mismatch while sampling points in actuation space.

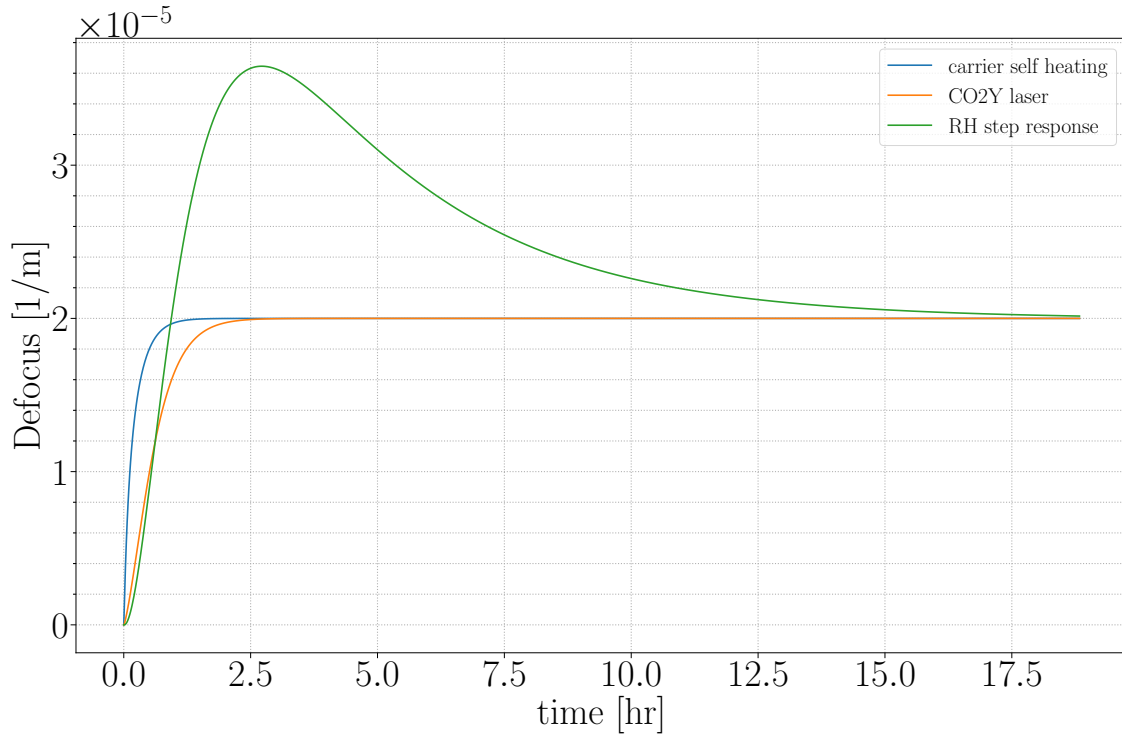
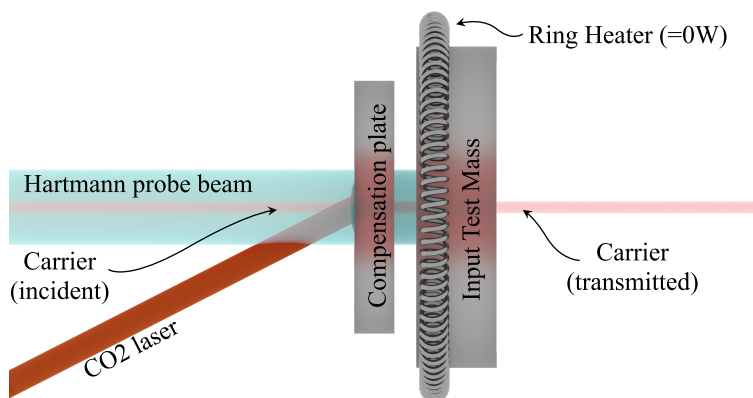
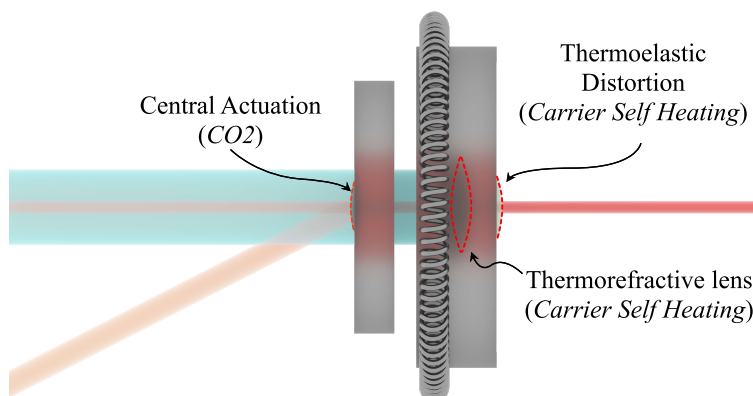


Figure 2.1: Transient defocus responses computed from carrier beam self heating and TCS actuation best fit filters (central CO2 laser heating and annular ring heating) § D.

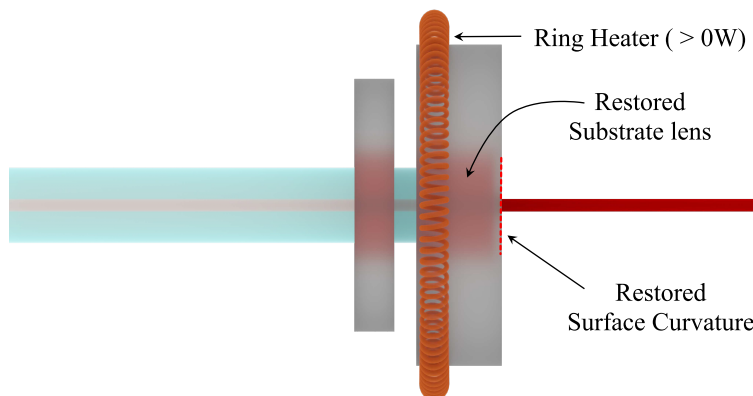
²Differing wavelengths of 800 nm and 833 nm are chosen for the X and Y arms in order to mitigate crosstalk between HWS chains and other auxiliary systems



(a) CO₂ actuator set to replicate projected carrier thermo-optic response, with an off resonance circulating beam.



(b) Arm cavity resonance, with reduced CO₂ central actuation power and increased arm cavity input power. The uniform thermo-optic distortion from the high power circulating carrier imposes a differential thermo-refractive lens and thermo-elastic HR surface change to the ITM, placing an upper limit to the circulating carrier power without annular ring heater actuation.



(c) Maximum circulating arm power, with annular heating and no central CO₂ actuation. The careful timing and calibration of the CO₂ / RH actuators can allow designed power / GW detector sensitivity to be reached.

Figure 2.2: aLIGO thermal compensation design at the input of a single Fabry-Pérot arm cavity. Though not the only location of thermal mode matching actuators, a careful look here demonstrates their capabilities and motivates carefully constructing a thermal pre-load strategy before commissioning and fine tuning during commissioning of the detector at high power.

The thermo-optic time constant of the carrier beam self-heating is similar to that seen from CO2 laser / CP central actuation, though demonstrably different from annular ring heating. Because of this, LHO applies central CO2 heating and static annular ring heating to a power level that respectively mimics and actuates for projected thermal deformation from circulating resonant carrier in the Fabry-Perot arm cavities. Once DRFPMI coupled cavities are configured or “locked”, the input carrier power is gradually increased while CO2 laser power is simultaneously decreased in order to mitigate any possible differential thermo-optic response from the arm cavity test masses when reaching maximum power.

2.2 Dynamic Thermal Compensation

Transient ring heater actuation from a radially symmetric thermal aberration ($\Psi(t, r)$) is realized in [27] and measured here:

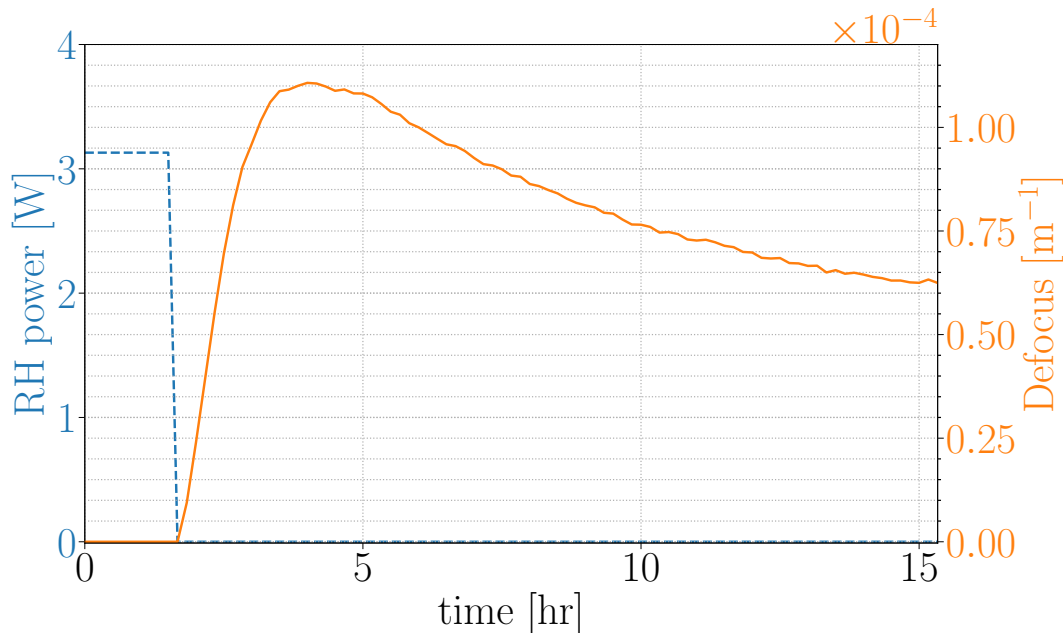


Figure 2.3: ITMY thermo-optic response to a 3.13 [W] combined power reduction to the top and bottom ring heater elements. It’s after ≈ 12 hours after the ring heater power control step do you start to see a small enough steady state differential defocus ($\frac{d\alpha_{sp}}{dt}$) and can assume a steady state thermal lens.

The measured transient thermo-optic response exhibits differential defocusing for ≈ 17.5

hours once the ring heater power has been changed; and with a large enough power steps, these adjustments to ring heater power can significantly stall precious detector observing/commissioning time due to differential mode matching. Thermo-optic time constants are reduced by applying real time digital filtering to ring heater power controls. The desired thermo-optic response is one that resembles a step from one defocus state to another with no overshoot.

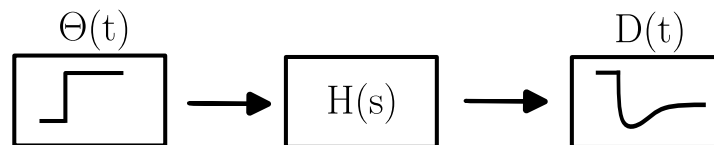


Figure 2.4: A pictograph of the plant $H(s)$ (test mass mirror and annular ring heater) transforming the ring heater power control step to a time-varying thermo-optic response. An example of this can be seen in Fig [2.3]

The RH power control transient resembles the Heaviside step function ($\Theta(t)$), motivating an inversion of the response function which provides a reasonable first order filter correction. Therefore, the prescription for creating an input filter is realized through inverting the known RH step response with additional low passing at high frequency to avoid aliasing due to low sampling rate of the slow control system. However, a full inversion of the thermal $1/f$ roll-off at high frequencies would lead to an infinite control signal on short time scales. Since the ring heater output is physically limited by its maximum power (10 Watt), as well as zero (no heating) for negative signals, a necessary constraint for the input filter to work with any command input is that its high frequency gain is less or equal to its DC gain. In the time domain, this guarantees that the initial fast transient is less or equal to the output required over long timescales. This condition can only be violated if extra control headroom can be guaranteed by some other means. See figure Figure 2.6 and Figure 2.8.

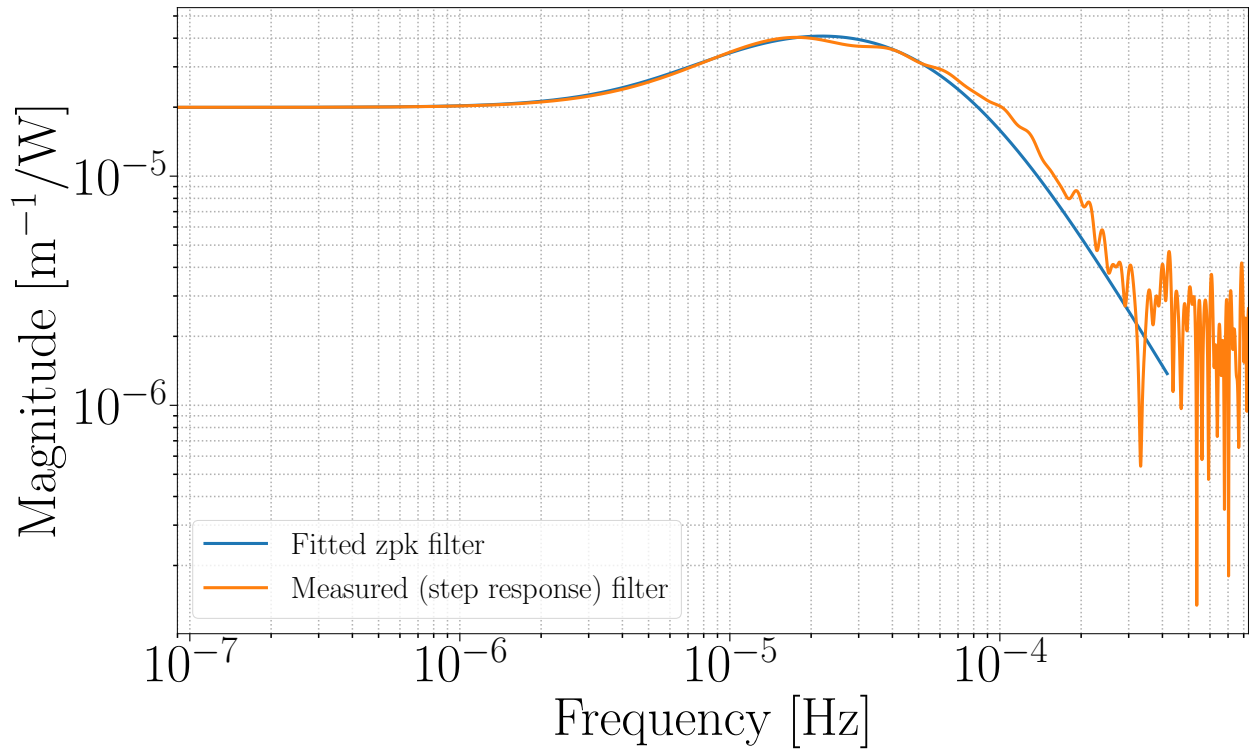


Figure 2.5: Showing the transfer function of the RH response (normalized by the input RH power) over a an ≈ 12.5 hour period. The zpk model of the fitted filter ($H(s)$) = $9.2545e-12 \left(\frac{(s+3.14210e-5)}{(s+8.168e-5)(s+0.0003142)(s+0.0005969)} \right)$

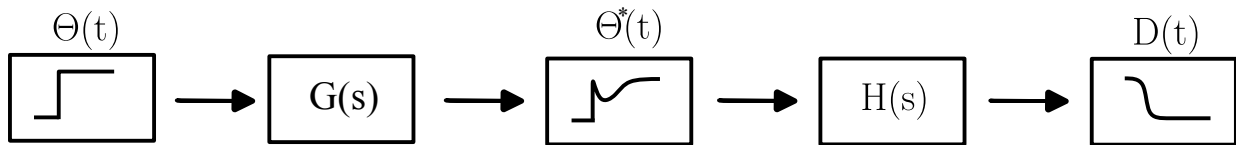


Figure 2.6: A pictograph showing the system with real time digital filtering for an improved thermo-optic response. The RH input filter ($G(s)$) is created by inverting the plant filter combine with a low pass and added poles to the zpk model to ensure stability. The time series $\Theta^*(t)$ illustrates the modified RH control input for an improved defocus response ($D(t)$).

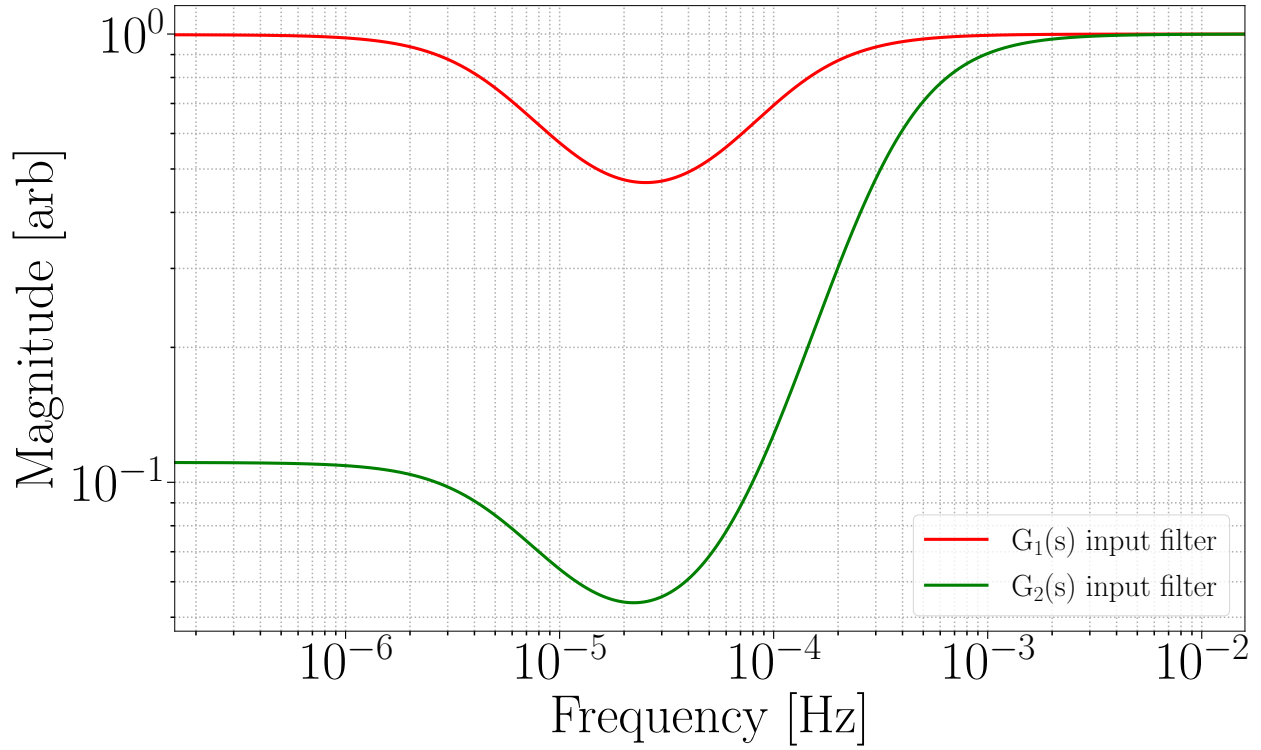


Figure 2.7: Two of the constructed RH pre-filter options:

The zpk models of the two RH pre-filters plotted in Figure 2.7:

$$\begin{aligned}
 G_1(s) &= \frac{(s + 8.16814090e-5)(s + 3.14159265e-4)(s + 5.96902604e-4)}{(s + 3.14159265e-5)(s + 6.99400000e-4)(s + 6.99400000e-4)} \\
 G_2(s) &= \frac{(s + 8.16814090e-5)(s + 3.14159265e-4)(s + 5.96902604e-4)}{(s + 3.14159265e-5)(s + 2.09820000e-3)(s + 2.09820000e-4)}
 \end{aligned} \tag{2.1}$$

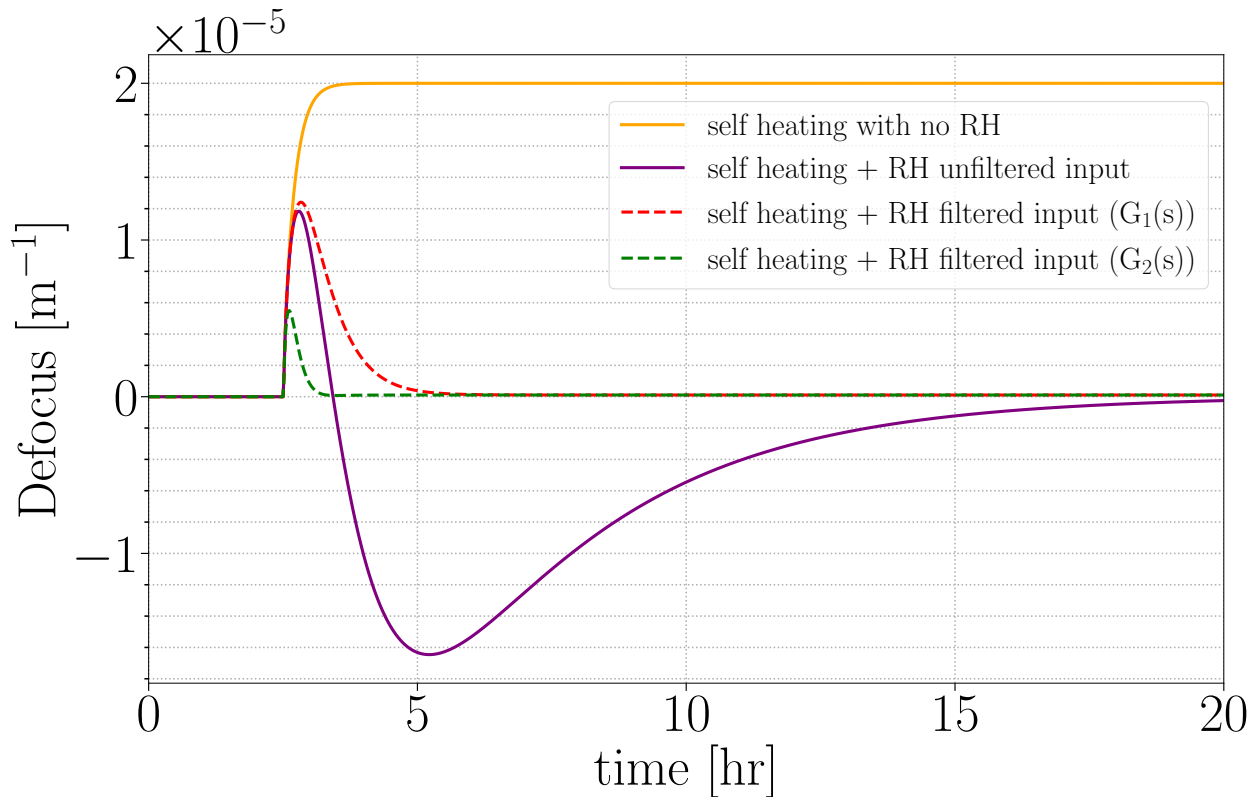


Figure 2.8: Comparison of the natural RH response and the response with the pre-filtered input against the transient carrier absorption response. “self heating” indicates a dataset generated by a COMSOL simulation computing the transient thermo-optic response from 1 [W] of absorbed carrier beam and scaled down. “self heating + RH unfiltered input” demonstrates the simultaneous transient response when changing the ring heater power alongside the carrier thermo-optic transient. The dotted curves indicate the elimination of long defocus period when changing RH power alongside the carrier transient using the two RH pre-filters provided Figure 2.7. Note that while G_1 has the slower response, its short-term response is guaranteed not to exceed the DC response, avoiding potential ring heater actuator saturations.

2.2.1 Reducing Parametric Instabilities

Another symptom of resonant high power optical cavities are parametric instabilities (PI); induced by the opto-mechanical interaction between test mass acoustic modes and higher order optical modes. PIs present a threat to achieving designed detector sensitivity, even driving the detector to lockloss. Passive methods of mitigating PIs by way of acoustic mode dampers (AMD) demonstrate significant reductions of problematic mechanical modes

though some (i.e. @ 15 kHz) remained problematic during O3a. Lingering PIs required manual intervention by way of adjusting test mass / cavity geometry to disrupt persistent modes and is now a much more feasible solution with DTC [1].

2.2.2 Limitations

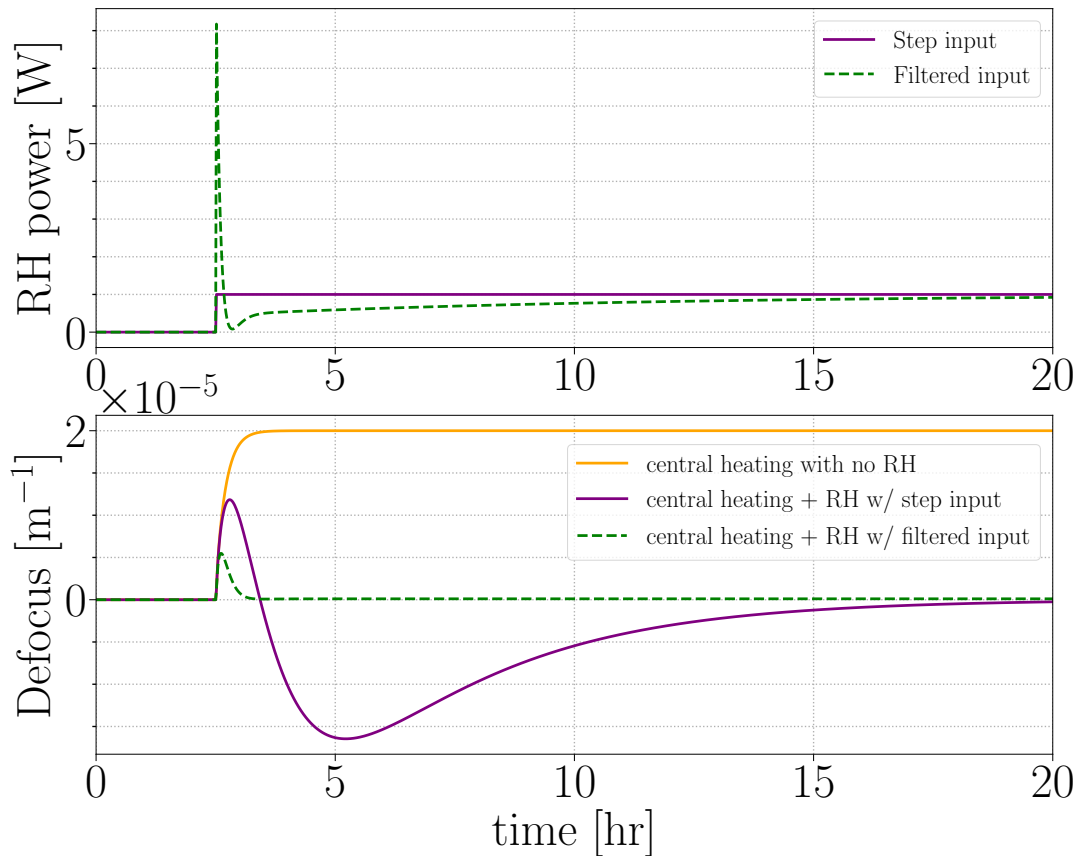


Figure 2.9: Comparison of the natural RH response and the response to the filtered input with RH power

When constructing the control pre-filter important considerations the physical limits of the thermal actuators need to be considered. For the aLIGO RHs, a 10 W limit is set on RH power control and sets a threshold on the high frequency gain of the pre-filter [28]. Failure to consider this limit may cause the actuator output to rail the initial power swing from your actuator response.

There must also be considerations when we cannot assume that we know the control output

history over the last 15 hours. Concurrent RH changes an example of this as the filter is designed with initial thermal equilibrium in mind. There is room to develop a more robust Dynamic Thermal Compensation strategy, with enough modeling, independent measurements spanning an actuation space, and integration of Kalman Filtering.

2.3 A priori TCS pre-load methodology for O3a

Preserving arm cavity resonance requires countering the positive thermal lens defocus of the nominal test mass lens induced by high circulating interferometer arm cavity power. Preparing for uniform test mass distortion from the carrier beam requires calibrated and well established thermal actuator settings; informing a ‘pre-load’ of the TCS actuators using test mass absorption measurements [29]. Initial order of magnitude estimates of wavefront distortion from ultra-low absorption fused silica test masses under the influence of a centered high power gaussian beam as well as annular ring heater actuation are available [24, 27]; though variations of the absorption between any two test mass mirrors are accounted for through calibrated defocus measurements using the Hartmann wavefront sensors sensitive to auxiliary beams imaged onto the test mass mirror surfaces.

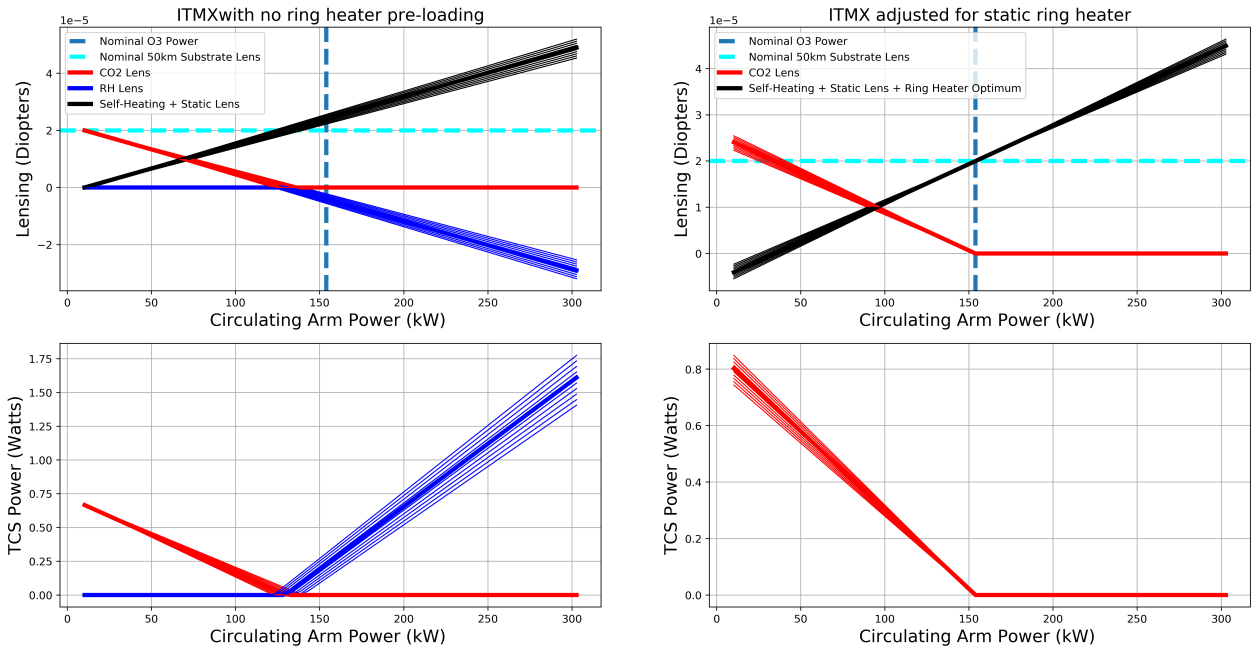


Figure 2.10: ITMX initial pre-load estimate O3a as provided in [19]

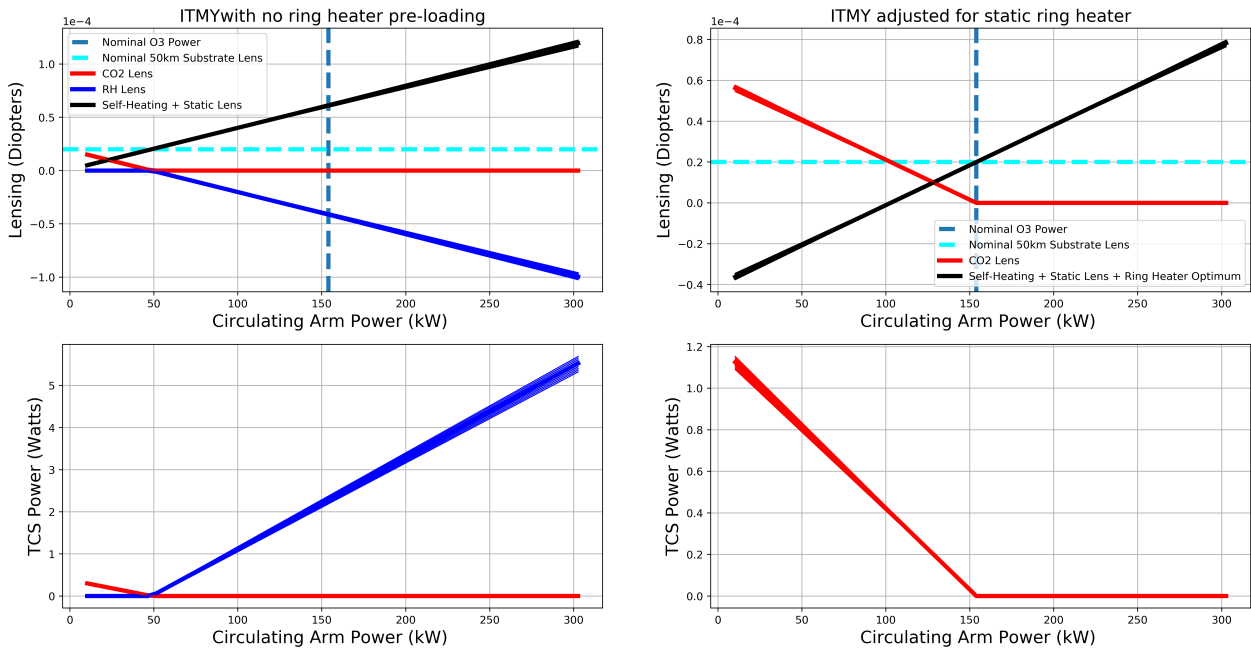


Figure 2.11: ITMY initial pre-load estimate O3a as provided in [19]

2.4 A posteriori thermal compensation for O3a

While approaching designed arm cavity power, the presence of non-uniform high absorption points on the test mass coating surface imposed limits to reaching designed power and hence designed sensitivity; simultaneously, this led to a significant deviation from the original TCS pre-load algorithm. The current thermal actuation solution is designed to control the TEM00 beam waist size and location, though adjustments and modifications of current actuators were tried. Assessment of these absorbers helps inform of ways to mitigate their effects with the hopes of reaching the designed detector sensitivity. We begin here with a characterization of these high absorption points including: characteristic optical path distortion profiles measured on the Hartmann wavefront sensors, as well as some impacts on interferometer operations at high power. The findings mentioned here indicate that these absorbers pose a risk to maintaining and reaching designed circulating power in the arm cavities if no further proactive measures are taken, or are not sufficient to bypass detector symptoms; whether they are a result of preventable surface particulates or can be masked with an improved adaptive optics schema.

2.4.1 Point absorption in O3a

A significant number of lockloss events during the O3a commissioning period were a direct result of select optical sideband power degradation used to maintain the delicate coupled cavity configuration during interferometer thermalization at input power ≥ 100 kW circulating in the FP arms. This was quickly realized to be caused by high absorption points discovered on ITMY.

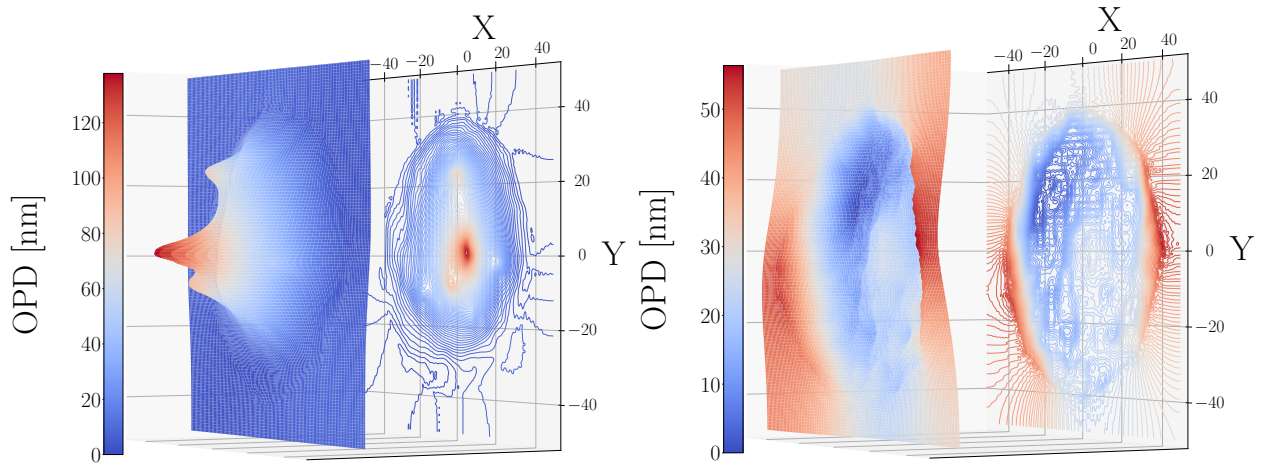


Figure 2.12: An isometric view of point absorption vs uniform cooling of the LHO ITMY.

Also, while sustaining interferometer DC readout the recycling cavities would generate higher order modes, sustained by a Output Mode Cleaner (OMC) co-resonance which contaminates the carrier field at the output photodiode. With continued observation and commissioning at high power (≥ 180 kW) point absorbers were also discovered on ETMX, though difficulties profiling due to unavoidable probe beam noise on that wavefront sensor.

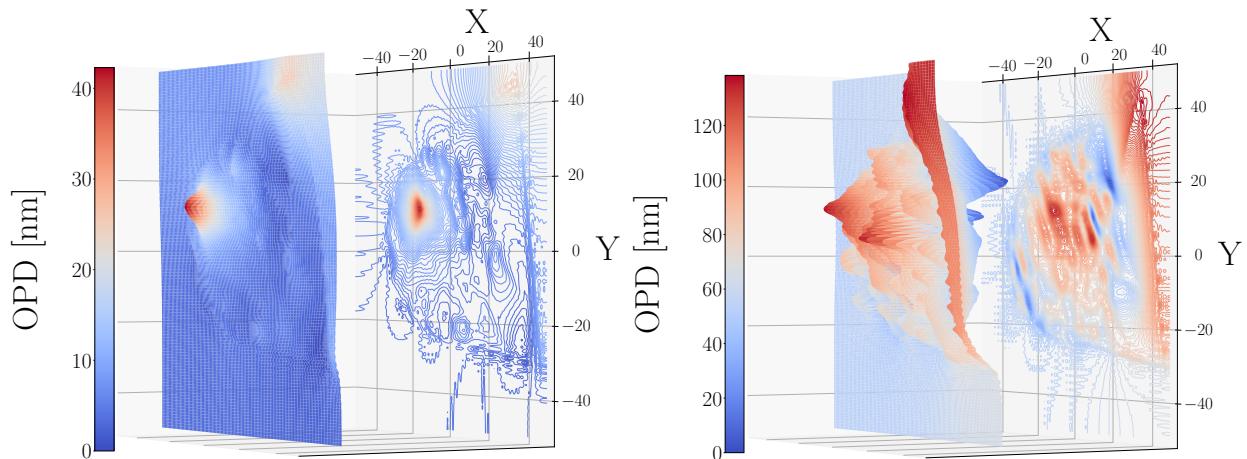


Figure 2.13: An isometric view of uniform absorption vs point absorption of LHO ETMX. The rippling / edge effects are a consequence of the Hartmann probe beam clipping on the baffle due to misalignment of in-vacuum optics.

2.4.1.1 Reduced Power Recycling Gain

As informed by Equation 1.18 the PRG can provide a reasonable metric for the arm losses in the FPMI and in fact suffered notable reductions with interferometer thermalization. At LHO there are reported PRG losses of $\approx 13\%$ increasing IFO input power from 2W to 30W, while LLO notes a $\approx 18\%$ change while increasing input power from 2W to 40 W [30].

2.4.1.2 Control signals

Holding delicate resonance conditions throughout the coupled cavity configuration necessitates a reasonable optical sideband relative carrier gain (dBc) for the PDH loops to function. And it is with careful planning that the macroscopic recycling cavity geometry is planned so that sideband resonance boosts the signal. The point absorber on an ITM directly impacted these sideband buildups and frequently lead to a lockloss.

2.4.1.3 Higher order modes at DCPD

For the detectors' DC readout configuration, power from higher order modes at the anti-symmetric port obscure the single element photodiode from measuring a pure TEM00 mode with the increased shot noise [31]. Among other higher order modes, the point absorber allowed resonance of a notable higher order mode (9th order Hermite-Gauss) from the 9MHz sideband which was co-resonant with the Output Mode Cleaner and in turn imparted intensity noise to the DCPD [32].

2.5 Results

With these high absorption points dramatically impacting interferometer high power operations, a variety of efforts to mitigate their effects were sampled. Using DTC the amount of sampling possible TCS states increased (for varied RH states specifically) though the current modes of actuation proved to still be too few and/or mixed to rely on TCS alone with a

static beam position on ITMY.

2.5.1 Custom CO2 mask

Attempts at increasing uniform distortion with a machined CO2 mask § F was tried. The intention was to actuate by imaging a negative of the optical path distortion from the high absorption points onto the surface with the CO2 laser combined with a static ring heater offset [33]. The installation location of the mask and size was established using the relevant propagation and imaging techniques applied to the CO2 actuation field while mitigation of the aforementioned impacts provided commissioners with mixed metrics of success [34, 35]. With varying interferometer conditions and an involved parameter space, alongside the slow nature of thermal actuation, attempts at restoring uniform absorption proved to be not as straightforward to improving the overall interferometer condition [26, 2].

2.5.2 Beam position offset

Commissioners found that the simplest and most accessible solution to reducing point absorber symptoms (i.e. decreasing power recycling gain, control sideband buildup, and reduced 9MHz intensity noise) was to shift the beam spot position on the offending test masses [36] though this was not without having to change the entire interferometer alignment along with the loops that control it [37]. Utilizing this solution also simplifies and reduces the TCS solution back to what was detailed in § 2.3.

2.5.3 Test Mass replacement

Unsuccessful attempts to remove these point absorbers have initiated pre-screening and replacement procedures for the test mass mirrors [2]. The ITMY and ETMX test masses were replaced at the LIGO Hanford observatory, though test mass replacement during an observation run requires venting vacuum, costing precious observing time. Simultaneous co-

development of improved adaptive optics / thermal compensation is worthwhile as it may mitigate the optical loss caused by point absorbers during a given observing run, and bypass venting during an observing period.

Chapter 3

Introduction to thermal noise, birefringence, and electro-optical noise of highly reflective crystalline coatings

3.1 Motivation

Contributions of categorized noises for gravitational wave detectors are organized in a “noise budget” (i.e. Figure 1.15): comprised of a collection of technical (noise imposed by the practical operation of the detector) and fundamental (inherent physical limitations of the DRFPMI design) noise that limit gravitational wave detection. Understanding how much differential phase noise is imparted on the interferometer carrier light passing through and reflecting from core optics is crucial. This section contains targeted discussions of coating thermal noise from highly reflective coatings as well as electro-optic noise from highly reflective crystalline coatings to motivate the construction and measurement of a calibrated estimate of the electro-optic noise from GaAs/Al_{0.92}Ga_{0.08}As coatings.

3.1.1 Coating Thermal Noise

One source of noise in high precision optical experiments operating at room temperature (and higher due to high power resonant beams), can be realized through Brownian thermal noise and the Fluctuation dissipation theorem.

Brownian Noise

In 1827 the Scottish botanist Robert Brown observed a constant motion of pollen particulates on the surface of water; witnessing randomized collisions of the water molecules holding a kinetic energy proportional to the temperature ($k_B T$) [38]. It is because of these documented observations we name the phenomena Brownian motion. And although the observations were on motion of particulates in liquids and gases, solids also exhibit similar fluctuations through their modes of dissipation.

Fluctuation Dissipation Theorem

Any movement or fluctuation in the core optic components at finite temperatures holds particular significance for gravitational wave detectors; this becomes clearer when reviewing the fluctuation dissipation theorem. Derived by H.B. Callen and T.A. Welton, the theorem states that for a randomly fluctuating linear force ($F_x^2(f)$) [39]:

$$F_x^2(f) = 4k_B T \Re[Z] \quad (3.1)$$

Where $\Re[Z]$ is the real part of the impedance of the system. This impedance directly relates to equations of motion:

$$Z = \frac{F}{\dot{x}} \quad (3.2)$$

Another useful form is the power spectrum of the fluctuating motion:

$$x^2(f) = \frac{4k_B T}{(2\pi f)^2} \Re[Y] \quad (3.3)$$

Where Y is the inverse impedance or admittance. The root mean square (RMS) displacement ($x^2(f)$) as informed by the FDT facilitates modelling and budgeting notable Brownian noise sources that fundamentally limit LIGO (i.e. by choice of materials used for highly reflective mirror coatings). Though adequate modelling of internal force couplings for the aforementioned components provides a more complete picture.

Internal friction in materials and loss angle

Zener provides a model of the internal friction of materials incorporating anelasticity into the equations of motion [40]:

$$F = k(1 + i\phi)x + m\ddot{x} \quad (3.4)$$

Where m is mass attached to a spring with a spring constant $k(1 + i\phi)$ incorporating the degree of anelasticity ϕ . From equations 3.5 and 3.3 we perform a Laplace transform and acquire the following form of admittance:

$$Y(s) = \frac{\dot{x}(s)}{F(s)} = \frac{-s}{k(1 + i\phi) + ms^2} \quad (3.5)$$

Or more transparently the Fourier representation since we assume a linear time invariant system:

$$Y(\omega) = \frac{\dot{x}(\omega)}{F(\omega)} = \frac{-i\omega}{k(1 + i\phi) - m\omega^2} = \frac{k\omega\phi - i\omega(k - m\omega^2)}{(k - m\omega^2)^2 + k^2\phi^2} \quad (3.6)$$

Plugging equation Equation 3.6 back into Equation 3.3:

$$x^2(f) = \frac{2k_B T}{\pi} \frac{k\phi}{(k - 4\pi^2 m f^2)^2 + k^2\phi^2} \quad (3.7)$$

Computing the admittance from a Gaussian beam impinging upon a HR mirror can

require expansion of all individual mechanical degrees of freedom of the test mass system across a relevant frequency range, and with such an approach convergence is not guaranteed. Saulson and Gonzalez provide an alternative method to computing the admittance coined the “direct approach” by Levin when computing the noise from a Gaussian beam on a LIGO HR test mass. The admittance can be acquired through:

$$\Re[Y] = \frac{W_{\text{diss}}}{F_o^2} \quad (3.8)$$

W_{diss} is the dissipated power from the system due to an oscillating force F_o . This form of the admittance reveals an important result of the fluctuation dissipation theorem where an undriven system with a dissipative actor, imparts motion to the degrees of freedom via a driving force by virtue of that same actor at finite temperatures. This direct approach also allows the surface pressure applied by the Gaussian beam to interrogate which mechanical modes of the test mass impose a significant energy when Equation 3.8 is plugged into Equation 3.3. In the case of the gaussian beam / uncoated test mass studied by Levin [41]:

$$S_x(f) = \frac{4k_B T}{f} \frac{1 - \sigma^2}{\pi^3 E_o r_o} I \phi \left[1 - O\left(\frac{r_o}{R}\right) \right] \quad (3.9)$$

Where σ and E_o are the Poisson ratio and Young’s modulus respectively, and $O(\frac{r_o}{R})$ is a correction term as a function of the small beam radius (r_o) relative to the mirror radius (R).

Thermal noise of HR mirror coatings

Further investigations into the beam/optic system utilizing this approach and elasticity theory led to a deeper understanding about Brownian thermal noise contributions from LIGO test masses (substrate, suspensions, HR coating). Levin mentions, with further detail from Harry, that the noise contributed by a lossy mirror coating is proven to be to be the most significant contributor of brownian thermal noise [42]. Hong provides a power spectral density [43]:

$$S_j^X = \frac{4k_B T \lambda \phi_x^j (1 - \sigma_j - 2\sigma_j^2)}{3\pi^2 f Y_j (1 - \sigma_j)^2 \omega_o^2} \quad (3.10)$$

/ Where X represents bulk and shear with $j = \text{odd}$ (material 1) and $j = \text{even}$ (material 2) alternating layers representing high and low index materials $j = \text{odd}$ (material 1) $j = \text{even}$ (material 2) for an HR coating.

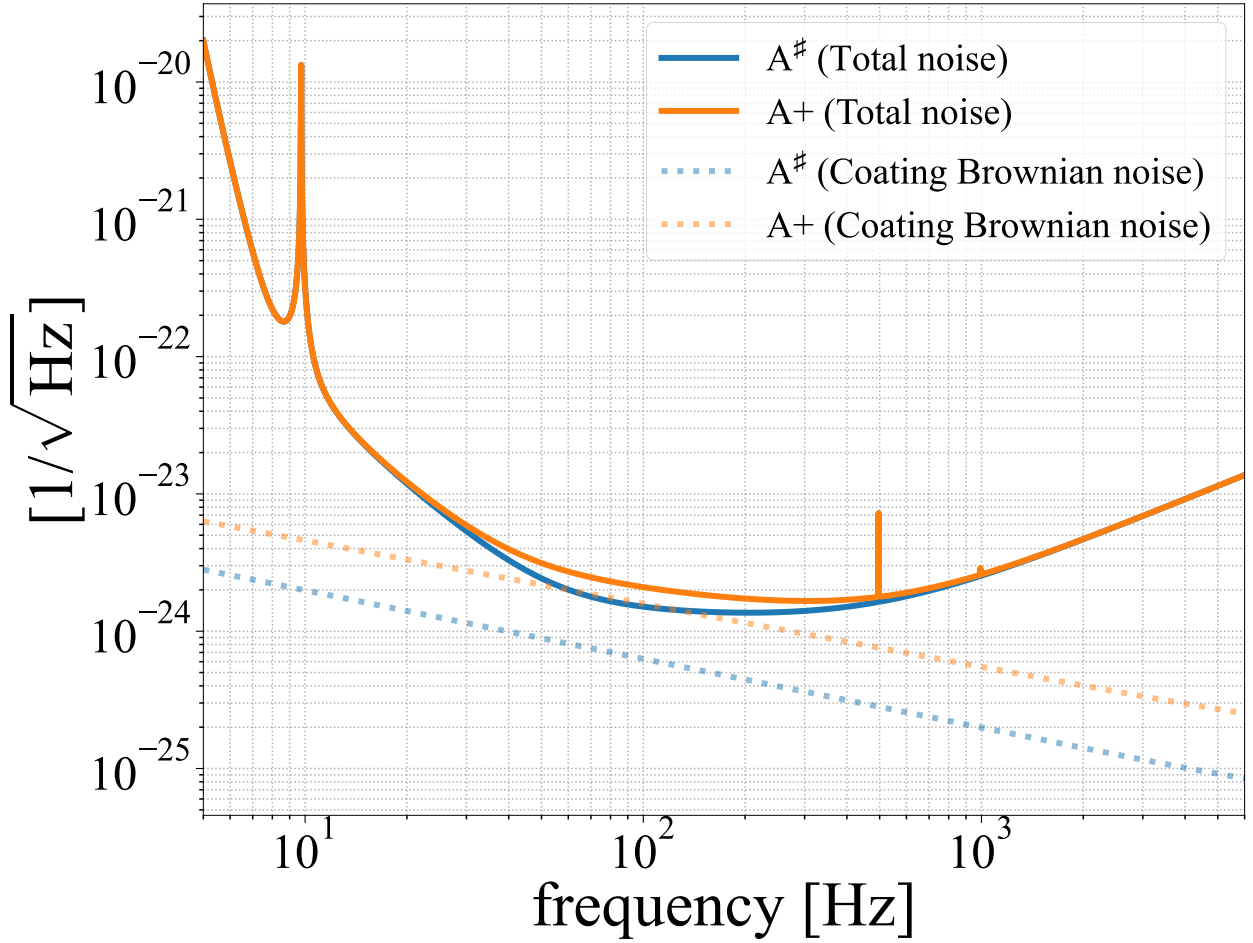


Figure 3.1: Comparison between $\text{SiO}_2\text{TiO}_2 : \text{Ta}_2\text{O}_5$ and $\text{GaAs}/\text{Al}_{0.92}\text{Ga}_{0.08}\text{As}$ coating brownian noise performance computed with a modified A+ GWINC model with coating parameters noted in [21].

As aLIGO approaches designed sensitivity, the thermal noise limit set by $\text{SiO}_2\text{TiO}_2 : \text{Ta}_2\text{O}_5$ HR coatings becomes an immediate limit to further improvements. Though there are proposals for the usage of alternative mirror coating solutions to push down this thermal noise

limit for increased detector sensitivity [44]. GaAs/Al_{0.92}Ga_{0.08}As is a crystalline coating candidate showing promise for next generation detectors with reduced coating Brownian noise by a factor of 10, corresponding to a potential strain reduction by a factor of 5 [45] when compared to the current aLIGO coating thermal noise limit.

3.1.2 Coating Electro-optic Noise

Applying crystalline HR mirror coatings to the core optics indiscriminately may introduce notable side effects; one being linear electro-optic noise of GaAs/Al_{0.92}Ga_{0.08}As (dn/dE), also known as the Pockels effect [46]. Although estimated to be nearly two orders of magnitude below the A[#] strain noise floor ($\approx 10^{-26}$), direct measurement is still merited and adequately motivates a thorough study of electro-optical properties of GaAs/Al_{0.92}Ga_{0.08}As coatings. The rest of this chapter discusses such a study by detailing: 1) birefringence in zincblende materials, 2) a preliminary estimation of differential phase noise of light reflected from a GaAs/Al_{0.92}Ga_{0.08}As coating stack caused by electric field noise are computed while considering potential impacts to the current generation gravitational wave detectors, and 3) a short experimental optical cavity designed to interrogate an estimate of dn/dE from a calibrated differential length PDH locked signal with a normal electric field driven across a HR GaAs/Al_{0.92}Ga_{0.08}As coating “witness” sample.

3.2 Birefringence in zincblende materials

3.2.1 The Indicatrix

The two index solutions for a uniaxial crystal given a general plane wave with unit wave vector \vec{k} can be found via a convenient geometrical construction known as the “index ellipsoid”.

The construction begins when considering a constant electric energy density (U_e) surface in electric displacement (\vec{D}) space; which forms an ellipsoid:

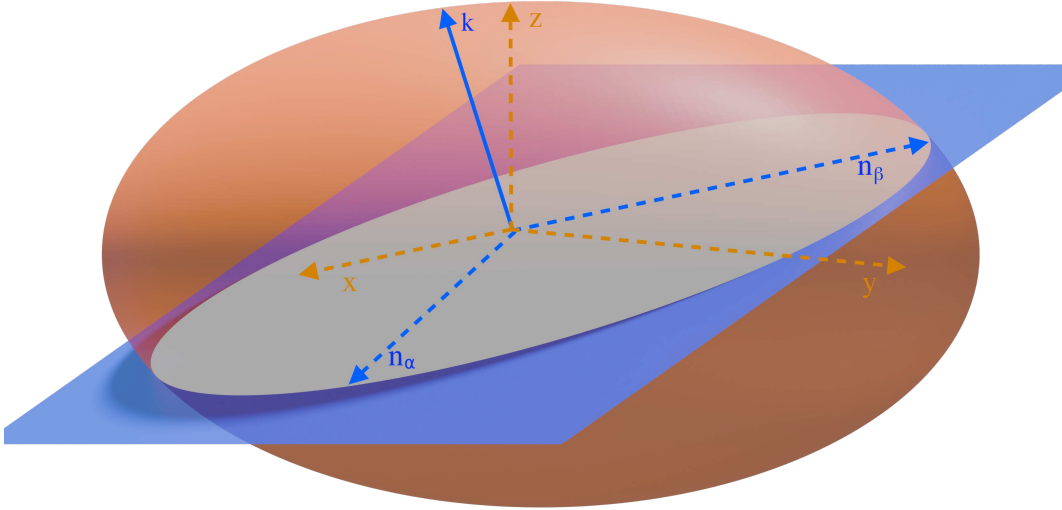


Figure 3.2: A surface of uniform energy density (U_E) forming an ellipsoid in D-space for a generalized uniaxial crystal with general wavefront propagation indicated by a plane normal \hat{k}' where the major and minor axes of the ellipse cross section indicate slow and fast axes n_β and n_α respectively.

$$\frac{D_x}{\varepsilon_x} + \frac{D_y}{\varepsilon_y} + \frac{D_z}{\varepsilon_z} = 2U_e \varepsilon_o \quad (3.11)$$

With redefined coordinates $(\vec{D}/\sqrt{2U_e \varepsilon_o}) \rightarrow \vec{r}$ and setting $\varepsilon_i = n_i^2$:

$$\frac{x^2}{n_x^2} + \frac{y^2}{n_y^2} + \frac{z^2}{n_z^2} = 1 \quad (3.12)$$

This equation for the ellipsoid is known as the indicatrix. Given the co-planar solution demonstrated in § G.2, we can impose the unit wave-normal direction (\vec{s}) to provide an additional equation:

$$\vec{r} \cdot \vec{s} = xs_x + ys_y + zs_z = 0 \quad (3.13)$$

Equation 3.11 and Equation 3.13 both contribute constraints to the method of finding extrema using Lagrange multipliers for the function:

$$r^2 = x^2 + y^2 + z^2 \quad (3.14)$$

The Lagrangian (\mathcal{L}) with the introduced multipliers (λ_1, λ_2) then becomes:

$$\mathcal{L}(\vec{r}, \vec{s}, \lambda_1, \lambda_2) = x^2 + y^2 + z^2 + \lambda_1(xs_x + ys_y + zs_z) + \lambda_2\left(\frac{x^2}{\varepsilon_x} + \frac{y^2}{\varepsilon_y} + \frac{z^2}{\varepsilon_z} - 1\right) \quad (3.15)$$

With the generated system of equations from the Lagrange multiplier method ($\partial F_i / \partial x_i = 0$, and $\partial F_j / \partial \lambda_j$) where index $i = x, y, z$ and $j = 1, 2$ we obtain a system of 3 equations:

$$i\left(1 - \frac{r^2}{\varepsilon_i}\right) + s_i\left(\frac{xs_x}{\varepsilon_x} + \frac{ys_y}{\varepsilon_y} + \frac{zs_z}{\varepsilon_z}\right) = 0 \quad (3.16)$$

The result is verified when substituting $r \rightarrow \frac{\vec{D}}{\sqrt{\vec{E} \cdot \vec{D} \varepsilon_o}}$ back which recovers Equation 15.

3.2.2 GaAs and Al_{0.92}Ga_{0.08}As crystal classification

GaAs as well as Al_{1-x}Ga_xAs are both within the $F\bar{4}3m$ space group. Crystals of this space group are commonly known as zincblende crystals; a common crystal configuration named after zinc sulfide (ZnS). Also categorized as a cubic crystal, their crystallographic structure displays linear optical isotropy when stress free and no DC and/or slowly varying electric fields are present [47].

Zincblende structures, like the crystalline materials in question can exhibit birefringent properties when under influence of mechanical stresses and static / low-frequency electric

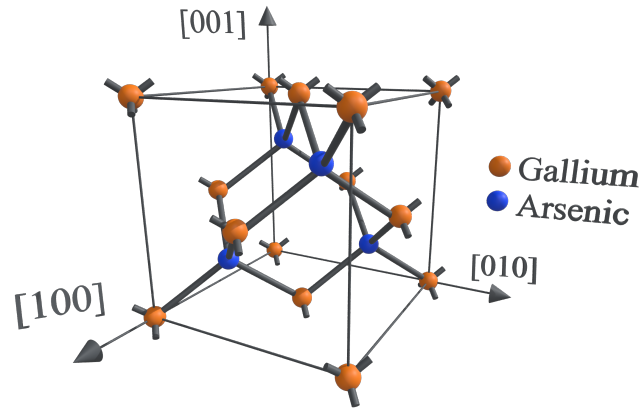


Figure 3.3: The unit cell of gallium arsenide (GaAs) with associated miller indices as coordinate axes

fields (E_{STLF}); characterized by photoelastic and electro-optic effects respectively. For realistic mirror coatings, heteroepitaxial bonding between GaAs/ $\text{Al}_{0.92}\text{Ga}_{0.08}\text{As}$ layers (potentially from a noticeable difference in lattice cell constant) may produce an intrinsic strain within the HR stack and can lead to the existence of a static non-negligible birefringence throughout the coating layers [48, 49].

3.2.3 Linear electro-optic effect (Pockel's effect)

For non-centrosymmetric crystalline media there exists a non-zero rank 2, 6×3 tensor (r_{ij}) connecting low-frequency ¹ electric fields $\vec{E}_{STLF}(f) = [E_x(f), E_y(f), E_z(f)]$ directly to the indicatrix [50, 51]:

$$\begin{bmatrix} \left(\frac{1}{\Delta n^2}\right)_1 \\ \left(\frac{1}{\Delta n^2}\right)_2 \\ \left(\frac{1}{\Delta n^2}\right)_3 \\ \left(\frac{1}{\Delta n^2}\right)_4 \\ \left(\frac{1}{\Delta n^2}\right)_5 \\ \left(\frac{1}{\Delta n^2}\right)_6 \end{bmatrix} = \begin{bmatrix} r_{11} & r_{12} & r_{13} \\ r_{21} & r_{22} & r_{23} \\ r_{31} & r_{32} & r_{33} \\ r_{41} & r_{42} & r_{43} \\ r_{51} & r_{52} & r_{53} \\ r_{61} & r_{62} & r_{63} \end{bmatrix} \begin{bmatrix} E_x(f) \\ E_y(f) \\ E_z(f) \end{bmatrix} \quad (3.17)$$

¹“low frequency” meaning orders of magnitude smaller relative to an optical field

The i index runs over the terms in the indicatrix equation:

$$\left(\frac{1}{\Delta n_x^2}\right)x^2 + \left(\frac{1}{\Delta n_y^2}\right)y^2 + \left(\frac{1}{\Delta n_z^2}\right)z^2 + 2\left(\frac{1}{\Delta n_{xz}}\right)xz + 2\left(\frac{1}{\Delta n_{yz}}\right)yz + 2\left(\frac{1}{\Delta n_{xy}}\right)xy = 1 \quad (3.18)$$

3.2.3.1 r_{ij} for zincblende crystals ($r_{43m,ij}$)

The form of the electro-optic tensor for zincblende crystals (including GaAs and $\text{Al}_{0.92}\text{Ga}_{0.08}\text{As}$) reduces such that $r_{ij} = r_{41} = r_{52} = r_{63} \neq 0$ with all other terms being zero:

$$r_{43m,ij} = \begin{bmatrix} 0 & 0 & 0 \\ 0 & 0 & 0 \\ 0 & 0 & 0 \\ r_{41} & 0 & 0 \\ 0 & r_{52} & 0 \\ 0 & 0 & r_{63} \end{bmatrix} \quad (3.19)$$

Where $r_{41} = r_{52} = r_{63}$

3.2.4 New principal (electro-optic) dielectric axis for zincblende structures

In general the principle dielectric axes of the new ellipsoid do **not** coincide with the axes of the ellipsoid of the unperturbed crystal. The form of the index ellipsoid for a zincblende crystalline material accounting for the electro-optic tensor and some generalized DC electric field \vec{E} expressed in terms of the crystallographic axes is given by:

$$\left(\frac{1}{n_o^2}\right)x^2 + \left(\frac{1}{n_o^2}\right)y^2 + \left(\frac{1}{n_o^2}\right)z^2 + 2r_{41}E_xyz + 2r_{41}E_yxz + 2r_{41}E_zxy = 1 \quad (3.20)$$

Where we have set $n_x = n_y = n_z = n_o$ for zincblende structures. Visualizing the above as a tensor:

$$\begin{bmatrix} \left(\frac{1}{n_o^2}\right) & r_{41}E_x & r_{41}E_y \\ r_{41}E_x & \left(\frac{1}{n_o^2}\right) & r_{41}E_z \\ r_{41}E_y & r_{41}E_z & \left(\frac{1}{n_o^2}\right) \end{bmatrix} \quad (3.21)$$

3.2.5 The photoelastic effect

General stresses and strains of a material may also cause transformations to the indicatrix connected by the rank 4 elasto-optical tensor p_{ijkl} :

$$\left(\frac{1}{\Delta n^2}\right)_{ij} = p_{ijkl}\epsilon_{kl} \quad (3.22)$$

Where the strain (ϵ) relates to stress (σ) using the generalized Hooke's law:

$$\begin{aligned} \epsilon_{ij} &= K_{ijkl}\sigma_{kl} \\ \sigma_{ij} &= C_{ijkl}\epsilon_{kl} \end{aligned} \quad (3.23)$$

A connection is also formed between the elasto-optical tensor (\mathbf{p}) to the piezo-optical tensor ($\boldsymbol{\pi}$):

$$\begin{aligned} p_{ijkl} &= \pi_{ijkl}C_{klrs} \\ \pi_{ijrs} &= p_{ijrs}K_{rskl} \end{aligned} \quad (3.24)$$

3.2.6 The generalized indicatrix

Both forms of the induced birefringence (electro-optic and photo-elastic) can be incorporated into a condensed form [51]:

$$\left(\frac{1}{\Delta n^2}\right)_{ij} = r_{ijk}E_k + p_{ijkl}\epsilon_{kl} \quad (3.25)$$

3.3 Electro-optic noise of a GaAs / Al_{0.92}Ga_{0.08}As stack

A comprehensive survey of relevant birefringent properties of a HR GaAs/Al_{0.92}Ga_{0.08}As mirrorstack is due, and for this body of work includes: 1) crystal coordinate considerations when asserting an optical axis on a highly reflective crystalline stack manufactured by the Thorlabs crystalline coatings division, 2) citations of coating parameters and observed intrinsic birefringence from the highly reflective coating stack in question, 3) analysis of the differential electro-optic effect on the phase of a reflected beam, and 4) estimating the differential phase noise in LIGO based on preliminary electric field measurements measured at LHO.

3.3.1 Static Birefringence / Miller indices from a HR GaAs / Al_{0.92}Ga_{0.08}As coating

Thorlab's crystalline coatings division grows their HR crystalline optical coating such that the coating surface is drawn out in the [100] plane, meaning that beam with a wavevector along the optical (z) axis draws a parallel line to the normal of said plane. Therefore since the beam's polarized E-field oscillates only within that plane, any differential splitting of the beam polarization occurs solely between rotated [010] and [001] axes. This allows us to restrict our interest to a field where $E_z \neq 0$ and $E_x = E_y = 0$ and compute the eigenvalues ($\lambda_{x',y',z'}^*$ / eigenpolarizations ($\vec{x}', \vec{y}', \vec{z}'$) which lead us to the relevant eigenindices ($n_{x',y'}$)²:

$$\begin{aligned}\lambda_{x'} &= \left(\frac{1}{n_o^2} - r_{41}E_z\right) \\ \lambda_{y'} &= \left(\frac{1}{n_o^2} + r_{41}E_z\right) \\ \lambda_{z'} &= \frac{1}{n_o^2}\end{aligned}\tag{3.26}$$

And the principal axes / eigenpolarizations are found when solving for the eigenvectors:

²There may appear to be an inconsistency between the miller indices and optical axes, but because of the isotropy of zinblende crystals prior to the field perturbation coordination of these axes is not quite relevant

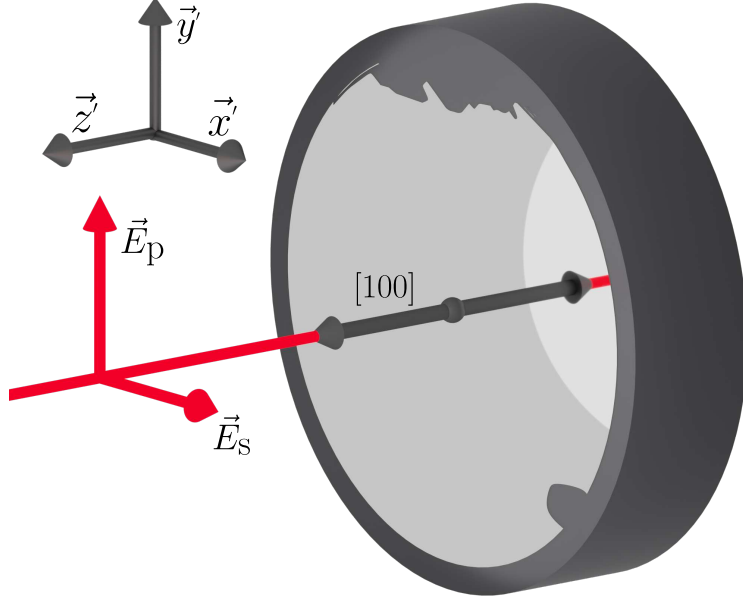


Figure 3.4: The beam propagation axis with respect to the GaAs/Al_{0.92}Ga_{0.08}As crystal axis. The axis formed by the [100] plane normal is drawn parallel with the beam axis (z -axis) and the polarizations of incident and reflected beam oscillate along vectors within the plane formed by the normal of that axis. The topmost coordinate axis triad is drawn to depict world vectors that can help visualize the plane of computed eigenvectors. Depicted here are also defects at the top and bottom right of the coating due to overhandling but do not effect the results of this study.

$$\begin{aligned}\vec{x}' &= \frac{1}{\sqrt{2}} (0, -1, 1) \\ \vec{y}' &= \frac{1}{\sqrt{2}} (0, 1, 1) \\ \vec{z}' &= (1, 0, 0)\end{aligned}\tag{3.27}$$

$$\lambda_{x'} x'^2 + \lambda_{y'} y'^2 + \lambda_{z'} z'^2 = 1\tag{3.28}$$

The eigenindices ($n_\alpha = n_{x'}$, $n_\beta = n_{y'}$) are therefore:

$$\begin{aligned}n_{x'} &= \sqrt{\lambda_{x'}} = \sqrt{\frac{1}{n_o^2} - r_{41} E_z} \\ n_{y'} &= \sqrt{\lambda_{y'}} = \sqrt{\frac{1}{n_o^2} + r_{41} E_z}\end{aligned}\tag{3.29}$$

And with $n_o r_{41} E_z \ll 1$:

$$\begin{aligned}
n_{x'} &\approx n_o + \frac{1}{2}n_o^3 r_{41} E_z \\
n_{y'} &\approx n_o - \frac{1}{2}n_o^3 r_{41} E_z
\end{aligned}
\tag{3.30}$$

3.3.2 Electro-optic coupling to the reflected phase of a HR mirror coating

Analytic estimate

Fejer and Bonilla takes on an analytical approach to finding the impact of the electric field to the change in phase of the light through a crystalline anisotropic thin film ($\lambda/4$) stack. The construction builds off of a pre-defined derivation of thermo-optic noise calculations for the HR stack and assuming a large enough number of high-low index coating pairs [52, 53]:

$$\left| \frac{\partial \phi}{\partial E} \right| = -\pi \frac{r_{41}}{2} (n_{\text{high}} n_{\text{low}}^2 + n_{\text{low}} n_{\text{high}}^2) \frac{n_{\text{high}}}{n_{\text{low}}}
\tag{3.31}$$

With $n_{\text{low}} = n_{\text{Al}_{0.92}\text{Ga}_{0.08}\text{As}} = 2.9369$, $n_{\text{high}} = n_{\text{GaAs}} = 3.4786$, and $r_{41} = -1.33 \times 10^{-12}$

The estimated differential phase from the electro-optic effect with a 1064nm E-field propagating along the [110] axis of the HR GaAs/Al_{0.92}Ga_{0.08}As stack:

$$\left| \frac{\partial \phi}{\partial E} \right| = 4.0253 \times 10^{-12} \frac{[\text{rad}]}{[\text{V/m}]}$$

Numerical estimate

In the appendix of [54] Ballmer constructs a coating layer transfer function for a given coating layer k with index n_k , and thickness d_k , defining right and left propagating modes $\psi^{R,L}$ respectively:

$$\begin{bmatrix} \psi^R \\ \psi^L \end{bmatrix}_{k+1} = Q_k D_k \begin{bmatrix} \psi^R \\ \psi^L \end{bmatrix}$$

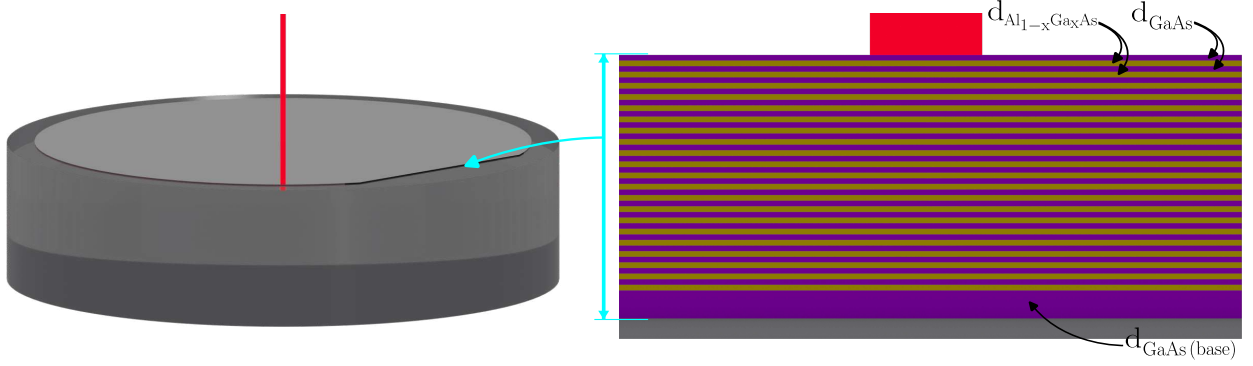


Figure 3.5: The beam propagation axis (\vec{S} , $[-100]$) with respect to the GaAs/ $\text{Al}_{0.92}\text{Ga}_{0.08}\text{As}$ crystal axes. The axis formed by the $[100]$ plane normal is drawn parallel with the beam axis (z -axis) and the polarizations of incident and reflected beam oscillate along vectors within the plane formed by the normal of that axis. Usually, these coatings made by Thorlab's crystalline mirror coatings division is grown with a flat indicating a line within the $[0-11]$ plane; where the plane normal points towards the sample center.

D_k applies the phase ($\phi_k = 4\pi n_k d_k / \lambda_0$) from a given coating layer, and Q_k applies the transfer function between high-low/low-high index layers transition:

$$D_k = \begin{bmatrix} e^{-i\phi_k/2} & 0 \\ 0 & e^{i\phi_k/2} \end{bmatrix} \quad (3.32)$$

$$Q_k = \frac{1}{2n_{k+1}} \begin{bmatrix} n_{k+1} + n_k & n_{k+1} - n_k \\ n_{k+1} - n_k & n_{k+1} + n_k \end{bmatrix} \quad (3.33)$$

Defining a HR coating stack, the total transfer matrix from vacuum Q_0 to the N th coating layer is:

$$M = Q_N D_N \dots Q_k D_k \dots Q_1 D_1 Q_0 \quad (3.34)$$

And the partial derivative at the k th coating layer is:

$$\frac{\partial M}{\partial \phi_k} = Q_N D_N \dots Q_k \begin{bmatrix} e^{-i\phi_k/2} & 0 \\ 0 & e^{i\phi_k/2} \end{bmatrix} \begin{bmatrix} -i/2 & 0 \\ 0 & i/2 \end{bmatrix} Q_{k-1} D_{k-1} \dots Q_1 D_1 Q_0 \quad (3.35)$$

The above representing a collective differential phase manifesting as a sum of these phase components. This explicit perturbed phase at the k th layer for the electro-optic effect ($\partial n_k / \partial E$) is found when:

$$\frac{\partial \phi_k}{\partial E} = \frac{4\pi d_k}{\lambda} \frac{\partial n_k}{\partial E} = \pm \frac{2\pi}{\lambda} n_k^3 d_k r_{41,k} \quad (3.36)$$

Where the electro-optic coefficients r_{41} for GaAs and $\text{Al}_{1-x}\text{Ga}_x\text{As}$ [55, 56, 49]:

$$\begin{aligned} r_{41,\text{GaAs}} &= -1.33 \times 10^{-12} \quad [\text{m/V}] \\ r_{41,\text{Al}_{1-x}\text{Ga}_x\text{As}} &= -(1.33 - 0.45x) \times 10^{-12} \quad [\text{m/V}] \end{aligned} \quad (3.37)$$

Rather than tagging on the phases individually, an easier computation is found when relying on the relationship between the transmission (t) and reflectivity (r) to a general transfer matrix (in our case M):

$$\begin{bmatrix} M_{11} & M_{12} \\ M_{21} & M_{22} \end{bmatrix} \begin{bmatrix} 1 \\ r \end{bmatrix} = \begin{bmatrix} t \\ 0 \end{bmatrix}$$

And using this relation, differentiating the reflectivity with respect to ϕ_k :

$$\frac{\partial r}{\partial \phi_k} = - \left(\frac{1}{M_{21}} \frac{\partial M_{21}}{\partial \phi_k} - \frac{1}{M_{22}} \frac{\partial M_{22}}{\partial \phi_k} \right) \frac{M_{21}}{M_{22}}$$

The differential reflectivity is normalized by the total reflectivity and taking the imaginary component as noted in Equation 3.35:

$$\frac{\partial \phi_c}{\partial \phi_k} = \text{Im} \left(\frac{1}{r} \frac{\partial r}{\partial \phi_k} \right) = \left(\frac{1}{M_{21}} \frac{\partial M_{21}}{\partial \phi_k} - \frac{1}{M_{22}} \frac{\partial M_{22}}{\partial \phi_k} \right) \quad (3.38)$$

The impact of a differential electric noise field (E_{STLF}) on M due to the electro-optic effect on the k th layer, we use the chain rule:

$$\left| \frac{\partial \phi_c}{\partial E_{\text{STLF}}} \right| = \left| \frac{\partial \phi_c}{\partial \phi_k} \frac{\partial \phi_k}{\partial E} \right| \quad (3.39)$$

The coating to be studied consists of 36 $\lambda/4$ thick layers of GaAs interspersed with 35 layers of $\lambda/4$ thick $\text{Al}_{0.92}\text{Ga}_{0.08}\text{As}$. GaAs forms the top and bottom layer to prevent oxygen absorption from the AlGaAs layer. The GaAs layers have an index of $n_{\text{GaAs}} = 3.480$ and a thickness of $\Delta d_{\text{GaAs}} = 76.43$ nm while the low index $\text{Al}_{0.92}\text{Ga}_{0.08}\text{As}$ layers are $n_{\text{Al}_{0.92}\text{Ga}_{0.08}\text{As}} = 2.977$ with thickness $\Delta d_{\text{Al}_{0.92}\text{Ga}_{0.08}\text{As}} = 89.35$ nm. With the constructed matrices, we apply these parameters and compute a differential phase of:

$$\left| \frac{\partial \phi_c}{\partial E_{\text{STLF}}} \right| = 3.9 \times 10^{-11} \frac{[\text{rad}]}{[\text{V/m}]} \quad (3.40)$$

3.3.3 Initial projected DARM coupling

Measured field spectra acquired from installed electric field meters located within LHO and LLO ETMX and ETMY vacuum chambers can help translate how much DARM coupling can occur from electro-optic coating noise. For O3 the EFMs were located next to the test mass mirrors and measured a consistent $3 [\mu\text{V/m}/\sqrt{\text{Hz}}]$ @ 100 Hz [2]. This along with computed estimate allows us to create an upper limit for what this noise might be assuming incoherent fields between the end stations and a flat frequency response within LIGO's bandwidth. An initial differential phase noise estimate of $\approx 4.5 \times 10^{-10}$ [rad/m/V], alongside measured LHO ambient field noise measured during O3 we compute an initial strain noise estimate [53, 2]:

$$\frac{\partial L}{\partial E} = \frac{\lambda}{4\pi} \left| \frac{\partial \theta_c}{\partial E} \right| = 3.3 \times 10^{-18} \frac{[\text{m}]}{[\text{V/m}]}$$

$$h_{\text{EO noise}} = 2 \frac{\Delta L_{\text{EO noise}}}{L} = 2 \frac{\partial L}{\partial E} \times \left| \frac{E_{\text{noise}}}{L_{\text{arm}}} \right| = 4.95 \times 10^{-27} [1/\sqrt{\text{Hz}}] \quad (3.41)$$

Chapter 4

Measurement of electro-optic noise in a GaAs/Al_{0.92}Ga_{0.08}As mirror coating

4.1 Electro-optic measurement apparatus

In order to experimentally investigate the EO effect in GaAs / Al_{0.92}Ga_{0.08}As coatings, we developed an optical setup using a Fabry-Pérot cavity. Figure 4.1 shows the schematic of the experimental setup. Parameters of this setup are listed in Table 4.1. The Fabry-Pérot cavity is composed of two high-reflectivity mirrors – an amorphous coating front mirror and GaAs/Al_{0.92}Ga_{0.08}As coating with the same composition used in § 3.3.2, transferred to a planar super-polished fused silica substrate.

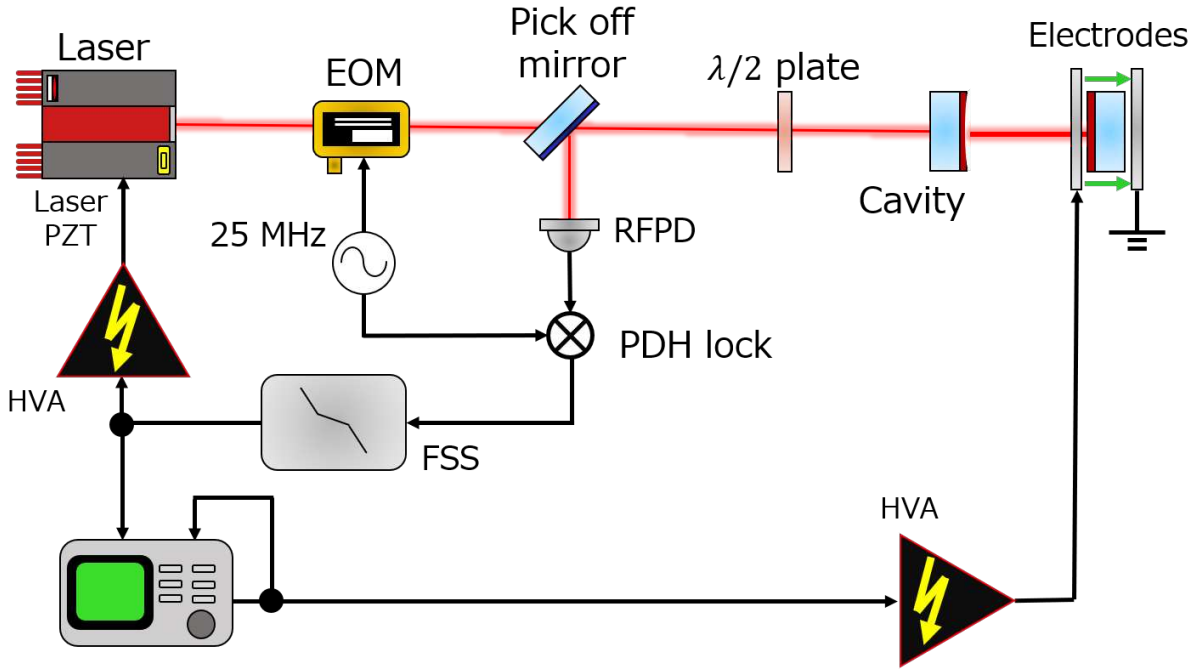


Figure 4.1: A simplified and modular schematic of the PDH servo used along with an electrostatic drive mount design comprised of a disk capacitor sandwiching the HR AlGaAs sample, a high voltage amplifier, and a signal / network analyzer.

Measurability of the electro-optic effect is contingent upon two initial design criteria: the sensitivity of the optical plant to be implemented in the PDH servo, and the maximum achievable electric field strength along the beam axis ($|E_z|_{\max}$).

4.1.1 Servo Parameters

The quantity we are attempting to measure is a differential length coupling on the order of 3.3×10^{-18} [m/(V/m)], motivating a short cavity design as the relative differential length (phase) change scales with the sensitivity Equation 1.13. Considerations of the lab mirror inventory and mode matching criteria lead us to two candidate plano-concave (ROC = 0.333m) HR IBS coated sample input couplers; one from CVI Melles-Griot and another from AT-Films. When paired with the plano-plano GaAs/Al_{0.92}Ga_{0.08}As mirror from the Crystalline Mirror Solutions (CMS) division of Thorlabs, designed cavity length was 0.105 m.

The implemented servo design uses a light source from a Mephisto 2000 NE Nd:YAG

laser with a 25 MHz phase modulation from a New Focus Model 4003 IR resonant phase modulator. As indicated in the figure above, the electronics chain can be decomposed into two primary filter components: $S(f)$ and $A(f)$. The following table provides a summary with relevant experiment parameters:

Table 4.1: Parameters of experimental setup.

Symbol	Description	Value
λ	Laser wavelength	1064 nm
L	Cavity length	0.105 m
T_i	Power transmissivity of input mirror	$\sim 0.5\%$
T_e	Power transmissivity of output mirror	~ 10 ppm
f_c	Cavity pole frequency	~ 600 kHz
x	Aluminum alloying fraction	0.92
d_H	Thickness of GaAs	76.43 nm
n_H	Refractive index of GaAs	3.48
d_L	Thickness of $\text{Al}_{0.92}\text{Ga}_{0.08}\text{As}$	89.35 nm
n_L	Refractive index of $\text{Al}_{0.92}\text{Ga}_{0.08}\text{As}$	2.98

The laser frequency is locked to the cavity length using the aforementioned Pound-Drever-Hall technique. The extracted error signal is then filtered by the Sensing chain ($S(f)$) before being passed to the Actuation chain ($A(f)$). When the laser is locked to the in-air cavity, the fluctuations of the laser frequency (Δf) obey Equation 1.13.

4.1.1.1 Sensing $S(f)$

Sensing electronics are composed of a single element photodiode mounted to a transimpedance amplifier circuit, splitting photocurrent to DC and RF filter chains. The RF path is within the feedback electronics chain and constructed to boost the RF signal prior to being passed to a frequency stabilization servo (FSS) § 4.2 where it is demodulated by mixing the 25 MHz oscillator phased with variable cable length. Once demodulated, the measured beat signal while sweeping through resonance generates the PDH error signal profiles Figure 1.8, and Figure 4.3.

4.2 FSS transfer function (LTSPICE)

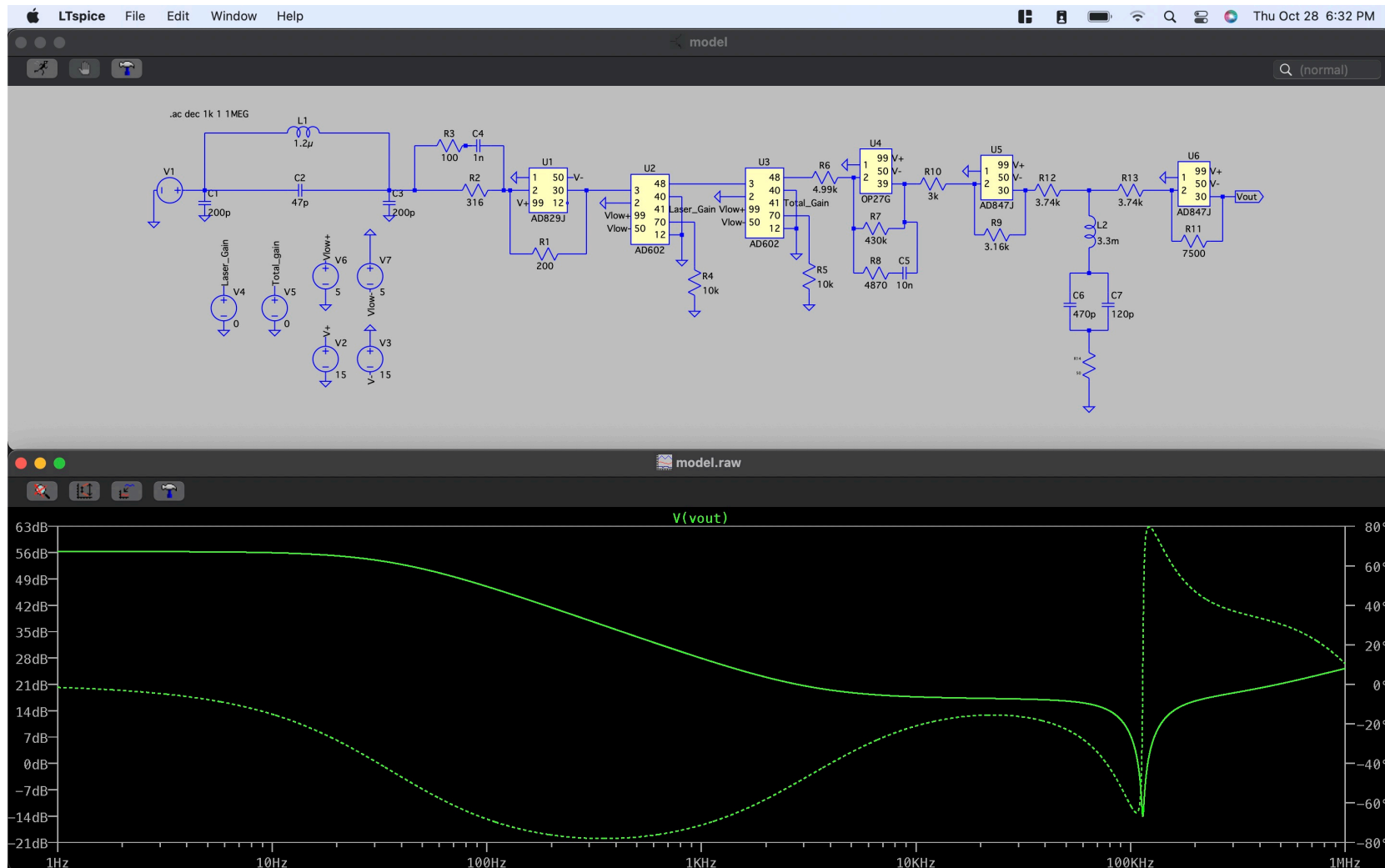


Figure 4.2: The FSS frequency response simulated in LTSpice

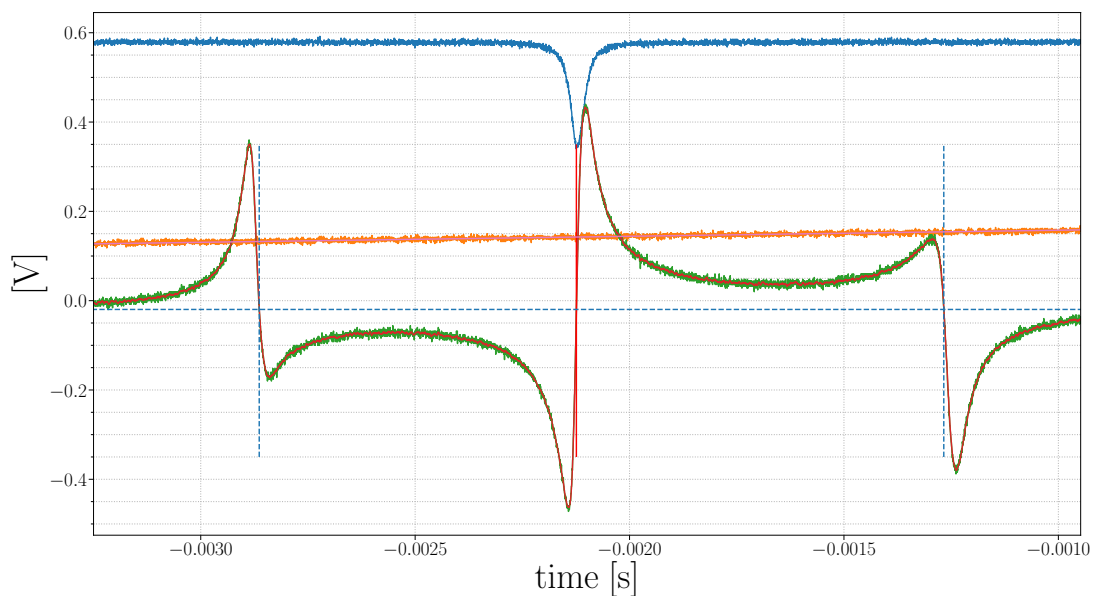


Figure 4.3: Ramping voltage sent to the laser PZT while probing the mixer output.

4.2.0.1 Actuation $A(f)$

The actuation portion of the loop amplifies the FSS output with a single I/O channel of the SVR 350-3 BIP High Voltage Amplifier from Piezomechanik GmbH with a custom pomona box fed back to the input [57]. The Mephisto 2220 laser cavity PZT actuator follows immediately after with a measured actuation factor of $1.7 \text{ [MHz]} / \text{[V]}$.

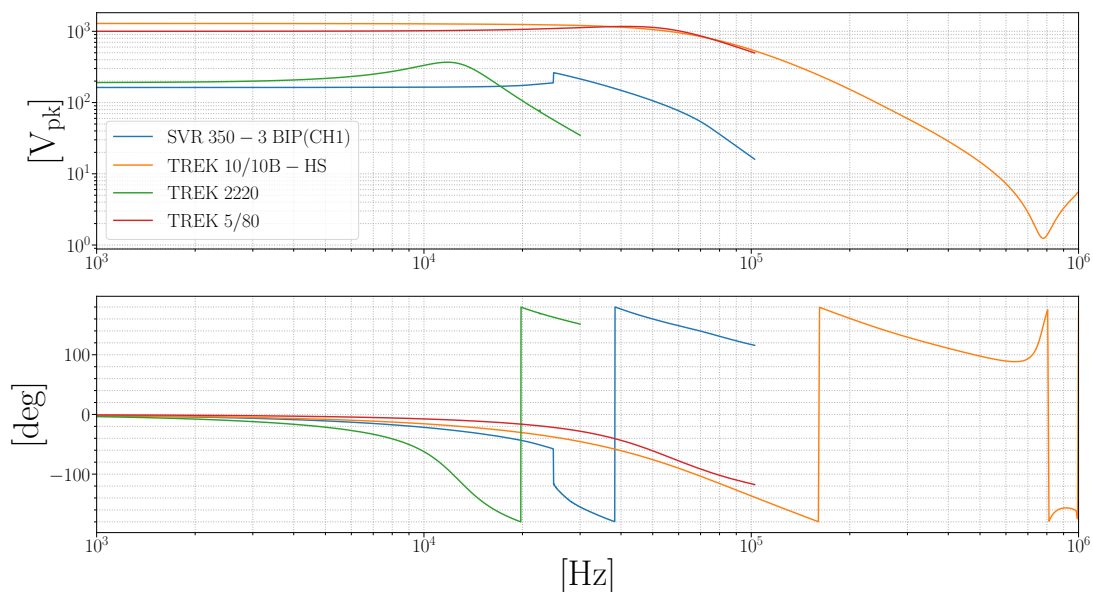


Figure 4.4: Different high voltage amplifier transfer functions used for the study

4.2.0.2 Loop Gain $G(f)$

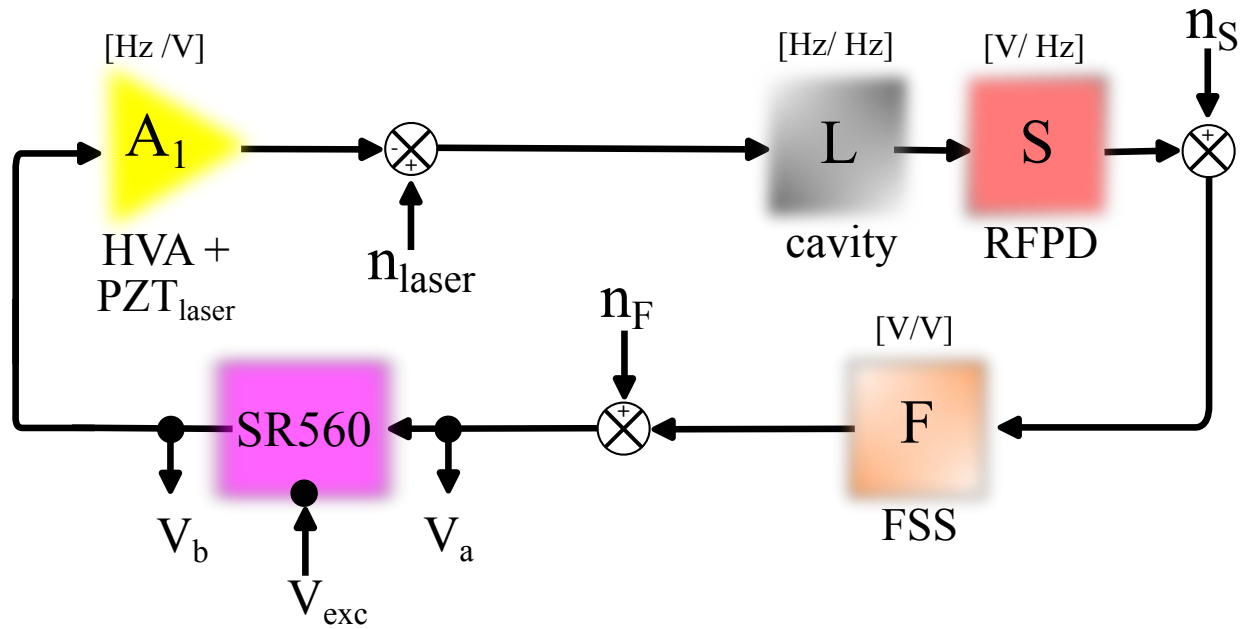


Figure 4.5: Open loop gain measurement diagram

$$V_b = (V_{exc} + n) + G(V_{exc} + n) + G^2(V_{exc} + n) + \text{H.O.T.s} = \frac{V_{exc} + n}{1 - G} \quad (4.1)$$

$$V_a = G \cdot V_{exc} + G^2 V_{exc} + G^3 V_{exc} + \text{H.O.T.s} = \frac{G V_{exc}}{1 - G} \quad (4.2)$$

We take the transfer function measurement ζ :

$$\zeta = \frac{V_a}{V_b} = \frac{G \cdot V_{exc} / (1 - G)}{(V_{exc} + n) / (1 - G)} \quad (4.3)$$

Assuming the excitation is appreciably larger than the noise ($e \gg n$):

$$\zeta \approx G \quad (4.4)$$

Isn't quite $A(f) * S(f)$ as stated. Doesn't entirely account for the optical plant. How the measurement is taken (important to take between installations to account for the changes

in the optical plant) [58].

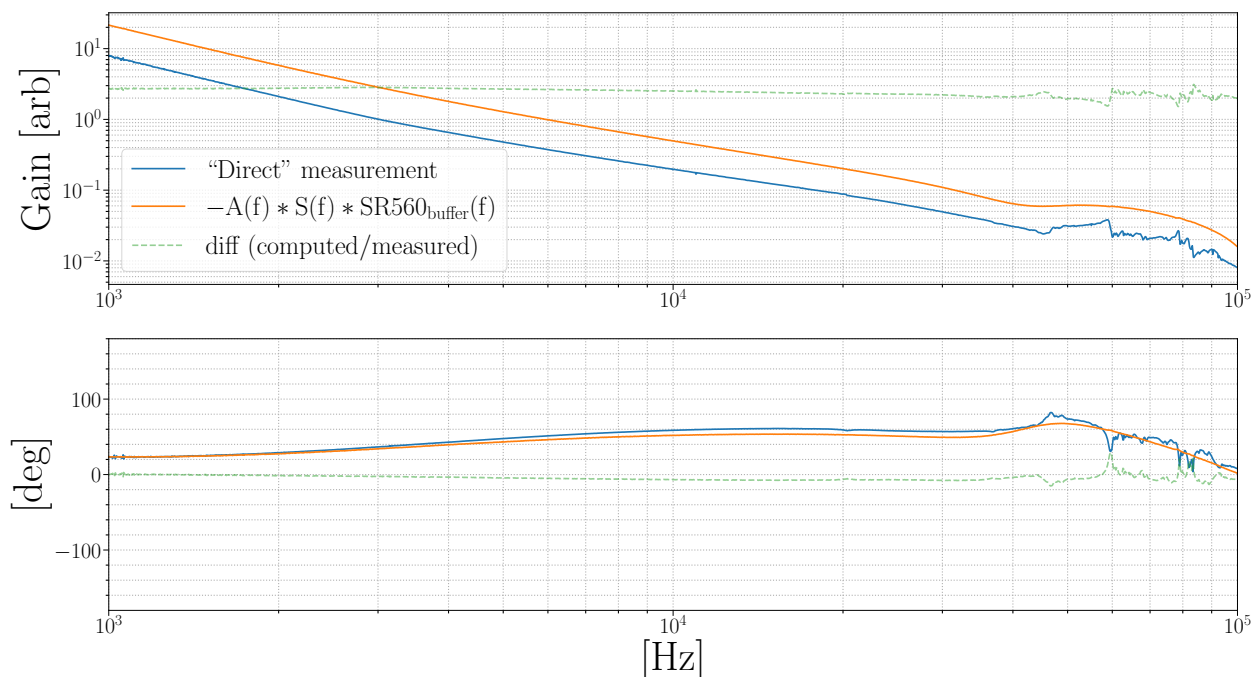


Figure 4.6: Comparison of the open loop gain measurement against the multiplied servo electronics measurements. The maximum gain difference is about a factor of 2.8 which is low passed to a difference of 2.0.

4.2.1 Longitudinal Pockels Cell mirror mount assembly

Maximizing a controlled and well defined electric field ($|E_z|$) within the coating while requiring a through beam to and through the HR coating lead us to a design very similar to that of a longitudinal pockels cell. The most common assembly used for this study is comprised of two electrodes with a 3mm central aperture which is chosen to be at least 5 times larger than the beam size at the plate locations; to avoid significant beam clipping while maximizing field strength (E_z) at the coating region of interest. There is also a required plate separation of at least 1/4" accounting for the thickness of the optical sample. Considering these constraints, modelling the system and computing the estimated field strength screened by the coating is the next step towards building the assembly.

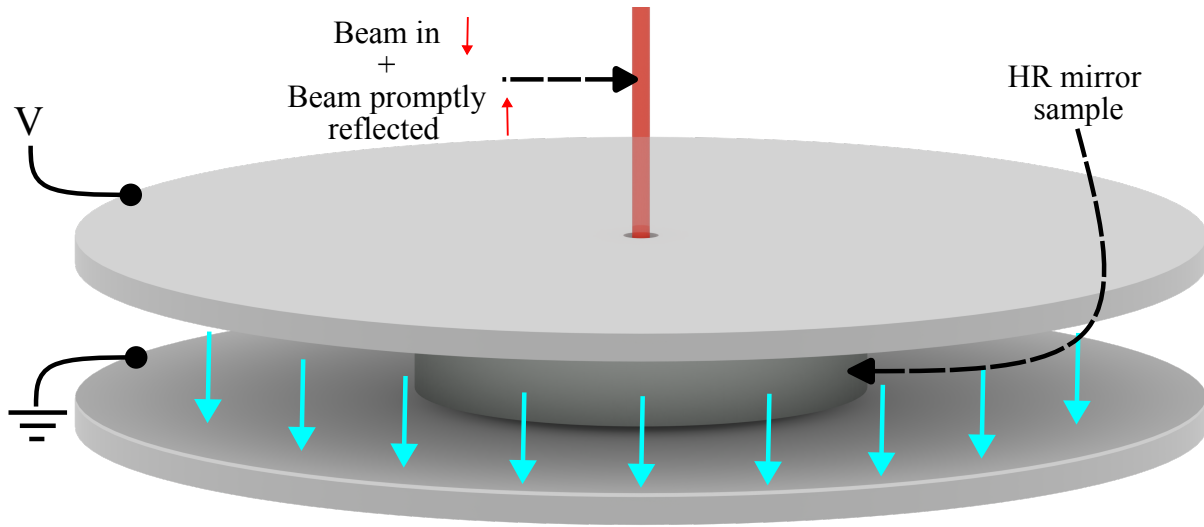


Figure 4.7: Concept image of the longitudinal Pockels cell assembly

Modeling

The field screened by the coating can be computed from Gauss' Law:

$$\nabla \cdot D = \rho_{\text{free}} \quad (4.5)$$

There is no free charge within the region of interest ($\rho_{\text{free}} = 0$), though the optic fused silica substrate with the AlGaAs coating imposes dielectric material between the plates. Boundary conditions are expressed in terms of the differential plate potential V , so it is natural to first solve the potential ($V(r, z)$) for all relevant system coordinate points.

$$\nabla^2 V = 0 \quad (4.6)$$

Boundary Conditions

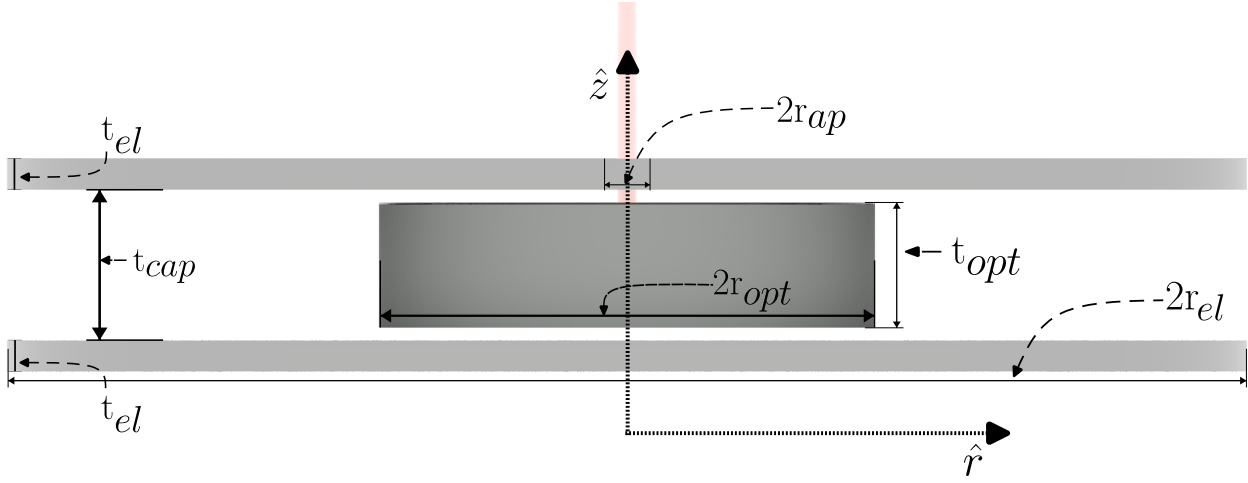


Figure 4.8: Side view of the longitudinal pockels cell mount. The figure is annotated with relevant parameters to build the numerical model: the finite thicknesses of the electrode plates (t_{el}), radius of the aperture at the center of the disk (r_{ap}), radius of the disk (r_d), thickness of the optic (t_{opt}), and radius of the optic substrate (r_{opt})

Substrate: $-t_{opt} < z < t_{opt}$ and $r < r_{opt}$

Coating $t_{opt} < z < t_{opt} + t_{coat}$ and $r < r_{opt}$

Driven Electrode (V): $t_{cap} < z < t_{cap} + 2t_{el}$ and $r_{ap} < r < r_d$

Grounded Electrode (GND): $-t_{cap} - 2t_{el} < z < -t_{cap}$ and $r_{ap} < r < r_d$

Simulation Area Edges: $z = z_{max}$ or $r = r_{max}$ or $r = r_{max}$

For assured simulation convergence, an exponential falloff was applied to the simulation boundaries other than the (free) $r = 0$ edge:

$$\text{Simulation Area Edges} \rightarrow A_o e^{(r+z)/r_o} \quad (4.7)$$

Where A_o is a characteristic voltage, and r_o is a chosen characteristic distance. Though

with the region of interest being at the coating surface, these edges are far enough away that a change in these characteristic values would cause a negligible difference to the resulting E-field estimate. Example parameters for various mount configurations can be found in the tables of the respective sections § 4.2.2.1 § 4.2.2.2 § 4.2.2.3.

Computing $V(r,z)$

Inspired by the second-order elliptic equation, operators are modified to incorporate the aforementioned boundary conditions [59]. The computation is noted in detail in § J.

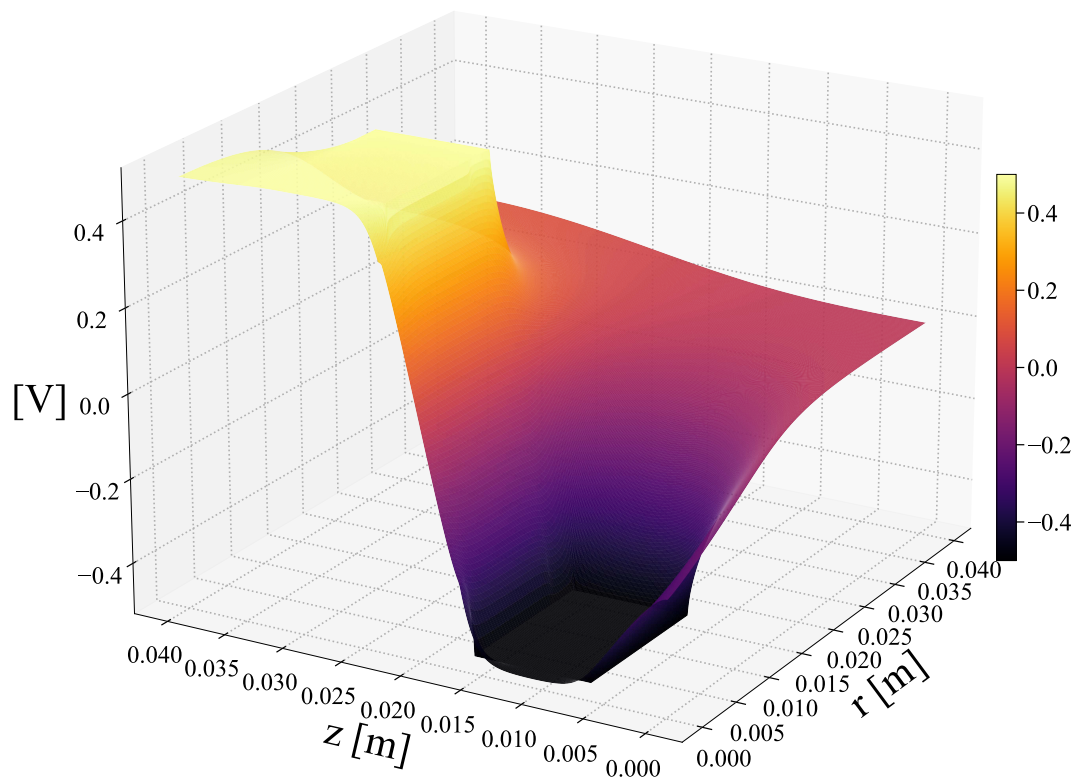


Figure 4.9: Numerically computed potential map estimate ($V(z, r)$ in cylindrical coordinates). The potential difference between the two plates (ΔV) is 1 [V] with a plate holding positive potential .5 [V] and a negative plate holding -.5 [V] to impose symmetry with the visualization. Although these held plate potentials differ from the ± 1 [V] and 0 [V] imposed in the experiment, the computation required to inform the field strength at the region of interest demonstrates a negligible difference between these two configurations.

Computing $|E_z|(\mathbf{r},z)$

The computed $|E_z|$ is screened by the coating at $r = 0$ for $V = 1$ and is estimated to be 13.3 [V/m] and will be included in the calibration as a pockels cell conversion efficiency of 13.3 [(V/m)/V]

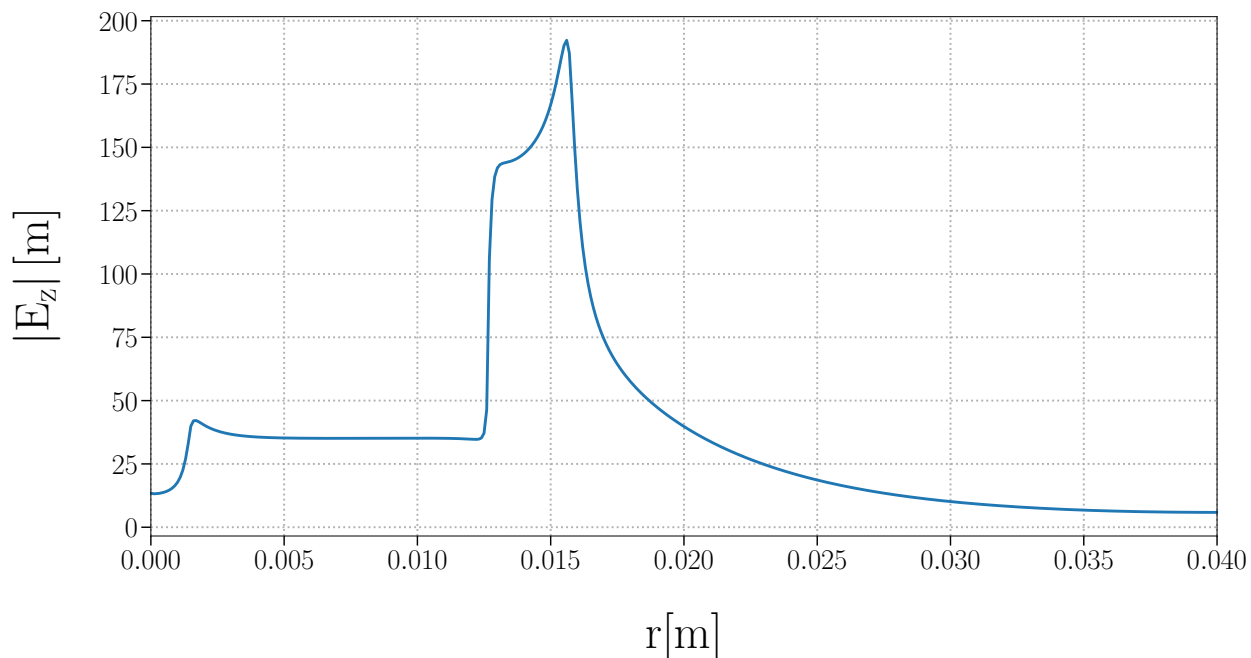


Figure 4.10: Plot of the $|E_z|$ field cross section sampled about the optic HR coating surface.

4.2.2 Assembly Mount Tests/Development

The following section briefly discusses the nature of early measurements performed with various longitudinal pockel cell mount assemblies. A significant barrier to low differential length noise sensitivity for this experiment was the lack of low-noise optical mounts in accessible non-conductive materials. Most commercial optical mounts are constructed with conductive materials which is problematic when seeking to isolate the coating from non-normal field gradients within the coating volume of interest. For this reason, efforts were focused on developing a suitable mounting solution that would provide adequate isolation from any uncontrolled field magnitudes while driving a field normally incident on the surface with enough strength and uniformity across the beam area to extract a measurement of the

differential length change from the Pockels effect. 3D printing for this project was initially used as a means to prototype optical mount designs but public health concerns at the time made testing with alternative materials aside from PLA and PETG difficult. There were multiple 3D prints tested within the optical schema depicted in Figure 4.1.

4.2.2.1 Assembly 0 and 1

Model Params

r_{ap} [m]	t_{cap} [m]	r_{el} [m]	t_{el} [m]	r_{opt} [m]	t_{opt} [m]
1.5e-3	4.5e-3	38.1e-3	1.5e-3	12.7e-3	6.35e-3

Electrodes

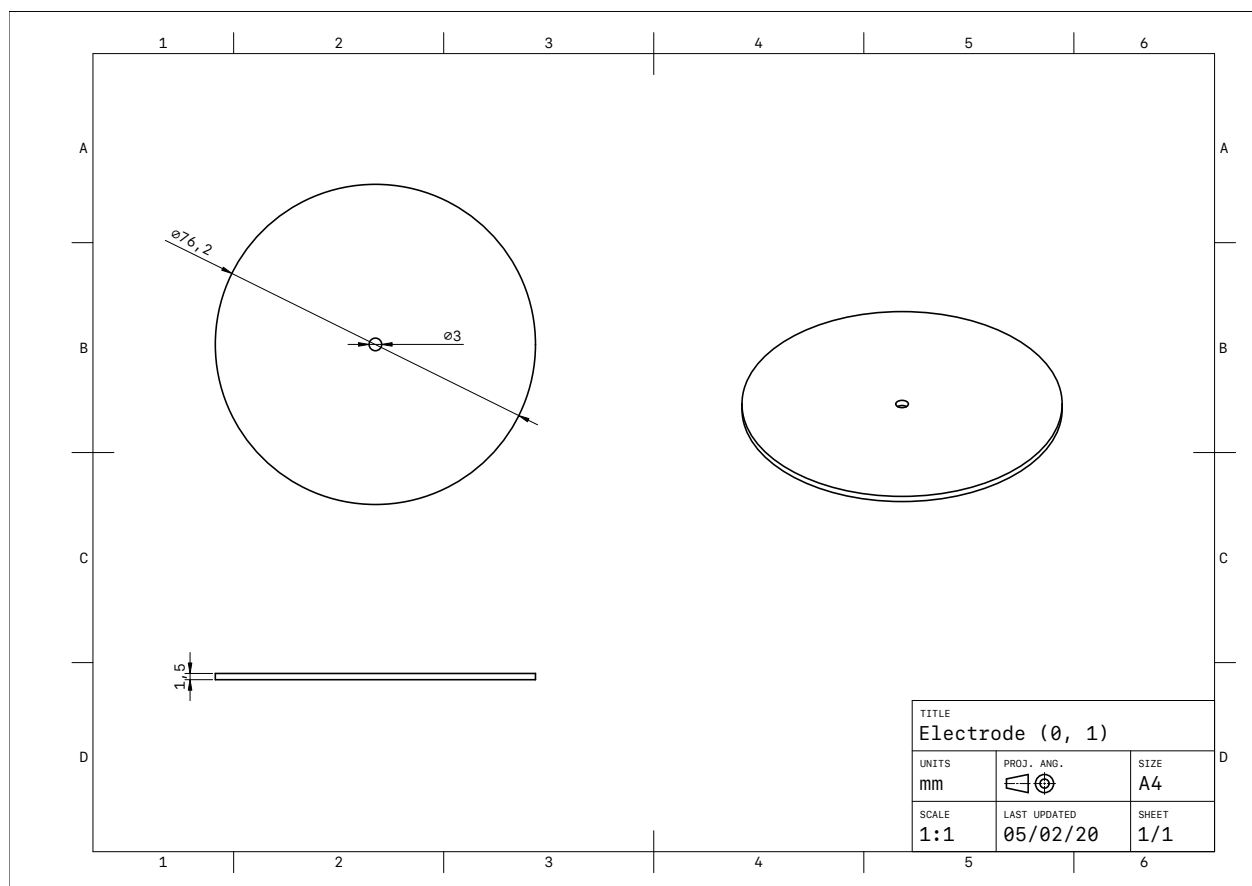


Figure 4.11: Technical drawing of the 3" disk electrode plates made of aluminum.

Mount 0

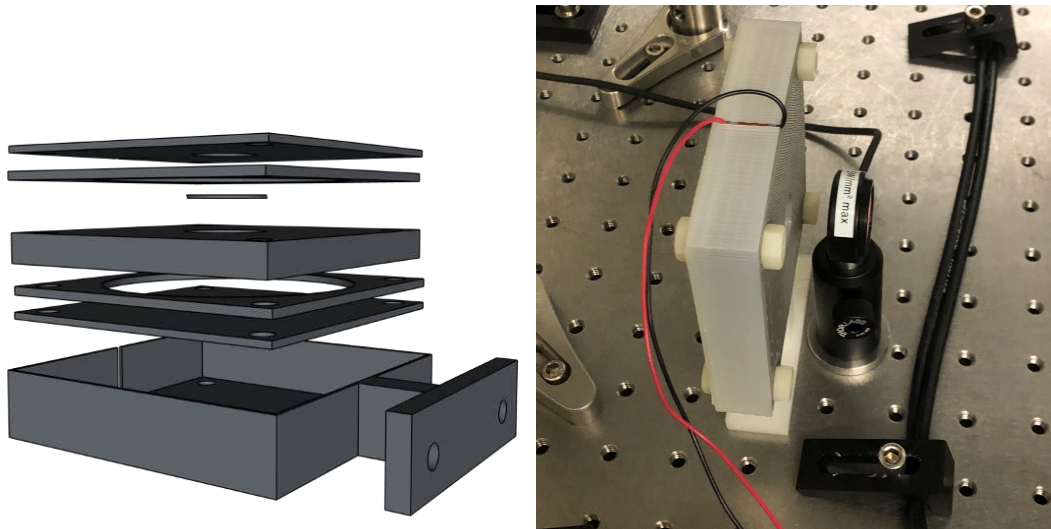


Figure 4.12: Assembly 0 was constructed to meet the criteria of providing a non-conductive housing for the electrode / sample assembly while maintaining a fixed length spacing using parts 3d printed with polylactic acid filament (PLA).

Mount 1.1

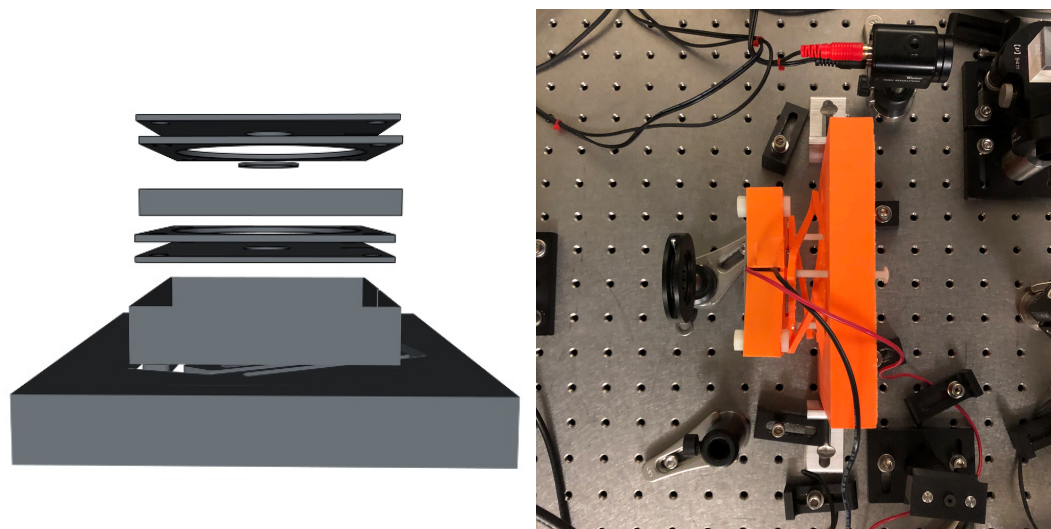


Figure 4.13: Assembly 1 was constructed to meet the criteria of providing a non-conductive housing for the electrode / sample assembly while maintaining a fixed length spacing using parts 3d printed with polylactic acid (PLA). The assembly is coupled to an ortho-planar spring to allow for a built-in pitch/yaw control

Mount 1.2

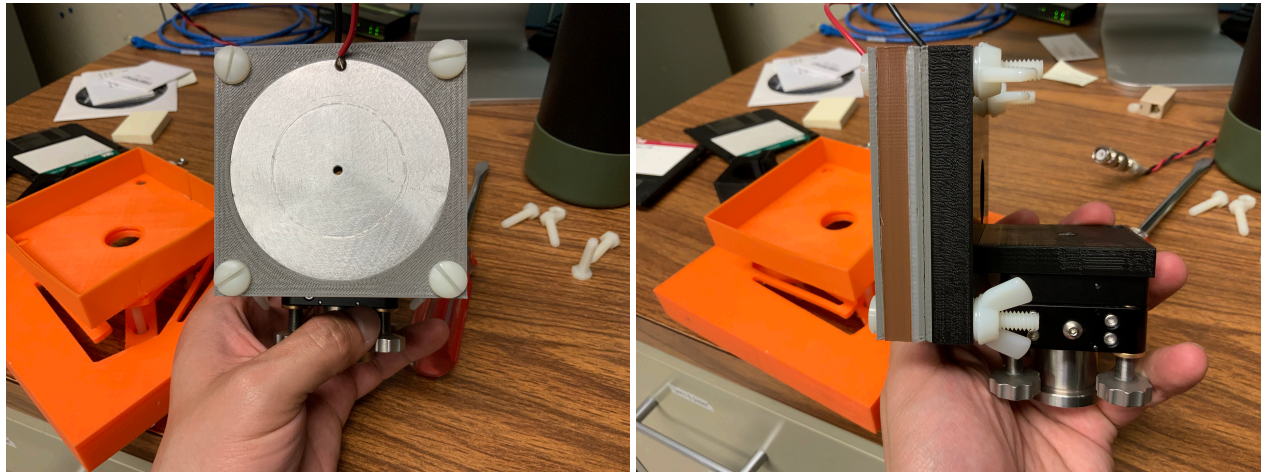


Figure 4.14: A modification implemented with the intention of reducing pitch dithering while still having control of DC YAW

4.2.2.2 Assembly 2

Model Params

r_{ap} [m]	t_{cap} [m]	r_{el} [m]	t_{el} [m]	r_{opt} [m]	t_{opt} [m]
1.5e-3	12.7e-3	N/A (rectangular)	1.27e-3	12.7e-3	6.35e-3

Electrodes

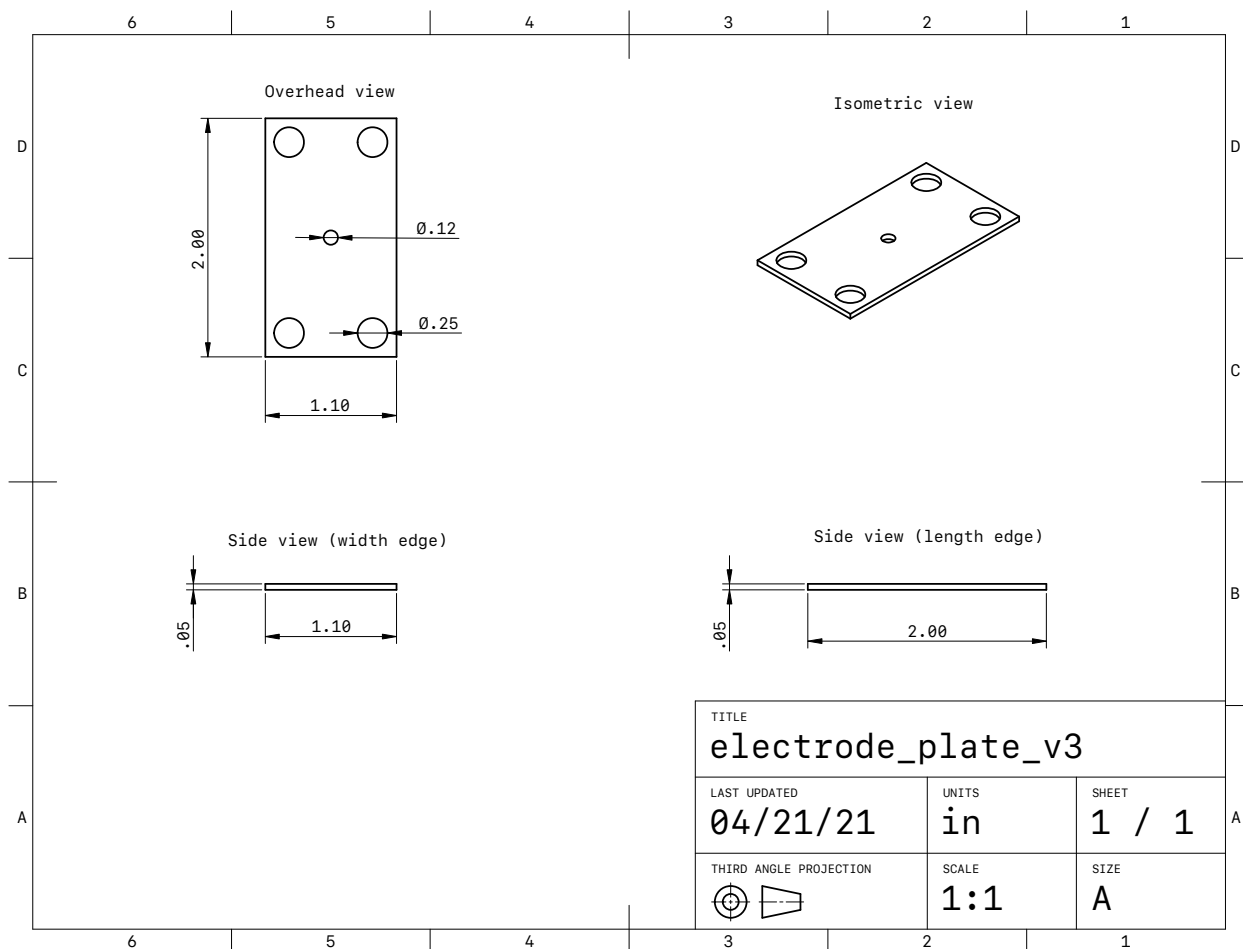


Figure 4.15: Rectangular (.05"X1.1"X2") plates made of aluminum.

Mount 2.0

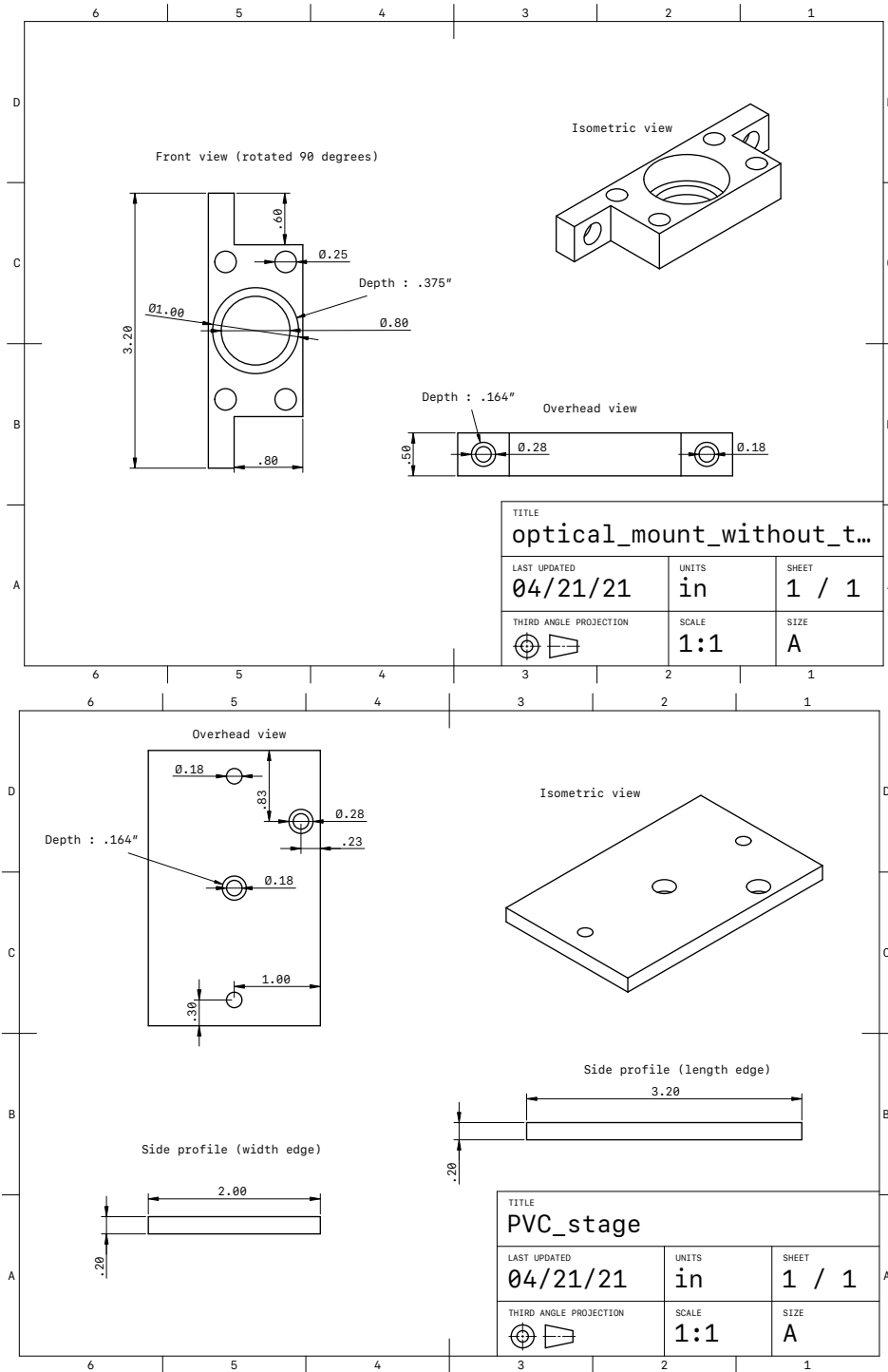


Figure 4.16: A design iteration of the assembly 2 mounts. Materials tried varied from PVC, PLA, and PETG. Quarter inch holes are bored in order to pass nylon screws holding electrode plates fixed to the mount.

Varying the mechanical configurations (i.e. differential electrode and / or optic set screw settings) to the slightest degree left us to discover a variety of drive couplings via excitations from the assembly sample-mount acoustic modes while driving the voltage on electrodes plates. Tracking consistent mechanical response for assemblies prior to Assembly 3 proved challenging due to inconsistent mechanical settings between some measurements and span different geometries / material properties. An adequate solution was dependent on selecting a material and geometry that would generate narrow acoustic resonances while simultaneously achieving adequately low noise within a bandwidth of interest (a not so uncommon experimental technique, esp. for optic suspensions, that is frequently used and mentioned within collaboration literature). Assembly 3 demonstrated such characteristics and is discussed further.

4.2.2.3 Assembly 3 (MACOR mount)

Model Params

r_{ap} [m]	t_{cap} [m]	r_{el} [m]	t_{el} [m]	r_{opt} [m]	t_{opt} [m]
1.5e-3	6.94e-3	15.75e-3	9.66e-3	12.7e-3	6.35e-3

Electrodes

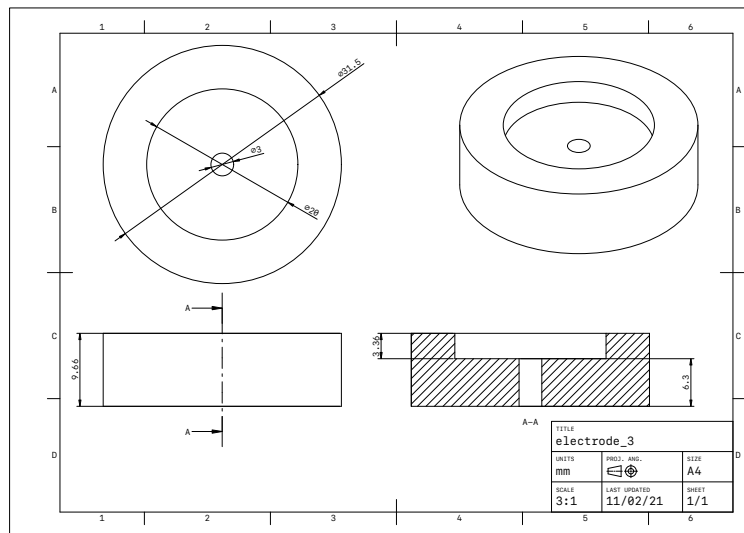


Figure 4.17: Technical drawing of thick disk electrode plates made of copper.

Mount 3.0

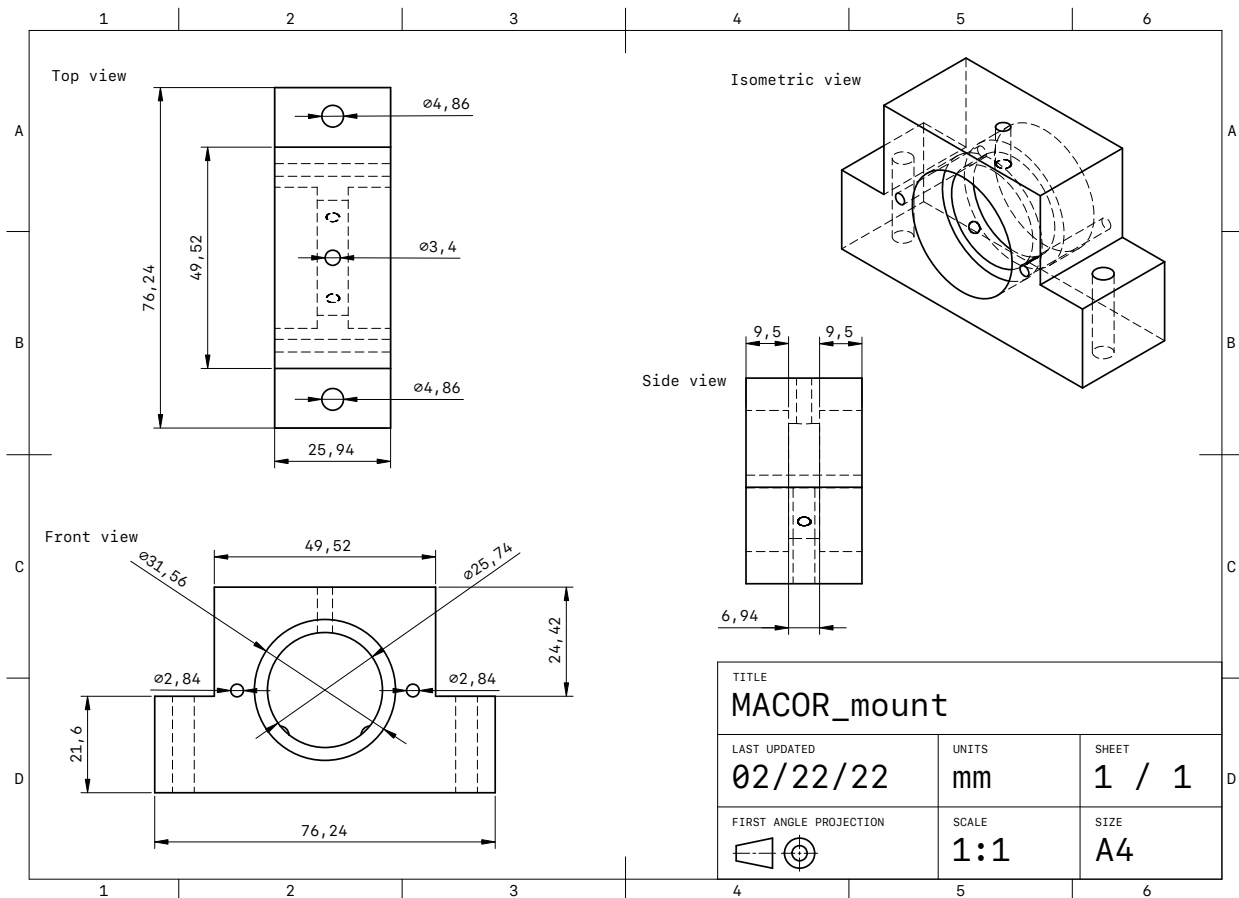


Figure 4.18: MACOR mount design constructed in Shapr3D

To maintain the aforementioned boundary conditions in situ, an optical mount made of MACOR, a machinable ceramic, was built and installed. With the material's high Young's modulus (66.9 GPa), and a moderate Poisson ratio (.29) [60] making it by far the most durable / non-conductive mounting solution tried.

An optical mount for the sample made with MACOR, along with spherical glass bearings with a $.48 \pm .01$ cm \varnothing , and a McMaster-Carr 8-32, 1/2" ceramic screw were used to clamp the optical sample within a bored $25.74 \pm .5$ mm \varnothing barrel. Two 1.24" \varnothing holes were also bored at a 9 mm depth about the front and back side of the optical mount to accommodate for a flush fit of copper electrodes. The construction suggests a $1 \pm .5$ mm clearance between the front and back surface of the sample to the electrode plates.

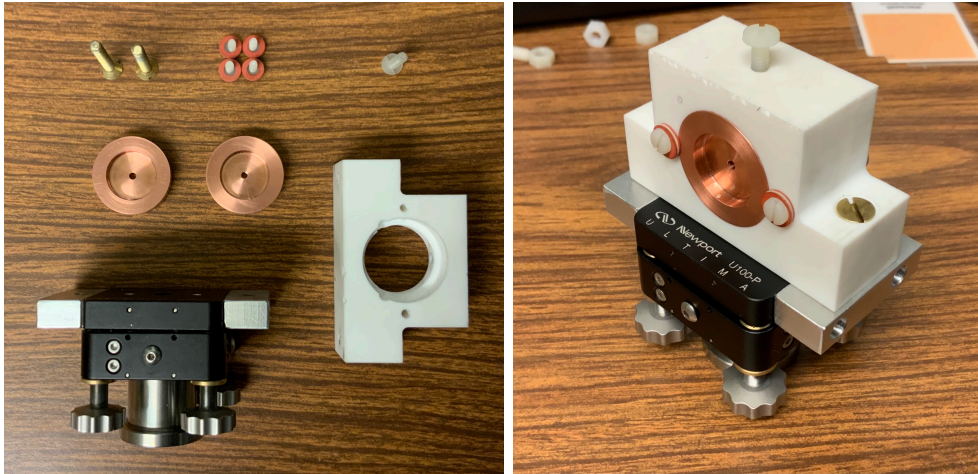


Figure 4.19: Assembly 3: [Left] disassembled configuration and [Right] an isometric view of the assembled configuration. The electrodes initially used were made of copper; a material chosen its high density with the intention of combatting inertial influence at high frequency, though aluminum plates with near identical geometry were used for later results.

This mount assembly lead to the published results discussed in the next chapter.

Chapter 5

Study on electro-optic noise in crystalline coatings toward future gravitational wave detectors

5.1 Foreword

The following section is comprised of a paper sharing the same title as this chapter. The paper was published in Physical Review D January 4th, 2022, and co-authored with Satoshi Tanioka, Garrett D. Cole, Steven D. Penn, and Stefan W. Ballmer [3].

5.2 Introduction

Direct detection of gravitational waves (GWs) by ground-based laser interferometric gravitational wave detectors (GWDs) has provided unique insight into the Universe [61, 7, 62]. In the current laser interferometric GWDs, km-scale Fabry-Pérot arm cavities are used which employ test mass mirrors coated with high-reflectivity amorphous coatings [63, 64].

The sensitivity of current GWD such as advanced LIGO (aLIGO) is partially limited by thermal noise arising from amorphous silica and titania-doped tantala coatings at their most

sensitive frequency band [42, 65]. Future GWDs are planned to employ low thermal noise coatings so that one can explore further into the Universe with improved sensitivity [66, 67, 68, 69]. Therefore, development of low thermal noise mirror coatings plays an important role in the development of future GWDs.

Crystalline gallium arsenide (GaAs) and aluminum-alloyed gallium arsenide ($\text{Al}_x\text{Ga}_{1-x}\text{As}$) coatings (referred to as AlGaAs coatings), which have demonstrated low thermal noise, are one of the coating candidates for future GWDs [45, 70]. In addition to exhibiting low elastic losses, optical absorption and scatter in AlGaAs are also low [48, 71]. Therefore, AlGaAs coatings have a potential to improve the performance of GWDs, resulting in fruitful scientific outcomes. There is a coordinated research effort to realize AlGaAs coating mirrors in future upgraded GWDs [72, 73, 74].

While crystalline AlGaAs coatings can reduce thermal noise, they may also be susceptible to coupling from fluctuations in the electric field. Refractive indices of AlGaAs coatings vary in proportion to the electric field via the electro-optic (EO) effect [75, 50]. Fluctuations in the electric field couples to the cavity length fluctuations through the change in refractive indices of coatings, and can show up as noise in a GWD [76, 52].

In order to investigate the impact of the noise induced by the EO effect in AlGaAs coatings, we have developed an experimental setup using a Fabry-Pérot cavity. In this study, we focused on the coupling between the electric field normal to the mirror surface and the cavity length. From this experiment, we estimated the noise level of the EO effect, which was well below the strain sensitivity of current and future proposed GWDs. We conclude that the EO noise in AlGaAs coating will not be a limiting noise source in these systems.

5.3 Theory of electro-optic effect

When an electric field is applied to certain materials, the refractive indices vary depending on this field. This effect is called the electro-optic (EO) effect. In this section, we briefly

review the theory of the EO effect. More details can be seen in the references [75, 50].

Refractive indices of a crystal can be expressed in terms of its index ellipsoid as

$$\frac{x^2}{n_x^2} + \frac{y^2}{n_y^2} + \frac{z^2}{n_z^2} = 1, \quad (5.1)$$

where x , y , and z represent the coordinate axes, with the z -axis along the [100] axis as shown in Fig. 5.1. And n_x , n_y , and n_z are the three principal refractive indices with the crystallographic axes as the optical axes [50]. For the case of zincblende crystals such as GaAs and AlGaAs, these refractive indices are $n_x = n_y = n_z = n_0$.

When the electric field is applied to the zincblende crystal, the index ellipsoid becomes [75, 50]

$$\frac{x^2}{n_0^2} + \frac{y^2}{n_0^2} + \frac{z^2}{n_0^2} + 2r_{41}(E_x yz + E_y zx + E_z xy) = 1, \quad (5.2)$$

where r_{41} represents the electro-optic coefficient. If the electric field is applied along the z axis, i.e., $E_x = E_y = 0$, Eq. (5.2) becomes

$$\frac{x^2}{n_0^2} + \frac{y^2}{n_0^2} + \frac{z^2}{n_0^2} + 2r_{41}E_z xy = 1. \quad (5.3)$$

We define the new principal axes, x' , y' , and z' , when the electric field is applied as

$$\begin{pmatrix} x' \\ y' \\ z' \end{pmatrix} = \frac{1}{\sqrt{2}} \begin{pmatrix} 1 & -1 & 0 \\ 1 & 1 & 0 \\ 0 & 0 & \sqrt{2} \end{pmatrix} \begin{pmatrix} x \\ y \\ z \end{pmatrix}. \quad (5.4)$$

By using the new coordinate, Eq. (5.3) can be rewritten as

$$\left(\frac{1}{n_0^2} - r_{41}E_z \right) x'^2 + \left(\frac{1}{n_0^2} + r_{41}E_z \right) y'^2 + \frac{z'^2}{n_0^2} = 1. \quad (5.5)$$

Therefore, refractive indices of new principal axes, $n_{x'}$ and $n_{y'}$, become

$$n_{x'} = \left[\frac{1}{n_0^2} (1 - n_0^2 r_{41} E_z) \right]^{-1/2}, \quad (5.6)$$

$$n_{y'} = \left[\frac{1}{n_0^2} (1 + n_0^2 r_{41} E_z) \right]^{-1/2}. \quad (5.7)$$

Assuming that $n_0^2 r_{41} E \ll 1$, these can be rewritten as

$$n_{x'} = n_0 + \frac{1}{2} n_0^3 r_{41} E_z, \quad (5.8)$$

$$n_{y'} = n_0 - \frac{1}{2} n_0^3 r_{41} E_z. \quad (5.9)$$

Thus, an electric field changes the refractive indices of zincblende crystals such as GaAs and AlGaAs, hence AlGaAs coatings. When the polarization of beams are aligned to new principal axes, x' or y' , of AlGaAs coatings, optical path lengths in the coatings can be perturbed by the EO effect, causing perturbations in the phase of the reflected beam. If the polarization is not aligned to x' or y' axes, the EO effect introduces birefringence.

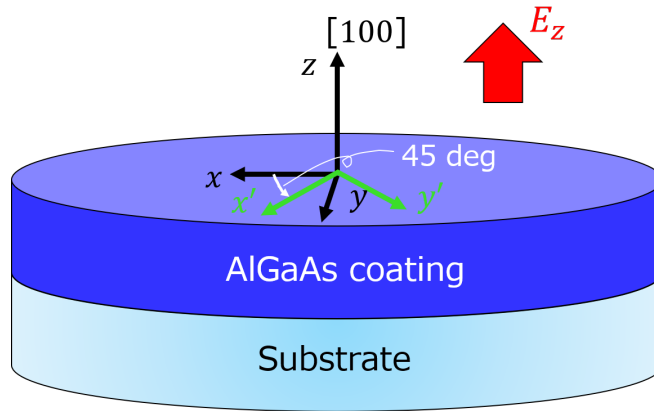


Figure 5.1: Schematic of the AlGaAs coating mirror. The AlGaAs coating has the [100] crystal axis normal to the surface. E_z represents the electric field along to z axis.

It should be noted that x' , and y' axes are 45 degree rotated with respect to the positive z -axis as shown in Fig. 5.1 [75, 50]. For the case of GaAs and AlGaAs, x and y axes correspond to [010] and [001] directions, respectively. Similarly, x' and y' axes are along the

[011] and $[0\bar{1}1]$. Therefore, the changes of refractive indices due to the normal electric field are induced in principal axes of [011] and $[0\bar{1}1]$ directions.

Crystalline AlGaAs coatings may be susceptible not only to the EO effect, but also to the piezoelectric effect [51]. However, this effect does not directly couple to the cavity length fluctuations when the electric field is normal to the surface [77]. In this study, we only consider the EO effect that is much more dominant coupling source than the piezoelectric effect.

5.4 Experiment

5.4.1 Setup

Table 5.1: Parameters of experimental setup.

Symbol	Description	Value
λ	Laser wavelength	1064 nm
L	Cavity length	0.105 m
T_i	Power transmissivity of input mirror	$\sim 0.5\%$
T_e	Power transmissivity of output mirror	~ 10 ppm
f_c	Cavity pole frequency	~ 600 kHz
x	Aluminum alloying fraction	0.92
d_H	Thickness of GaAs	76.43 nm
n_H	Refractive index of GaAs	3.48
d_L	Thickness of $\text{Al}_{0.92}\text{Ga}_{0.08}\text{As}$	89.35 nm
n_L	Refractive index of $\text{Al}_{0.92}\text{Ga}_{0.08}\text{As}$	2.98

In order to experimentally investigate the EO effect in AlGaAs coatings, we developed an optical setup using a Fabry-Pérot cavity. Fig. 5.2 shows the schematic of the experimental setup. Parameters of this setup are listed on Table 5.1. The Fabry-Pérot cavity is composed of two high-reflectivity mirrors — an amorphous coating front mirror and AlGaAs coating end mirror. The AlGaAs coating is composed of 35.5 periods (71 layers) of alternating GaAs and $\text{Al}_{0.92}\text{Ga}_{0.08}\text{As}$, that have been transferred to a planar super-polished fused silica substrate. The front mirror is curved mirror, and the end AlGaAs coating mirror has flat

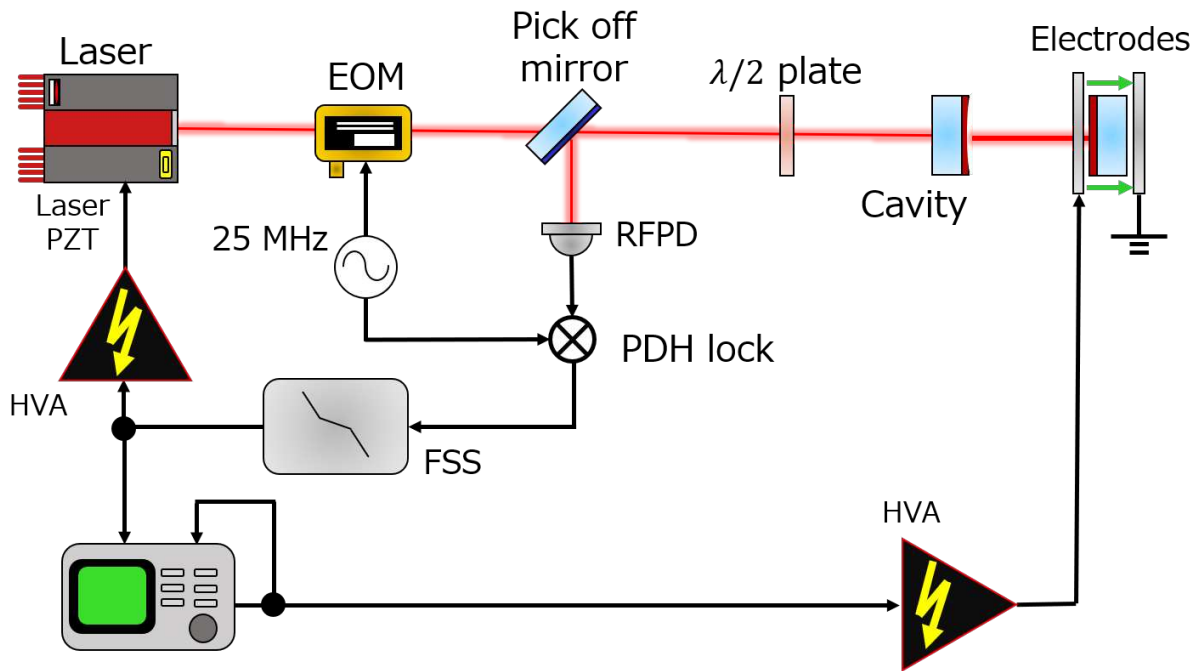


Figure 5.2: Schematic figure of experimental setup. Laser frequency is locked to the cavity by PDH method. The reflected beam is detected by a radio frequency photo detector (RFPD) and then the signal is electrically demodulated. The demodulated signal is filtered by frequency stabilization servo (FSS) and then fed back to the laser PZT through a high-voltage amplifier (HVA). The input mirror is an amorphous coating mirror which has a radius of curvature of 0.33 m. The end AlGaAs coating mirror, which is a flat mirror, is placed between two aluminum electrodes which apply the electric field normal to the mirror surface. Voltage is applied to the front electrode through an HVA, and back electrode is grounded. Polarization of the input beam is adjusted by a $\lambda/2$ plate.

surface. The finesse of the cavity is about 10^3 .

The laser frequency is locked to the cavity length by the Pound-Drever-Hall (PDH) technique [78]. The extracted error signal is filtered by the frequency stabilization servo, and fed back to the PZT (piezo transducer) of an NPRO laser which actuates the laser frequency. When the laser is locked to the cavity, fluctuations of the laser frequency, $\Delta\nu$ satisfies

$$\frac{\Delta\nu}{\nu} = -\frac{\Delta L}{L}, \quad (5.10)$$

where ΔL is the cavity length fluctuations, and ν is the laser frequency. The phase perturbation in AlGaAs coatings induced by the electric field is imprinted onto the cavity displacement, hence the PDH error signal. By probing the PDH feedback signal, the displacement due to the EO effect can be measured.

The input beam is linearly polarized, and its polarization can be aligned to the crystal axes of AlGaAs coatings by rotating a $\lambda/2$ plate in front of the Fabry-Pérot cavity. The AlGaAs sample mirror is installed as shown in Fig. 5.3.

It is important to mention that AlGaAs coatings show larger birefringence than amorphous coatings, though an ideal unstrained [100] oriented AlGaAs is optically symmetric. Non-uniform strain relaxation during the coating epitaxial growth process can be considered as a possible cause of this birefringence [79]. Further investigations are needed to reveal the root cause of this effect. Due to this static birefringence, AlGaAs coatings have two orthogonal distinct axes — fast and slow axes which are aligned to $[0\bar{1}1]$ and $[011]$ orientations, respectively [80, 71]. When the polarization of the beam is not aligned to the fast or slow axis, two distinct split resonant peaks can be generated as reported in previous works [45, 48]. No resonant peak splitting due to the birefringence was observed with our cavity used to measure the EO effect whose full-width-half-maximum (FWHM) line-width is about 1.2 MHz. However, as described in the next section, two orthogonal polarization

eigenmodes separated by about 500 kHz were observed when we replaced the input mirror to the one with higher reflectivity. The AlGaAs fast and slow axes were identified by utilizing those split peaks. The green arrows shown in Fig. 5.3 indicate the fast and slow axes of the AlGaAs coating.

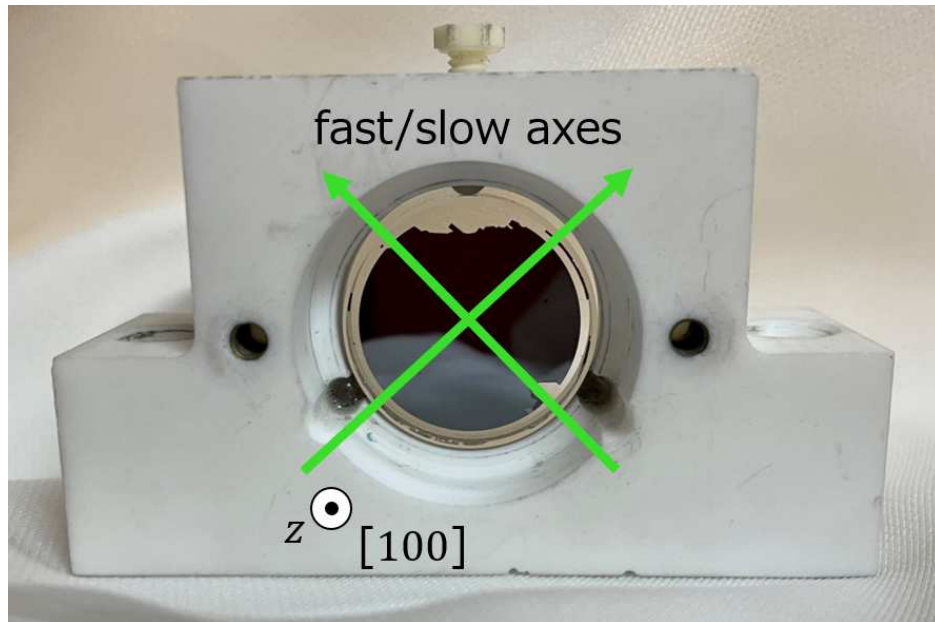


Figure 5.3: Front view of actual mirror mount for AlGaAs mirror without electrodes. The AlGaAs mirror is clamped by a nylon screw with moderate torque. The green arrows indicate the fast or slow axis where the refractive index is disturbed by the EO effect. The visible defects near the edges of the coating are due to excessive handling and are not typical of AlGaAs coatings. These defects do not impact the EO effect nor any results of this study.

The AlGaAs coated mirror and two electrodes are housed in the same mirror mount made of machinable glass, MACOR [60]. Each electrode has a hole with 3 mm diameter to pass the beam through. The distances between the mirror surface and front electrode and back electrode are 0.39 mm and 0.20 mm, respectively. Source voltage is amplified to the front electrode by a HVA up to 2 kV peak to peak. On the other hand, the back electrode is grounded, which introduces an electric field normal to the AlGaAs sample mirror surface.

5.4.2 Axis identification

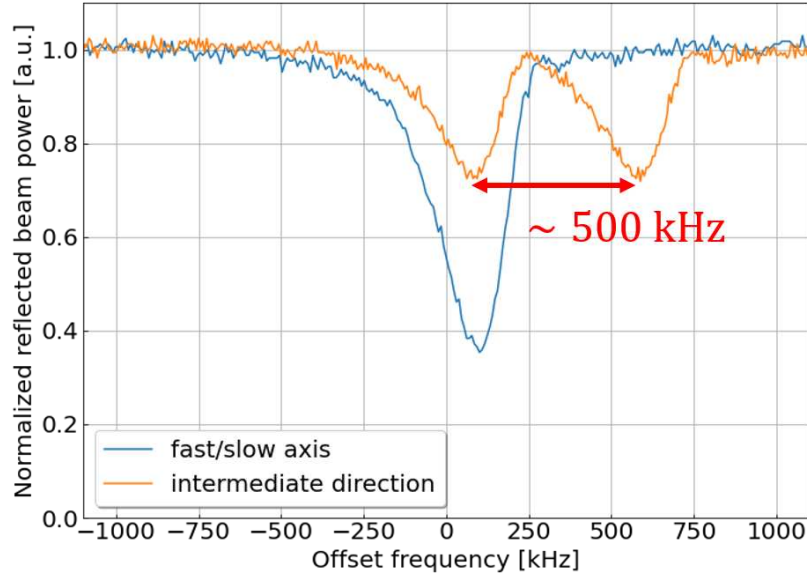


Figure 5.4: Response of the reflected beam power when the laser frequency is scanned. As long as the input beam polarization is aligned to the fast or slow axis, the cavity shows single eigenmode as shown in blue curve. On the other hand, when the polarization is misaligned from the fast or slow axis, two separated eigenmodes are observed due to the birefringence in the AlGaAs coating (orange curve).

As described in the previous section, AlGaAs coatings have the fast and slow axes i.e., $[0\bar{1}1]$ and $[011]$ orientations, whose refractive indices are perturbed by the EO effect. Prior to the measurements of the EO effect, we identified the fast and slow axes of the AlGaAs coating. In order to determine the fast and slow axes, we used the higher-reflectivity mirror as the input mirror instead of the one used for the EO measurement. With this configuration, the finesse of the cavity increased to about 4.5×10^3 , and the FWHM line-width was about 300 kHz.

Fig. 5.4 shows the response of the reflected beam power when the laser frequency is scanned. The laser frequency was swept by actuating the laser PZT with a triangle wave at 100 Hz. Then we adjusted the $\lambda/2$ plate to maximize or minimize the amount of the split peak. When the beam polarization was aligned to the fast or slow axis, only single

eigenmode was observed as shown by the blue curve. Thus, we determined the angle of $\lambda/2$ plate which can align the input beam polarization to the fast or slow axis. By tilting the $\lambda/2$ plate, the distinct split peak appeared as indicated by the orange line. In our case, the split frequency of these two eigenmodes was about 500 kHz.

After identifying the fast and slow axes, we switched the input mirror to what we originally used. The reason why we employed the lower-reflectivity input mirror is because the lock to the cavity was more stable and the cavity-pole was much higher than the frequency region where we measured the EO effect. We then tuned the $\lambda/2$ plate so that the laser polarization was aligned to the fast or slow axis where the EO effect can be observed. As the birefringence in amorphous coatings are so small that the impact of replacing the input mirror is negligible [81].

5.4.3 Measurement scheme

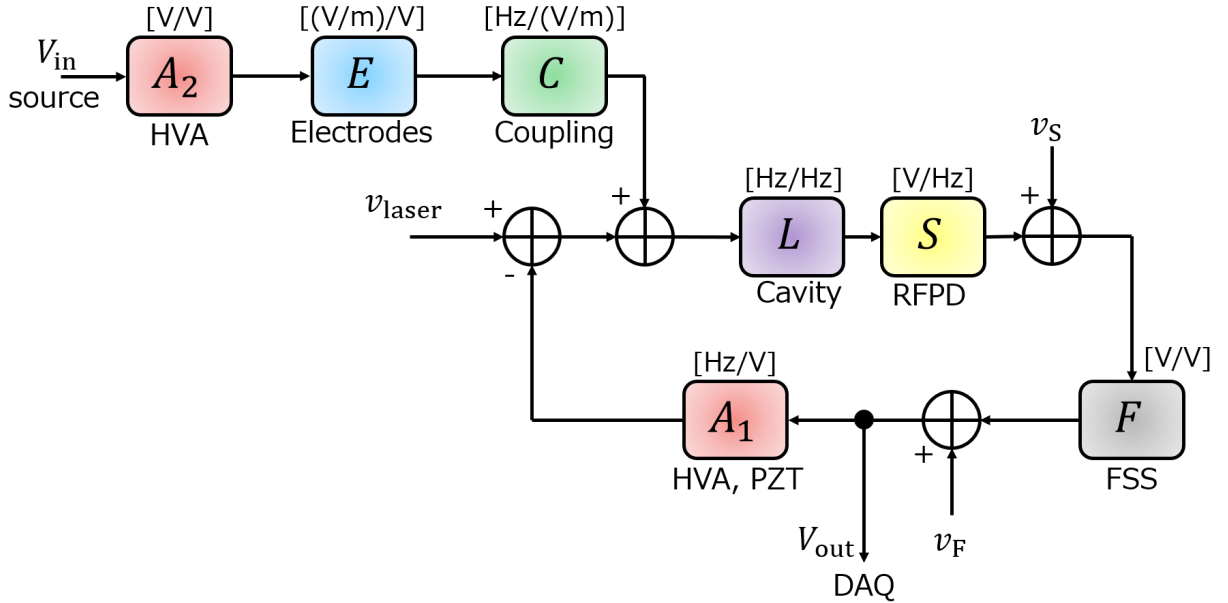


Figure 5.5: Block diagram of measurement scheme. Transfer function from source signal V_{in} to PDH feedback signal V_{out} is measured by using a SR785. v_{laser} , v_{S} , and v_{F} denote the noises of the laser, RFPD, and FSS, respectively.

Fig. 5.5 shows the measurement scheme of our setup. In this scheme, fluctuations in the

cavity displacement are probed by using the transfer function from the source signal, V_{in} , to the feedback signal, V_{out} .

The feedback signal can be calculated as

$$V_{\text{out}} = \frac{FSL}{1+G}CEA_2V_{\text{in}} + \frac{FSL}{1+G}v_{\text{laser}} + \frac{F}{1+G}v_{\text{S}} + \frac{1}{1+G}v_{\text{F}}, \quad (5.11)$$

where $G \equiv A_1FSL$ is the open-loop gain. Then, the transfer function, $V_{\text{out}}/V_{\text{in}}$, can be written as

$$\frac{V_{\text{out}}}{V_{\text{in}}} = \frac{FSL}{1+G}CEA_2 + \frac{FSL}{1+G}\frac{v_{\text{laser}}}{V_{\text{in}}} + \frac{F}{1+G}\frac{v_{\text{S}}}{V_{\text{in}}} + \frac{1}{1+G}\frac{v_{\text{F}}}{V_{\text{in}}}. \quad (5.12)$$

If the source signal V_{in} is much larger than the noises, v_{laser} , v_{S} , and v_{F} , Eq. 5.12 can be approximated as

$$\frac{V_{\text{out}}}{V_{\text{in}}} \approx \frac{FSL}{1+G}CEA_2 = \frac{G}{1+G}CE\frac{A_2}{A_1}. \quad (5.13)$$

When G , E , A_1 , and A_2 are known, coupling level of the EO effect, C , can be obtained from Eq. (5.13).

5.4.4 Calibration

5.4.4.1 Transfer function

Figs. 5.6 and 5.7 show the measured transfer functions, $V_{\text{out}}/V_{\text{in}}$, and the open-loop gain, G when the polarization is aligned to fast or slow axis, respectively. As the unity gain frequency of PDH loop is about 4.5 kHz, the fluctuations below 4.5 kHz are suppressed. The electric field couples to the cavity length fluctuations through not only the EO effect, but

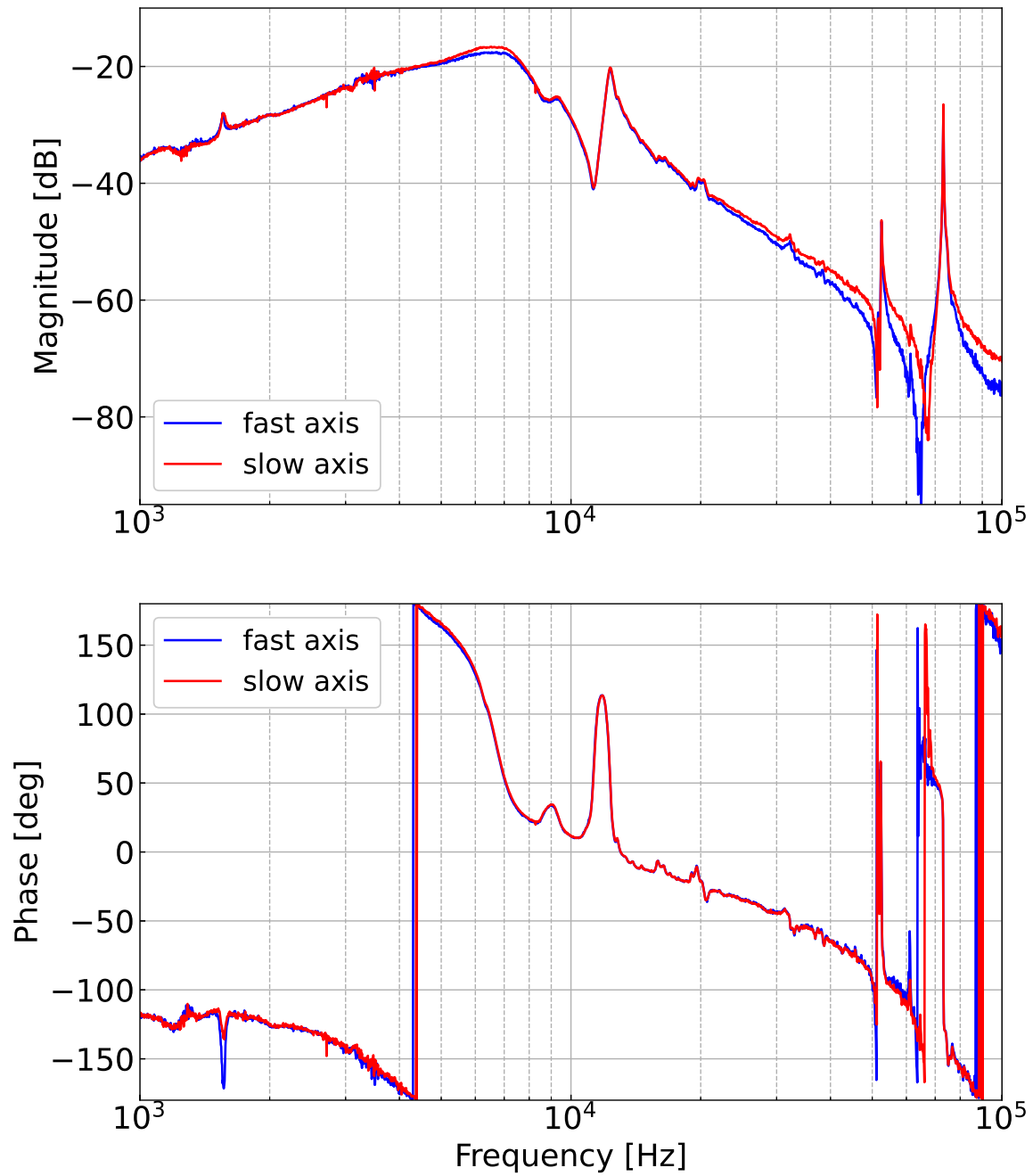


Figure 5.6: Measured transfer functions, $V_{\text{out}}/V_{\text{in}}$, for fast and slow axes.

also mechanical vibration. Mechanical coupling through the mirror mount has a resonant peak around 10 kHz. Also, the peaks around 50 kHz and 70 kHz are mechanical resonances of the sample mirror. Therefore, the measurements of the EO effect can be disturbed by the mechanical couplings in these frequency regions.

5.4.4.2 Electric field

Voltage applied to the electrode is converted into an electric field which penetrates the AlGaAs sample mirror. This conversion efficiency, E [(V/m)/V], is numerically computed by a 3D static solution based on the geometry of the electrode and the AlGaAs mirror. By assuming the cylindrical symmetric geometry, we solved the Laplace equation for the electric potential. Then, the conversion efficiency, E , was derived from the obtained electric potential. Fig. 5.8 shows the computed electric field when the unit voltage is applied to the front electrode i.e., the conversion efficiency, E [(V/m)/V]. The electric field close to the mirror center where the beam hits is 42 V/m. In our setup, the beam spot size on the AlGaAs mirror is about 100 μ m, and the electric field within the beam spot on the AlGaAs mirror can be treated as uniform. Therefore, we apply the conversion efficiency as $E = 42$ (V/m)/V and assume it is constant within the frequency region of interest.

5.4.4.3 PZT response

The internal PZT of the NPRO laser is used to actuate the laser frequency. Its actuation efficiency is measured by scanning the laser frequency by a triangle wave. Generally, the NPRO's laser PZT response has frequency dependence. However, we cannot drive enough voltage to scan the laser frequency above a few kHz due to the low-pass filter of the HVA connected to the laser PZT. On the other hand, the laser PZT response can be regarded as constant between 1 – 100 kHz [82]. Therefore, we measured the actuation efficiency with 1 kHz triangle wave and assume that observed laser PZT efficiency is flat between 1–100 kHz.

Fig. 5.9 shows the response of the PDH error signal scanned by 1 kHz triangle wave. We

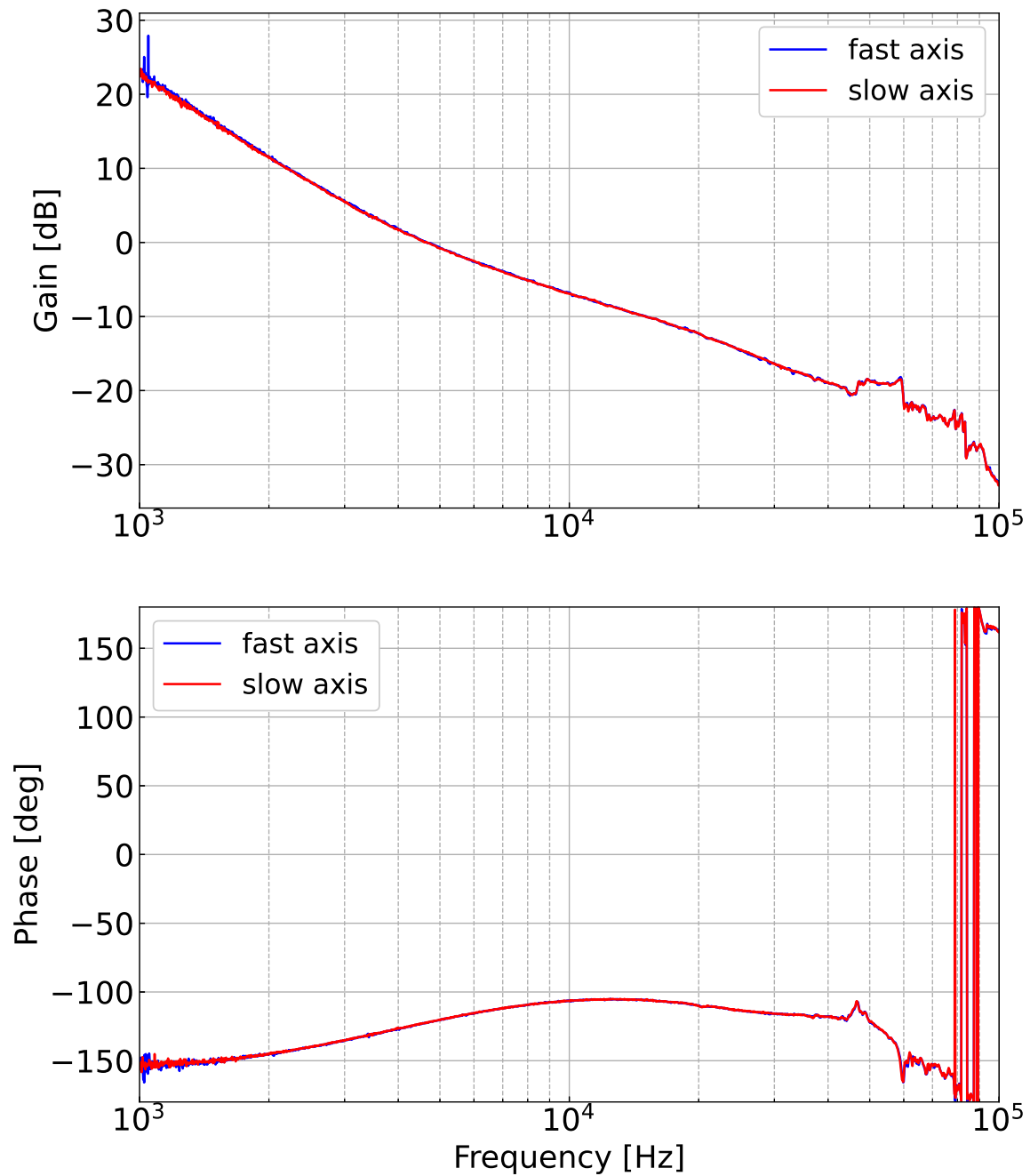


Figure 5.7: Measured open-loop gain of PDH loop, G , for fast and slow axes. The unity gain frequency is about 4.5 kHz.

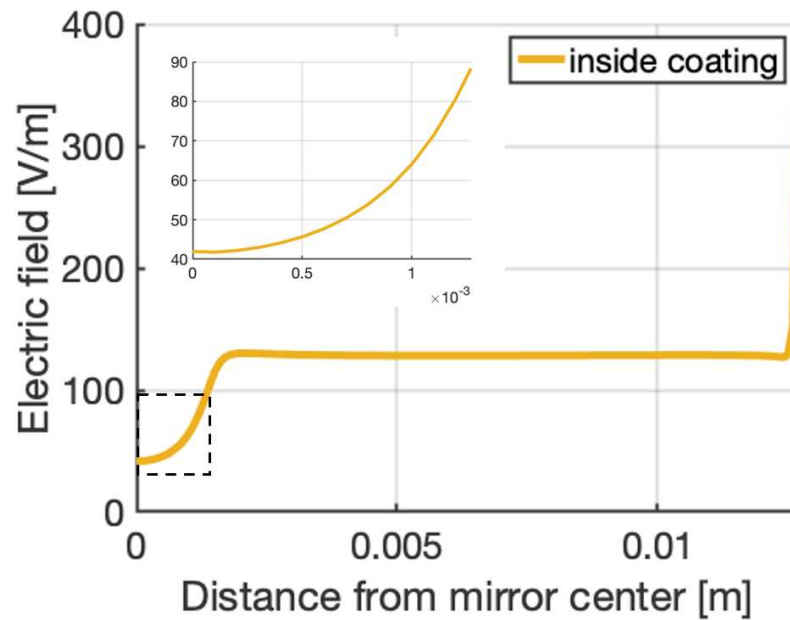


Figure 5.8: Calculated electric field normal to the AlGaAs coatings. The horizontal axis is the distance from mirror center, and the vertical axis is the electric field [V/m] when the unit voltage is applied to the front electrode, i.e., the conversion efficiency, E [(V/m)/V].

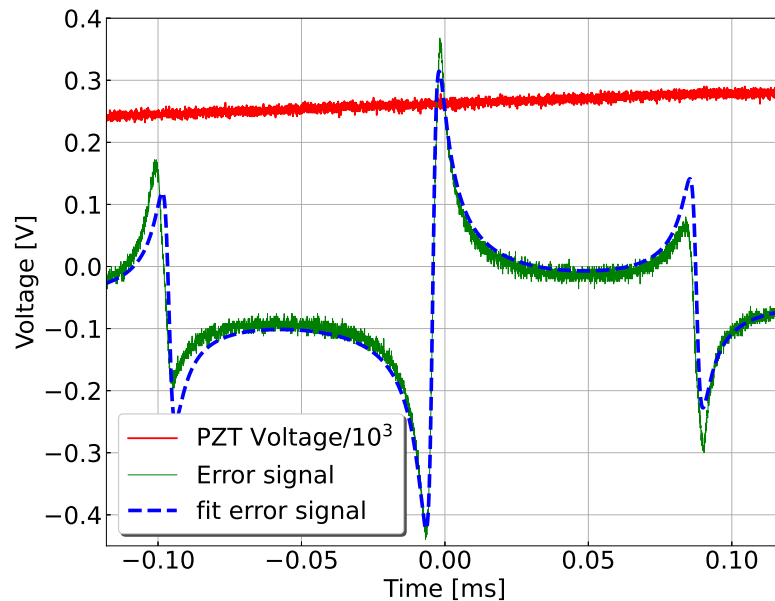


Figure 5.9: Error signal obtained by scanning the laser frequency with 1 kHz triangle wave. Red and green solid lines correspond to the monitored voltage sent to NPRO's PZT and measured error signal, respectively. Blue dashed line is fitted curve of error signal.

calculated the actuation efficiency by fitting the error signal. From the fitting result, the PZT efficiency is estimated as 1.7 MHz/V.

5.5 Results

From Eq. (5.13) and the obtained calibration data, one can evaluate the coupling between the electric field and cavity length, C . Fig. 5.10 shows the calibrated results of the coupling. Here we used Eq. 5.10 to convert the unit from [Hz/(V/m)] to [m/(V/m)]. Measured coupling levels at both axes are almost the same at the order of 10^{-16} m/(V/m).

The coupling, C , can be decomposed to mechanical coupling, C_m , and the EO effect, C_{EO} , as $C = C_m + C_{EO}$. As described later, the signs of phase perturbation due to the EO effect are opposite between fast and slow axes. This can be expressed as

$$C_{EO,slow} = |C_{EO}|e^{i\psi}, \quad (5.14)$$

$$C_{EO,fast} = -|C_{EO}|e^{i\psi} (= |C_{EO}|e^{i(\psi+\pi)}), \quad (5.15)$$

where ψ is the phase offset. Assuming that the mechanical coupling is common to both fast and slow axes at this frequency region, differential between these two transfer functions becomes

$$\begin{aligned} \text{Diff.} &= C_{slow} - C_{fast} \\ &= (C_{m,slow} + C_{EO,slow}) - (C_{m,fast} + C_{EO,fast}) \\ &= 2|C_{EO}|e^{i\psi}. \end{aligned} \quad (5.16)$$

Therefore, the magnitude of differential between the TFs of fast and slow axes ideally becomes twice the magnitude of the EO effect in AlGaAs coatings.

The green dashed line shown in Fig. 5.10 is the differential between transfer functions of fast and slow axes, $2|C_{EO}|e^{i\psi}$. Mechanical couplings from the mirror mount and resonances

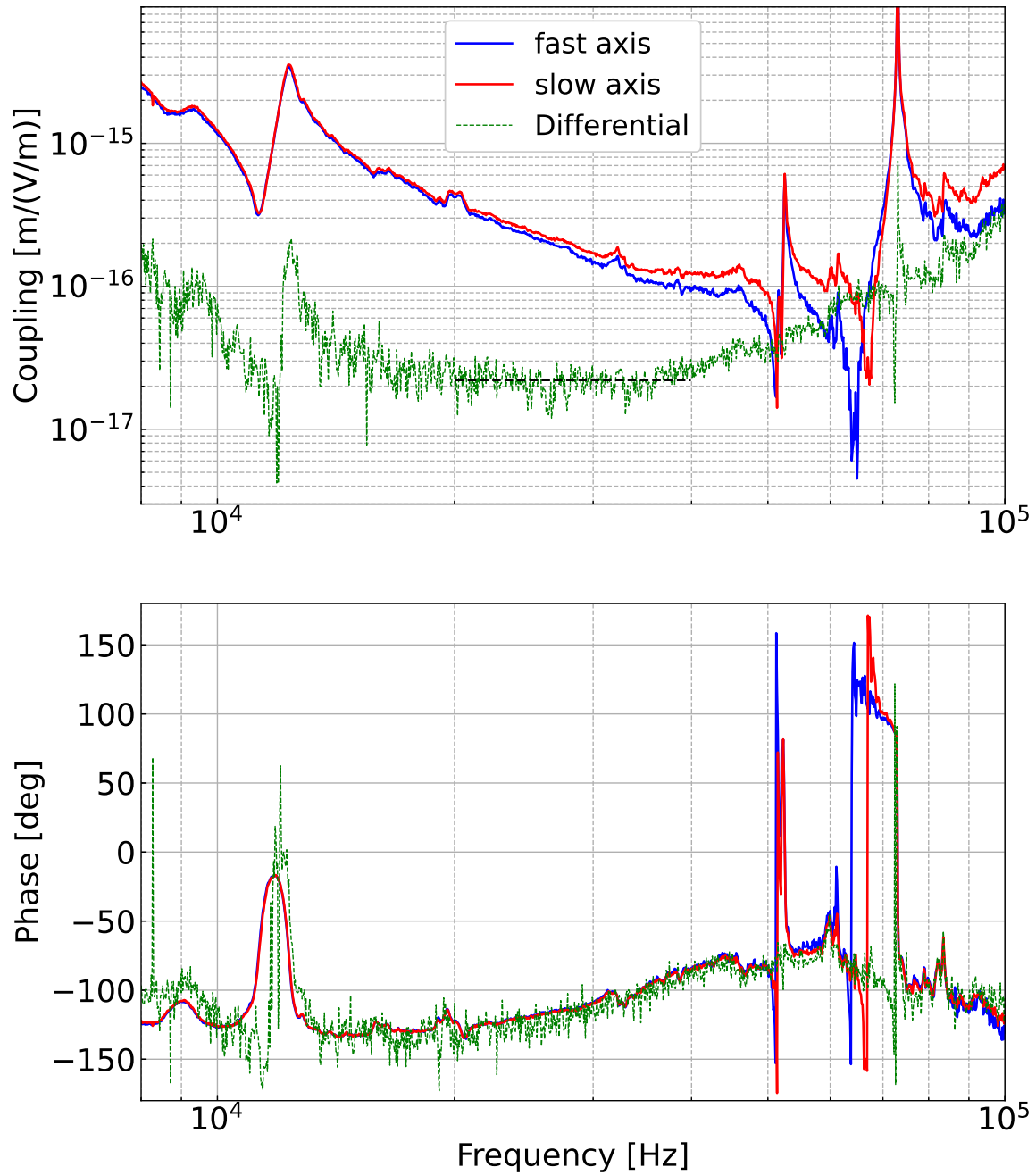


Figure 5.10: Calibrated transfer functions. The black dashed line shows the fitted result between 20 – 40 kHz.

of mirror itself disturb the cavity length below ~ 10 kHz and around $\sim 50 - 80$ kHz. Above ~ 40 kHz, the differential shows the frequency dependence. One possibility of this behavior is that the frequency dispersion of the electro-optic coefficients of GaAs and AlGaAs [83]. Further studies may be needed to fully understand the behavior at those higher frequency region. On the other hand, for the case of current terrestrial GWDs, the important frequency region is between ~ 10 Hz and several kHz. In order to estimate the EO effect, we focus on the frequency region $20 - 40$ kHz where the impacts of mechanical couplings can be considered small and the differential has flat response. The electro-optic coefficient shows the flat response below a few tens of kHz where the acoustic contribution is dominant as shown in previous studies [84, 85]. As acoustic phonons can respond quickly enough against fluctuations in the electric field, the electro-optic coefficient kHz becomes flat at lower frequency. Therefore, the estimated C at $20 - 40$ kHz can be used to predict the noise level in GWDs in the $10 - 3$ kHz frequency region. From the above assumptions, we obtain $2|C_{\text{EO}}| = 2.2 \times 10^{-17} \text{ m}/(\text{V}/\text{m})$ by fitting the result. Therefore, the coupling level of the EO effect is estimated as $|C_{\text{EO}}| = 1.1 \times 10^{-17} \text{ m}/(\text{V}/\text{m})$.

5.6 Discussions

5.6.1 Comparison to theoretical estimation

The level of EO effect can be numerically computed by using a transfer matrix calculation of the coating multilayer. The perturbation of the reflected field phase induced by k -th coating layer can be described as [86, 54]

$$\frac{\partial \phi_c}{\partial \phi_k} = \Im \left(\frac{1}{M_{21}} \frac{\partial M_{21}}{\partial \phi_k} - \frac{1}{M_{22}} \frac{\partial M_{22}}{\partial \phi_k} \right), \quad (5.17)$$

where M_{ij} are elements of the transfer matrix of coatings, M , and \Im denotes the imaginary part. The transfer matrix of the total coating can be given by

$$M = Q_N D_N \cdots Q_k D_k \cdots Q_1 D_1 Q_0, \quad (5.18)$$

where Q_0 is the transition between vacuum and 1st layer, and Q_k is the transition matrix from k -th layer to $(k + 1)$ -th layer defined as

$$Q_k = \frac{1}{2n_{k+1}} \begin{pmatrix} n_{k+1} + n_k & n_{k+1} - n_k \\ n_{k+1} - n_k & n_{k+1} + n_k \end{pmatrix}. \quad (5.19)$$

D_k is the propagator through the k -th coating layer expressed as

$$D_k = \begin{pmatrix} e^{-i\phi_k/2} & 0 \\ 0 & e^{i\phi_k/2} \end{pmatrix}, \quad (5.20)$$

where $\phi_k = 4\pi n_k d_k / \lambda$ is round trip phase change. From Eqs. (5.18) – (5.20), partial derivative of transfer matrix can be calculated as

$$\begin{aligned} \frac{\partial M}{\partial \phi_k} &= Q_N D_N \cdots Q_k D_k \begin{pmatrix} -i/2 & 0 \\ 0 & i/2 \end{pmatrix} \\ &\quad Q_{k-1} D_{k-1} \cdots Q_1 D_1 Q_0. \end{aligned} \quad (5.21)$$

From the definition of round trip phase change, ϕ , $\partial \phi_k / \partial E$ becomes

$$\frac{\partial \phi_k}{\partial E} = \frac{4\pi d_k}{\lambda} \frac{\partial n_k}{\partial E} = \pm \frac{2\pi}{\lambda} n_k^3 d_k r_{41,k}, \quad (5.22)$$

where the signs depend on the AlGaAs axes. By using the chain rule, the phase perturbation induced by the electro-optic effect can be expressed as

$$\frac{\partial\phi_c}{\partial E} = \frac{\partial\phi_c}{\partial\phi_k} \frac{\partial\phi_k}{\partial E}. \quad (5.23)$$

Here we assume the EO coefficients of GaAs and $\text{Al}_x\text{Ga}_{1-x}\text{As}$ as $r_{41,\text{GaAs}} = -1.33 \times 10^{-12} \text{ m/V}$, and $r_{41,\text{AlGaAs}} = -(1.33 - 0.45x) \times 10^{-12} \text{ m/V}$, respectively [49, 87]. As a result, one can compute the phase perturbation induced by the electro-optic effect as

$$\left| \frac{\partial\phi_c}{\partial E} \right| = \left| \frac{\partial\phi_c}{\partial\phi_k} \frac{\partial\phi_k}{\partial E} \right| = 3.9 \times 10^{-11} \text{ rad/(V/m)}. \quad (5.24)$$

This phase perturbation can be converted to the Fabry-Pérot cavity displacement, $\partial L/\partial E$. Round trip phase of a Fabry-Pérot cavity, ϕ , satisfies the relationship as

$$\phi = \frac{2L\omega}{c} = \frac{4\pi L}{\lambda}, \quad (5.25)$$

where L , ω , c , and λ are the cavity length, angular frequency, the speed of light, and the wavelength of laser, respectively. From Eq. (5.25), one can obtain

$$\frac{\partial\phi}{\partial E} = \frac{4\pi}{\lambda} \frac{\partial L}{\partial E}. \quad (5.26)$$

Consequently, the coupling of EO effect to cavity length can be calculated as

$$\left| \frac{\partial L}{\partial E} \right| = \frac{\lambda}{4\pi} \left| \frac{\partial\phi_c}{\partial E} \right| = 3.3 \times 10^{-18} \text{ m/(V/m)}. \quad (5.27)$$

This value is about one-third of the measured value.

5.6.2 Implications for gravitational wave detectors

We evaluate the impacts of noise induced by the EO effect on future GWDs. In GWDs such as aLIGO, horizontally polarized beam is employed for laser interferometry [18]. The impacts of the EO effect on GWDs depend on the alignment between the beam polarization and AlGaAs axes.

Firstly, we consider the case that the polarization of the beam is aligned to the AlGaAs $[011]$ or $[0\bar{1}1]$ axes (x' or y') where the reflected optical phase is perturbed by the EO effect. The measured fluctuations in the electric field next to the test mass in aLIGO is $3 \times 10^{-6} \text{ (V/m)}/\sqrt{\text{Hz}}$ at 100 Hz [2]. Assuming that the fluctuations in the electric fields next to each of the four test masses are the same level, and uncorrelated with each other, the strain noise due to the EO effect at 100 Hz can be calculated as

$$\frac{\sqrt{4} \times 1.1 \times 10^{-17} \text{ m}/(\text{V/m})^1 \times 3 \times 10^{-6} \text{ (V/m)}/\sqrt{\text{Hz}}}{4 \times 10^3 \text{ m}} = 1.6 \times 10^{-26} 1/\sqrt{\text{Hz}}. \quad (5.28)$$

Here we assumed that the EO effect has flat response and the arm cavity length is 4 km. The target sensitivity of A+, future upgrade plan of aLIGO, is about $2 \times 10^{-24} 1/\sqrt{\text{Hz}}$ at 100 Hz [88]. Therefore, the noise level of EO effect is about two orders of magnitude smaller than the sensitivity of A+. As long as fluctuations in the electric field are kept below $\sim 2 \times 10^{-5} \text{ (V/m)}/\sqrt{\text{Hz}}$ at 100 Hz, the noise level of the EO effect is below $10^{-25} 1/\sqrt{\text{Hz}}$, and will not affect the sensitivity of GWDs.

Secondly, we consider the case when the x' and y' axes are misaligned θ degrees from the beam polarization as shown in Fig. 5.11. We assume that the beam is linear polarization in horizontal axis as same as the aLIGO case [18]. Therefore, its electric field can be expressed

¹Correction to published value of 1.1×10^{-18}

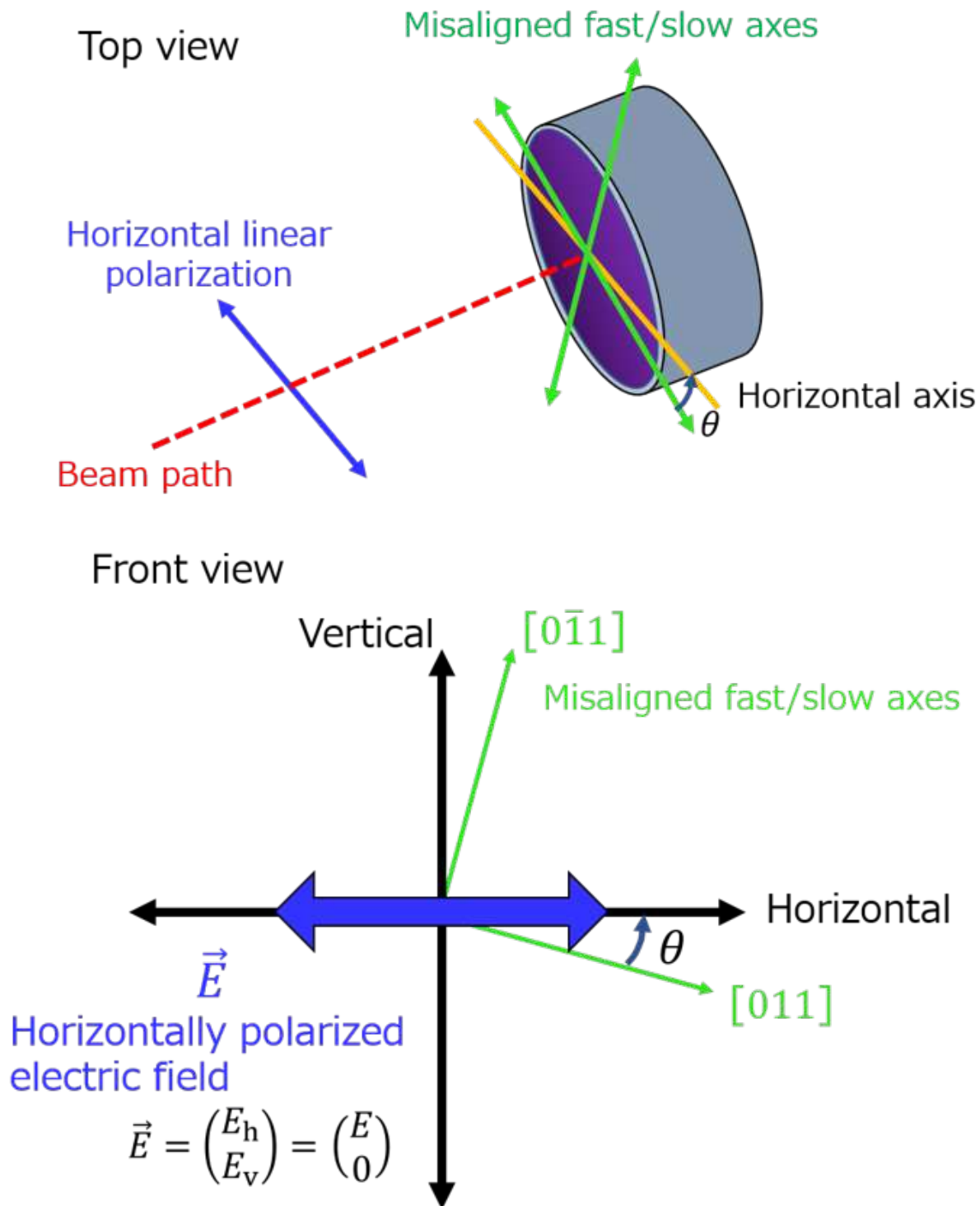


Figure 5.11: Schematic of the relationship between the electric field of horizontally polarized beam, \vec{E} , and misaligned AlGaAs fast and slow axes. The blue arrow indicates the electric field of horizontally polarized beam used in a GWD. The green arrows represent the direction of the AlGaAs fast and slow axes. Here we assume that the AlGaAs $[011]$ and $[0\bar{1}1]$ axes are tilted θ from the horizontal and vertical axes, respectively.

as

$$\vec{E} = \begin{pmatrix} E_h \\ E_v \end{pmatrix} = \begin{pmatrix} E_0 \\ 0 \end{pmatrix}, \quad (5.29)$$

where E_h and E_v represent the horizontal and vertical polarization components of the electric field, respectively. Then, its projection onto $[011]$ and $[0\bar{1}1]$ axes can be expressed as

$$\begin{pmatrix} E_{[011]} \\ E_{[0\bar{1}1]} \end{pmatrix} = \begin{pmatrix} \cos \theta & -\sin \theta \\ \sin \theta & \cos \theta \end{pmatrix} \begin{pmatrix} E_0 \\ 0 \end{pmatrix} = E_0 \begin{pmatrix} \cos \theta \\ \sin \theta \end{pmatrix}. \quad (5.30)$$

We denote the optical phase perturbation induced by the EO effect as ϕ_{EO} . Then the field perturbed by the EO effect becomes

$$\begin{pmatrix} \tilde{E}_{[011]} \\ \tilde{E}_{[0\bar{1}1]} \end{pmatrix} = E_0 \begin{pmatrix} e^{i\phi_{\text{EO}}} & 0 \\ 0 & e^{-i\phi_{\text{EO}}} \end{pmatrix} \begin{pmatrix} \cos \theta \\ \sin \theta \end{pmatrix}. \quad (5.31)$$

By converting the coordinates from AlGaAs axes to beam polarization axes, one can get

$$\begin{aligned} \begin{pmatrix} E_h \\ E_v \end{pmatrix} &= \begin{pmatrix} \cos \theta & \sin \theta \\ -\sin \theta & \cos \theta \end{pmatrix} \begin{pmatrix} \tilde{E}_{[011]} \\ \tilde{E}_{[0\bar{1}1]} \end{pmatrix}, \\ &= E_0 \begin{pmatrix} e^{i\phi_{\text{EO}}} \cos^2 \theta + e^{-i\phi_{\text{EO}}} \sin^2 \theta \\ -e^{i\phi_{\text{EO}}} \cos \theta \sin \theta + e^{-i\phi_{\text{EO}}} \cos \theta \sin \theta \end{pmatrix}. \end{aligned} \quad (5.32)$$

Assuming $|\phi_{\text{EO}}| \ll 1$, Eq. (5.32) can be approximated as

$$\begin{pmatrix} E_h \\ E_v \end{pmatrix} \approx E_0 \begin{pmatrix} 1 + i\phi_{\text{EO}}(\cos^2 \theta - \sin^2 \theta) \\ -2i\phi_{\text{EO}} \cos \theta \sin \theta \end{pmatrix}. \quad (5.33)$$

When the polarization of the beam is aligned to the [100] axis, $\theta = 45$ deg, Eq. (5.33) becomes

$$\begin{pmatrix} E_h \\ E_v \end{pmatrix} \approx E_0 \begin{pmatrix} 1 \\ -i\phi_{\text{EO}} \end{pmatrix}. \quad (5.34)$$

Therefore, the EO effect in AlGaAs coatings induces birefringence, and vertically beam is generated by this effect, leading to elliptical polarization. However, the amplitude of the vertically polarized beam converted from the main horizontally polarized beam is the order of $|\phi_{\text{EO}}| \sim 10^{-16}$, and it can be negligible. Moreover, the reflected phase of the main beam is not disturbed by the EO effect. As a result, in the ideal case, the impacts of the EO effect can be mitigated when the polarization is aligned to [010] or [001] axis. However, those axes can show the static birefringence as shown in Fig. 5.4. From Eq. (5.25) and the laser frequency scan measurement, the birefringence in our AlGaAs coating is $\Delta\theta_b \approx 2.2 \times 10^{-3}$ rad, which is within the range of reported values in previous studies ($\sim 1 - 5 \times 10^{-3}$ rad) [45, 48]. Considering the case of a km-scale GWD such as aLIGO, the resonant frequency split of arm cavity becomes

$$\begin{aligned} \Delta\nu &= \frac{c}{4\pi L} 2\Delta\theta_b \\ &\approx 26 \text{ Hz}. \end{aligned} \quad (5.35)$$

Here we assumed that the arm cavity length L is 4 km and the both input and end mirrors of the arm cavity have the same amount of birefringence, $\Delta\theta_b = 2.2 \times 10^{-3}$ rad. Two orthogonal eigenmodes generated by the static birefringence in AlGaAs coatings will be within the FWHM of arm cavity (~ 80 Hz), and have a potential to interfere with control loops that have a similar bandwidth.

Even when the beam polarization is aligned to the AlGaAs [011] or [0 $\bar{1}$ 1] axis where the EO effect is maximized, the noise induced by the EO effect is well below the design sensitivity. Moreover, when [010] or [001] axis is aligned to the beam polarization, further reduction in

the EO effect could be realized without serious birefringence. As a result, the EO effect in AlGaAs coatings will not be a limiting noise source in future GWDs, and employing AlGaAs test masses will enhance the scientific outcomes which can be obtained from observations.

It should be noted that further studies are needed to realize AlGaAs coating test masses in future GWDs. The beam spot size on the test masses will be larger than 5 cm. In order to avoid clipping losses of the beam, the coating will need to be scaled to 30 cm diameter for current detectors and to about 50 cm for next generation detectors. Moreover, AlGaAs coatings are opaque to 532 nm laser light, which is currently used in GWDs for cavity-length stabilization [89, 90]. Thus, a new scheme with a transparent stabilization beam will need to be defined. Finally, the impact of the birefringence of AlGaAs coatings on GWDs with a focus on identifying the root cause of this effect must continue to be investigated [71, 91, 92]. We suggest this research include exploring alternative orientations of the crystalline structure that may minimize this effect.

5.7 Conclusion

Crystalline AlGaAs coatings, with their lower coating thermal noise, have the potential to dramatically improve the sensitivity and detection rate of GWDs and greatly bolster the new field of GW astrophysics. We investigate the noise induced by the EO effect in AlGaAs coating caused by the fluctuations in the electric field. This study yields that the EO effect will not be a limiting noise source in future upgraded GWDs.

Our study helps pave a path for utilizing AlGaAs mirror coatings in future upgraded GWDs. Further studies will lead to the large-area substrate transferred crystalline test mass coatings.

5.8 Acknowledgments

The authors thank Gregg Harry, Martin Fejer, Joshua Smith, David Wu, and the LIGO Scientific Collaboration Optics Working Group for useful discussions and feedback. This work was supported with funding from the National Science Foundation grants: PHY-1707863, PHY-1912699, PHY-2011688, and PHY-2011723. A portion of this work was performed in the UCSB Nanofabrication Facility, an open access laboratory. This paper has LIGO Document number LIGO-P2200244.

Chapter 6

Conclusion

6.1 Adaptive optics comissioning

Since the comissioning that had taken place in O3a, there has been heavy consideration into how point absorbers manifest on the core optic surfaces and ways to mitigate their effects. Some of these considerations include but are not exclusive to: non-invasive pre-installation measurements of the ITM surface / coating quality [93], upgrades to TCS to expand upon the current thermal compensation actuation modes, and scheduled vaccum chamber venting specifically for replacing the offending test mass mirror(s).

Increasing interferometer input power is an inevitability to reaching designed detector sensitivity and developing mode matching contingency plans is a natural progression of the current adaptive optics schema. The technique for improving the ring heater transient response represents an iterative step of pushing the existing and future thermal mode matching infrastructure towards a larger scale adaptive optics feedback schema. Central Heater for Transient Attenuation (CHETA) and a FRont Surface type Irradiator (FROSTI) are notable thermal compensation upgrades that have adopted some of the techniques layed out in this work.

FROSTI

FROSTI is a additional ceramic actuator placed promptly in front of the ETM HR surface and will project an annular heating pattern onto the test mass surface. The primary motivation of adding these actuators is to reduce optical loss to higher order modes in the FP arm from point absorbers as well as correct for uniform coating absorption that current TCS alone cannot sufficiently compensate at 1.5 [MW] circulating arm power [94].

CHETA

CHETA is a formally proposed upgrade to the central CO₂ pre-heating procedure detailed in § 2.3 and [29]. The primary motivation of this project is to upgrade the CO₂ actuator to better replicate the carrier self heating when high circulating power in the arms is lost. The addition of this improved actuation can aid comissioners by avoiding long periods of mode mismatch from thermal transients [95].

Both actuators are currently on track to be installed for Observing Run 5 [96]. Comissioners may find that clean measurements (with the Hartmann Wavefront sensors) characterizing the thermo-optic responses for individual thermal actuators and building pre-filters as discussed in § 2.2 may be a helpful supplement for improved control in modifying the transient response.

6.2 GaAs/Al_{0.92}Ga_{0.08}As **Electro-optic noise**

Though with limited sensitivity, an upper limit with the measurement is established. The discovery of driven mechanical couplings within the longitudinal pockels cell mount are discussed and were shown to be a major limitation with driven electric field injections indicated and have lead to an improved dual-polarization locked experimental design for improved sensitivity. Some additional considerations that can be taken with similar experiments:

- Improved mechanical design for improved measurement SNR (esp. between 10 Hz to 1kHz)
- Further modelling of opto-mechanical resonances to study a possible separation (if any) between the photo-elastic and electro-optic effects.

Appendices

A Paraxial equation

The general three dimensional wave equation for an E-field $E(x, y, z, t)$ is provided by Maxwell:

$$\left(\nabla^2 + \frac{1}{c^2} \frac{\partial^2}{\partial t^2} \right) E(x, y, z, t) = 0$$

For a coherent beam ($k = \frac{2\pi}{\lambda}$), we analyze the purely spatial component of the solution and select a longitudinal propagation (\vec{z}) direction such that our solution will look like the following (utilizing Helmholtz's equation):

$$E(x, y, z) = E_0(x, y, z)e^{-ikz}$$

The above wavefunction combined with the Helmholtz equation requires the complex form of E_0 and obeys the paraxial equation [97]:

$$\left(\frac{\partial^2}{\partial x^2} + \frac{\partial^2}{\partial y^2} - 2ik \frac{\partial}{\partial z} \right) E_0(x, y, z) = 0 \quad (1)$$

B Cavity stability criteria ($G(g_1, g_2)$)

Using spherical mirror resonators to match the phasefront of the beam mode is standard practice that has some additional geometric considerations to maximize reonance for a given beam. Choosing two mirrors with ROCs (R_1, R_2) and a set distance between them d , a implicit containment condition is set on the resonator [10]:

$$0 \leq \left(1 + \frac{d}{R_1}\right) \left(1 + \frac{d}{R_2}\right) \leq 1$$

Where we define $g_i = 1 + \frac{d}{R_i}$ so that we define a single parameter for the two mirror resonator G :

$$0 \leq G(g_1, g_2) \leq 1 \tag{2}$$

C The Equipartition theorem and the Fluctuation dissipation theorem

The Fluctuation Dissipation Theorem connects fluctuations on a microscopic level to fluctuations of macroscopic observables, and allows one to bypass having to venture into overly involved microscopic processes; a profound finding for experiments that are or will become thermal noise limited. Though after revisiting the equipartition theorem, there might still be some confusion how the two statements might contradict each other. We quickly revisit the 1D harmonic oscillator to provide some clarity:

$$1/2(k\bar{x}^2) = 1/2(k_B T) \quad (3)$$

\bar{x}^2 indicates an average position which the theorem indicates when root square mean motion is assumed. This is to say that FDT by no means is a modification of our understanding of the equipartition theorem but rather enriches providing insight on the the microscopic fluctuating phenomenon when measuring the power spectral density of the fluctuations [9]:

$$x^2 = \frac{k_B T}{\pi^2 f^2} \Re(Y) \quad (4)$$

D Misc. thermo-optic filters

D.1 COMSOL self heating filter

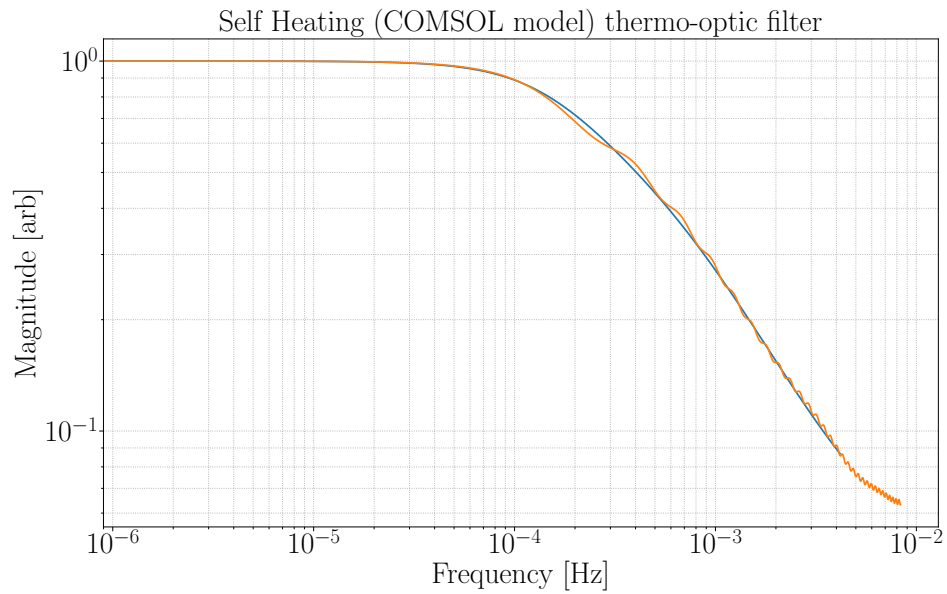


Figure 1: Fitted zpk filter to transient response of self heating COMSOL model.

D.2 CO2 filter

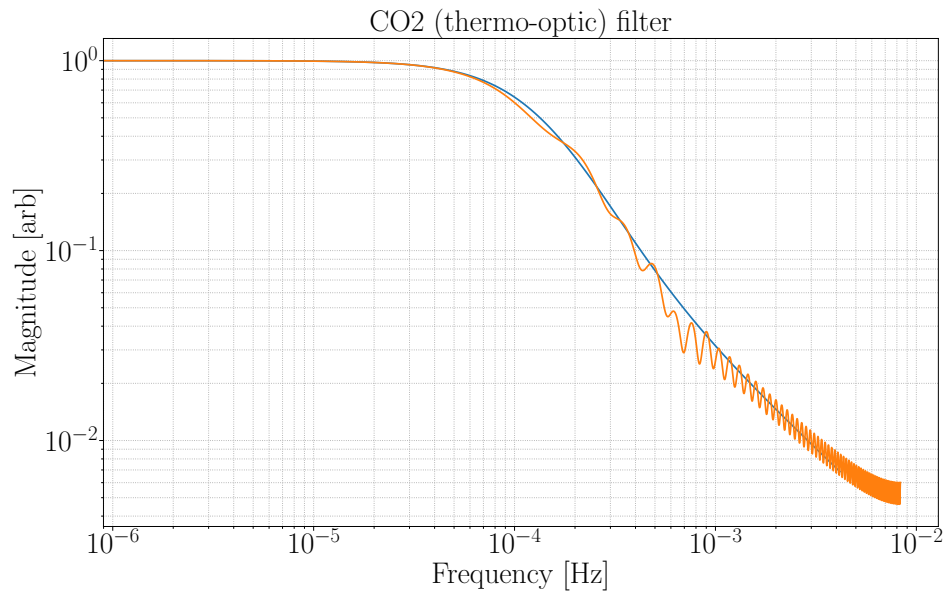


Figure 2: Fitted zpk filter to transient CO2 actuation response.

E Thermo-optic Path Distortion

E.1 Thermorefractive aberration

Consider an aberration of a substrate with an uninfluenced index of n_0 and a thermo-refractive term ($\frac{dn}{dT}$):

$$n(x, y, z) = n_0 + \frac{dn}{dT}[T(x, y, z) - T_0] \quad (5)$$

The above coorelates the material index (n) to a path distortion (Ψ) (to first order) from thermal aberrations on a cylindrical substrate volume [24]:

$$\Psi(r) = \frac{dn}{dT} \int_{-h/2}^{h/2} [T(r, z) - T_0] dz \quad (6)$$

E.2 Thermoelastic aberration

A much more involved derivation with a significantly larger result than above is computed in [98], though best computed for oneself especially for coatings and substrates alternative to $\text{SiO}_2\text{TiO}_2 : \text{Ta}_2\text{O}_5$ and fused silica respectively. It is worth mentioning that the effect for an approximate 1W absorbed power yields a 10 times smaller optical path distortion than that mentioned for the thermal lens [24].

F CO2 mask

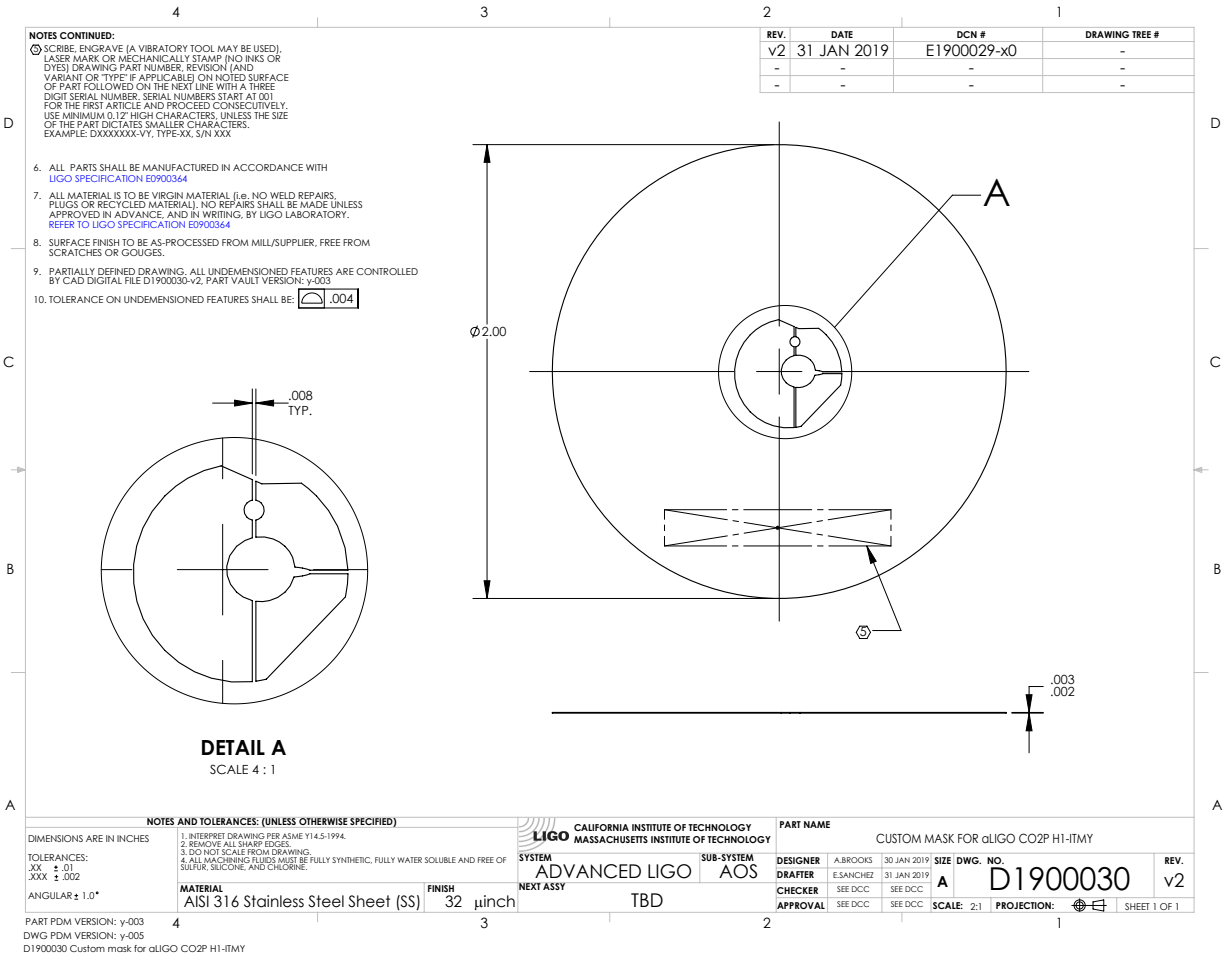


Figure 3: A CAD drawing of the first CO2 mask installed in the CO2 beam path.

G Anisotropic media

Unlike isotropic media, we do not assume that the index of refraction of anisotropic media is the same for all chosen wave vectors. This is a direct consequence of the birefringence of anisotropic media; characterized by the dielectric, permittivity, and polarization tensors.

G.1 Monochromatic plane wave propagation

Revisiting Maxwell's equations for a simple monochromatic plane wave solution provides further direction on how crystalline media may effect incident light. Further elaborating, the following assumptions are made:

$$\vec{E} = E_o e^{(i\omega(\frac{n}{c}\vec{r}\cdot\vec{s}-t))} \quad (7)$$

Where n is the index of refraction, c is the speed of light, \vec{r} is the position vector and \vec{s} is the unit wave normal.

$$\nabla \times \vec{H} = \frac{\partial \vec{D}}{\partial t} \quad (8)$$

Where \vec{H} is the magnetic field assuming permeability μ , and the generalized displacement vector \vec{D} and electric field vector \vec{E} .

$$\nabla \times \vec{E} = -\mu \vec{H} \quad (9)$$

Reducing to only the displacement and electric fields:

$$\vec{D} = \frac{n^2}{\mu} [\vec{E} - \vec{s}(\vec{s} \cdot \vec{E})] \quad (10)$$

Maxwell's equations show that the electric field is not necessarily parallel to the displacement field and in most materials with non-zero polarizability tensors and dielectric tensors, it is not. But as specified above, the displacement vector, Electric field and unit wave normal are

co-planar while remaining orthogonal to \vec{H} . Assuming we are operating within a coordinate system aligned with the principal dielectric axes, we substitute Equation 12 into Equation 10:

$$E_i = \frac{n^2 s_i (\vec{E} \cdot \vec{s})}{n^2 - \mu \varepsilon_i} \quad (11)$$

From here it can be shown that for a general plane wave there exist two unique refractive index solutions within the constructed dielectric [51].

G.2 The Dielectric tensor

Further elaborating on the nature of a generalized dielectric tensor (ε) for any wavevector is required to proceed:

$$D_i = \varepsilon_{ij} E_j \quad (12)$$

Where D is the displacement vector, E is the electric field vector, and ε is the dielectric tensor. The displacement vector for isotropic media is retrieved when $i = j$ and $\varepsilon_i = \varepsilon$. To further understand the nature of the dielectric tensor we assert Poynting's theorem providing an energy conservation requirement:

$$\nabla \cdot \vec{S} = \frac{dU}{dt} \quad (13)$$

Where $\vec{S} = \vec{E} \times \vec{H}$ is the poynting vector and $U = \frac{1}{8\pi} (\vec{E} \cdot \vec{D} + \vec{B} \cdot \vec{H})$ is the electromagnetic field density. The reader is left to perform the exercise and show that in order for Equation 13 to hold true given Equation 12

$$\varepsilon_{ij} = \varepsilon_{ji} \quad (14)$$

Demonstrating that the dielectric tensor is symmetric - exhibiting only six unique terms. Diagonalizing the tensor, the presence of two unique eigenvectors and eigenvalues indicates the existence of two eigenpolarizations with paired eigenindices.

$$E_i = \frac{n^2 s_i (\vec{E} \cdot \vec{s})}{n^2 - \mu \varepsilon_i} \quad (15)$$

Though this result requires revisiting geometrical conditions that are best visualized using a method introduced in the next section [51].

H EO Modulation (Application)

Imparting phase modulations onto an optical carrier field is a common application of the electro-optic effect. Electro-optic modulators (EOMs) or Pockel cells are sold as a standard optical components usually composed of a monolithic crystalline material sandwiched between two capacitor plates connected to a single electrical input port (typically coaxial for RF) designed to take in a voltage input of frequency (Ω) within a specified modulation amplitude and frequency bandwidth. When the field amplitude across the crystal is driven by a voltage controlled oscillation, the amplitudes of the electro-optic tensor vary linearly.

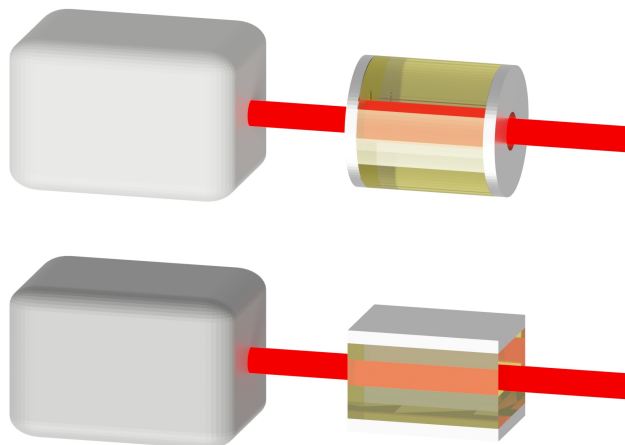


Figure 4: Longitudinal and transverse electro-optic modulators

The voltage amplitude of the signal input is proportional to the strength of the modulated phase on the optical carrier frequency (ω); commonly quantified in terms of a modulation index (β):

$$E_{\text{out}} = E_o e^{i\omega t + \beta \sin(\Omega t)} \approx E_o [J_0(\beta) e^{i\omega t} + J_1(\beta) e^{i(\omega + \Omega)t} - J_1(\beta) e^{i(\omega - \Omega)t}]$$

Where we have approximated with the Jacobi-Anger expansion utilizing Bessel functions of the first kind ($J_n(x)$) [99]:

$$e^{iz\sin(\theta)} \approx J_0(z) + 2 \sum_{n=1}^{\infty} i^n J_n(z) \sin(n\theta) \quad (16)$$

1.14 sufficiently demonstrates that, to the first order, a carrier field that is phase modulated is also, in essence, imparting power to separate optical sideband fields separated in frequency by an integer multiple of the modulation $n \cdot \Omega$. Typically Ω is a chosen frequency used for optical heterodyne detection; while for a noise-driven modulation, the phase coupling is coorelated to the local directionally relevant E-field spectra alongside the propogation length of the beam propogation within the electro-optic media.

I Miller indices for highly reflective GaAs/Al_{0.92}Ga_{0.08}As coatings

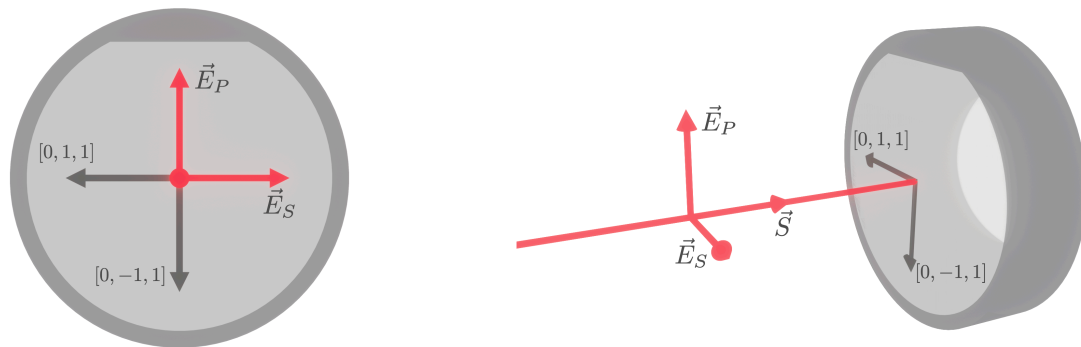


Figure 5: The beam propagation axis (\vec{S} , $[-100]$) with respect to the GaAs/Al_{0.92}Ga_{0.08}As crystal axes. The axis formed by the $[100]$ plane normal is drawn parallel with the beam axis (z-axis) and the polarizations of incident and reflected beam oscillate along vectors within the plane formed by the normal of that axis. The coating is grown with a flat tracing a line within the $[0-11]$ plane; where the plane normal points towards the sample center.

Up to this point three varieties of orthonormal coordinates are addressed: the crystal axis (as indicated by Miller index plane normals), the principal dielectric axis (based on diagonalization of the indicatrix), and an optical beam axis (when considering a desired (laser) light propagation). The asserted beam axis can be cited Figure 5.

J Laplacian in Cylindrical coordinates (Numerical Recipe)

We exploit the chosen optic / disk symmetry about the polar angle ($\partial V/\partial\theta = 0$) and compute for the longitudinal (z) and radial (r) coordinates with the use of the appropriate Laplacian:

$$\left[\frac{1}{r} \frac{\partial}{\partial r} \left(r \frac{\partial}{\partial r} \right) + \frac{\partial^2}{\partial z^2} \right] (\varepsilon V) = 0 \quad (17)$$

Where ε is the dielectric

Observing equation Equation 4.6 we parse the non-zero expression into it's individual parts:

$$\left[\underbrace{\frac{\partial^2}{\partial z^2}}_{(c)} + \underbrace{\frac{\partial^2}{\partial r^2}}_{(b)} + \underbrace{\frac{1}{r} \frac{\partial}{\partial r}}_{(a)} \right] (\varepsilon V) = 0 \quad (18)$$

Term (a) Starting with the first derivative, we use the central difference approximation:

$$\frac{\partial}{\partial r} \rightarrow \frac{f(r+h, z) - f(r-h, z)}{2h} \rightarrow \begin{bmatrix} -\frac{1}{2} & 0 & \frac{1}{2} \end{bmatrix} \quad (19)$$

Term (b) Second derivative approximation, we use the standard 2d laplace stencil

$$\frac{\partial}{\partial r^2} \rightarrow \frac{f(r+h, z) - 2f(r, z) + f(r-h, z)}{h^2} \rightarrow \begin{bmatrix} 1 & -2 & 1 \end{bmatrix} \quad (20)$$

Term (c) Equivalent to the second derivative approximation used above:

$$\frac{\partial}{\partial z^2} \rightarrow \frac{f(r, z+h) - 2f(r, z) + f(r, z-h)}{h^2} \rightarrow \begin{bmatrix} 1 & -2 & 1 \end{bmatrix} \quad (21)$$

To build the stencil terms at the boundaries, we look at the specialized finite difference condition @ $r = 0$, with the symmetry about $r = 0$ allowing the application of a ghost point $V(-h, z) = V(h, z)$:

$$\frac{\partial V}{\partial r} = 0 \rightarrow V(h, z) = V(-h, z) \quad (22)$$

$$\frac{\partial^2 V}{\partial r^2} = \frac{2}{h} \left(\frac{V(h, z) - V(0, z)}{h} \right) \quad (23)$$

Equation 22 alone does not define $V(0, z)$, to establish the form of this point, we proceed to (Taylor) expand the function about it:

$$V \approx V_0 + C_1 r + C_2 r^2 + \mathcal{O}(r^4) \quad (24)$$

Symmetry about the origin imposes an even function of V :

$$\frac{\partial V}{\partial r} \approx C_1 + 2C_2 r + \mathcal{O}(r^3)$$

$$\frac{1}{r} \frac{\partial V}{\partial r} \approx 2C_2 + \mathcal{O}(r^2) \quad (25)$$

Where $C_1 = 0$ to avoid a singular point.

$$\frac{\partial^2 V}{\partial r^2} \approx 2C_2 + \mathcal{O}(r^2) \quad (26)$$

Substituting Equation 25 and Equation 26 back into equation Equation 18 :

$$\nabla^2(\varepsilon V) = \frac{\partial^2}{\partial z^2} + 4C_2 \quad (27)$$

The radial portion of the operator $\nabla^2 V$ given Equation 24 and Equation 23:

$$\left(\frac{r_0}{h} - \frac{2}{h^2} \right) C_1 + \left(\frac{r_h}{h} + \frac{2}{h^2} \right) C_2 h^2 = 4C_2 \quad (28)$$

Where again, we found $C_1 = 0$:

$$\rho_{\text{indexing}} \rightarrow \begin{bmatrix} \rho_0 & \rho_1 & \rho_2 & \rho_3 & \rho_4 & \rho_5 & \rho_6 & \rho_7 & \rho_8 & \cdots & \rho_n \\ \rho_0 & \rho_1 & \rho_2 & \rho_3 & \rho_4 & \rho_5 & \rho_6 & \rho_7 & \rho_8 & \cdots & \rho_n \\ \rho_0 & \rho_1 & \rho_2 & \rho_3 & \rho_4 & \rho_5 & \rho_6 & \rho_7 & \rho_8 & \cdots & \rho_n \\ \rho_0 & \rho_1 & \rho_2 & \rho_3 & \rho_4 & \rho_5 & \rho_6 & \rho_7 & \rho_8 & \cdots & \rho_n \\ \rho_0 & \rho_1 & \rho_2 & \rho_3 & \rho_4 & \rho_5 & \rho_6 & \rho_7 & \rho_8 & \cdots & \rho_n \\ \rho_0 & \rho_1 & \rho_2 & \rho_3 & \rho_4 & \rho_5 & \rho_6 & \rho_7 & \rho_8 & \cdots & \rho_n \\ \rho_0 & \rho_1 & \rho_2 & \rho_3 & \rho_4 & \rho_5 & \rho_6 & \rho_7 & \rho_8 & \cdots & \rho_n \\ \rho_0 & \rho_1 & \rho_2 & \rho_3 & \rho_4 & \rho_5 & \rho_6 & \rho_7 & \rho_8 & \cdots & \rho_n \\ \rho_0 & \rho_1 & \rho_2 & \rho_3 & \rho_4 & \rho_5 & \rho_6 & \rho_7 & \rho_8 & \cdots & \rho_n \\ \rho_0 & \rho_1 & \rho_2 & \rho_3 & \rho_4 & \rho_5 & \rho_6 & \rho_7 & \rho_8 & \cdots & \rho_n \\ \vdots & \ddots & \vdots \\ \vdots & \ddots \end{bmatrix}$$

Parallel computation of the potential over the entire meshgrid is done by vectorizing the potential:

$$V = \left[\begin{array}{c}
 V(\rho_0, z_0) \\
 V(\rho_1, z_0) \\
 \vdots \\
 V(\rho_n, z_0) \\
 \hline
 V(\rho_0, z_1) \\
 V(\rho_1, z_1) \\
 \vdots \\
 V(\rho_n, z_1) \\
 \hline
 \vdots \\
 \hline
 V(\rho_0, z_{n-1}) \\
 V(\rho_1, z_{n-1}) \\
 \vdots \\
 V(\rho_n, z_{n-1}) \\
 \hline
 V(\rho_0, z_n) \\
 V(\rho_1, z_n) \\
 \vdots \\
 V(\rho_n, z_n)
 \end{array} \right]$$

K Mode matching data for Electro-optic sample cavity

K.1 Pre MMT beam scan

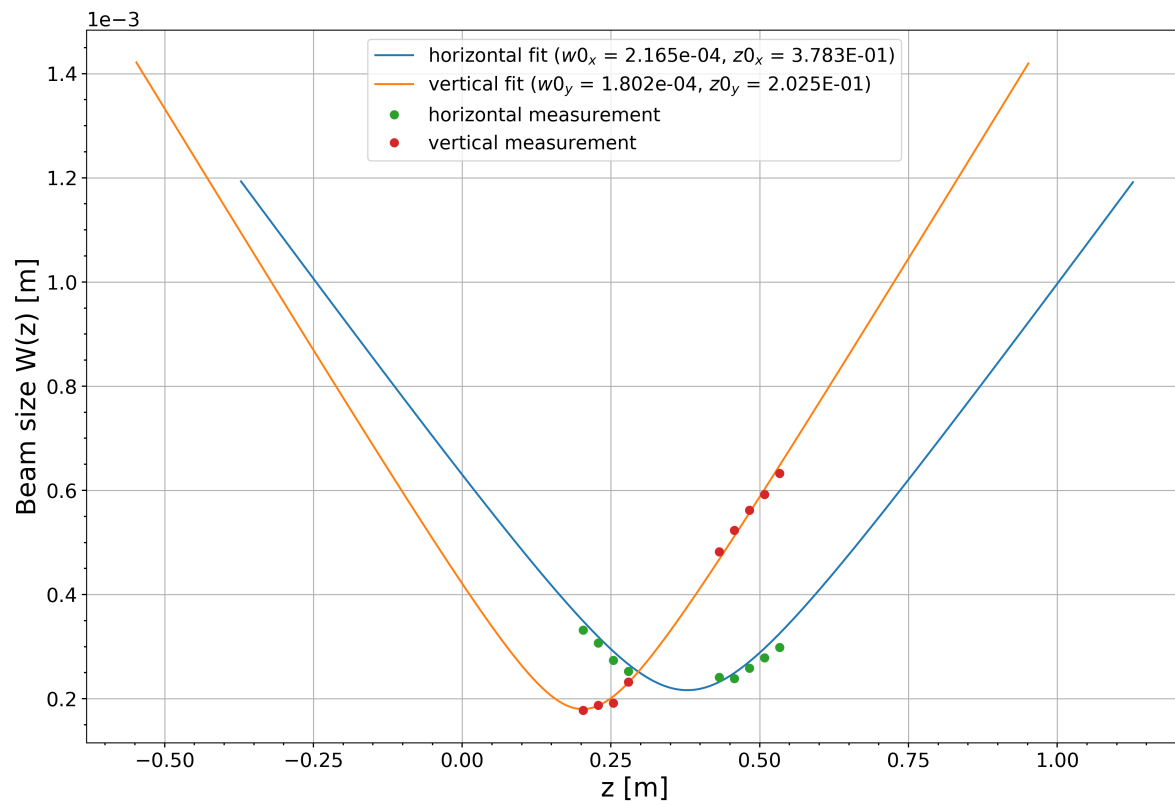


Figure 6: Beam scan taken from SM5 (Steering mirror 5)

K.2 Post MMT beam scan

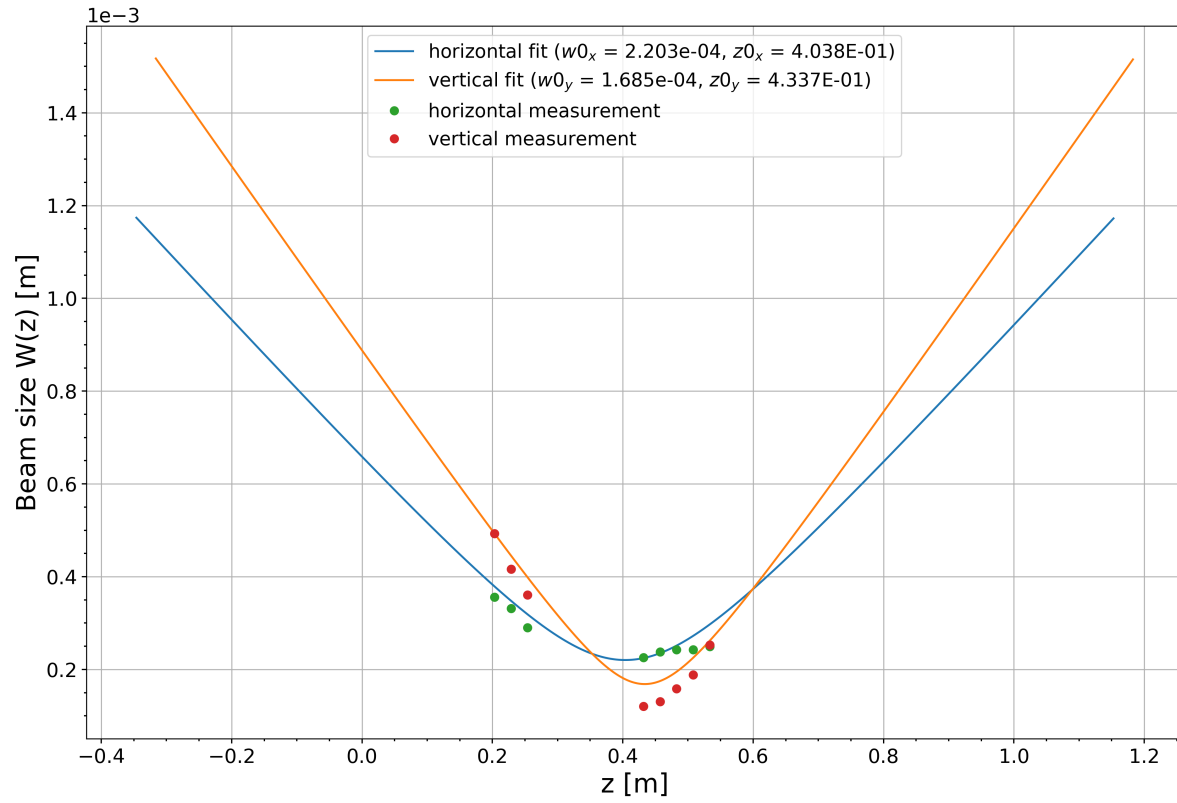


Figure 7: Beam scan taken from SM6. Sampling points before SM7 and after the first cavity iris.

L Interferometer Configurations (code)

L.1 ifo_configs.py

```

1 import numpy as np
2
3 # Bode tools
4 def bode_amp(H):
5     """
6     Returns amplitude information on transfer function (H)
7     """
8     return np.sqrt(np.real(H)**2 + np.imag(H)**2)
9
10 def bode_ph(H):
11     """
12     Returns phase information on transfer function (H)
13     """
14     return (180/np.pi)*np.arctan(np.imag(H)/np.real(H))
15
16 # some constants:
17 cee = np.float64(299792458) ## speed of light [m/s]
18 h_bar = (6.626e-34)/(2*np.pi) ## planck's constant
19
20
21 # IFO params
22 def finesse(r_i, r_e):
23     """
24     r_i : ITM reflectivity coefficient
25     r_e : ETM reflectivity coefficient
26     """
27     return np.pi*np.sqrt(r_i*r_e)/(1-(r_i*r_e))
28
29
30 # Michelson frequency response
31 def mich_freq_resp(freq, Length, phi_0, P_in, OMEGA):
32     """
33     MICHELSON FREQUENCY RESPONSE CALCULATOR
34     freq : standard (gravitational wave) frequency [Hz]
35     Length : Michelson ifo arm length [m]
36     phi_0 : static differential arm length tuning phase [rad]
37     P_in : input power [W]
38     """
39     return (P_in*OMEGA*np.sin(phi_0))*Length*
40     np.exp((-1j*Length*2.0*np.pi*freq)/cee)*

```

```

41     np.sin((Length*2.0*np.pi*freq)/cee)/(Length*2.0*np.pi*freq)
42
43 def fpmi_freq_resp(freq, r_1, t_1, r_2, L, phi_0, P_in, OMEGA, low_pass=False):
44     """
45     FABRY PEROT MICHELSON FREQUENCY RESPONSE CALCULATOR
46     freq : standard (gravitational wave) frequency [Hz]
47     r_1, t_1, r_2: Assuming arm symmetry where the ITM has r_1, t_1 coefficients
48                   and the ETM has a r_2 reflectivity coefficient.
49                   Also assumes no loss. [arb]
50     OMEGA: OPTICAL angular frequency [rad Hz]
51     Length: Michelson ifo arm length [m]
52     phi_0 : static differential arm length tuning phase [rad]
53     """
54     if low_pass:
55         f_pole = 1/(((4*np.pi*L)*np.sqrt(r_1*r_2))/(cee*(1-r_1*r_2)))
56         fpmi_resp = 1/(1 + 1j*(freq/f_pole))
57     else:
58         fpmi_resp = ((t_1**2 * r_2)/((t_1**2 + r_1**2)*r_2 - r_1))*
59                     (mich_freq_resp(freq, L, phi_0, P_in, OMEGA)/
60                     (1-r_1*r_2*np.exp(-1j*L*4.0*np.pi*freq/cee)))
61     return fpmi_resp
62
63 def PRG(L_rt, Finn, r_PRM, max=0):
64     """
65     POWER RECYCLING GAIN (@ optimal reflectivity)
66     * Assuming a FPMI with symmetric arms *
67     L_rt : Round trip loss
68     Finn : Cavity finesse
69     """
70     if max == 1:
71         G_PR = np.pi/(2*Finn*L_rt*(1-((Finn*L_rt)/(2*np.pi))))
72     else:
73         G_PR = (1-r_PRM**2)/(1-r_PRM*(1-(Finn/np.pi)*L_rt))**2
74
75
76     return G_PR
77
78 def drfpmi_freq_resp(freq, G_PRC_opt, r_1, t_1, r_2, r_SRM, t_SRM, phi_SRC, L,
79                     phi_0, P_in, OMEGA):
80     """
81     DUAL RECYCLED FABRY PEROT MICHELSON FREQUENCY RESPONSE
82     CALCULATOR
83
84     freq: standard (gravitational wave) frequency [Hz]
85     G_PRC_opt: maximum power recycling gain (optimal) [arb]

```

```

86 r_1: ITM reflection coefficient [arb]
87 t_1: ITM transmission coefficient [arb]
88 r_2: ETM reflection coefficient [arb]
89 r_SRM: Signal recycling mirror reflection coefficient [arb]
90 t_SRM: Signal recycling mirror transmission coefficient [arb]
91 L: Length of the Fabry–Perot arms [m]
92 OMEGA: OPTICAL angular frequency [rad Hz]
93 """
94  $r\_SRC = (r\_1 - r\_SRM * np.exp(1j * 2 * phi\_SRC)) /$ 
95  $(1 - r\_1 * r\_SRM * np.exp(1j * 2 * phi\_SRC))$ 
96  $t\_SRC = t\_1 * t\_SRM * np.exp(1j * phi\_SRC) / (1 - r\_1 * r\_SRM * np.exp(1j * 2 * phi\_SRC))$ 
97
98 return  $((t\_1 ** 2 * r\_2) / ((t\_1 ** 2 + r\_1 ** 2) * r\_2 - r\_1)) *$ 
99  $G\_PRC\_opt * t\_SRC * (P\_in * L * OMEGA * np.exp((-1j * L * 2.0 * np.pi * freq) / cee) *$ 
100  $np.sin((L * 2.0 * np.pi * freq) / cee) / (L * 2.0 * np.pi * freq)) /$ 
101  $(1 - r\_SRC * r\_2 * np.exp(-1j * L * 4.0 * np.pi * freq / cee))$ 
102
103
104 # Shot noise
105 def N_shot(OMEGA, P_in):
106 """
107 Interferometer shot noise calculator
108 OMEG: OPTICAL angular frequency [rad Hz]
109 Length : ifo arm length [m]
110 phi_0 : static differential arm length tuning phase [rad]
111 P_in : Input power [W]
112 """
113 return np.sqrt(2 * h_bar * OMEGA * P_in)

```

L.2 MICH

```

1 import numpy as np
2 import matplotlib.pyplot as plt
3 import os
4 import sys
5 sys.path.insert(0, '../')
6 plt_style_dir = '../..//stash/'
7 fig_exp_dir = '../..//..//figs/'
8 from ifo_configs import N_shot
9 from ifo_configs import mich_freq_resp as MICH

```

```

10 from ifo_configs import bode_amp, bode_ph
11 %matplotlib inline
12 if os.path.isdir(plt_style_dir) == True:
13     plt.style.use(plt_style_dir + 'ppt2latexsubfig.mplstyle')
14 plt.rcParams["font.family"] = "Times New Roman"

1 # Some parameters
2 cee = np.float64(299792458)
3 h_bar = (6.626e-34)/(2*np.pi)
4 OMEG = np.float64(2*np.pi*cee/(1064.0*1e-9))
5 L = np.float64(4000.0)
6 nu = np.arange(1, 1000000, 1)
7 PHI_0 = np.pi/2 #[rad]
8 P_IN = 125 #[W]

```

L.2.1 Derivation

For the simple Michelson we know that a change in arm length correlates to light at the AS port We also know that a differential arm length corresponds to a difference in phase of the light that impinges upon the BS For a gravitational wave we can quantify the phase difference in this following way:

$$\phi_A - \phi_B = \int_{t-2L/c}^t \Omega \left[1 + \frac{1}{2}h(t) \right] dt - \int_{t-2L/c}^t \Omega \left[1 - \frac{1}{2}h(t) \right] dt \quad (30)$$

The phase difference can then be quantified by:

$$\phi_A - \phi_B = \int_{t-2L/c}^t \Omega h(t) dt \quad (31)$$

where

$$h(t) = h_0 e^{i\omega t} \quad (32)$$

Ω is the **optical angular frequency**

After evaluating this integral we get:

$$\Delta\phi = \phi_A - \phi_B = \frac{2L\Omega}{c} e^{-iL\omega/c} \frac{\sin(L\omega/c)}{L\omega/c} \cdot h_0 e^{i\omega t} \quad (33)$$

Where the first term in the phase difference carries all the time independent frequency information. This is what we are calculating below.

For the sake of being explicit, we are going to plot:

$$\Delta\phi(\omega) = h_0 \frac{2L\Omega}{c} e^{-iL\omega/c} \frac{\sin(L\omega/c)}{L\omega/c} \quad (34)$$

This accounts for the differential phase as a function of gravitational wave frequency, though we have not established the amount of optical gain the Michelson offers. This can be understood through a first order Taylor approximation about a selected Michelson offset angle ϕ_0 :

$$P(\omega, \phi_0) = \frac{P_{\text{in}}}{4} [r_x^2 + r_y^2 - 2r_x r_y \cos(\phi_0 + \Delta\phi(\omega))] \quad (35)$$

$$P(\omega, \phi_0) \approx \frac{P_{\text{in}}}{4} [r_x^2 + r_y^2 - 2r_x r_y (\cos(\phi_0) - \Delta\phi(\omega) \cdot \sin(\phi_0))] = \frac{P_{\text{in}}}{2} [1 - (\cos(\phi_0) - \Delta\phi(\omega) \cdot \sin(\phi_0))] \quad (36)$$

Where we define a response gain function H_{MICH} :

$$H_{\text{MICH}}(\omega, \phi_0) = \frac{P_{\text{in}}}{2} \cdot \Delta\phi(\omega) \cdot \sin(\phi_0) \quad (37)$$

```
1 H = MICH(nu, L, PHI_0, P_IN, OMEG)
```

```
1 fig, ax1 = plt.subplots()
```

```
2 ax1.set_xlabel('frequency [Hz]')
```

```
3 ax1.set_ylabel('H_{\mathdefault{MICH}} [\mathdefault{W/m}]', color='C0')
```

```
4 #ax1.plot(w/(FSR), F_w_cc_modsq*100)
```

```

5 ax1.loglog(bode_amp(H),linewidth=7.5, color='C0')
6 #plt.ylim([10e-6, 10e0])
7 ax2 = ax1.twinx()
8 #ax2.plot(w/(FSR), (180/np.pi)*np.arctan(F_w_cc.imag/F_w_cc.real), '--')
9 ax2.semilogx(nu,(180/np.pi)*np.arctan(np.imag(H)/np.real(H)), '--', linewidth=7.5,
10             color='C1')
11 #plt.xlabel('frequency [FSR]')
12 plt.xlim([1,1e5])
13 plt.ylabel('phase [deg]',color='C1')
14 fig.savefig(fig_exp_dir + 'INTRO/mich_fr.pdf', dpi=300, bbox_inches='tight')

```

Though with the provided frequency dependence and optical gain, we still need to understand a starting noise floor spectra and compare to our anticipated limiting noise

Shot noise

* A fundamental limit imposed by the statistical nature of photon counting

* The photon counting follows Poisson statistics

* Photon counting variance (variance is equal to the mean)

$$\langle (n - \bar{n})^2 \rangle = \frac{P\Delta t}{\hbar\Omega} \quad (38)$$

* Power variance:

$$\langle (P - \bar{P})^2 \rangle = \hbar\Omega\bar{P}\Delta t \quad (39)$$

* PSD of the measured power between two uncoorelated moments in time:

$$S_P(\omega) = \lim_{T \rightarrow \infty} \frac{2}{T} \left\langle \left| \int_{-T}^T (P(t) - \bar{P}) e^{-i\omega t} dt \right|^2 \right\rangle \quad (40)$$

$$= \lim_{T \rightarrow \infty} \frac{2}{T} \int_{-T}^T \hbar\Omega\bar{P} dt \quad (41)$$

$$= 2\hbar\Omega\bar{P} \quad (42)$$

* Where the ASD is:

$$[S_P(\omega)]^{1/2} = [2\hbar\Omega\bar{P}]^{1/2} \quad (43)$$

The signal to noise is established by dividing the frequency dependent optical gain times the gravitational wave ASD ($[S_h(\Omega)]^{1/2}$) by the noise ASD:

$$\text{SNR} = G_{\text{opt}}(\omega)[S_h(\omega)]^{1/2}/S_N(\omega) = H_{\text{MICH}}/[S_P]^{1/2} = \left(\frac{\Delta\phi(\omega)}{h_0} \frac{P_{\text{in}}}{2} \sin(\phi_0) \right) / [2\hbar\Omega\bar{P}]^{1/2} \quad (44)$$

This is to say that for the stated gravitational wave ASD, and for an SNR of 1, we establish the following threshold for detector:

$$[S_h(\omega)]^{1/2} \{ \text{SNR} \geq 1 \} \geq \frac{[S_N(\omega)]^{1/2}}{H_{\text{MICH}}(\omega)} \quad (45)$$

Where

$$\frac{[S_N(\omega)]^{1/2}}{H_{\text{MICH}}(\omega)} = \frac{[2\hbar\omega\bar{P}]^{1/2}}{\Delta\phi(\omega)[P_{\text{in}}/2]\sin(\phi_0)} = \left(\frac{\hbar\Omega}{\omega P_{\text{in}}} \right)^{1/2} \frac{[r_x^2 + r_y^2 - 2r_x r_y \cos(\phi_0)]^{1/2}}{\sin(L\omega/c)} e^{iL\omega/c} \quad (46)$$

```
1 S_h = N_shot(OMEG, P_IN)
```

```
2 print(S_h)
```

```
1 plt.loglog(nu, S_h/bode_amp(H), linewidth=7.5, color='C0')
```

```
2 plt.ylim([1e-21, .5e-14])
```

```
3 plt.xlabel('frequency [Hz]')
```

```
4 plt.ylabel('$\mathdefault{S}_h$ \;
```

```
5 \mathdefault{[ 1 / \sqrt{\mathdefault{Hz}}]} $')
```

```
6 plt.xlim([1,1e5])
```

```
7 plt.grid(visible=True)
```

```
8 plt.savefig(fig_exp_dir + 'INTRO/mich_sensi.pdf', dpi=300, bbox_inches='tight')
```

L.3 FPMI

```
1 import numpy as np
```

```

2 import matplotlib.pyplot as plt
3 import scipy.signal as sig
4 import os
5 import sys
6 sys.path.insert(0,'../')
7 plt_style_dir = '../..//stash/'
8 fig_exp_dir = '../..//..//figs/'
9 from ifo_configs import mich_freq_resp as MICH
10 from ifo_configs import fpmi_freq_resp as FPMI
11 from ifo_configs import N_shot, bode_amp, bode_ph
12 if os.path.isdir(plt_style_dir) == True:
13     plt.style.use(plt_style_dir + 'ppt2latexsubfig.mplstyle')
14 plt.rcParams["font.family"] = "Times New Roman"
15 line_width=7.5

```

Let's start with the simple Fabry Perot cavity. The following are equations that characterize the circulating and reflected fields (both critical to measuring the phase response of the FP cavity to GWs):

$$E(t) = t_1 E_{in} + r_1 r_2 E(t - 2T) e^{-i\Delta\phi(t)} \quad (47)$$

$$E_r(t) = -r_1 E_{in} + t_1 r_2 E(t - 2T) e^{-i\Delta\phi(t)} \quad (48)$$

$T = L/c$ is the time it takes light to reach the end of the cavity and $\Delta\phi(t)$ is the phase rotation.

We can define the static phase rotation (no GW passing through) as :

$$\Delta\phi = 2kL = 4\pi L/\lambda_{opt} \quad (49)$$

And if L is tuned just right $2kL = 2\pi n$ so the cavity is just tuned for resonance

If we put a gravitational wave in the mix we redefine this phase rotation as such that:

$$\Delta\phi = \frac{\omega_0}{2} \int_{t-\frac{2L}{c}}^t h(t') dt' \quad (50)$$

This assumes that the static phase rotation satisfies $2\omega_0 L/c = 2\pi n$. Say that we have something that throws the cavity slightly off resonance.. doesn't have to be a gravitational wave... but that's what we hope for. If the $\Delta\phi$ becomes such that the cavity is thrown off resonance we get a time dependent intra-cavity field:

$$E(t) = \bar{E} + \delta E(t) \quad (51)$$

and if the phase rotation ($\Delta\phi$) is super small... which is pretty much guaranteed with gravitational waves, we can say:

$$e^{i\Delta\phi} = 1 - i\Delta\phi \quad (52)$$

Using equations 51 and 52 in 47 we get:

$$\bar{E} + \delta E(t) = t_1 E_{in} - r_1 r_2 \bar{E} + r_1 r_2 \delta E(t - 2T) - i r_1 r_2 \bar{E} \Delta\phi(t) \quad (53)$$

We can parse this into time dependent and time independent terms:

$$\bar{E} = t_1 E_{in} - r_1 r_2 \bar{E} \quad (54)$$

$$\delta E(t) = r_1 r_2 \delta E(t - 2T) - i r_1 r_2 \bar{E} \Delta\phi(t) \quad (55)$$

Since the time dependent phase information is encoded in 55 we will take the laplace transform of this equation to yield:

$$\delta E(s) = -i \frac{r_1 r_2 \bar{E}}{1 - r_1 r_2 e^{-2sT}} \Delta \phi(s) \quad (56)$$

We are now one step closer to getting a useful expression for the phase response. But let's reiterate what this last equation means. The last equation is how the change in the electric field directly relates to a small perturbation in phase (which could be either a small change in laser frequency or length modulation)

Now.. we're not done yet because that last expression does not tell us the entire story yet.. we want to see how this effects the phase differential with the **reflected** electric field.

To do this.. we have to combine equations 47 and 48. (an easy way to do this is to get rid of the $r_2 E(t - 2T) e^{-i\Delta\phi(t)}$) :

$$E_r(t) = \frac{t_1}{r_1} E(t) - \frac{t_1^2 + r_2^2}{r_1} E_{in} \quad (57)$$

if the cavity is unperturbed:

$$\bar{E}_r = \left(\frac{r_2(r_1^2 + t_1^2) - r_1}{t_1} \right) \bar{E} \quad (58)$$

and if we perturb the cavity we see that the change in the intra-cavity field is directly related to the change in the reflected field:

$$\Delta \phi_r(s) \equiv \frac{\delta E(s)}{\bar{E}} = \frac{t_1^2 r_2}{(t_1^2 + r_1^2) r_2 - r_1} \frac{\Delta \phi(s)}{1 - r_1 r_2 e^{-2sT}} \quad (59)$$

This implies that there is an additional frequency dependent factor in your phase shift and this translates into your FPPI transfer function as:

$$H_{FPPI}(\omega_g) = \frac{2\Delta\phi_r(\omega_g)}{h(\omega_g)} = \frac{t_1^2 r_2}{(t_1^2 + r_1^2) r_2 - r_1} \frac{H_{MI}(\omega_g, L)}{1 - r_1 r_2 e^{-2i\omega_g L/c}} \quad (60)$$

Now let's code it up. Since we can separate the calculation into two, I'm going to parse out the calculation between the constant Fabry Perot term and the term with the frequency

dependence. But first, lets set up our parameters for our FPMI:

```

1 # Some parameters
2 cee = np.float64(299792458)
3 OMEG = np.float64(2*np.pi*cee/(1064.0*1e-9))
4 L = np.float64(4000.0)
5 nu = np.arange(1, 1000000, 1)
6 nat_nu = [np.float64(i*2*np.pi) for i in nu]
7 h_0 = np.float64(1)
8
9 PHI_0 = np.pi/2 #[rad]
10 P_IN = 25
11
12 T_1 = .014
13 T_2 = 50e-6
14 R_1 = 1-T_1
15 R_2 = 1-T_2
16
17 t_1 = T_1**.5
18 r_1 = R_1**.5
19 r_2 = R_2**.5

```

Now we can compute:

$$H_{FPMI}(\omega_g) = \frac{t_1^2 r_2}{(t_1^2 + r_1^2) r_2 - r_1} \cdot \frac{H_{MI}(\omega_g, L)}{1 - r_1 r_2 e^{-2i\omega_g L/c}} \quad (61)$$

```

1 H_FPMI = FPMI(nu, r_1, t_1, r_2, L, PHI_0, P_IN, OMEG)

```

We estimate the FP's pole frequency

$$1 - r_1 r_2 e^{-2i\omega_g L/c} = 0 \quad (62)$$

therefore when:

$$e^{-i\omega_g L/c} = \frac{1}{\sqrt{r_1 r_2}} \quad (63)$$

we acquire the pole frequency ω_{pole} as indicated in the low pass

$$f_{\text{pole}} = \frac{1}{4\pi\tau_s} = \frac{c}{4\pi L} \frac{1 - r_1 r_2}{\sqrt{r_1 r_2}} = \frac{\nu_{\text{FSR}}}{2\pi} \frac{1 - r_1 r_2}{\sqrt{r_1 r_2}} = \frac{\nu_{\text{FSR}}}{\mathcal{F}} \quad (64)$$

Also, understanding that the cavity Finesse can be defined as

$$\mathcal{F} = \frac{\pi\sqrt{r_i r_e}}{1 - r_i r_e} \quad (65)$$

we also can invert for a high value of finesse $\mathcal{F} \gg \pi$:

$$r_i r_e \approx 1 - \frac{\pi}{\mathcal{F}} \quad (66)$$

```

1 f_pole = 1/(((4*np.pi*L)*np.sqrt(r_1*r_2))/(cee*(1-r_1*r_2)))
2 def fpmi_lp(freq, cav_pole):
3     return 1/(1 + 1j*(freq/cav_pole))#*np.exp(1j*freq/cav_pole)
4 H_FPMLP = fpmi_lp(nu, f_pole)

```

Might as well compare it to our Michelson response:

$$H_{\text{M}}(\omega_g) = \frac{2L\Omega}{c} e^{-iL\omega/c} \frac{\sin(L\omega/c)}{L\omega/c} \quad (67)$$

```

1 H_MICH = MICH(nu, L, PHI_0, P_IN, OMEG)

```

```

1 fig, ax1 = plt.subplots()
2 ax1.set_xlabel('frequency [Hz]')
3 ax1.set_ylabel('H$\mathcal{FPMI}$ \; \mathdefault{ [W / m] }$', color='C0')
4 ax1.loglog(bode_amp(H_FPMLP), label='FPMLP', linewidth=line_width,color='C0')
5     linewidth = 20.0, alpha=0.25,color='C2')
6 ax2 = ax1.twinx()
7 ax2.semilogx(nu,bode_ph(H_FPMLP),'--', linewidth=line_width, color='C1')
8 plt.xlim([1,1e5])
9 plt.ylabel('phase [deg]', color='C1')

```

```

1 Text(0, 0.5, 'phase [deg]')

```

```

1 plt.loglog(nu,bode_amp(H_MICH), label= 'MICH', linewidth= line_width, alpha=.5)

```

```

2 plt.loglog(nu,bode_amp(H_FPMI), label='FPMI', linewidth=line_width)
3     linewidth = 20.0, alpha=0.25)
4 plt.axvline (x=f_pole,ymin=1e-11, color='red', linestyle='dotted', linewidth=3.0)
5 plt.ylim([5e7, 5e14])
6 plt.xlim([1e0, 1e5])
7 plt.xlabel('frequency [Hz]')
8 plt.ylabel('H(f) $\mathdefault{[W/m]}$')
9 lgd=plt.legend()
10 plt.savefig('../figs/INTRO/fpmi_fr.pdf', dpi=300, bbox_inches='tight')

```

```

1 plt.semilogx(nu,bode_ph(H_MICH), '--', label='MICH', linewidth= line_width, alpha=.5)
2 plt.semilogx(nu,bode_ph(H_FPMI),'--', label='FPMI', linewidth= line_width)
3 plt.xlim([1,100000])
4 plt.ylabel('phase [deg]')
5 plt.xlabel('Frequency [Hz] ')
6 lgd=plt.legend()

```

```

1 Sh_noise = N_shot(OMEG, P_IN)

```

```

1 plt.loglog(nu,Sh_noise/bode_amp(H_MICH), label= 'MICH',
2     linewidth= line_width, alpha=.5)
3 plt.loglog(nu,Sh_noise/bode_amp(H_FPMI), label='FPMI', linewidth=line_width)
4     label='FPMI LP', linewidth = 20.0, alpha=0.25)
5 plt.ylim([1e-23, 1e-16])
6 plt.xlim([1e0, 1e5])
7 plt.xlabel('frequency [Hz]')
8 plt.ylabel('H(f) $\mathdefault{[1/\sqrt{\mathdefault{Hz}}]}$')
9 lgd=plt.legend()
10 fig.savefig('../figs/INTRO/fpmi_sensi.pdf', dpi=300, bbox_inches='tight')

```

L.4 DRFPMI

```

1 import numpy as np
2 import matplotlib.pyplot as plt
3 import scipy.signal as sig
4 import os
5 import sys

```

```

6 sys.path.insert(0,'../')
7 plt_style_dir = '.././stash/'
8 fig_exp_dir = '../././figs/'
9 import ifo_configs as ifco
10 if os.path.isdir(plt_style_dir) == True:
11     plt.style.use(plt_style_dir + 'ppt2latexsubfig.mplstyle')
12 plt.rcParams["font.family"] = "serif"
13 plt.rcParams["font.serif"] = ["Times New Roman"] + plt.rcParams["font.serif"]
14 line_width=7.5

```

Up to this point we can understand how the FPMI response function works:

$$H_{FPMI}(\omega_g) = \frac{2\Delta\phi_r(\omega_g)}{h(\omega_g)} = \frac{t_1^2 r_2}{(t_1^2 + r_1^2)r_2 - r_1} \frac{H_{MI}(\omega_g, L)}{1 - r_1 r_2 e^{-2i\omega_g L/c}} \quad (68)$$

```

1 # Some parameters
2 cee = np.float64(299792458)
3 OMEG = np.float64(2*np.pi*cee/(1064.0*1e-9))
4 L = np.float64(4000.0)
5 nu = np.arange(1, 1000000, 1)
6 nat_nu = [np.float64(i*2*np.pi) for i in nu]
7 h_0 = np.float64(1)
8
9 T_1 = .014
10 T_2 = 50e-6
11 R_1 = 1-T_1
12 R_2 = 1-T_2
13
14 t_1 = T_1**.5
15 r_1 = R_1**.5
16 r_2 = R_2**.5
17
18 PHI_0 = np.pi/2
19 P_IN = 25

```

POWER RECYCLING

With all the power going to the symmetric port, the nominal operating state of the FPPI involves a significant amount of dumped / wasted power. Placing a mirror at the symmetric port can allow that power to be recycled. Though considerations must be made to maximize the amount of recycling gain you can acquire with your GW detector. This is dependent on the placement of the power recycling mirror (PRM) and its reflectivity, transmission, and loss coefficients.

But first, the field at the symmetric port:

$$E_{\text{SYM}} = \frac{E_i}{2} e^{2ikl} (r_{\text{FP},X} + r_{\text{FP},Y}) \quad (69)$$

This is realized through observing the circulating power between the PRM and the short Michelson:

$$E_{\text{PRC}} = \frac{t_{\text{PRM}}}{1 - r_{\text{PRM}} r_{\text{FPPI}} e^{2ik(L_{\text{PRC}2\text{BS}} + L_{\text{SMICH}})}} E_{\text{in}} \quad (70)$$

Where:

$$L_{\text{SMICH}} = l_x + l_y \quad (71)$$

Now let's observe the cavity reflection parameter:

$$r_{\text{FP}} = -r_1 + \frac{t_1^2 r_2 e^{i2kL}}{1 - r_1 r_2 e^{i2kL}} = -\frac{\mathcal{F}}{\pi} \left[-\left(\frac{r_1}{r_2}\right)^{1/2} + \left(\frac{r_2}{r_1}\right)^{1/2} (r_1^2 + t_1^2) \right] \quad (72)$$

But with loss considerations:

$$r_{\text{FP}} = -r_1 + \frac{t_1^2 r_2 e^{-t_{\text{RT}}/\tau_{\text{loss}}} e^{i2kL}}{1 - r_1 r_2 e^{-t_{\text{RT}}/\tau_{\text{loss}}} e^{i2kL}} \approx -\frac{\mathcal{F}}{\pi} \left[\frac{-r_1 + r_2 (r_1^2 + t_1^2) (1 - \mathcal{L}_{\text{RT}})}{\sqrt{r_1 r_2}} \right] \quad (73)$$

we know that $t_1^2 \ll r_1^2$:

$$r_{\text{FP}} \approx -\frac{\mathcal{F}}{\pi} \left[\frac{r_1(-1 + (1 - \pi/\mathcal{F})(1 - \mathcal{L}_{\text{RT}}))}{\sqrt{r_1 r_2}} \right] \approx -\left(\frac{r_1}{r_2}\right)^{1/2} \frac{\mathcal{F}}{\pi} \left[-\pi/\mathcal{F} - \mathcal{L}_{\text{RT}} + (\mathcal{L}_{\text{RT}}\pi)/\mathcal{F} \right] \quad (74)$$

And $\mathcal{L}_{\text{RT}} \ll 1$ with $r_1/r_2 \approx 1$ we get:

$$r_{\text{FP}} \approx -1 + \frac{\mathcal{F}}{\pi} \mathcal{L}_{\text{RT}} \quad (75)$$

If we're operating at a dark fringe, at the symmetric port we see superimposed fields:

$$E_{\text{SYM}} = \frac{E_i}{2} \left[r_{\text{FPX}} e^{2ik_x} + r_{\text{FPY}} e^{2ik_y} \right] \quad (76)$$

Where we assume that the short Michelson arms and reflection coefficients are roughly equal ($x = y$, $r_{\text{FPX}} = r_{\text{FPY}}$)

We also can average the short Michelson arm lengths $(x + y)/2$ such that the effective reflection coefficient is: $r_{\text{FPMI}} = e^{2ik}(-1 + \frac{\mathcal{F}}{\pi} \mathcal{L}_{\text{RT}})$ Knowing this we create the following expression for the circulating power within the cavity:

$$P_{\text{PRC}} = \frac{|t_{\text{PRM}}|^2}{|1 - r_{\text{PRM}} r_{\text{FPMI}} e^{2ik(L_{\text{PRC}2\text{BS}} + L_{\text{SMICH}})}|^2} P_{\text{in}} \quad (77)$$

where $|t_{\text{PRM}}|^2 = 1 - |r_{\text{PRM}}|^2$ and given a carrier resonance condition we want to maximize the power with a variable PRM reflectivity:

$$\frac{\partial P_{\text{PRC}}}{\partial r_{\text{PRM}}} = \frac{2r_{\text{PRM}}^2(r_{\text{FPMI}} - r_{\text{PRM}})}{(1 - r_{\text{PRM}} r_{\text{FPMI}})^3} = 0 \quad (78)$$

which sets $r_{\text{PRM}} = r_{\text{FPMI}}$ On resonance, the power recycling gain ($G_{\text{PR}} = \frac{P_{\text{PRC}}}{P_{\text{in}}}$):

$$G_{\text{PR}} = \frac{\pi}{2\mathcal{F}\mathcal{L}_{\text{RT}}} \left[\frac{1}{1 - \frac{\mathcal{F}\mathcal{L}_{\text{RT}}}{2\pi}} \right] \quad (79)$$

$$1 \left[r_{\text{FPMI}} = -r_1 + (\mathcal{L}_{\text{RT}} r_1 r_2) / (1 - r_1 r_2) \right]$$

```

2 T_PRM = .03
3 R_PRM = 1-T_PRM
4 t_PRM = (T_PRM)**.5
5 r_PRM = (R_PRM)**.5
6 G_PRC = 1/(1-r_PRM*(r_FPMI))

1 L_rt = 75e-6
2 Finn = (np.pi*np.sqrt(r_1*r_2))/(1-r_1*r_2)
3 print(Finn)

1 444.0741558169753

1 r_FPMI_approx = (1 - Finn*L_rt/np.pi)

1 r_range = np.arange(.9,1,1/(2**16))

1 G_PRC_ = ifco.PRG(L_rt, Finn, r_range, max=0)

1 G_PRC_opt = ifco.PRG(L_rt, Finn, r_FPMI, max=1)

1 plt.plot(r_range, G_PRC_, linewidth=line_width)
2 plt.axhline(G_PRC_opt, linestyle='--',linewidth=line_width, color='r')
3 plt.xlim(r_range[0], r_range[-1])
4 plt.xlabel('$\mathdefault{r_{PRM}}$ [arb]')
5 plt.ylabel('$\mathdefault{G_{PRC}}$ [arb]')

1 Text(0, 0.5, '$\mathdefault{G_{PRC}}$ [arb]')

1 G_PRC_actual = ifco.PRG(L_rt, Finn, r_PRM, max=1)

1 H_FPMI = ifco.fpml_freq_resp(nu, r_1, t_1, r_2, L, PHI_0, P_IN, OMEG)
2 H_FPMI_LP = ifco.fpml_freq_resp(nu, r_1, t_1, r_2, L, PHI_0, P_IN, OMEG,
3 low_pass='True')

1 H_PRFPMI = ((G_PRC_actual)**.5)*H_FPMI

```

We estimate the FP's pole frequency

$$1 - r_1 r_2 e^{-2i\omega_g L/c} = 0 \quad (80)$$

therefore when:

$$e^{-i\omega_g L/c} = \frac{1}{\sqrt{r_1 r_2}} \quad (81)$$

we acquire the pole frequency ω_{pole} as indicated in the low pass

$$f_{\text{pole}} = \frac{1}{4\pi\tau_s} = \frac{c}{4\pi L} \frac{1 - r_1 r_2}{\sqrt{r_1 r_2}} = \frac{\nu_{\text{FSR}}}{2\pi} \frac{1 - r_1 r_2}{\sqrt{r_1 r_2}} = \frac{\nu_{\text{FSR}}}{\mathcal{F}} \quad (82)$$

Might as well compare it to our Michelson response:

$$H_{\text{MI}}(\omega_g) = \frac{2L\Omega}{c} e^{-iL\omega/c} \frac{\sin(L\omega/c)}{L\omega/c} \quad (83)$$

```

1 H_MI = ifco.mich_freq_resp(nu, L, PHI_0, P_IN, OMEG)
1 plt.loglog(nu, ifco.bode_amp(H_MI), label= 'MICH', linewidth= line_width, alpha=.3)
2 plt.loglog(nu, ifco.bode_amp(H_FPFI), label='FPFI', linewidth=line_width, alpha=.3)
3 plt.loglog(nu, ifco.bode_amp(H_PRFPFI), label='PRFPFI', linewidth = line_width)
4 plt.xlim([1e0, 1e5])
5 plt.ylim([1e9,2e15])
6 plt.xlabel('frequency [Hz]')
7 plt.ylabel('H(f) [W/m]')
8 lgd=plt.legend()
9 plt.savefig('../figs/INTRO/prfpfi_fr.pdf', dpi=300, bbox_inches='tight')

1 plt.semilogx(nu,(180/np.pi)*np.arctan(np.imag(H_FPFI)/np.real(H_FPFI)), '---',
2             linewidth=line_width)
3 plt.semilogx(nu,(180/np.pi)*np.arctan(np.imag(H_MI)/np.real(H_MI)), '---',
4             linewidth=line_width)
5 plt.semilogx(nu,(180/np.pi)*np.arctan(np.imag(H_PRFPFI)/np.real(H_PRFPFI)),
6             linestyle='---', linewidth=line_width,dashes=(3,10))
7 plt.xlim([1,100000])
8 plt.ylabel('phase [deg]')
9 plt.xlabel('Frequency [Hz]')

1 Text(0.5, 0, 'Frequency [Hz]')
```

SIGNAL RECYCLING

Initially not used in early iterations of LIGO (initial LIGO and enhanced LIGO) signal recycling imagines using a partially reflective mirror at the anti-symmetric port. And at first glance it seems to not very much make sense to have a mirror at detector output as you would potentially attenuate gravitational wave signals by said mirror reflection coefficient.

While true, it is important to analyze the multi-state configurations offered by such a mirror with various microscopic length tuning configurations. What do I mean by this? Well, it helps to start imagining by analogy of couple cavity relationship as established in the power recycling discussion. The relationship of the differential signal output of the PRFPMI with respect to the newly placed mirror at the anti-symmetric port is represented by the following:

$$t_{\text{SRC}} = \frac{t_{\text{ITM}}t_{\text{SRM}}e^{i(k+\Omega/c)_{\text{SRC}}}}{1 - r_{\text{ITM}}r_{\text{SRM}}e^{2i(k+\Omega/c)_{\text{SRC}}}} \quad (84)$$

$$r_{\text{SRC}} = \frac{r_{\text{ITM}} - r_{\text{SRM}}e^{2i(k+\Omega/c)_{\text{SRC}}}}{1 - r_{\text{ITM}}r_{\text{SRM}}e^{2i(k+\Omega/c)_{\text{SRC}}}} \quad (85)$$

as $k \gg \Omega_{\text{gw}}/c$ for $1 < \Omega_{\text{gw}} < 5 \cdot 10^3$

Therefore with a pre-defined $T_{\text{ITM}} + R_{\text{ITM}} + L_{\text{ITM}} = 1$ the coupled cavity pole AND gain is a function of the SRM reflectivity and microscopic length tuning:

$$t_{\text{SRC}} = \frac{t_{\text{ITM}}t_{\text{SRM}}e^{ik_{\text{SRC}}}}{1 - r_{\text{ITM}}r_{\text{SRM}}e^{2ik_{\text{SRC}}}} \quad (86)$$

$$r_{\text{SRC}} = \frac{r_{\text{ITM}} - r_{\text{SRM}}e^{2ik_{\text{SRC}}}}{1 - r_{\text{ITM}}r_{\text{SRM}}e^{2ik_{\text{SRC}}}} \quad (87)$$

We now observe the tuning extrema: - On resonance $2ik_{\text{SRC}} = 2i\phi_{\text{SRC}} = 0$:

$$r_{\text{SRC}, \phi_{\text{SRC}}=0} = \frac{r_{\text{ITM}} - r_{\text{SRM}}}{1 - r_{\text{ITM}}r_{\text{SRM}}} \quad (88)$$

- On resonance $2ik_{\text{SRC}} = 2i\phi_{\text{SRC}} = \frac{\pi}{2}$:

$$r_{\text{SRC}, \phi_{\text{SRC}}=\pi} = \frac{r_{\text{ITM}} + r_{\text{SRM}}}{1 + r_{\text{ITM}}r_{\text{SRM}}} \quad (89)$$

$$H_{\text{DRFPMI}} = G_{\text{PR}}P_{\text{in}}L\Omega \left[\frac{t_{\text{ITM}}^2 r_{\text{ETM}}}{(t_{\text{ITM}}^2 + r_{\text{ITM}}^2)r_{\text{ETM}} - r_{\text{ITM}}} \frac{t_{\text{SRM}}t_{\text{ITM}}e^{i\phi_{\text{SRC}}}}{1 - r_{\text{ITM}}r_{\text{SRM}}e^{i2\phi_{\text{SRC}}}} \times \frac{e^{-i2\pi Lf/c} \sin(2\pi f/c)}{2\pi Lf} \times \frac{\sin(\phi_0)}{1 - [(r_{\text{ITM}} - r_{\text{SRM}}e^{i2\phi_{\text{SRC}}})/(1 - r_{\text{ITM}}r_{\text{SRM}}e^{i2\phi_{\text{SRC}}})]r_{\text{ETM}}e^{-i4\pi Lf/c}} \right]$$

```

1 L_SRC = 56 #[m]
2 T_SRM = .30
3 R_SRM = 1-T_SRM
4 t_SRM = T_SRM**.5
5 r_SRM = R_SRM**.5
6 phi_SRC = np.pi

1 H_DRFPMI = ifco.drfpmi_freq_resp(nu, G_PRC_opt, r_1, t_1, r_2, r_SRM, t_SRM,
2 phi_SRC, L, PHI_0, P_IN, OMEG)

1 bode_test=False
2 if bode_test:
3     fig, ax1 = plt.subplots()
4     ax1.set_xlabel('frequency [Hz]')
5     ax1.set_ylabel('H$_{\text{DRFPMI}}$ [W/m]', color='C0')
6     ax1.loglog(nu, ifco.bode_amp(H_FPMI), label='FPMI', linewidth=line_width,
7               linestyle=':', color='C0')
8     ax1.loglog(nu, ifco.bode_amp(H_PRFPMI), label='PRFPMI',
9               linewidth=line_width, color='C0')
10    ax1.loglog(nu, ifco.bode_amp(H_DRFPMI), label='DRFPMI',
11              linewidth=line_width, color='C1')
12    ax1.legend()
13    ax2 = ax1.twinx()
14    ax2.semilogx(nu, ifco.bode_ph(H_FPMI), '--', linewidth=7.5, color='C0', alpha=.3)
15    ax2.semilogx(nu, ifco.bode_ph(H_DRFPMI), '--', linewidth=7.5, color='C1', alpha=.3)
16    ax2.grid(b=False, which='both', axis='y')
```

```

17 plt.xlim([1,1e5])
18 plt.ylabel('phase [deg]', color='C1', alpha=.5)

```

```

1 plt.loglog(nu, ifco.bode_amp(H_MI), label= 'MICH', linewidth= line_width, alpha=.4)
2 plt.loglog(nu, ifco.bode_amp(H_FPFI), label='FPFI', linewidth=line_width, alpha=.4)
3 plt.loglog(nu, ifco.bode_amp(H_PRFPFI), label='PRFPFI', linewidth = line_width,
4           alpha=.4)
5 plt.loglog(nu, ifco.bode_amp(H_DRFPFI), label='DRFPFI', linewidth = line_width)
6 plt.xlim([1e0, 1e5])
7 plt.ylim([1e9, 2e15])
8 plt.xlabel('frequency [Hz]')
9 plt.ylabel('H(f) [ $\text{W/m}$ ]')
10 lgd=plt.legend()
11 plt.savefig('../figs/INTRO/drfpfi_fr.pdf', dpi=300, bbox_inches='tight')

```

```

1 plt.semilogx(nu,ifco.bode_ph(H_MI), '--', linewidth=line_width,
2             alpha=.4, label='MICH')
3 plt.semilogx(nu,ifco.bode_ph(H_FPFI),'--', linewidth=line_width,
4             alpha=.4, label='FPFI')
5 plt.semilogx(nu,ifco.bode_ph(H_PRFPFI),linestyle='--',
6             linewidth=line_width,dashes=(3,10), alpha=.4, label='PRFPFI')
7 plt.semilogx(nu,ifco.bode_ph(H_DRFPFI),'--', linewidth=line_width, label='DRFPFI')
8 plt.xlim([1,100000])
9 plt.ylim([-91,91])
10 plt.ylabel('phase [deg]')
11 plt.xlabel('Frequency [Hz]')
12 plt.legend()

```

```

1 Sn = ifco.N_shot(OMEG, P_IN)

```

```

1 plt.loglog(nu, Sn/ifco.bode_amp(H_MI), label= 'MICH', linewidth=line_width)
2 plt.loglog(nu, Sn/ifco.bode_amp(H_FPFI), label='FPFI', linewidth=line_width)
3 plt.loglog(nu, Sn/ifco.bode_amp(H_PRFPFI), label='PRFPFI', linewidth=line_width)
4 plt.loglog(nu, Sn/ifco.bode_amp(H_DRFPFI), label='DRFPFI', linewidth=line_width)
5 plt.ylim([1e-24,2e-19])
6 plt.xlim([1e0, 1e5])
7 plt.xlabel('frequency [Hz]')
8 plt.ylabel('$\mathdefault{[ 1 / \sqrt{\mathdefault{Hz}}]}$')
9 lgd=plt.legend()

```

```
10 plt.savefig('../figs/INTRO/strain_compare.pdf', dpi=300, bbox_inches='tight')
```

M RH control pre-filter

M.1 recipe

The following is a brief recipe to build a filter that can better optimize the RH thermo-optic response:

1. Fit step response to a zpk filter $H(s)$ (see Figure 2.5)
2. Invert fitted filter ($H(s) \rightarrow H^{-1}(s)$)

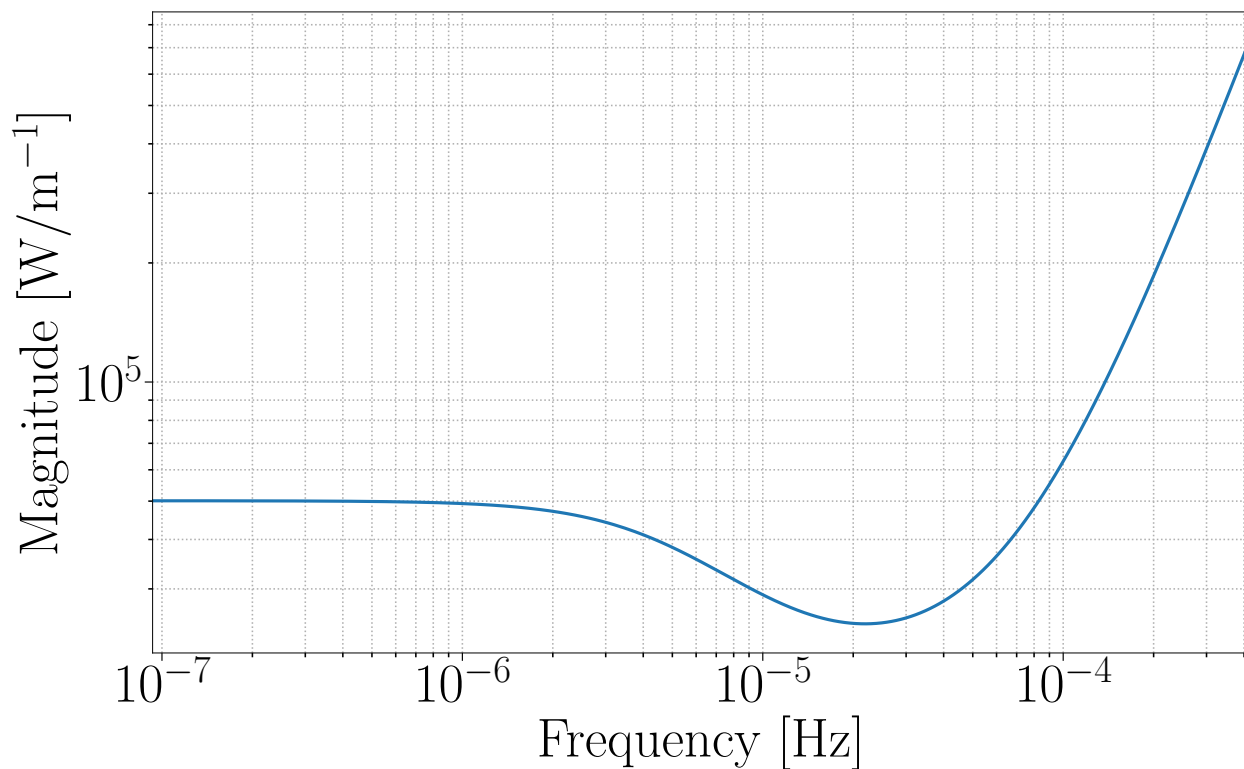


Figure 8: Fitted zpk filter, inverted.

3. Apply correction filter $G(s)$ for stability and speed tuning ($H^{-1}(s) * G(s)$)

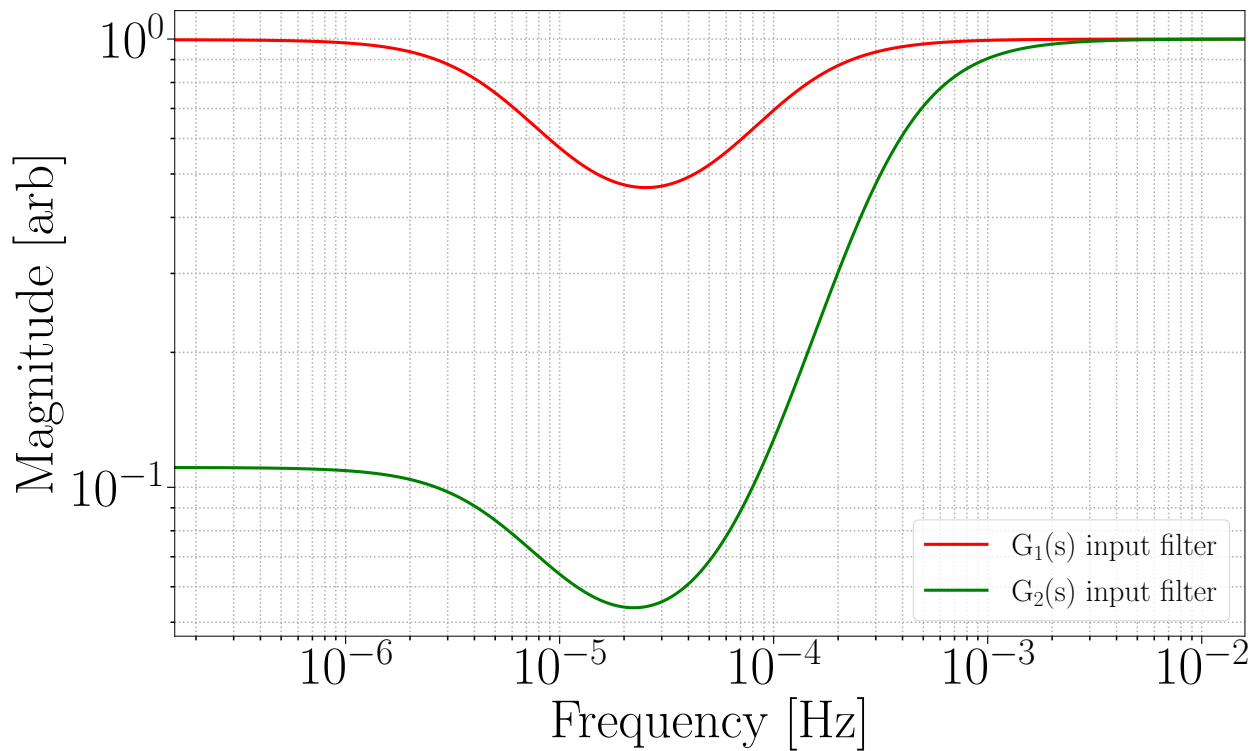


Figure 9: Fitted zpk filter to transient response of self heating COMSOL model.

M.2 code

```

1 import matplotlib
2 import matplotlib.pyplot as plt
3 import numpy as np
4 from scipy import signal
5 import h5py
6 import os
7
8 plt_style_dir = '../..../my_python/matplotlib/stylelib/'
9 if os.path.isdir(plt_style_dir) == True:
10     plt.style.use(plt_style_dir + 'ppt2latex')
11 plt.rcParams["font.family"] = "Times New Roman"

```

```

1 # Establish default color array
2 prop_cycle = plt.rcParams['axes.prop_cycle']
3 colors = prop_cycle.by_key()['color']
4 lin_thickness=4

```

```

1  ## Set figure saving directory
2  thesis_dir = '../doc/figures/python/'
3  thesis_dir='../dissertation/figs/TCS/IRHF/'

```

Generating / plotting plant filter

```

1  ITMYRH_data = np.loadtxt('../data/ITMY_trend_10min_int_longer.dat')
2  t = np.arange(0, len(ITMYRH_data[:,0][2:])*60.0*10.0
3  normalize = 3.13
4  print(len(t))
5  data_in = ITMYRH_data[:,1][2:]
6  b, a = signal.butter(2, .2)
7  data_new = data_in
8  plt.figure()
9  ir = (data_new[1:] - data_new[:-1])/normalize
10 ir_new = ir
11 fig1 = plt.figure(figsize=(13,10))
12 plt.plot(t, data_new, label='Step response', linewidth=lin_thickness)
13 plt.xlabel('time [s]')
14 plt.ylabel('Defocus [m-1 $]')
15 plt.show()
16
17 Fs = 1/(t[2]-t[1])
18
19 [F,H]=signal.freqz(ir_new,1, worN=3000,whole=False)
20 fig2 = plt.figure(figsize=(13,10))
21 plt.loglog(F*Fs/(2*np.pi), abs(H), label='Plant filter', linewidth=lin_thickness)
22 plt.ylabel('Magnitude [m-1 $/W]')
23 plt.xlabel('Frequency [Hz]')
24 plt.legend()
25 plt.show()
26
27 print(max(ir_new))

```

```

1  adj_data = data_new + abs(min(data_new))
2  mod_data = np.concatenate([np.zeros((10,)), adj_data])
3  mod_t = np.arange(0, len(mod_data))*60.0*10.0/(3600)
4  mod_rh_inp = np.concatenate([np.ones((10,))*3.13, np.zeros(adj_data.shape)])

```

```

1 fig, ax1 = plt.subplots()
2
3 ax1.set_xlabel('time [hr]')
4 ax1.set_ylabel('Primary-axis')
5 ax1.plot(mod_t, mod_rh_inp,'--',linewidth=lin_thickness, color = colors[0])
6 ax1.tick_params(axis='y', labelcolor=colors[0])
7 ax1.set_ylabel('RH power [W]', color=colors[0])
8 ax1.minorticks_off()
9 ax1.set_xlim([0,mod_t[-1]])
10 ax1.set_ylim([-0.01,4])
11
12 ax2 = ax1.twinx()
13 ax2.plot(mod_t, mod_data,linewidth=lin_thickness, color = colors[1])
14 ax2.set_ylabel('Defocus [m$^{-1}$]',color= colors[1])
15 ax2.set_xlim([0,mod_t[-1]])
16 ax2.tick_params(axis='y', labelcolor=colors[1])
17 ax2.ticklabel_format(style='sci', axis='y',scilimits=(0,-5))
18
19 ax2.set_ylim([-0.003e-4,1.2e-4])
20
21 fig.savefig(thesis_dir + 'Meas_response.pdf', dpi=300, format='pdf', bbox_inches='tight')

```

```

1 print('Only plots up to the nyquist frequency: {} Hz'.format(F[-1]*Fs/(2*np.pi)))

```

```

1 Only plots up to the nyquist frequency: 0.000833055555555556 Hz

```

```

1 zeros = 5.0e-6
2 fit_zeros = -2.0*np.pi*zeros
3 poles = np.array([1.3e-5, 5.0e-5 ,9.5e-5])
4 fit_poles = -2.0*np.pi*poles
5
6 k = 1 #This gain is not initally correct
7
8 s1 = signal.ZerosPolesGain(fit_zeros, fit_poles, k)
9 F_2, H_2 = signal.freqresp(s1, F*(Fs/2.0))
10
11 k_new = abs(H[0])/abs(H_2[0])
12

```

```

13 plt.loglog(F_2/(2*np.pi), abs(H_2)*k_new, label='Fitted zpk filter',linewidth=lin_thickness)
14 plt.loglog(F/(2*np.pi)*Fs, abs(H), label='Measured (step response) filter',
15     linewidth=lin_thickness)
16 plt.ylabel('Magnitude [W/m$^{-1}$]')
17 plt.xlabel('Frequency [Hz]')
18 plt.legend()
19 plt.xlim([0,(F[-1]/(2*np.pi)*Fs)])
20 print(k_new) #Spit out the new gain
21
22 model_zpk = signal.ZerosPolesGain(fit_zeros, fit_poles,k_new)
23
24 plt.savefig(thesis_dir+'RH_plant_filter_fit.pdf',bbox_inches = 'tight')

```

```
1 model_zpk
```

```

1 ZerosPolesGainContinuous(
2 array([-3.14159265e-05]),
3 array([-8.16814090e-05, -3.14159265e-04, -5.96902604e-04]),
4 9.729529652779821e-12,
5 dt: None
6 )

```

Now to invert the plant filter (just swapping the poles and the zeros and inverting gain)

($H^{-1}(s)$)

```

1 inv_model = signal.ZerosPolesGain(fit_poles, fit_zeros,1/k_new)
2 F_3, H_3 = signal.freqresp(inv_model, F*(Fs/2.0))
3 fig4 = plt.figure()
4 plt.loglog(F_3/(2*np.pi), abs(H_3), label='Fitted zpk Filter',linewidth=lin_thickness)
5 plt.ylabel('Magnitude [W/m$^{-1}$]')
6 plt.xlabel('Frequency [Hz]')
7 plt.xlim([0, F_3[-1]/(2*np.pi)])
8 plt.savefig(thesis_dir+'RH_inv_filt.pdf',bbox_inches = 'tight')

```

Stabilize the high frequencies to DC (Generating $H^{-1}(s) * G_n(s)$)

Will also attempt to reduce the time constant

```

1 Hinv_G_1_filt = signal.ZerosPolesGain(fit_poles, [fit_zeros,-2.0*np.pi*.0001113129672, -2.0*np.pi*.
2     0001113129672],1)
3 pole_shift = 3

```

```

4 Hinv_G_2_filt = signal.ZerosPolesGain(fit_poles, [fit_zeros,-2.0*np.pi*.0001113129672*pole_shift,
5     -2.0*np.pi*.0001113129672*pole_shift],1)
6
7 ## Plotting
8 freq = np.arange(10e-7,10e-2,1e-7)
9 F_4, H_4 = signal.freqresp(Hinv_G_1_filt,freq)
10 F_5, H_5 = signal.freqresp(Hinv_G_2_filt,freq)
11
12 fig5= plt.figure()
13 plt.loglog(F_4/(2*np.pi), abs(H_4), label='RH input filter',linewidth=lin_thickness)
14 plt.xlim([F_4[0]/(2*np.pi),F_4[-1]/(2*np.pi)])
15 plt.ylabel('Magnitude [arb]')
16 plt.xlabel('Frequency [Hz]')
17
18 plt.savefig(thesis_dir+'RH_input_filt.pdf',bbox_inches='tight')

```

```
1 Hinv_G_1_filt
```

```

1 ZerosPolesGainContinuous(
2 array([-8.16814090e-05, -3.14159265e-04, -5.96902604e-04]),
3 array([-3.14159265e-05, -6.99400000e-04, -6.99400000e-04]),
4 1,
5 dt: None
6 )

```

```
1 Hinv_G_2_filt
```

```

1 ZerosPolesGainContinuous(
2 array([-8.16814090e-05, -3.14159265e-04, -5.96902604e-04]),
3 array([-3.14159265e-05, -2.09820000e-03, -2.09820000e-03]),
4 1,
5 dt: None
6 )

```

```

1 fig79= plt.figure()
2 plt.loglog(F_4/(2*np.pi), abs(H_4), label='G$1$(s) input filter',linewidth=lin_thickness)
3 plt.loglog(F_5/(2*np.pi), abs(H_5), label='G$2$(s) input filter',linewidth=lin_thickness)
4 plt.legend()
5 plt.xlim([F_4[0]/(2*np.pi),F_4[-1]/(2*np.pi)])
6 plt.ylabel('Magnitude [arb]')

```

```

7 plt.xlabel('Frequency [Hz]')
8
9 plt.savefig(thesis_dir+'RH_input_filt_G1_G2.pdf',bbox_inches='tight')

```

COMSOL self heating filter

Import COMSOL self heating data

```

1 COM_data = np.loadtxt('../data/1W_self_heating_defocus_doublepass.txt')
2 t_com = COM_data[:,0]*3600
3 defocus = COM_data[:,1]/max(COM_data[:,1])

```

```

1 fig6 = plt.figure()
2 plt.plot(t_com/3600,defocus,linewidth=lin_thickness)
3 plt.title('COMSOL self heating time series')
4 plt.xlabel('time [hrs]')
5 plt.ylabel('defocus [arb]')
6 max(defocus)

```

```

1 ir_com = (defocus[1:] - defocus[:-1])
2 t_ir = t_com[:,(len(t_com)-1)]

```

```

1 [F_ir,H_ir]=signal.freqz(ir_com, 1, worN=3000,whole=False)
2 Fs_com =1/(t_com[1]-t_com[0])

```

```

1 zeros_com = np.array([.9e-3,.3e-3])
2 fit_zeros_com = -2.0*np.pi*zeros_com
3 poles_com = np.array([.25e-3,.25e-3,1.6e-3])
4 fit_poles_com = -2.0*np.pi*poles_com
5
6 k_com = 1 #This gain is not initally correct
7
8 zpk_com = signal.ZerosPolesGain(fit_zeros_com, fit_poles_com, k_com)
9 F_com, H_com = signal.freqresp(zpk_com, F_ir*(Fs_com/2.0))
10 k_new_com = abs(H_ir[0])/abs(H_ir[0]*H_com[0])
11
12 fig6 = plt.figure()
13 plt.loglog(F_com/(2*np.pi), abs(H_com)*k_new_com, label='Fitted zpk Filter',
14           linewidth=lin_thickness)
15 plt.loglog(F_ir*Fs_com/(2*np.pi), abs(H_ir)/abs(H_ir[0]), label='Plant filter',
16           linewidth=lin_thickness)

```

```

17 plt.ylabel('Magnitude [arb]')
18 plt.xlabel('Frequency [Hz]')
19 plt.title('Self Heating filter')

1 G_2 = signal.ZerosPolesGain(fit_zeros_com, fit_poles_com, k_new_com)
2 unit_step_testing = np.zeros(np.shape(t_com))
3 unit_step_testing[t_com>0] = 1
4 [ _,y_self_test, _] = signal.lsim(G_2, unit_step_testing, t_com)

1 fig7= plt.figure()
2 plt.plot(t_com/3600,defocus,label='measured',linewidth=lin_thickness)
3 plt.plot(t_com/3600,y_self_test,label='fit',linewidth=lin_thickness)
4 plt.title('Self heating time series (fit vs measured)')
5 plt.legend()

```

Generating time series

Step input time series

```

1 unit_step = np.zeros((t.shape[0]*30))
2 t_new = np.arange(0,len(unit_step))*60.0*1.0
3 ## Generating simulated response
4 unit_step[t_new>9000] = 1
5 [t_mod_new,y_mod_sim,xout] = signal.lsim(model_zpk, unit_step, t_new)

```

Conditioned input time series

```

1 unit_step2 = np.zeros((t.shape[0]*30))
2 unit_step2[t_new>(9000)] = pole_shift**2
3
4 [ _,y_inp_inv_L, _] = signal.lsim(Hinv_G_2_filt, unit_step2, t_new)
5 [ _,y_inp_inv_H, _] = signal.lsim(Hinv_G_1_filt, unit_step, t_new)
6 [ _,y_mod_sim_inv_L, _] = signal.lsim(model_zpk, y_inp_inv_L, t_new)
7 [ _,y_mod_sim_inv_H, _] = signal.lsim(model_zpk, y_inp_inv_H, t_new)

```

Self heating time series

```

1 unit_step3 = np.zeros((t.shape[0]*30))
2 t_offset =0
3 unit_step3[t_new>(9000+t_offset)] = 1

```

```
1 [-, y_sh_resp, -] = signal.lsim(G_2, unit_step3, t_new)
```

Basic Performance

```
1 fig = plt.figure()
2 plt.subplot(211)
3 plt.plot(t_new/3600, unit_step, linewidth = lin_thickness, label='RH step input')
4 plt.plot(t_new/3600, y_inp_inv_H, '--', linewidth = lin_thickness,
5         color = 'red', label='RH filtered input')
6 plt.ylabel('RH power [W]')
7 plt.legend()
8 plt.xlim([0, t_new[-1]/3600])
9 plt.subplot(212)
10 plt.plot(t_new/3600, -y_mod_sim, linewidth = lin_thickness, label = 'RH step input')
11 plt.plot(t_new/3600, -y_mod_sim_inv_H, '--', linewidth = lin_thickness,
12         color='red', label = 'RH filtered input')
13 plt.ylabel('Defocus [m-1]'')
14 plt.xlabel('time [hr]')
15 plt.xlim([0, t_new[-1]/3600])
16 plt.ticklabel_format(style='sci', axis='y', scilimits=(0, -5))
17 fig.savefig(thesis_dir+'IRHF_step_vs_filt_step.pdf', bbox_inches='tight')
```

All curves together

```
1 fig = plt.figure()
2 plt.subplot(211)
3 plt.plot(t_new/3600, unit_step, linewidth = lin_thickness, label='RH unfiltered step input')
4 plt.plot(t_new/3600, y_inp_inv_L, '--', linewidth = lin_thickness, color = 'green',
5         label='RH conditioned input (G1(s))')
6 plt.plot(t_new/3600, y_inp_inv_H, '--', linewidth = lin_thickness, color = 'red',
7         label='RH conditioned input (G2(s))')
8 plt.ylabel('RH power [W]')
9 plt.title('RH filtered response w/ self-heating')
10 plt.legend(fontsize='medium')
11 plt.xlim([0, 20])
12 plt.subplot(212)
13 plt.plot(t_new/3600, -y_mod_sim, linewidth = lin_thickness, label = 'RH unfiltered step input')
14 plt.plot(t_new/3600, y_sh_resp*20e-6, linewidth = lin_thickness, color='orange',
15         label = 'self heating')
```

```

16 plt.plot(t_new/3600,-y_mod_sim_inv_L,'--', linewidth = lin_thickness,color='green',
17         label = 'RH conditioned input (G$_{1}$$(s))')
18 plt.plot(t_new/3600,-y_mod_sim_inv_H,'--', linewidth = lin_thickness,color='red',
19         label = 'RH conditioned input (G$_{2}$$(s))')
20 plt.plot(t_new/3600,y_sh_resp*20e-6 -y_mod_sim_inv_L,linewidth = lin_thickness,
21         label='self heating + RH conditioned input (G$_{1}$$(s)',color='purple')
22 plt.plot(t_new/3600,y_sh_resp*20e-6 -y_mod_sim_inv_H,linewidth = lin_thickness,
23         label='self heating + RH conditioned input (G$_{2}$$(s))',color='magenta')
24 plt.ylabel('Defocus [m$^{-1}$]')
25 plt.xlabel('time [hr]')
26 plt.legend(fontsize='medium')
27 plt.xlim([0,20])
28 fig.savefig(thesis_dir+'IRHF_compare_self_w_filter_compare.pdf',bbox_inches='tight')

```

```

1 fig8 = plt.figure()
2 plt.rc('font', size=25)
3 plt.plot(t_new/3600,y_sh_resp*20e-6, linewidth = lin_thickness,color='orange',
4         label = 'self heating with no RH')
5 plt.plot(t_new/3600,y_sh_resp*20e-6 -y_mod_sim,linewidth = lin_thickness,
6         label='self heating + RH unfiltered input',color='purple')
7 plt.plot(t_new/3600,y_sh_resp*20e-6 -y_mod_sim_inv_H,'--',linewidth = lin_thickness,
8         label='self heating + RH filtered input (H$^{-1}$$(s)*G$_{1}$$(s))',color='red')
9 plt.plot(t_new/3600,y_sh_resp*20e-6 -y_mod_sim_inv_L,'--',linewidth = lin_thickness,
10        label='self heating + RH filtered input (H$^{-1}$$(s)*G$_{2}$$(s))',color='green')
11 plt.ylabel('Defocus [m$^{-1}$]')
12 plt.xlabel('time [hr]')
13 plt.ticklabel_format(style='sci', axis='y',scilimits=(0,-5))
14 plt.xlim([0,20])
15 plt.legend(loc='upper right',bbox_to_anchor=(1.0,.95))
16 fig8.savefig(thesis_dir+'IRHF_compare_w_self.pdf',bbox_inches='tight')

```

Set RH upper limit

```

1 upper_lim = np.ones(np.shape(t_new))*40

```

```

1 fig9= plt.figure(figsize=(25,20))
2 plt.rc('font', size=30)
3 plt.subplot(211)
4 plt.plot(t_new/3600, unit_step,linewidth = lin_thickness,

```

```

5     label='Step input', color= 'purple')
6 plt.plot(t_new/3600, y_inp_inv_L,'--', linewidth = lin_thickness, color = 'green',
7     label='Filtered input')
8 plt.ylabel('RH power [W]')
9 plt.xlim([0,20])
10 plt.legend(fontsize='large')
11 plt.subplot(212)
12 plt.ylabel('Defocus [m$^{-1}$]')
13 plt.plot(t_new/3600,y_sh_resp*20e-6, linewidth = lin_thickness,color='orange',
14     label = 'central heating with no RH')
15 plt.plot(t_new/3600,(y_sh_resp*20e-6 -y_mod_sim),linewidth = lin_thickness,
16     label='central heating + RH w/ step input',color='purple')
17 plt.plot(t_new/3600,(y_sh_resp*20e-6 -y_mod_sim_inv_L),'--',linewidth = lin_thickness,
18     label='central heating + RH w/ filtered input',color='green')
19 plt.xlabel('time [hr]')
20 plt.ticklabel_format(style='sci', axis='y',scilimits=(0,-5))
21 plt.legend(loc='upper right', bbox_to_anchor=(1.0,.95),fontsize='large')
22 plt.xlim([0,20])
23
24 fig9.savefig(thesis_dir+'IRHF_compare_filts_PI_paper.pdf',bbox_inches='tight')

```

```

1 fig9= plt.figure(figsize=(25,20))
2 plt.rc('font', size=30)
3 plt.subplot(211)
4 plt.plot(t_new/3600, unit_step,linewidth = lin_thickness,
5     label='Step input', color= 'purple')
6 plt.plot(t_new/3600, y_inp_inv_L,'--', linewidth = lin_thickness, color = 'green',
7     label='Filtered input(H$^{-1}$)(s)G$_{2}$ (s)')
8 plt.plot(t_new/3600, y_inp_inv_H,'--', linewidth = lin_thickness,color = 'red',
9     label='Filtered input (H$^{-1}$)(s)G$_{1}$ (s)')
10 plt.ylabel('RH power [W]')
11 plt.xlim([0,20])
12 plt.legend(fontsize='large')
13 plt.subplot(212)
14 plt.ylabel('Defocus [m$^{-1}$]')
15 plt.plot(t_new/3600,y_sh_resp*20e-6, linewidth = lin_thickness,color='orange',
16     label = 'self heating with no RH')
17 plt.plot(t_new/3600,(y_sh_resp*20e-6 -y_mod_sim),linewidth = lin_thickness,

```

```

18     label='self heating + RH w/ step input',color='purple')
19 plt.plot(t_new/3600,(y_sh_resp*20e-6-y_mod_sim_inv_L),'--',linewidth = lin_thickness,
20     color='green',label = 'Filtered input ( $H^{-1}(s)G_{-2}(s)$ )')
21 plt.plot(t_new/3600,(y_sh_resp*20e-6-y_mod_sim_inv_H),'--',linewidth = lin_thickness,
22     color='red',label = 'Filtered input ( $H^{-1}(s)G_{-1}(s)$ )')
23 plt.xlabel('time [hr]')
24 plt.ticklabel_format(style='sci', axis='y',scilimits=(0,-5))
25 plt.legend(loc='upper right', bbox_to_anchor=(1.0,.97),fontsize='large')
26 plt.xlim([0,20])
27
28 fig9.savefig(thesis_dir+'IRHF_compare_filts.pdf',bbox_inches='tight')
29 fig9.savefig(thesis_dir+'IRHF_compare_filts.pdf',bbox_inches='tight')

```

```

1 fig9= plt.figure(figsize=(17,15))
2 plt.rc('font', size=25)
3 plt.subplot(211)
4 plt.plot(t_new/3600, unit_step,linewidth = lin_thickness, color= 'purple',
5     label='Step input')
6 plt.plot(t_new/3600, y_inp_inv_L,'--', linewidth = lin_thickness, color = 'green',
7     label='Filtered input ( $H^{-1}(s)G_{-1}(s)$ )')
8 plt.plot(t_new/3600, y_inp_inv_H,'--', linewidth = lin_thickness,color = 'red',
9     label='Filtered input ( $H^{-1}(s)G_{-2}(s)$ )')
10 plt.ylabel('RH power [W]')
11 plt.xlim([0,t_new[-1]/3600])
12 plt.legend(fontsize='medium')
13 plt.subplot(212)
14 plt.ylabel('Defocus [ $m^{-1}$ ](s)')
15 plt.plot(t_new/3600,y_sh_resp*20e-6, linewidth = lin_thickness,color='orange',
16     label = 'self heating w/ no RH')
17 plt.plot(t_new/3600,y_sh_resp*20e-6 -y_mod_sim,linewidth = lin_thickness,
18     label='self heating + step input',color='purple')
19 plt.plot(t_new/3600,y_sh_resp*20e-6 -y_mod_sim_inv_L,'--',linewidth = lin_thickness,
20     label='self heating + filtered input ( $H^{-1}(s)G_{-1}(s)$ )',color='green')
21 plt.plot(t_new/3600,y_sh_resp*20e-6 -y_mod_sim_inv_H,'--',linewidth = lin_thickness,
22     label='self heating + filtered input ( $H^{-1}(s)G_{-2}(s)$ )',color='red')
23 plt.xlabel('time [hr]')
24 plt.xlim([0,t_new[-1]/3600])
25 plt.ticklabel_format(style='sci', axis='y',scilimits=(0,-5))

```

```

26 plt.legend(loc='upper right', bbox_to_anchor=(1.0,.97),fontsize='medium')
27
28 fig9.savefig(thesis_dir+'IRHF_compare_filts.pdf',bbox_inches='tight')

1 fig = plt.figure(figsize=(17,15))
2 plt.subplot(311)
3 plt.plot(t_new/3600, unit_step,linewidth = lin_thickness,
4         label='Unfiltered step input')
5 plt.plot(t_new/3600, y_inp_inv_L,'--', linewidth = lin_thickness, color = 'green',
6         label='Conditioned input (G$_{1}$$(s))')
7 plt.plot(t_new/3600, y_inp_inv_H,'--', linewidth = lin_thickness,color = 'red',
8         label='Conditioned input (G$_{1}$$(s))')
9 plt.ylabel('RH power [W]')
10 plt.legend(fontsize='small')
11 plt.subplot(312)
12 plt.ylabel('RH Defocus [m$^{-1}$]')
13 plt.plot(t_new/3600,-y_mod_sim, linewidth = lin_thickness,
14         label = 'Unfiltered step input')
15 plt.plot(t_new/3600,-y_mod_sim_inv_L,'--', linewidth = lin_thickness, color='green',
16         label = 'Conditioned input (G$_{2}$$(s))')
17 plt.plot(t_new/3600,-y_mod_sim_inv_H,'--', linewidth = lin_thickness, color='red',
18         label = 'Conditioned input (G$_{1}$$(s))')
19 plt.legend(fontsize='x-small',loc='upper right')
20 plt.subplot(313)
21 plt.plot(t_new/3600,y_sh_resp*20e-6, linewidth = lin_thickness,color='orange',
22         label = 'Self heating')
23 plt.plot(t_new/3600,y_sh_resp*20e-6 -y_mod_sim,linewidth = lin_thickness,
24         label='Self heating + RH unfiltered input',color='C0')
25 plt.plot(t_new/3600,y_sh_resp*20e-6 -y_mod_sim_inv_H,'--',linewidth = lin_thickness,
26         label='Self heating + RH conditioned input (G$_{1}$$(s))',color='red')
27 plt.plot(t_new/3600,y_sh_resp*20e-6 -y_mod_sim_inv_L,'--',linewidth = lin_thickness,
28         label='Self heating + RH conditioned input (G$_{2}$$(s))',color='green')
29 plt.ylabel('Total Defocus [m$^{-1}$]')
30 plt.xlabel('time [hr]')
31 plt.legend(fontsize='xx-small')
32 fig.savefig(thesis_dir+'IRHF_compare_all.pdf')

```

$G_1(s) \rightarrow$ The “response function”

For the above scenario we have the following G_s (a double pole low pass at $1.113e-4$)

```
G_1 = signal.ZerosPolesGain([], [-2.0np.pi.0001113129672, -2.0np.pi.0001113129672],1)
```

```
1 fig2 = plt.figure(figsize=(15,8))
2 plt.loglog(F_5/(2*np.pi), abs(H_5)*k_upd, label='G$_{1}$ (s)')
3 plt.loglog(F_com/(2*np.pi), abs(H_com)*k_new_com, label='G$_{2}$ (s)')
4 plt.ylabel('Magnitude [arb]')
5 plt.xlabel('Frequency [Hz]')
6 plt.title('G$_{1}$ vs. G$_{2}$')
7 plt.legend()
```

The Livingston filter is what we will construct here. To do that, we will first attempt multiplying $G_2(s)$ (the self heating response) to $H^{-1}(s)$

```
1 FILT_LIV_zeros= np.append(fit_zeros_com,fit_poles)
2 FILT_LIV_poles= np.append(fit_poles_com,fit_zeros)
3 FILT_LIV = signal.ZerosPolesGain(FILT_LIV_zeros, FILT_LIV_poles, 1)
4 _, H_G2 = signal.freqresp(FILT_LIV,np.arange(10e-7,10e-3,1e-7))
5 plt.loglog(np.arange(10e-7,10e-3,1e-7)/(2*np.pi), abs(H_G2)/abs(H_G2[0]))
```

Not enough zeros to set high frequency to unity gain (would be an unphysical without one more pole)

```
1 FILT_LIV_poles_2= np.append(FILT_LIV_poles,-0.00020951281288038756)
```

```
1 FILT_LIV = signal.ZerosPolesGain(FILT_LIV_zeros, FILT_LIV_poles_2, 1)
2 _, H_G2 = signal.freqresp(FILT_LIV,freq)
3 plt.loglog(freq/(2*np.pi), abs(H_G2)/abs(H_G2[0]))
```

```
1 [-,y_G2, _] = signal.lsim(FILT_LIV, unit_step, t_new)
```

```
1 [-,y_G2_time, _] = signal.lsim(model_zpk, y_G2, t_new)
```

```
1 fig = plt.figure(figsize=(17,10))
2 plt.subplot(211)
3 plt.plot(t_new/3600, unit_step,linewidth = lin_thickness,
4          label='RH step input')
5 plt.plot(t_new/3600, y_inp_inv,'--', linewidth = lin_thickness,
6          label='G$_{1}$')
```

```
7 plt.plot(t_new/3600,y_G2,'--', linewidth = lin_thickness,color='purple',
8         label = 'G$_{2}$')
9 plt.ylabel('RH power [W]')
10 plt.title('Comparison between RH inverted response with self heating')
11 plt.legend(fontsize='xx-large')
12 plt.subplot(212)
13 plt.plot(t_new/3600,-y_mod_sim, linewidth = lin_thickness,
14         label = 'RH step input')
15 plt.plot(t_new/3600,-y_sh_resp*20e-6, linewidth = lin_thickness,color='magenta',
16         label = 'self heating (negative)')
17 plt.plot(t_new/3600,-y_mod_sim_inv,'--', linewidth = lin_thickness,color='orange',
18         label = 'G$_{1}$')
19 plt.plot(t_new/3600,-y_G2_time,'--', linewidth = lin_thickness,color='purple',
20         label = 'G$_{2}$')
21 plt.ylabel('Defocus [m$^{-1}$]')
22 plt.xlabel('time [hr]')
23 plt.legend(fontsize='xx-large')
24 fig.savefig('G1_and_G2.pdf',bbox_inches='tight')
```

N LaplacE code

N.1 laplace.py

```

1 import numpy as np
2 import matplotlib.pyplot as plt
3 import h5py
4 from scipy.sparse import lil_matrix
5 from scipy.sparse import spdiags
6 import torch
7
8 # Computes Laplace's equation in cartesian and cylindrical coordinates
9 # For some related detailed documentation: Numerical recipies (3rd edition)
10 (Chapter 20 [Partial Differential Equations])
11
12 ## Initialize fields
13
14 def init_coords(pdct):
15     """
16     Looks at params file to start implementing coordinate choices for simulation
17     """
18     if pdct['coords'] == 'cylindrical':
19         if pdct['torch']:
20             i_rho = torch.arange(pdct['origin'][0],pdct['N'][0])
21             i_z = torch.arange(pdct['origin'][1],pdct['N'][1])
22             rho_ = i_rho*torch.tensor(pdct['res'][0])
23             z_ = i_z*torch.tensor(pdct['res'][1])
24             rho, z = torch.meshgrid(rho_, z_, indexing='ij')
25             invrho_ = 1/rho_
26             invrho_[0] = 0
27             invrho, z0 = torch.meshgrid(invrho_, z_, indexing='ij')
28
29         else:
30             i_rho = np.arange(pdct['origin'][0],pdct['N'][0])
31             i_z = np.arange(pdct['origin'][1],pdct['N'][1])
32             rho_ = i_rho*pdct['res'][0]
33             z_ = i_z*pdct['res'][1]

```

```

34     rho = (rho_ * np.ones((pdict['N'][0],1)))
35     rho = rho.reshape(pdict['N'][0]*pdict['N'][1],1)
36     z = (np.ones((pdict['N'][1],1)) * z_).T
37     z = z.reshape(pdict['N'][0]*pdict['N'][1],1)
38     invrho = 1/rho
39     invrho[rho==0] = 0 # addresses inf elements
40
41     coord_dict = {
42         'coords' : {
43             'rho' : rho, #np.round(rho,abs(int(np.log10(pdict['res']+[0])))),
44             'z' : z, #np.round(z,abs(int(np.log10(pdict['res']+[0])))),
45             'invrho' : invrho}, #np.round(invrho,abs(int(np.log10(pdict['res']+[0])))),
46         'indices' : {
47             'rho' : i_rho,
48             'z' : i_z}
49     }
50
51     #elif pdict['coords'] == 'cartesian':
52
53     return coord_dict
54
55 def indx(icoord1, icoord2, N):
56     """
57     formalized lambda function reshaping potential (vectorizing V):
58     indx = lambda i_rho, i_z : np.int32(i_rho + i_z*(N))
59     """
60     return np.int32(icoord1 + icoord2*N)
61
62 def idx_match(vec,N,step):
63     """
64     Acquire nearest matching ind(ex/ices) for queried location(s) in potential map
65     """
66     idx = np.int32(np.round(vec/step, decimals=0))
67     idx = 1 if idx<1 else N if idx>N else idx
68     return idx
69
70 def init_V(N):

```

```

71 """
72 Initialize (square) potential map
73 """
74 return np.zeros((N**2,1))
75
76
77 def build_lambda(i1, i2, N):
78     """
79     Constructs a matrix for a lambda function,
80     which operates on all available indices in the simulation.
81     Preallocates memory so that the indx function
82     doesn't need to be used twice (reducing computations).
83     """
84     LAMBD = np.array([indx(i, i2, N) for i in i1])
85
86     return LAMBD
87
88 def bc_set(pdict, BC, N, V):
89     """
90     Establishes simulation boundary conditions
91     """
92     #global R, d, step, indx, V, rho, z, bc0set
93
94     #Plate bcs
95     if pdict['coords'] == 'cylindrical':
96
97         #Setting up the edge boundaries (for faster convergence)
98         if not bc0set:
99             rho0 = False
100             rhoend = np.interp(np.arange(0,N), np.array([0,N-1]),
101                               np.array([pdict['back_plate']['voltage'],
102                                         pdict['front_plate']['voltage']])).reshape(N,1)
103             z0 = pdict['back_plate']['voltage']
104             zend = pdict['front_plate']['voltage']
105             edge_vals =np.array(rho0, rhoend, z0, zend)
106             V = bc_edge(pdict, edge_vals, V)
107             bc0set = True

```

```

108
109     #Set potentials
110     for i in range(BC['cont']):
111         V = set_pot(V,BC[i]['coords'],BC[i]['values'],LAMBD)
112
113     # exponential boundary conditions
114     V0 = 0
115     R0 = 1
116     V[idx(np.arange(0,N),N-1)] = V0 +
117         np.exp(-step/R0)*(V[idx(np.arange(0,N), N-2)]-V0)
118     V[idx(np.arange(0,N),0)] = V0 +
119         np.exp(-step/R0)*(V[idx(np.arange(0,N),1)]-V0)
120     V[idx(N-1,np.arange(0,N))]= V0 +
121         np.exp(-step/R0)*(V[idx(N-2, np.arange(0,N))]-V0)
122
123     return V
124
125 # Constructing the operator(s)
126
127 def build_lap(pdickt, LAMBD, i_rho):
128     """
129     constructs first order structure of the laplace operator
130     """
131     if pdickt['coords'] == 'cylindrical':
132
133         op_shape = (pdickt['N'][0]**2, pdickt['N'][1]**2)
134
135         if pdickt['torch'] == True:
136             idx_1 = LAMBD[0,1:-1]
137             idx_2 = LAMBD[1,1:-1]
138             idx_3 = LAMBD[0,:-2]
139             idx_4 = LAMBD[0,2:]
140             size_ = (pdickt['N'][0]-2)**2
141             idx_5 = LAMBD[1:-1,1:-1].reshape(size_)
142             idx_6 = LAMBD[1:-1,:-2].reshape(size_)
143             idx_7 = LAMBD[1:-1,2:].reshape(size_)
144             idx_8 = LAMBD[: -2,1:-1].reshape(size_)

```

```

145     idx_9 = LAMBD[2:,1:-1].reshape(size_)
146     ones_1 = np.ones(idx_1.shape)
147     ones_2 = np.ones(idx_5.shape)
148     const_ = (np.ones((1,i_rho[1:-1].shape[0])).T
149              *(((1/2)/(i_rho[1:-1])))).reshape(size_)
150     lap1 = torch.sparse_coo_tensor(np.array([idx_1, idx_1]),
151                                  -6*ones_1, op_shape, dtype=torch.float32)
152     lap2 = torch.sparse_coo_tensor(np.array([idx_1, idx_2]),
153                                  4*ones_1, op_shape, dtype=torch.float32)
154     lap3 = torch.sparse_coo_tensor(np.array([idx_1, idx_3]),
155                                  ones_1, op_shape, dtype=torch.float32)
156     lap4 = torch.sparse_coo_tensor(np.array([idx_1, idx_4]),
157                                  ones_1, op_shape, dtype=torch.float32)
158     lap5 = torch.sparse_coo_tensor(np.array([idx_5, idx_5]),
159                                  -4*ones_2, op_shape, dtype=torch.float32)
160     lap6 = torch.sparse_coo_tensor(np.array([idx_5, idx_6]),
161                                  ones_2, op_shape, dtype=torch.float32)
162     lap7 = torch.sparse_coo_tensor(np.array([idx_5, idx_7]),
163                                  ones_2, op_shape, dtype=torch.float32)
164     lap8 = torch.sparse_coo_tensor(np.array([idx_5, idx_8]),
165                                  1 - const_, op_shape, dtype=torch.float32)
166     lap9 = torch.sparse_coo_tensor(np.array([idx_5, idx_9]),
167                                  1 + const_, op_shape, dtype=torch.float32)
168     lap_ = lap1 + lap2 + lap3 + lap4 + lap5 + lap6 + lap7 + lap8 + lap9
169     lap = lap_/(pdict['res'][0]**2)
170 else:
171     lap = lil_matrix(op_shape,dtype=pdict['bitres'])
172     lap[LAMBD[0,1:-1], LAMBD[0,1:-1]] = -6
173     lap[LAMBD[0,1:-1], LAMBD[1,1:-1]] = 4
174     lap[LAMBD[0,1:-1], LAMBD[0,:-2]] = 1
175     lap[LAMBD[0,1:-1], LAMBD[0,2:]] = 1
176     lap[LAMBD[1:-1,1:-1], LAMBD[1:-1,1:-1]] = -4
177     lap[LAMBD[1:-1,1:-1], LAMBD[1:-1,:-2]] = 1
178     lap[LAMBD[1:-1,1:-1], LAMBD[1:-1,2:]] = 1
179     lap[LAMBD[1:-1,1:-1], LAMBD[:,-2,1:-1]] = 1 - ((1/2)/(i_rho[1:-1]))
180     lap[LAMBD[1:-1,1:-1], LAMBD[2:,1:-1]] = 1 + ((1/2)/(i_rho[1:-1]))
181     lap = lap/(pdict['res'][0]**2)

```

```

182
183     #elif pdict['coords'] == 'cartesian':
184
185     return lap
186
187 def build_grad(pdickt, LAMBD):
188     """
189     Gradient operators
190     """
191     if pdickt['coords'] == 'cylindrical':
192         if pdickt['torch'] == True:
193
194             idx1 = LAMBD[1:-1,:]
195             idx2 = LAMBD[:-2,:]
196             idx3 = LAMBD[2:,:]
197             idx4 = LAMBD[:,1:-1]
198             idx5 = LAMBD[:,:-2]
199             idx6 = LAMBD[:,2:]
200
201             gradrho1 = torch.sparse_coo_tensor(np.array([idx1, idx2]),
202                 -1/2, op_shape, dtype=pdickt['bitres'])
203             gradrho2 = torch.sparse_coo_tensor(np.array([idx1, idx3]),
204                 -1/2, op_shape, dtype=pdickt['bitres'])
205             GRADrho = (gradrho1+gradrho2)/pdickt['res'][0]
206
207             gradrhopos1 = torch.sparse_coo_tensor(np.array([idx1, idx1]),
208                 -1, op_shape, dtype=pdickt['bitres'])
209             gradrhopos2 = torch.sparse_coo_tensor(np.array([idx1, idx3]),
210                 -1, op_shape, dtype=pdickt['bitres'])
211             GRADrhopos = (gradrhopos1+gradrhopos2)/pdickt['res'][0]
212
213             gradrhoneg1 = torch.sparse_coo_tensor(np.array([idx1, idx2]),
214                 -1, op_shape, dtype=pdickt['bitres'])
215             gradrhoneg2 = torch.sparse_coo_tensor(np.array([idx1, idx1]),
216                 -1, op_shape, dtype=pdickt['bitres'])
217             GRADrhoneg = (gradrhoneg1+gradrhoneg2)/pdickt['res'][0]
218

```

```

219     gradz1 = torch.sparse_coo_tensor(np.array([idx4, idx5]),
220                                     -1/2, op_shape, dtype=pdict['bitres'])
221     gradz2 = torch.sparse_coo_tensor(np.array([idx4, idx6]),
222                                     -1/2, op_shape, dtype=pdict['bitres'])
223     GRADz = (gradz1+gradz2)/pdict['res'][1]
224
225     gradzpos1 = torch.sparse_coo_tensor(np.array([idx4, idx4]),
226                                         -1, op_shape, dtype=pdict['bitres'])
227     gradzpos2 = torch.sparse_coo_tensor(np.array([idx4, idx6]),
228                                         1, op_shape, dtype=pdict['bitres'])
229     GRADzpos = (gradzpos1 + gradzpos2)/pdict['res'][1]
230
231     gradzpos1 = torch.sparse_coo_tensor(np.array([idx4, idx5]),
232                                         -1, op_shape, dtype=pdict['bitres'])
233     gradzpos2 = torch.sparse_coo_tensor(np.array([idx4, idx4]),
234                                         1, op_shape, dtype=pdict['bitres'])
235     GRADzneg = (gradzpos1 + gradzpos2)/pdict['res'][1]
236
237     else:
238
239     init_sparmat = lambda shape, res : lil_matrix(shape, dtype = res)
240
241     op_shape = (pdict['N'][0]**2, pdict['N'][1]**2)
242
243     GRADrho = init_sparmat(op_shape, pdict['bitres'])
244     GRADrho[LAMBD[1:-1,:], LAMBD[:-2,:]] = -1/2
245     GRADrho[LAMBD[1:-1,:], LAMBD[2,:]] = 1/2
246     GRADrho = GRADrho/pdict['res'][0]
247
248     GRADrhopos = init_sparmat(op_shape, pdict['bitres'])
249     GRADrhopos[LAMBD[1:-1,:], LAMBD[1:-1,:]] = -1
250     GRADrhopos[LAMBD[1:-1,:], LAMBD[2,:]] = 1
251     GRADrhopos = GRADrhopos/pdict['res'][0]
252
253     GRADrhoneg = init_sparmat(op_shape, pdict['bitres'])
254     GRADrhoneg[LAMBD[1:-1,:], LAMBD[:-2,:]] = -1
255     GRADrhoneg[LAMBD[1:-1,:], LAMBD[1:-1,:]] = 1

```

```

256     GRADrhoneg = GRADrhoneg/pdict['res'][0]
257
258     GRADz= init_sparmat(op_shape, pdict['bitres'])
259     GRADz[LAMBD[:,1:-1], LAMBD[:,:-2]] = -1/2
260     GRADz[LAMBD[:,1:-1], LAMBD[:,2:]] = 1/2
261     GRADz = GRADz/pdict['res'][1]
262
263     GRADzpos= init_sparmat(op_shape, pdict['bitres'])
264     GRADzpos[LAMBD[:,1:-1], LAMBD[:,1:-1]] = -1
265     GRADzpos[LAMBD[:,1:-1], LAMBD[:,2:]] = 1
266     GRADzpos = GRADzpos/pdict['res'][1]
267
268     GRADzneg= init_sparmat(op_shape, pdict['bitres'])
269     GRADzneg[LAMBD[:,1:-1], LAMBD[:,:-2]] = -1
270     GRADzneg[LAMBD[:,1:-1], LAMBD[:,1:-1]] = 1
271     GRADzneg = GRADzneg/pdict['res'][1]
272
273
274     return GRADrho, GRADrhopos, GRADrhoneg, GRADz, GRADzpos, GRADzneg
275
276 def build_disp(pdict, LAMBD):
277     """
278     Displacement operators
279     """
280
281     if pdict['coords'] == 'cylindrical':
282         DISPrhopos = lil_matrix((pdict['N'][0]**2, pdict['N'][1]**2), dtype=pdict['bitres'])
283         DISPrhopos[LAMBD[1:,:], LAMBD[:,:-1,:]] = 1
284
285         DISPrhoneg = lil_matrix((pdict['N'][0]**2, pdict['N'][1]**2), dtype=pdict['bitres'])
286         DISPrhoneg[LAMBD[:,:-1,:], LAMBD[1:,:]] = 1
287
288         DISPzpos = lil_matrix((pdict['N'][0]**2, pdict['N'][1]**2), dtype=pdict['bitres'])
289         DISPzpos[LAMBD[:,1:], LAMBD[:,:-1]] = 1
290
291         DISPzneg = lil_matrix((pdict['N'][0]**2, pdict['N'][1]**2), dtype=pdict['bitres'])
292         DISPzneg[LAMBD[:,:-1], LAMBD[:,1:]] = 1

```

```

293
294     return DISPrhupos, DISPrhoneg, DISPzpos, DISPzneg
295
296 def build_LAP(pdickt, coord_dict, lap, grad, disp, chi_e):
297     """
298     full laplace operator (dielectric considerations)
299     """
300     if pdickt['coords'] == 'cylindrical':
301         GRADrho = grad[0]
302         GRADrhupos = grad[1]
303         GRADrhoneg = grad[2]
304         GRADz = grad[3]
305         GRADzpos = grad[4]
306         GRADzneg = grad[5]
307
308         DISPrhupos = disp[0]
309         DISPrhoneg = disp[1]
310         DISPzpos = disp[2]
311         DISPzneg = disp[3]
312
313         chi_e_half = chi_e/2
314
315         CHI1 = spdiags((1/(1+chi_e_half)).T,0, pdickt['N'][0]*pdickt['N'][1],
316                     pdickt['N'][0]*pdickt['N'][1], format='lil')
317         CHI2 = spdiags((chi_e_half*coord_dict['coords']['invrho']).T,0,
318                     pdickt['N'][0]*pdickt['N'][1], pdickt['N'][0]*pdickt['N'][1], format='lil')
319         DNEG = spdiags(DISPrhoneg.dot(chi_e_half).T,0, pdickt['N'][0]*pdickt['N'][1],
320                     pdickt['N'][0]*pdickt['N'][1], format='lil')
321         DPOS = spdiags(DISPrhupos.dot(chi_e_half).T,0, pdickt['N'][0]*pdickt['N'][1],
322                     pdickt['N'][0]*pdickt['N'][1], format='lil')
323         ZNEG = spdiags(DISPzneg.dot(chi_e_half).T,0, pdickt['N'][0]*pdickt['N'][1],
324                     pdickt['N'][0]*pdickt['N'][1], format='lil')
325         ZPOS = spdiags(DISPzpos.dot(chi_e_half).T,0, pdickt['N'][0]*pdickt['N'][1],
326                     pdickt['N'][0]*pdickt['N'][1], format='lil')
327         LAP = lap + CHI1.dot(CHI2.dot(GRADrho) + (DNEG.dot(GRADrhupos) -
328             DPOS.dot(GRADrhoneg))/pdickt['res'][0] + (ZNEG.dot(GRADzpos) -
329             ZPOS.dot(GRADzneg))/pdickt['res'][1])

```

```

330
331     #elif pdict['coords'] == 'cartesian':
332
333     return LAP
334
335 def anal_sol(pdickt):
336     z_p1 = pdickt['front_plate']['zpos']
337     z_p2 = pdickt['back_plate']['zpos']
338     d_plates = z_p1 - z_p2
339     V_p1 = pdickt['front_plate']['voltage']
340     V_p2 = pdickt['back_plate']['voltage']
341     V_diff = V_p1 - V_p2
342     d_opt = pdickt['optic']['thickness']
343     d_sub = pdickt['optic']['sub_thickness']
344     d_coat = pdickt['optic']['coat_thickness']
345     d_air = pdickt['cap_params']['d_air']
346     z_opt = pdickt['optic']['z_com']
347     p1_2_opt = z_p1 - (d_opt/2.0) - z_opt
348     opt_2_p2 = z_opt - (d_opt/2.0) - z_p2
349     eps_air = pdickt['cap_params']['air_eps']
350     eps_sub = pdickt['optic']['sub_eps']
351     eps_coat = pdickt['optic']['coat_eps']
352     CoA = pdickt['cap_params']['cap_div_area']
353     cap_ratio = CoA
354     air_ratio = d_air/eps_air
355     sub_ratio = d_sub/eps_sub
356     coat_ratio = d_coat/eps_coat
357     V_air = cap_ratio*air_ratio*V_diff
358     V_coat = cap_ratio*coat_ratio*V_diff
359     V_sub = cap_ratio*sub_ratio*V_diff
360
361     #E_front = V_diff/(p1_2_opt + opt_2_p2 + (d_opt-d_coat)/eps_sub + d_coat/eps_coat)
362     #E_sub = V_diff/((p1_2_opt + opt_2_p2 + d_coat/eps_coat)*eps_sub + (d_opt-d_coat))
363     #E_coat = V_diff/((p1_2_opt + opt_2_p2 + (d_opt-(d_coat)))/eps_sub)*eps_coat +
364         d_coat)
365     #E_back = E_front
366     z_anal = z_p2+np.array([0, opt_2_p2, (opt_2_p2 + d_sub), (opt_2_p2 + d_sub + d_coat),

```

```

367     (opt_2_p2 + d_sub + d_coat + opt_2_p2)])
368     V_anal = np.array([V_p2, V_p2 + V_air, V_p2 + V_air + V_sub, V_p2 + V_air +
369         V_sub + V_coat, V_p1])
370     anal_dict = {
371         'V_anal' : lambda z: np.interp(z, z_anal, V_anal)
372     }
373     return anal_dict
374
375 def pltxssect(loc_params, coord_dict, V):
376     if loc_params['cross_section_coord'] == 'z':
377         rho_ = coord_dict['coords']['rho'] == np.around(loc_params['rho'],
378             int(abs(np.log10(coord_dict['coords']['rho'][1]))))
379         z_ = np.logical_and(coord_dict['coords']['z']<=loc_params['z1_bound'],
380             coord_dict['coords']['z']>=loc_params['z2_bound'])
381         plt.plot(coord_dict['coords']['z'][np.logical_and(rho_,z_)],
382             V[np.logical_and(rho_, z_)])
383     if loc_params['cross_section_coord'] == 'rho':
384         z_ = coord_dict['coords']['z'] == np.around(loc_params['z'],
385             int(abs(np.log10(coord_dict['coords']['z'][1]))))
386         rho_ = np.logical_and(coord_dict['coords']['rho']<=loc_params['rho2_bound'],
387             coord_dict['coords']['rho']>=loc_params['rho1_bound'])
388         plt.plot(coord_dict['coords']['rho'][np.logical_and(rho_,z_)],
389             V[np.logical_and(rho_, z_)])

```

N.2 set_params.py

```

1 import numpy as np
2 ## Setting parameters
3 pdict = {
4     'coords' : 'cylindrical' , # coordinate system chosen for simulation box
5     'assembly' : 1 , # Establish plate geometry / location and voltage based on assembly
6     'origin' : np.array([0,0]) , # Origin of the simulation space / map
7     'size' : np.array([.04, .04]) , # Size of simulation box [m]
8     'res' : np.array([1,1])*1e-6 , # relative resolution [coord1, coord2]
9     'iters' : 100000 , # total number of time iterations

```

```

10     'iter_step' : 0.1 , # time step
11     'expbc' : False , # Exponential boundary conditions?
12     'bitres' : 'float32' , # matrix element data type ('float32' vs 'float64')
13     'in2m' : .0254 , # frequently used conversion
14     'torch': True
15 }
16
17 pdict['res_exp'] = np.ans(np.log10(pdict['res'])).astype('int')
18 pdict['aspect'] = pdict['size'][0] == pdict['size'][1]
19 pdict['N'] = (pdict['size']*(1/pdict['res']) + 1).astype('int')
20     # number of points sampled 1 dimension of simulation box
21
22 # Sample parameters
23 pdict['optic'] = {
24     "diam" : 1.0*pdict['in2m'],
25     "thickness" : .25*pdict['in2m'],
26     "z_com" : pdict['size'][1]/2,
27     "sub_eps" : 3.82, # dielectric constant for substrate (fused silica)
28     "coat_eps" : 13.436, # dielectric constant for coating material (AlGaAs / GaAs)
29     "coat_thickness" : 9.5e-6
30 }
31
32 pdict['optic']['sub_thickness'] = pdict['optic']['thickness'] - pdict['optic']['coat_thickness']
33
34 # CHOOSING ASSEMBLY CONFIGURATION
35     # Parameters established to characterize the assembly configurations:
36     # Front and back plate dimensions (usually disk diameters)
37     # Central aperture diameter
38     # Plate positioning along the beam axis with respect to simulation size center
39     # Maximum AC voltage sent on respective plates
40
41 maxhva_settings = {
42     "SVR350" : 210, # [Vpk]
43     "TREK2220" : 220, # [Vpk]
44     "TREK5/80" : 1000, # [Vpk]
45     "TREK10/10B-HS" : 1040 # [Vpk]
46 }

```

```

47
48 if pdict['assembly'] == 0 or pdict['assembly'] == 1:
49     # Setting front and back plate params (including spacing between
50     # them and voltage on respective plates)
51     # This assembly has an assortment of 3d printed spacer components
52     pdict['HVA'] = "SVR350"
53     pdict['mount_zdims'] = {
54         "back_ring" : 1e-3, # +/- 2e-4 [m]
55         "sample_holder" : 9e-3, # +/- 2e-4 [m]
56         "electrode_brace": 3e-3 , # +/- 2e-4 [m]
57         "electrode_backing": 2e-3 # +/- 2e-4 [m]
58     }
59     pdict['front_plate'] = {
60         "diam" : 3* pdict['in2m'], # diameter of plate [m]
61         "hole_diam" : 3e-3, # aperture diameter [m]
62         "thickness" : 1.5e-3,
63         "zpos" : pdict['size'][1]/2 + pdict['mount_zdims']['sample_holder']/2,
64         # location of plate surface (com) [m]
65         "voltage" : maxhva_settings[pdict['HVA']] # Voltage on front plate [V]
66     }
67     pdict['back_plate'] = {
68         "diam" : 3*pdict['in2m'],
69         "hole_diam" : 3e-3,
70         "thickness" : 1.5e-3,
71         "zpos" : pdict['size'][1]/2 - pdict['mount_zdims']['sample_holder']/2,
72         "voltage" : - maxhva_settings[pdict['HVA']]
73     }
74 elif pdict['assembly'] == 2 :
75     # Overall thickness was approximately .5 inches with a
76     # .125 inch lip on one end and .125 gap on the other end of sample.
77     # Once the sample was dropped into the mount with the
78     # surface hugging the PVC lip, it was held down with a nylon set screw
79     (with a rubberized tip.)
80     # This plate used is an aluminum rectangular plate
81     # (will incorporate cartesian coordinates into program soon.)
82     pdict['HVA'] = "SVR350"
83     pdict['mount_zdims'] = {

```

```

84     "sample_holder" : .5*pdict['in2m']
85 }
86 if pdict['coords'] == 'cartesian':
87     pdict['front_plate'] = {
88         "diam" : 0.02794, # diameter of plate [m]
89         "hole_diam" : 3e-3, # aperture diameter [m]
90         "thickness" : 1.27e-3,
91         "zpos" : pdict['size'][1]/2 + pdict['mount_zdims']['sample_holder']/2,
92         # location of plate surface (com) [m]
93         "voltage" : maxhva_settings[pdict['HVA']]/2
94         # Voltage on front plate [V] (MAX value for associated HVA)
95     }
96     pdict['back_plate'] = {
97         "diam" : 0.02794,
98         "hole_diam" : 3e-3,
99         "thickness" : 1.27e-3,
100        "zpos" : pdict['size'][1]/2 - pdict['mount_zdims']['sample_holder']/2,
101        "voltage" : - maxhva_settings[pdict['HVA']]/2
102    }
103 elif pdict['coords'] == 'cylindrical':
104     pdict['front_plate'] = {
105         "diam" : 0.02794, # diameter of plate [m]
106         "hole_diam" : 3e-3, # aperture diameter [m]
107         "thickness" : 1.27e-3,
108         "zpos" : pdict['size'][1]/2 + pdict['mount_zdims']['sample_holder']/2,
109         # location of plate surface (com) [m]
110         "voltage" : maxhva_settings[pdict['HVA']]/2 # Voltage on front plate [V]
111     }
112     pdict['back_plate'] = {
113         "diam" : 0.02794,
114         "hole_diam" : 3e-3,
115         "thickness" : 1.27e-3,
116         "zpos" : pdict['size'][1]/2 - pdict['mount_zdims']['sample_holder']/2,
117         "voltage" : maxhva_settings[pdict['HVA']]/2
118     }
119
120 elif pdict['assembly'] == 3 :

```

```

121  #Set front and back plate params
122  pdict['HVA'] = "TREK10/10B-HS"
123  pdict['mount_zdims'] = {
124      "total_zthickness" : 25.94e-3 , # holds both sample and both electrodes [m]
125      "sample_holder" : 6.94e-3 # width of lip that separates sample from electrodes [m]
126  }
127  pdict['front_plate'] = {
128      "diam" : 31.5e-3, # diameter of plate [m]
129      "hole_diam" : 3e-3, # aperture diameter [m]
130      "thickness" : 9.66e-3,
131      "zpos" : pdict['size'][1]/2 + (pdict['mount_zdims']['sample_holder']/2),
132      # location of plate surface (com) [m]
133      "voltage" : maxhva_settings[pdict['HVA']]/2
134      # Voltage on front plate [V]
135  }
136  pdict['back_plate'] = {
137      "diam" : 31.5e-3,
138      "hole_diam" : 3e-3,
139      "thickness" : 9.66e-3,
140      "zpos" : pdict['size'][1]/2 - (pdict['mount_zdims']['sample_holder']/2),
141      "voltage" : -maxhva_settings[pdict['HVA']]/2
142  }
143
144  elif pdict['assembly'] == 4 :
145      #Set front and back plate params
146      pdict['mount_zdims'] = {
147          "total_zthickness" : 25.94e-3 , # holds both sample and both electrodes [m]
148          "sample_holder" : 6.94e-3 # width of lip that separates sample from electrodes [m]
149      }
150      pdict['front_plate'] = {
151          "diam" : 31.5e-3, # diameter of plate [m]
152          "hole_diam" : 3e-3, # aperture diameter [m]
153          "thickness" : 9.66e-3,
154          "zpos" : pdict['size'][1]/2 + (pdict['mount_zdims']['sample_holder']/2),
155          # location of plate surface (com) [m]
156          "voltage" : maxhva_settings[pdict['HVA']]/2 # Voltage on front plate [V]
157      }

```

```

158 pdict['back_plate'] = {
159     "diam" : 31.5e-3,
160     "hole_diam" : 3e-3,
161     "thickness" : 9.66e-3,
162     "zpos" : pdict['size'][1]/2 - (pdict['mount_zdims']['sample_holder']/2),
163     "voltage" : - maxhva_settings[pdict['HVA']]/2
164 }
165
166 pdict['cap_params'] = {
167     "area" : np.pi*((pdict['front_plate']['diam']/2.0)**2),
168     "d_air": (pdict['mount_zdims']['sample_holder']-pdict['optic']['thickness']/2.0,
169     "air_eps" : 1.0006
170 }
171
172 pdict['cap_params']['cap_div_area'] = (pdict['optic']['sub_eps']*pdict['optic']['coat_eps']*
173     pdict['cap_params']['air_eps'])/((2.0*pdict['optic']['sub_eps']*pdict['optic']['coat_eps']*
174     pdict['cap_params']['d_air']) + (pdict['optic']['sub_eps']*pdict['cap_params']['air_eps']*
175     pdict['optic']['coat_thickness']) + (pdict['optic']['coat_eps']*
176     pdict['cap_params']['air_eps]*(pdict ['optic']['sub_thickness'])))
177 pdict['cap_params']['capacitance'] = pdict['cap_params']['cap_div_area']*
178     pdict['cap_params']['area']
179
180 # system location params / metadata
181 pdict['loc_params'] = {
182     'center of optic' : {
183         'cross_section_coord' : 'z',
184         'rho' : 0,
185         'z1_bound' : pdict['front_plate']['zpos'],
186         'z2_bound' : pdict['back_plate']['zpos']
187     },
188     'edge of hole' : {
189         'cross_section_coord' : 'z',
190         'rho' : pdict['front_plate']['hole_diam'],
191         'z1_bound' : pdict['front_plate']['zpos'],
192         'z2_bound' : pdict['back_plate']['zpos']
193     },
194     'edge of optic' : {

```

```

195     'cross_section_coord' : 'z',
196     'rho' : pdict['optic']['diam'] /2,
197     'z1_bound' : pdict['front_plate']['zpos'],
198     'z2_bound' : pdict['back_plate']['zpos']
199 },
200 'edge of plate' : {
201     'cross_section_coord' : 'z',
202     'rho' : pdict['front_plate']['diam']/2,
203     'z1_bound' : pdict['front_plate']['zpos'],
204     'z2_bound' : pdict['back_plate']['zpos']
205 },
206 'halfway out on optic' : {
207     'cross_section_coord' : 'z',
208     'rho' : pdict['optic']['diam']/4,
209     'z1_bound' : pdict['front_plate']['zpos'],
210     'z2_bound' : pdict['back_plate']['zpos']
211 },
212 'front of plate' : {
213     'cross_section_coord' : 'rho',
214     'rho1_bound' : 0,
215     'rho2_bound' : pdict['size'],
216     'z' : pdict['back_plate']['zpos']
217 },
218 'front of optic' : {
219     'cross_section_coord' : 'rho',
220     'rho1_bound' : 0,
221     'rho2_bound' : pdict['size'],
222     'z' : pdict['optic']['z.com'] + pdict['optic']['thickness']/2
223 },
224 'middle of optic' : {
225     'cross_section_coord' : 'rho',
226     'rho1_bound' : 0,
227     'rho2_bound' : pdict['size'],
228     'z' : pdict['optic']['z.com']
229 },
230 'back of optic' : {
231     'cross_section_coord' : 'rho',

```

```

232     'rho1_bound' : 0,
233     'rho2_bound' : pdict['size'],
234     'z' : pdict['optic']['z.com'] - pdict['optic']['thickness']/2
235 },
236 'back plate' : {
237     'cross_section_coord' : 'rho',
238     'rho1_bound' : 0,
239     'rho2_bound' : pdict['size'],
240     'z' : pdict['back_plate']['zpos']
241 }
242 }

```

N.3 run.py

The numerical recipe is written up fabulously in Chapter 20 of [59] for any inquiring minds.

```

1 import set_params
2 import laplace
3 import matplotlib.pyplot as plt
4 import numpy as np
5 plt.style.use('stylelib/surftex')
6 from matplotlib import cm
7 from matplotlib import rcParams
8 import time
9 import torch

```

Params Import

```

1 pdict = set_params.pdict
2 pdict

```

```

1 {'coords': 'cylindrical',
2  'assembly': 1,
3  'origin': array([0, 0]),
4  'size': array([0.04, 0.04]),
5  'res': array([0.0001, 0.0001]),
6  'iters': 100000,

```



```

44     'z2_bound': 0.0155},
45 'edge of hole': {'cross_section_coord': 'z',
46     'rho': 0.003,
47     'z1_bound': 0.0245,
48     'z2_bound': 0.0155},
49 'edge of optic': {'cross_section_coord': 'z',
50     'rho': 0.0127,
51     'z1_bound': 0.0245,
52     'z2_bound': 0.0155},
53 'edge of plate': {'cross_section_coord': 'z',
54     'rho': 0.038099999999999995,
55     'z1_bound': 0.0245,
56     'z2_bound': 0.0155},
57 'halfway out on optic': {'cross_section_coord': 'z',
58     'rho': 0.00635,
59     'z1_bound': 0.0245,
60     'z2_bound': 0.0155},
61 'front of plate': {'cross_section_coord': 'rho',
62     'rho1_bound': 0,
63     'rho2_bound': array([0.04, 0.04]),
64     'z': 0.0155},
65 'front of optic': {'cross_section_coord': 'rho',
66     'rho1_bound': 0,
67     'rho2_bound': array([0.04, 0.04]),
68     'z': 0.023175},
69 'middle of optic': {'cross_section_coord': 'rho',
70     'rho1_bound': 0,
71     'rho2_bound': array([0.04, 0.04]),
72     'z': 0.02},
73 'back of optic': {'cross_section_coord': 'rho',
74     'rho1_bound': 0,
75     'rho2_bound': array([0.04, 0.04]),
76     'z': 0.016825},
77 'back plate': {'cross_section_coord': 'rho',
78     'rho1_bound': 0,
79     'rho2_bound': array([0.04, 0.04]),
80     'z': 0.0155}}}]

```

Initializing coordinates / simulation space

```

1 # initialize coordinates
2 coord_dict = laplace.init_coords(pdict)
3
4 # Imposing a square simulation space
5 N = pdict['N'][0]
6
7 # coord vecs
8 rho = coord_dict['coords']['rho']
9 z = coord_dict['coords']['z']
10 inv_rho = coord_dict['coords']['invrho']
11
12 #indices
13 irho = coord_dict['indices']['rho']
14 iz = coord_dict['indices']['z']

```

Potential map initialization (V) with Dielectric tensor initialization (chi_e)

```

1 fV = laplace.anal_sol(pdict)

```

```

1 plt.plot(coord_dict['indices']['z']*1e-4,fV['V_anal'](coord_dict['indices']['z']*1e-4))

```

```

1 # intialize potential map, electric susceptibility, and LAMBD operator
2 V = laplace.init_V(N)
3 chi_e = laplace.init_V(N)
4 chi_e_sub = pdict['optic']['sub_eps']-1
5 chi_e_coat = pdict['optic']['coat_eps']-1
6 LAMBD = laplace.build_lambda(irho, iz, N)

```

```

1 # Translating (Dirichlet) boundary conditions to sim
2
3 # Initial value
4
5 ## (For faster convergence) setting edge values
6
7 ### Edge locations
8 r_max = (rho == max(rho))
9 r_min = (rho == min(rho))
10 z_max = (z == max(z))
11 z_min = (z == min(z))

```

```

12
13 # Boundary values
14
15 ## Plate potentials
16 fp = 'front_plate'
17 bp = 'back_plate'
18 loc_fp = np.logical_and(np.logical_and(rho>=pdict[fp]['hole_diam']/2,
19     rho<=pdict[fp]['diam']/2),z == pdict[fp]['zpos'])
20 loc_bp = np.logical_and(np.logical_and(rho>=pdict[bp]['hole_diam']/2,
21     rho<=pdict[bp]['diam']/2),z == pdict[bp]['zpos'])
22 #bc_fp = laplace.BC_dict([[pdict[fp]['hole_diam']/2, pdict[fp]['diam']/2],
23     pdict[fp]['zpos']],pdict[fp]['voltage'],fp, LAMBD)
24 #bc_bp = laplace.BC_dict([[pdict[bp]['hole_diam']/2, pdict[bp]['diam']/2],
25     pdict[bp]['zpos']],pdict[fp]['voltage'],bp, LAMBD)
26
27 # Exponential boundary conditions
28 exp_rend = rho==(max(rho)-pdict['res'][0])
29
30 exp_z0 = z==(min(z)+pdict['res'][1])
31
32 exp_zend = z==(max(z)-pdict['res'][1])
33
34 # Setting sample dielectric
35 loc_sub = np.logical_and(np.abs(z - pdict['optic']['z_com']) <
36     np.round((pdict['optic']['thickness']/2),pdict['res_exp'][1]),
37     (rho<np.round((pdict['optic']['diam']/2),pdict['res_exp'][0])))
38 loc_coat1 = np.logical_and((z==np.round(pdict['loc_params']['front of optic']['z'],
39     pdict['res_exp'][1])), (rho < np.round((pdict['optic']['diam']/2),
40     pdict['res_exp'][0])))
41 loc_coat2 = np.logical_and((z==np.round((pdict['loc_params']['front of optic']['z']-
42     pdict['res'][1]),pdict['res_exp'][1])), (rho < (np.round(pdict['optic']['diam']/2,
43     pdict['res_exp'][0])))

1 ## Initialize BCs
2
3 ##### Set susceptibility
4 chi_e[loc_sub] = chi_e_sub
5 chi_e[loc_coat1] = chi_e_coat

```

```

6 chi_e[loc_coat2] = chi_e_coat
7
8 ## Electro-static conditions
9
10 ### Electrode plates
11 V[loc_fp] = pdict[fp]['voltage']
12 V[loc_bp] = pdict[bp]['voltage']
13
14 #### Boundary values
15
16 #### Edge for faster convergance
17 V[z_min] = pdict['back_plate']['voltage']
18 V[z_max] = pdict['front_plate']['voltage']
19 V[r_max] = np.interp(np.arange(0,pdict['N'][0]),
20     np.array([0,pdict['N'][0]-1]), np.array([pdict['back_plate']['voltage'],
21     pdict['front_plate']['voltage']]))
22
23 ### Exponential (Dirichlet) boundary conditions
24 V_exp = lambda V_0, R_0, V , R : V_0 + np.exp(-R/R_0)*(V - V_0)
25 V_char = 0
26 R_char = 1.0
27
28 #rho=rho_max
29 V[r_max] = V_exp(V_char, R_char, V[exp_rend], pdict['res'][0])
30 #z=z_min
31 V[z_min] = V_exp(V_char, R_char, V[exp_z0], pdict['res'][1])
32 #z=z_max
33 V[z_max] = V_exp(V_char, R_char, V[exp_zend], pdict['res'][1])

1 #### Build operators
2 lap = laplace.build_lap(pdict, LAMBD, irho)
3 grad = laplace.build_grad(pdict, LAMBD)
4 disp = laplace.build_disp(pdict, LAMBD)
5 LAP = laplace.build_LAP(pdict, coord_dict, lap, grad, disp, chi_e)

1 t = time.time()
2 #### run sim
3 for itr in range(0, pdict['iters']):

```

```

4
5     V = V + (pdict['res'][0]*pdict['res'][0]*pdict['iter_step']*LAP.dot(V))
6
7     ## Re-applying exponential condition
8     #rho=rho_max
9     V[r_max] = V_exp(V_char, R_char, V[exp_rend], pdict['res'][0])
10    #z=z_min
11    V[z_min] = V_exp(V_char, R_char, V[exp_z0], pdict['res'][1])
12    #z=z_max
13    V[z_max] = V_exp(V_char, R_char, V[exp_zend], pdict['res'][1])
14
15    ### Re-apply Electro-static condition
16    V[loc_fp] = pdict[fp]['voltage']
17    V[loc_bp] = pdict[bp]['voltage']
18    elapsed = time.time() - t
19    print(elapsed)

```

```

1 84.81229615211487

```

```

1 fig = plt.figure(figsize = (18.5,21))
2 ax = plt.axes(projection='3d')
3 surf = ax.plot_surface(rho.reshape(N,N), z.reshape(N,N),
4     V.reshape(N,N),rstride=1,cstride=1,cmap=cm.inferno,alpha=1,
5     linewidth=10,rasterized=True)
6 fig.tight_layout()
7 ax.view_init(20,210)
8 ax.set_xlabel('r [m]')
9 ax.set_ylabel('z [m]')
10 ax.set_zlabel('[V]')
11 fig.colorbar(surf, shrink=0.4, aspect=20, pad=-0.025)
12 axes_width = fig.get_size_inches()[1]*(fig.subplotpars.right-fig.subplotpars.left)
13 right =1.095
14 left =-.15
15 fig.subplots_adjust(left=left,right=right)
16 fig.set_size_inches((fig.get_size_inches()[0],axes_width/(right-left)))
17 ax.tick_params(axis='both', pad=15)
18 axes_height = fig.get_size_inches()[1]*(fig.subplotpars.top-fig.subplotpars.bottom)
19 top = 1.15
20 bottom=-.09

```

```

21 fig.subplots_adjust(top=top,bottom=bottom)
22 fig.set_size_inches((fig.get_size_inches()[0],axes_height/(top-bottom)))

1  # Plotting potential and field profiles
2  laplace.pltxsect(pdickt['loc_params']['halfway out on optic'], coord_dict, V)
3  plt.plot(coord_dict['indices']['z']*1e-4,fV['V_anal'](coord_dict['indices']['z']*1e-4))
4
5  ## Comparison to analytical solutions

```

O Calibration code

```

1  #####
2  ##### CALIBRATION script #####
3  #####
4
5  import numpy as np
6  import matplotlib.pyplot as plt
7
8  plt.style.use('ppt2latex2')
9  plt.rcParams["font.family"] = "Times New Roman"
10
11 def transfer_function(amplitude, phase,load_corr=False,anal_tag='sr785',\
12 zload=50):
13     """
14     Takes frequency response data (amplitude and phase) combines it into a
15     complex vector
16     """
17     volt_div = lambda a, b : a/(a + b)
18
19     if load_corr == True:
20         if anal_tag == 'sr785':
21             corr = volt_div(1e6,zload)
22         if anal_tag == 'agilent':
23             corr = volt_div(50,zload)
24     else:

```

```

25     corr = 1
26
27     return 10**(amplitude/20)* np.exp(1j*(phase/180)*np.pi)/corr
28
29     # Constants
30     ef_eff = 13.3 # [[V/m]/V]
31     #ef_eff = 42 # [[V/m]/V]
32     v2hz = 1.7e6 # [Hz/V]
33     c = 299792458 # [m/s]
34     L_cav = .105 # [m]
35     nu_laser = c/(1064e-9) # [m]
36
37     # Relevant data imports
38
39     ## tf imports
40
41     tffastmag_data = np.loadtxt('fast/' + 'db.TXT').transpose()
42     tffastphase_data = np.loadtxt('fast/' + 'deg.TXT').transpose()
43     tf_fast = transfer_function(tffastmag_data[1], tffastphase_data[1])
44
45     tfslowmag_data = np.loadtxt('slow/' + 'db.TXT').transpose()
46     tfslowphase_data = np.loadtxt('slow/' + 'deg.TXT').transpose()
47     tf_slow = transfer_function(tfslowmag_data[1], tfslowphase_data[1])
48
49     home_dir = 'calib_tfs/'
50
51     ## OLG
52     G_dir = home_dir + 'OLG/'
53     Gf_mag_data = np.loadtxt(G_dir + 'SCRN0530.TXT').transpose()
54     Gf_phase_data = np.loadtxt(G_dir + 'SCRN0531.TXT').transpose()
55     Gs_mag_data = np.loadtxt(G_dir + 'SCRN0534.TXT').transpose()
56     Gs_phase_data = np.loadtxt(G_dir + 'SCRN0535.TXT').transpose()
57
58     Gf = transfer_function(Gf_mag_data[1], Gf_phase_data[1])
59     Gs = transfer_function(Gs_mag_data[1], Gs_phase_data[1])
60
61     ## A1 (HVA CH3) -> in-loop

```

```

62 A1_dir = home_dir + 'HVA_3ch/'
63 A1_mag_data = np.loadtxt(A1_dir + 'SCRN0494.TXT').transpose()
64 A1_phase_data = np.loadtxt(A1_dir + 'SCRN0495.TXT').transpose()
65 A1 = transfer_function(A1_mag_data[1], A1_phase_data[1])
66
67 ## SR560 (Summing port)
68 SR560_dir = home_dir + 'SR560/'
69 SR560_mag_data = np.loadtxt(SR560_dir + 'SCRN0454.TXT').transpose()
70 SR560_phase_data = np.loadtxt(SR560_dir + 'SCRN0455.TXT').transpose()
71 SR560_mag2_data = np.loadtxt(SR560_dir + 'SCRN0456.TXT').transpose()
72 SR560_phase2_data = np.loadtxt(SR560_dir + 'SCRN0457.TXT').transpose()
73 SR560_tf1 = transfer_function(SR560_mag_data[1], SR560_phase_data[1])
74 SR560_tf2 = transfer_function(SR560_mag2_data[1], SR560_phase2_data[1])
75
76 ## A2 (HVA trek) -> electrodes
77 A2_dir = home_dir + 'HVA_trek/'
78 A2_mag_data = np.loadtxt(A2_dir + 'trek_mag.TXT').transpose()
79 A2_phase_data = np.loadtxt(A2_dir + 'trek_phase.TXT').transpose()
80 A2 = transfer_function(A2_mag_data[1], A2_phase_data[1])
81
82 # Compute coupling efficiency (C)
83 C = lambda tf, G_, E : (L_cav/nu_laser)*
84 (tf*(1-G_)*A1*(v2hz*SR560_tf1))/(G_*A2*E)
85
86 C_fast = C(tf_fast, Gf, ef_eff)
87 C_slow = C(tf_slow, Gs, ef_eff)
88 diff = C_slow - C_fast
89
90 ## Compute differential (between fast and slow axes)
91 C_slow_mag = np.sqrt(C_slow*np.conj(C_slow))
92 C_fast_mag = np.sqrt(C_fast*np.conj(C_fast))
93 diff_mag = np.sqrt(diff*np.conj(diff))
94
95 fig, (ax1, ax2) = plt.subplots(nrows=2, sharex=True)
96 ax1.loglog(tffastmag_data[0], C_slow_mag, label = 'slow\_axis')
97 ax1.loglog(tffastmag_data[0], C_fast_mag, label = 'fast\_axis')
98 ax1.loglog(tffastmag_data[0], diff_mag, ...

```

```

99         alpha=.5, label='differential')
100 ax1.hlines(y=7e-17, xmin=20e3, xmax=40e3, ...
101           linestyle='--', linewidth=5.0, color='m')
102 ax1.tick_params(axis='y', which='minor')
103 ax1.set_xlim(tffastmag_data[0][0], tffastmag_data[0][-1])
104 ax1.set_ylabel('Coupling [[m]/[V/m]]')
105 ax1.legend()
106 ax2.semilogx(tffastmag_data[0], ...
107              (np.arctan2(np.imag(C_slow), np.real(C_slow)))...
108               *(180/np.pi), label = 'slow\_axis')
109 ax2.semilogx(tffastmag_data[0], ...
110              (np.arctan2(np.imag(C_fast), np.real(C_fast)))...
111               *(180/np.pi), label = 'fast\_axis')
112 ax2.semilogx(tffastmag_data[0], ...
113              (np.arctan2(np.imag(diff), np.real(diff))*...
114               (180/np.pi) , alpha=.5, label = 'differential')
115 ax2.set_xlim(tffastmag_data[0][0], tffastmag_data[0][-1])
116 ax2.set_ylim(-180.0, 180.0)
117 ax2.legend()
118 ax2.set_xlabel('Frequency [Hz]')
119 ax2.set_ylabel('Phase [deg]')
120 #plt.show()
121 plt.savefig('.././../figs/ALGAAS/coupling_tf.pdf', ...
122             dpi=300, format='pdf', bbox_inches='tight')

```

References

- [1] T. Hardwick, V. J. Hamedan, C. Blair, A. Green, and D. Vander-Hyde, “Demonstration of dynamic thermal compensation for parametric instability suppression in advanced ligo,” *Classical and Quantum Gravity*, vol. 37, p. 205021, Sep 2020.
- [2] A. Buikema, C. Cahillane, G. L. Mansell, C. Blair, R. Abbott, . D. Vander-Hyde ..., and J. Zweizig, “Sensitivity and performance of the advanced ligo detectors in the third observing run,” *Phys. Rev. D*, vol. 102, p. 062003, Sep 2020.
- [3] S. Tanioka, D. Vander-Hyde, G. D. Cole, S. D. Penn, and S. W. Ballmer, “Study on electro-optic noise in crystalline coatings toward future gravitational wave detectors,” *Phys. Rev. D*, vol. 107, p. 022003, Jan 2023.
- [4] A. Einstein, “Über gravitationswellen,” *Sitzungsberichte*, p. 154–167, 1918.
- [5] C. W. Misner, K. S. Thorne, and J. A. Wheeler, *Gravitation*. W. H. Freeman and Company, 1973.
- [6] B. P. Abbott, R. Abbott, T. D. Abbott, *et al.*, “Observation of gravitational waves from a binary black hole merger,” *Phys. Rev. Lett.*, vol. 116, p. 061102, Feb 2016.
- [7] B. P. Abbott *et al.*, “Gw170817: Observation of gravitational waves from a binary neutron star inspiral,” *Phys. Rev. Lett.*, vol. 119, p. 161101, Oct 2017.
- [8] A. H. Nitz, S. Kumar, Y.-F. Wang, S. Kasta, S. Wu, M. Schäfer, R. Dhurkunde, and

- C. D. Capano, “4-ogc: Catalog of gravitational waves from compact binary mergers,” *The Astrophysical Journal*, vol. 946, p. 59, mar 2023.
- [9] P. Saulson, *Interferometric Gravitational Wave Detectors (2nd edition)*. World Scientific Publishing Co. Pte. Ltd., 2017.
- [10] B. E. A. Saleh and M. C. Teich, *Fundamentals of Photonics*. Wiley Series in Pure and Applied Optics, New Jersey: Wiley, 2 ed., 2007.
- [11] R. W. P. Drever, J. L. Hall, F. V. Kowalski, J. Hough, G. M. Ford, A. J. Munley, and H. Ward, “Laser phase and frequency stabilization using an optical resonator,” *Applied Physics B*, vol. 31, pp. 97–105, 1983.
- [12] E. D. Black, “An introduction to pound–drever–hall laser frequency stabilization,” *American Journal of Physics*, vol. 69, no. 1, pp. 79–87, 2001.
- [13] C. Bond, D. Brown, A. Freise, and K. A. Strain, “Interferometer techniques for gravitational-wave detection,” *Living Reviews in Relativity*, vol. 19, p. 3, feb 2017.
- [14] D. Z. Anderson, “Alignment of resonant optical cavities,” *Appl. Opt.*, vol. 23, pp. 2944–2949, Sep 1984.
- [15] B. J. Meers, “Recycling in laser-interferometric gravitational-wave detectors,” *Phys. Rev. D*, vol. 38, pp. 2317–2326, Oct 1988.
- [16] B. P. Abbott *et al.*, “Ligo: the laser interferometer gravitational-wave observatory,” *Reports on Progress in Physics*, vol. 72, p. 076901, jun 2009.
- [17] G. Vajente, “Experimental techniques in interferometric gravitational wave detectors.” unpublished (Chapter : Optical Configurations, Accessed : 2018).
- [18] T. L. S. Collaboration, J. Aasi, *et al.*, “Advanced ligo,” *Classical and Quantum Gravity*, vol. 32, p. 074001, mar 2015.

- [19] T. Vo, *Adaptive Mode Matching in Advanced LIGO and beyond*. PhD thesis, Syracuse University, Syracuse, NY, 2019.
- [20] E. Oelker, L. Barsotti, S. Dwyer, D. Sigg, and N. Mavalvala, “Squeezed light for advanced gravitational wave detectors and beyond,” *Opt. Express*, vol. 22, pp. 21106–21121, Aug 2014.
- [21] L. S. Collaboration, “Instrument science white paper 2022-2023,” tech. rep., LIGO Scientific Collaboration, 2022. LIGO-T2200384–v2.
- [22] K. Kuns. personal communication.
- [23] J. Aasi *et al.*, “Advanced ligo,” *Classical and Quantum Gravity*, vol. 32, p. 074001, Mar. 2015.
- [24] P. Hello and J.-Y. Vinet, “Analytical models of thermal aberrations in massive mirrors heated by high power laser beams,” *Journal de Physique*, vol. 51, pp. 1267–1282, 1990.
- [25] A. F. Brooks, *Hartmann Wavefront Sensors for Advanced Gravitational Wave Interferometers*. PhD thesis, University of Adelaide, 2007.
- [26] A. F. Brooks and V. Fafone, “Thermal adaptive optics,” in *Advanced Interferometric Gravitational-Wave Detectors* (D. Reitze, P. Saulson, and H. Grote, eds.), pp. 609–637, World Scientific, 2019.
- [27] J. Ramette, M. Kasprzack, A. Brooks, C. Blair, H. Wang, and M. Heintze, “Analytical model for ring heater thermal compensation in the advanced laser interferometer gravitational-wave observatory,” *Applied Optics*, vol. 55, p. 2619, Mar 2016.
- [28] M. Jacobson, S. O’Connor, and P. Willems, “Final design of aligo tcs ring heaters and associated electronics,” tech. rep., LIGO Scientific Collaboration, 2011. LIGO-T1100034–v5.

- [29] V. J. Hamedan, C. Zhao, L. Ju, C. Blair, and D. G. Blair, "Suppression of thermal transients in advanced ligo interferometers using co2 laser preheating," *Classical and Quantum Gravity*, vol. 35, p. 115006, may 2018.
- [30] C. Cahillane, "Power up thermalization." <https://alog.ligo-wa.caltech.edu/aLOG/index.php?callRep=46553>, 2019. [aligo elog 46553].
- [31] T. T. Fricke, N. D. Smith-Lefebvre, R. Abbott, R. Adhikari, K. L. Dooley, M. Evans, P. Fritschel, V. V. Frolov, K. Kawabe, J. S. Kissel, B. J. J. Slagmolen, and S. J. Waldman, "Dc readout experiment in enhanced ligo," *Classical and Quantum Gravity*, vol. 29, p. 065005, Feb. 2012.
- [32] D. Brown, "Model of 9mhz rin higher order mode coupling." <https://alog.ligo-wa.caltech.edu/aLOG/index.php?callRep=47253>, 2019. [aligo elog 47253].
- [33] A. Brooks, "Commissioning guide for the custom hlitmy co2 mask: Step 1." <https://alog.ligo-wa.caltech.edu/aLOG/index.php?callRep=46976>, 2019. [aligo elog 46976].
- [34] G. Mansell, "Demodulating injected lines during ring heater steps so far." <https://alog.ligo-wa.caltech.edu/aLOG/index.php?callRep=47968>, 2019. [aligo elog 47968].
- [35] D. Brown, "Initial itmy mask test and 9mhz rin line." <https://alog.ligo-wa.caltech.edu/aLOG/index.php?callRep=47081>, 2019. [aligo elog 47081].
- [36] J. Driggers, "Moving itmy spot position changes 9 mhz rin coupling." <https://alog.ligo-wa.caltech.edu/aLOG/index.php?callRep=47101>, 2019. [aligo elog 27101].
- [37] J. Driggers, "Moving itmy spot position with rest of ifo aligned to match." <https://alog.ligo-wa.caltech.edu/aLOG/index.php?callRep=47117>, 2019. [aligo elog 47117].

- [38] R. B. F. H. M. . R. A. V.P.L.S., “Xxvii. a brief account of microscopical observations made in the months of june, july and august 1827, on the particles contained in the pollen of plants; and on the general existence of active molecules in organic and inorganic bodies,” *The Philosophical Magazine*, vol. 4, no. 21, pp. 161–173, 1828.
- [39] H. B. Callen and T. A. Welton, “Irreversibility and generalized noise,” *Phys. Rev.*, vol. 83, pp. 34–40, Jul 1951.
- [40] C. Zener, *Elasticity and Anelasticity of Metals*. University of Chicago Press, 1948.
- [41] Y. Levin, “Internal thermal noise in the ligo test masses: A direct approach,” *Physical Review D*, vol. 57, p. 659–663, Jan 1998.
- [42] G. M. Harry, H. Armandula, E. Black, D. R. M. Crooks, G. Cagnoli, J. Hough, P. Murray, S. Reid, S. Rowan, P. Sneddon, M. M. Fejer, R. Route, and S. D. Penn, “Thermal noise from optical coatings in gravitational wave detectors,” *Appl. Opt.*, vol. 45, pp. 1569–1574, Mar 2006.
- [43] T. Hong, H. Yang, E. K. Gustafson, R. X. Adhikari, and Y. Chen, “Brownian thermal noise in multilayer coated mirrors,” *Physical Review D*, vol. 87, Apr 2013.
- [44] G. Harry and G. Billingsley, “Fused silica, optics and coatings,” in *Advanced Interferometric Gravitational-Wave Detectors* (D. Reitze, P. Saulson, and H. Grote, eds.), pp. 521–554, World Scientific, 2019.
- [45] G. Cole, W. Zhang, M. Martin, J. Ye, and M. Aspelmeyer, “Tenfold reduction of brownian noise in high-reflectivity optical coatings,” *Nature Photonics*, vol. 7, pp. 644–650, 07 2013.
- [46] M. Abernathy, “Noise in crystalline coatings,” Tech. Rep. G1401060-v1, LIGO Scientific Collaboration, August 2014.

- [47] R. W. Boyd, *Nonlinear Optics, Third Edition*. USA: Academic Press, Inc., 3rd ed., 2008.
- [48] G. D. Cole, W. Zhang, B. J. Bjork, D. Follman, P. Heu, C. Deutsch, L. Sonderhouse, J. Robinson, C. Franz, A. Alexandrovski, M. Notcutt, O. H. Heckl, J. Ye, and M. Aspelmeyer, “High-performance near- and mid-infrared crystalline coatings,” *Optica*, vol. 3, pp. 647–656, Jun 2016.
- [49] S. Adachi, “GaAs, AlAs, and $\text{Al}_x\text{Ga}_{1-x}\text{As}$: Material parameters for use in research and device applications,” *Journal of Applied Physics*, vol. 58, pp. R1–R29, aug 1985.
- [50] A. Yariv, *Quantum Electronics (3rd. ed)*. John Wiley and Sons, 1989.
- [51] J. F. Nye, *Physical properties of crystals (Their representation by tensors and matrices)*. Oxford University Press, 1985.
- [52] E. Bonilla and M. Fejer, “Optical phase perturbations on the reflected wave of a dielectric mirror. application to the electro-optic effect in algaas coatings,” Tech. Rep. T1800528-v1, LIGO Scientific Collaboration, December 2018.
- [53] M. Fejer, “Electro-optic effects in algaas mirrors.” Private LIGO scientific collaboration document, August 2018.
- [54] S. W. Ballmer, “Photothermal transfer function of dielectric mirrors for precision measurements,” *Physical Review D*, vol. 91, Jan 2015.
- [55] N. Suzuki and K. Tada, “Elastooptic and electrooptic properties of gaas,” *Japanese Journal of Applied Physics*, vol. 23, no. 8, pp. 1011–1016, 1984.
- [56] S. Adachi, *The Handbook on Optical Constants of Semiconductors*. WORLD SCIENTIFIC, 2012.
- [57] S. Ballmer. [Syracuse University Gravitational Wave Group elog 412].

- [58] D. Vander-Hyde. [Syracuse University Gravitational Wave Group elog 831].
- [59] W. Press, *Numerical Recipes 3rd Edition: The Art of Scientific Computing*. Numerical Recipes: The Art of Scientific Computing, Cambridge University Press, 2007.
- [60] Corning, *MACOR (Machinable glass ceramic for industrial applications)*, 2012. Available at <https://www.corning.com/media/worldwide/csm/documents/71759a443535431395eb34ebeat091cb.pdf>.
- [61] B. P. Abbott *et al.*, “Observation of Gravitational Waves from a Binary Black Hole Merger,” *Phys. Rev. Lett.*, vol. 116, p. 061102, Feb 2016.
- [62] R. Abbott *et al.*, “Tests of general relativity with binary black holes from the second LIGO-Virgo gravitational-wave transient catalog,” *Phys. Rev. D*, vol. 103, p. 122002, Jun 2021.
- [63] J. Degallaix, C. Michel, B. Sassolas, A. Allocca, G. Cagnoli, L. Balzarini, V. Dolique, R. Flaminio, D. Forest, M. Granata, B. Lagrange, N. Straniero, J. Teillon, and L. Pinard, “Large and extremely low loss: the unique challenges of gravitational wave mirrors,” *J. Opt. Soc. Am. A*, vol. 36, pp. C85–C94, Nov 2019.
- [64] M. Granata, A. Amato, L. Balzarini, M. Canepa, J. Degallaix, D. Forest, V. Dolique, L. Mereni, C. Michel, L. Pinard, B. Sassolas, J. Teillon, and G. Cagnoli, “Amorphous optical coatings of present gravitational-wave interferometers,” *Classical and Quantum Gravity*, vol. 37, p. 095004, apr 2020.
- [65] S. Gras and M. Evans, “Direct measurement of coating thermal noise in optical resonators,” *Phys. Rev. D*, vol. 98, p. 122001, Dec 2018.
- [66] M. Punturo *et al.*, “The einstein telescope: a third-generation gravitational wave observatory,” *Classical and Quantum Gravity*, vol. 27, p. 194002, sep 2010.

- [67] R. X. Adhikari *et al.*, “A cryogenic silicon interferometer for gravitational-wave detection,” *Classical and Quantum Gravity*, vol. 37, p. 165003, jul 2020.
- [68] M. Evans, R. X. Adhikari, C. Afle, S. W. Ballmer, S. Biscoveanu, S. Borhanian, D. A. Brown, Y. Chen, R. Eisenstein, A. Gruson, A. Gupta, E. D. Hall, R. Huxford, B. Kamai, R. Kashyap, J. S. Kissel, K. Kuns, P. Landry, A. Lenon, G. Lovelace, L. McCuller, K. K. Y. Ng, A. H. Nitz, J. Read, B. S. Sathyaprakash, D. H. Shoemaker, B. J. J. Slagmolen, J. R. Smith, V. Srivastava, L. Sun, S. Vitale, and R. Weiss, “A horizon study for Cosmic Explorer: Science, observatories, and community,” 2021.
- [69] V. Srivastava, D. Davis, K. Kuns, P. Landry, S. Ballmer, M. Evans, E. D. Hall, J. Read, and B. S. Sathyaprakash, “Science-driven Tunable Design of Cosmic Explorer Detectors,” *The Astrophysical Journal*, vol. 931, p. 22, may 2022.
- [70] S. D. Penn, M. M. Kinley-Hanlon, I. A. O. MacMillan, P. Heu, D. Follman, C. Deutsch, G. D. Cole, and G. M. Harry, “Mechanical ringdown studies of large-area substrate-transferred GaAs/AlGaAs crystalline coatings,” *J. Opt. Soc. Am. B*, vol. 36, pp. C15–C21, Apr 2019.
- [71] G. Winkler, L. W. Perner, G.-W. Truong, G. Zhao, D. Bachmann, A. S. Mayer, J. Fellingner, D. Follman, P. Heu, C. Deutsch, D. M. Bailey, H. Peelaers, S. Puchegger, A. J. Fleisher, G. D. Cole, and O. H. Heckl, “Mid-infrared interference coatings with excess optical loss below 10 ppm,” *Optica*, vol. 8, pp. 686–696, May 2021.
- [72] T. Chalermongsak, E. D. Hall, G. D. Cole, D. Follman, F. Seifert, K. Arai, E. K. Gustafson, J. R. Smith, M. Aspelmeyer, and R. X. Adhikari, “Coherent cancellation of photothermal noise in GaAs/Al_{0.92}Ga_{0.08}As bragg mirrors,” *Metrologia*, vol. 53, pp. 860–868, mar 2016.
- [73] M. Marchiò, R. Flaminio, L. Pinard, D. Forest, C. Deutsch, P. Heu, D. Follman, and

- G. D. Cole, “Optical performance of large-area crystalline coatings,” *Opt. Express*, vol. 26, pp. 6114–6125, Mar 2018.
- [74] P. Koch, G. D. Cole, C. Deutsch, D. Follman, P. Heu, M. Kinley-Hanlon, R. Kirchhoff, S. Leavey, J. Lehmann, P. Oppermann, A. K. Rai, Z. Tornasi, J. Wöhler, D. S. Wu, T. Zederbauer, and H. Lück, “Thickness uniformity measurements and damage threshold tests of large-area GaAs/AlGaAs crystalline coatings for precision interferometry,” *Opt. Express*, vol. 27, pp. 36731–36740, Dec 2019.
- [75] S. Namba, “Electro-Optical Effect of Zincblende,” *J. Opt. Soc. Am.*, vol. 51, pp. 76–79, Jan 1961.
- [76] M. Abernathy, D. S. Penn, and E. Gustafason, “Noise Sources in Crystalline Coatings,” *LIGO Document: LIGO-G1401096*, 2014.
- [77] K. Fricke, “Piezoelectric properties of GaAs for application in stress transducers,” *Journal of Applied Physics*, vol. 70, no. 2, pp. 914–918, 1991.
- [78] R. W. P. Drever, J. L. Hall, F. V. Kowalski, J. Hough, G. M. Ford, A. J. Munley, and H. Ward, “Laser phase and frequency stabilization using an optical resonator,” *Applied Physics B: Lasers and Optics*, vol. 31, pp. 97–105, June 1983.
- [79] M. Bückle, V. C. Hauber, G. D. Cole, C. Gärtner, U. Zeimer, J. Grenzer, and E. M. Weig, “Stress control of tensile-strained $\text{In}_{1-x}\text{Ga}_x\text{P}$ nanomechanical string resonators,” *Applied Physics Letters*, vol. 113, no. 20, p. 201903, 2018.
- [80] Thorlabs Crystalline Solutions. https://www.thorlabs.com/newgrouppage9.cfm?objectgroup_ID=14069.
- [81] F. Bielsa, A. Dupays, M. Fouché, R. Battesti, C. Robilliard, and C. Rizzo, “Birefringence of interferential mirrors at normal incidence : Eeexperimental and computational study,” *Applied Physics B*, vol. 97, 07 2009.

- [82] Y. Enomoto. <https://klog.icrr.u-tokyo.ac.jp/osl/?r=8378>, 2019.
- [83] M. Abarkan, J. Salvestrini, M. Aillerie, and M. Fontana, “Frequency dispersion of electro-optical properties over a wide range by means of time-response analysis,” *Applied optics*, vol. 42, pp. 2346–53, 06 2003.
- [84] R. Spreiter, C. Bosshard, F. Pan, and P. Günter, “High-frequency response and acoustic phonon contribution of the linear electro-optic effect in dast,” *Opt. Lett.*, vol. 22, pp. 564–566, Apr 1997.
- [85] C. Bosshard, R. Spreiter, L. Degiorgi, and P. Günter, “Infrared and raman spectroscopy of the organic crystal dast: Polarization dependence and contribution of molecular vibrations to the linear electro-optic effect,” *Phys. Rev. B*, vol. 66, p. 205107, Nov 2002.
- [86] M. Evans, S. Ballmer, M. Fejer, P. Fritschel, G. Harry, and G. Ogin, “Thermo-optic noise in coated mirrors for high-precision optical measurements,” *Phys. Rev. D*, vol. 78, p. 102003, Nov 2008.
- [87] M. Abernathy *et al.*, “Crystalline Properties of Aluminum Gallium Arsenide,” *LIGO Document: LIGO-T1400344*, 2014.
- [88] L. Barsotti *et al.*, “The A+ design curve,” *LIGO Document: LIGO-T1800042*, 2018.
- [89] K. Izumi, K. Arai, B. Barr, J. Betzwieser, A. Brooks, K. Dahl, S. Doravari, J. C. Driggers, W. Z. Korth, H. Miao, J. Rollins, S. Vass, D. Yeaton-Massey, and R. X. Adhikari, “Multicolor cavity metrology,” *J. Opt. Soc. Am. A*, vol. 29, pp. 2092–2103, Oct 2012.
- [90] A. Staley *et al.*, “Achieving resonance in the Advanced LIGO gravitational-wave interferometer,” *Classical and Quantum Gravity*, vol. 31, p. 245010, nov 2014.
- [91] Y. Michimura, “Note on mirror birefringence in a Fabry-Perot cavity,” *LIGO Document: LIGO-T2200272*, 2022.

- [92] J. Yu *et al.*, “Noise contributions in crystalline mirror coatings,” *Joint Conference of the European Frequency and Time Forum & the IEEE International Frequency Control Symposium*, 2022.
- [93] A. Ananyeva, S. Appert, B. G., A. Brooks, P. Fritschel, S. Gras, M. Kasprzack, K. Kuns, and L. Zhang, “Core optics and point absorber mitigation,” tech. rep., LIGO Scientific Collaboration, 2022. LIGO-G2200853-v2.
- [94] H. T. Cao, T. Rosauer, A. Brooks, and J. Richardson, “Design requirements document for the FRont Surface Type Irradiator (FROSTI),” Tech. Rep. T2200339-v1, LIGO Scientific Collaboration, 2023.
- [95] C. Compton, D. Brown, and G. Vajente, “Design requirements document for CHETA: Central Heater for Transient Attenuation,” Tech. Rep. T2300387-v1, LIGO Scientific Collaboration, 2023.
- [96] G. Vajente, A. Brooks, M. Kasprzack, G. Billingsley, *et al.*, “Summary of the TCS and high power operation for O5 workshop,” Tech. Rep. T2300336, LIGO Scientific Collaboration, 2023.
- [97] H. Kogelnik and T. Li, “Laser beams and resonators,” *Appl. Opt.*, vol. 5, pp. 1550–1567, Oct 1966.
- [98] P. Hello and J.-Y. Vinet, “Analytical models of transient thermoelastic deformations of mirrors heated by high power cw laser beams,” *Journal De Physique*, vol. 51, pp. 2243–2261, 1990.
- [99] F. W. J. Oliver, “Bessel functions of integer order,” in *Handbook of Mathematical Functions with Formulas, Graphs, and Mathematical Tables (Partially Mathcad-enabled)* (M. Abramowitz and I. Stegun, eds.), pp. 9.1.41–45, U.S. Department of Commerce, NIST, 1972.

Daniel Vander-Hyde

Experimental Physicist / Engineer

EXPERIENCE

Graduate Student Researcher

LIGO / Syracuse University Center of Coatings Research

MAY 2019 — AUG 2024

Syracuse, NY

- Designed an innovative electro-optical study for highly reflective (HR) crystalline coatings, implementing Pound-Drever-Hall feedback.
- Successfully locked a fundamental laser mode from a Mephisto 2000 (1064 nanometer wavelength) laser to a high finesse, short length optical cavity (0.105 [meter]).
- Simulated and prototyped feedback and sensing electronics in LTspice to be built and installed in closed-loop feedback control.
- Constructed numerical simulations and computations to inform experiment design and calibration.
- Rapidly prototyped and developed custom non-conductive tabletop optical suspensions using CAD tools and 3D printing.
- Measured and published a calibrated electro-optic response from a novel HR Gallium Arsenide / Aluminum alloyed Gallium Arsenide coating, influencing the future of mirror coating investigations.

LIGO Research Fellow

LIGO Hanford Observatory (LHO)

JUN 2018 — MAY 2019

Hanford, WA

- Worked with state of the art optical components at a large scale Laser Interferometric Gravitational wave Observatory to help achieve collaboration goals during Observing Run 3 (O3).
- Led alignment / imaging and maintenance of CO2 lasers and optical sensors (Hartmann wavefront sensors) at the LHO as part of the adaptive optics commissioning.
- Demonstrated analytical skills designing digital (zero-pole-gain) filters for control loops.
- Developed and implemented a digital filter to existing thermal adaptive optics actuators for improved thermal compensation (85% faster), positively impacting productivity.
- Used optical spectrum analyzers to quantify diverse transverse optical mode content from the carrier beam at the detector output.
- Collaborated with a large team of senior engineers and physicists on a daily basis, coordinating work over weekly meetings, electronic log entries, and submitted job requests.

Undergraduate Research Assistant

LIGO, Fullerton Scatterometer

MAY 2012 — MAY 2015

Fullerton, CA

- Recorded images of scattered light from optical samples illuminated by 1064 nanometer wavelength laser light over a wide range of angles.
- Conducted experiment calibration and analysis to compute the bi-directional reflectance distribution function (BRDF) and total integrated scatter (TIS) with recorded data.
- Improved measurement and analysis techniques with upgrades to LabVIEW and Matlab code to improve measurement taking efficiency and accuracy.
- Collaborated in a small team environment (3-4 other members) with constant communication and coordination over weekly meetings and electronic logs to achieve research objectives.
- Measured and published an optical loss measurement from a novel coating solution for next-generation, quantum noise reducing, gravitational wave detector technology.

Daniel Vander-Hyde

Experimental Physicist / Engineer

EDUCATION

PhD in Physics , Syracuse University	AUG 2024
MS in Physics , Syracuse University	MAY 2017
BS in Physics , California State University, Fullerton	MAY 2015
LIGO Hanford Fellowship	2018 — 2019
STEM Fellowship	2015 — 2018

PATENTS AND PUBLICATIONS

1. Fabian Magaña Sandoval, Stefan Ballmer, Thomas Vo, Daniel Vander-Hyde, and Jax Sanders. Mode converter and quadrant photodiode for sensing optical cavity mode mismatch. U.S. Patent 10453971, Oct 2019
2. Satoshi Tanioka, Daniel Vander-Hyde, Garrett D. Cole, Steven D. Penn, and Stefan W. Ballmer. Study on electro-optic noise in crystalline coatings toward future gravitational wave detectors. *Phys. Rev. D*, 107:022003, Jan 2023
3. T Hardwick, V J Hamedan, C Blair, A C Green, and D Vander-Hyde. Demonstration of dynamic thermal compensation for parametric instability suppression in advanced ligo. *Classical and Quantum Gravity*, 37(20):205021, sep 2020
4. Fabian Magaña Sandoval, Thomas Vo, Daniel Vander-Hyde, J. R. Sanders, and Stefan W. Ballmer. Sensing optical cavity mismatch with a mode-converter and quadrant photodiode. *Phys. Rev. D*, 100:102001, Nov 2019
5. Daniel Vander-Hyde, Claude Amra, Michel Lequime, Fabian Magaña-Sandoval, Joshua R Smith, and Myriam Zerrad. Optical scatter of quantum noise filter cavity optics. *Classical and Quantum Gravity*, 32(13):135019, Jun 2015